INSTITUTE FOR NUCLEAR RESEARCH
OF THE RUSSIAN ACADEMY OF SCIENCES

EMIN-2006

Proceedings of XI International Seminar on Electromagnetic Interactions of Nuclei

Moscow, September 21-24, 2006

MOSCOW
2007

УДК 539.17

ЭМИН-2006

Труды XI Международного семинара по электромагнитным взаимодействиям ядер

Москва, 21-24 сентября 2006 года

В сборник включены доклады, представленные на XI международный семинар по электромагнитным взаимодействиям ядер. Тематика Семинара: образование мезонов и комптоновское рассеяние; нуклоны и малонуклонные системы; гигантские резонансы и ядерные взаимодействия; новые разработки и перспективы.

ISBN 978-5-94274-045-0

Содержание

MESON PRODUCTION AND COMPTON SCATTERING

NUCLEONS AND FEW-BODY SYSTEMS

GIANT RESONANSES AND NUCLEAR INTERACTIONS

NEW DEVELOPMENTS AND PERSPECTIVES

POSTERS

SUM RULES FOR TOTAL PHOTOABSORPTION CROSS-SECTIONS ON NUCLEONS AND LIGHTEST NUCLEI

S.B.Gerasimov

Bogoliubov Laboratory of Theoretical Physics, JINR, 141980 Dubna, Russia

Abstract

The questions on the presence and quantitative role of the constant terms in the real part of the high-energy photon-nucleon and photon-nucleus amplitudes, representing the contribution of the non-Regge (the fixed $j = 0$-pole) singularities in the finite-energy sum rules (FESR) for the photoabsorption cross sections on nucleons and the lightest atomic nuclei are discussed and new testable relations are presented for relevant combinations the Compton scattering amplitudes.

1 Introduction

In the 1954 seminal paper of Gell-Mann, Goldberger and Thirring (GGT)[1] on the use of the causality condition in quantum theory the first idea of the "superconvergence" sum rule technique was suggested and applied to the photonuclear absorption processes. The GGT sum rule follows from the assumption of validity of the unsubtracted dispersion relations for the presumably vanishing at $\nu \to \infty$ difference

$$\Delta T = T_{\gamma A}(\nu) - ZT_{\gamma p}(\nu) - NT_{\gamma n}(\nu) \tag{1}$$

of the forward Compton scattering amplitudes on the nucleus with atomic number $A = Z + N$ and the sum of amplitudes on the Z free protons and N free neutrons, and after inclusion of the Thompson value $-(\alpha Q^2)/M$ (M(Q) being the hadron mass and electric charge in the units of the electron charge), for every hadron amplitude $T(\nu = 0)$ at zero photon energy, the sum rule reads

$$2\pi^2 \frac{\alpha}{M_n}(\frac{-Z^2}{A} + Z) + \int_{\nu_{\gamma\pi}}^{\infty} d\nu[Z\sigma_{\gamma p}(\nu) + N\sigma_{\gamma n}(\nu) - \sigma_{\gamma A}(\nu)] = \int_{\nu_{thr}}^{\nu_{\gamma\pi}} d\nu\sigma_{\gamma A}(\nu) \tag{2}$$

The first term in l.h.s. of (2) practically coincides with the "kinetic" part of the long-known Thomas-Reiche-Kuhn sum rule for the electric dipole nuclear photoabsorption

$$\begin{aligned}\sigma_0(E1) &\equiv \int_{\nu_{thr}}^{\infty} \sigma_{E1}(\nu)d\nu = 4\pi^2\Sigma_n(E_n - E_0)|\langle n|D_z|A\rangle|^2 = 2\pi^2\langle A|[D_z[H, D_z]]|A\rangle \\ &= (2\pi^2\alpha NZ)/(AM_n) + 2\pi^2\langle A|[D_z[\hat{V}_{NN}, D_z]]|A\rangle \end{aligned} \tag{3}$$

where the first term results from the double commutator with the kinetic energy operator of the nuclear hamiltonian H. The present work is partly stemming from earlier papers of author [2, 3, 4] dealing with sum rules for total photon-hadron cross-sections

2 Towards generalized GGT sum rule

It was always tempting and rewarding to combine the power of dispersion relation approach, which is based on very general underlying assumptions and enable to explain many general properties of the scattering amplitudes as well as to get useful relations between them in a rather simple way, with particular dynamical ingredients of a given quantum system such as, for instance, implications of the broken chiral symmetry and pionic dynamics dominating peripheral properties and low-energy interactions of hadrons and nuclei.

2.1 A glance on possible role of pion degrees of freedom in GGT sum rule

In the references [2, 4] an attempt was maid to introduce the corrections to the GGT approach understood as a familiar Impulse Approximation (IA) scheme applied to the γA -forward scattering amplitude. The approximate relevance of IA is seen from the fact, that it corresponds to taking into account the singularities closest to the physical region of the peripheral scattering process ($t \leq 0$, $t = (k - k')^2$ is the invariant 4-momentum transfer for elastic scattering). The respective cut in the complex t-plane is defined by the diagrams schematically presented in Fig.1a, while the next to the leading "anomalous" threshold given by Fig.1a will be the "normal" 2π -exchange diagrams,presented in Fig.1b, with the cut starting at $t = 4m_\pi^2$.

Fig.1

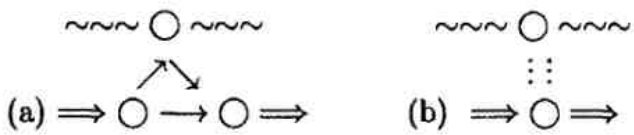

In Fig.1 the solid lines refer to nucleons and nuclei, the wavy (dotted) lines represent photons and pions. Graph (a) represents the impulse approximation (IA), while (b) defines the correction related with the nuclear "collective" pion cloud and that is effective due to short-ranged NN-correlation inside nuclei. Their relative role can qualitatively be characterized by the ratio

$$\frac{t_0(IA)}{t_0(2\pi)} \simeq \frac{8m_n\varepsilon_b}{(A-1)\cdot 4m_\pi^2} \tag{4}$$

where t_0 refers to the beginning of the respective cut in complex t-plane, m_n-mass of the nucleon, ε_b- the nuclear binding energy. For instance, this ratio is $\sim .22$ (.40 and .66) for the d (^3He and ^4He, respectively). This indicates that, naturally, the "pionic" contributions will be significantly more important compared to deuteron. The Eq.(4) also signals that, in the considered respect, the heavier nuclei situation is expected to be much alike the ^4He case because of nearly equal binding energy per nucleon.

2.2 Per aspera ad...$< A|\phi^*\phi|A >$

The further step in relevant implementation of pionic d.o.f. into the GGT sum rule was an observation inferred from models providing the convergence of the $\sigma_0(tot)$-integral. It

was first suggested [3] and then perturbatively (to one-loop order) checked [5] in scalar, ϕ^3-type "super-renormalizable" model, that the generalized Thomas-Reiche-Kuhn is valid for total photoabsorption cross section

$$\sigma_0 = \int d\nu \sigma_{tot}(\nu) = 2\pi^2 \langle \phi_1 | [D[H, D]] | \phi_1 \rangle \tag{5}$$

where the charged scalar field ϕ_1 is locally connected with two scalar fields,the ϕ_2 being charged one and other, ϕ_3,neutral. The double commutator is then interpreted via the known Schwinger-term, *i.e.* the equal-time commutator of the time- and spacial-component of e.m. current operator. Hence, the generalized, "GGT'"-sum rule, implicitly including the integrals of the absorptive parts of the amplitudes presented by the diagrams with 2π-exchanges,was written [4] in the form

$$\sigma_0^{\gamma A} - Z\sigma_0^{\gamma p} - N\sigma_0^{\gamma n} = 2\pi^2 \alpha [\frac{NZ}{Am} + \int d\vec{x} (\langle A|\phi^*\phi|A\rangle - \Sigma_i \langle N_i|\phi^*(x)\phi(x)|N_i\rangle)]. \tag{6}$$

The photonuclear sum rule including the terms $< A|\phi^*\phi|A >$ and $< N|\phi^*\phi|N >$, represented by the Feynman diagram in Fig.2

Fig.2

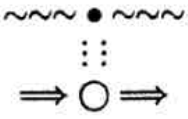

was later rediscovered [6], found as a useful exploration tool [7] and widely discussed (*e.g.*, [8] and further references therein) in view of the interesting idea about possible partial restoration of the chiral symmetry in real nuclei. The matter is that up to constant factors the matrix element corresponding to the seagull graph in Fig.2, which in the forward direction is gauge invariant and may have a direct bearing to measurable quantities, is essentially of the same structure as the matrix element represented by Fig.3

Fig.3

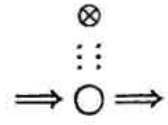

The symbol $\otimes$ denotes the local, scalar quark-current and therefore it is directly connected with the Σ_π-term, hence with the chiral symmetry breaking and its possible (partial) restoration in nuclear matter.

2.3 FESR and problem of "Big Circle" contribution

The standard FESR techniques enables one to deal with amplitudes defined in the finite region of the complex energy plane

$$f(\nu) = \frac{1}{2\pi i} \oint dz \frac{f(z)}{z - \nu} \tag{7}$$

where $f(\nu)$ is the spin-averaged, forward Compton scattering amplitude and the integration contour includes both sides of the cuts along the real axes $-R \leq \nu \leq R$ closed by a circle of a "big" radius R. As usual the problem consists in the justified and economical choice for the representation of amplitudes in the complex energy plane to fulfil the integration over the large but finite-radius circle in the complex plane.

We keep the original GGT idea of a relation between the photon-nucleus scattering amplitude and a relevant combination of the photon-nucleon amplitudes at sufficiently large photon energies, but our choice of the "superconvergent" combination of Compton amplitudes $f_{\gamma A(p,n)}$ is different from GGT.It includes amplitudes of two nuclei with $A_1 = Z_1 + N_1$, $A_2 = Z_2 + N_2$ and is assumed to satisfy the condition:

$$lim_{|\nu|\to R}[\frac{1}{A_1}f_{A_1} - \frac{1}{A_2}f_{A_2}] = \frac{Z_1N_2 - N_1Z_2}{A_1A_2}(f_p - f_n)|_{\nu=R} + \frac{S_\pi(A_1)}{A_1} - \frac{S_\pi(A_2)}{A_2} \qquad (8)$$

where

$$S_\pi(A_i) \simeq \frac{\alpha}{3}\int d^3x\langle A_i|\vec{\phi}(x)\vec{\phi}(x)|A_i\rangle \qquad (9)$$

and the scalar product in the integrand is understood to be in the isospin space.
The upper limit $\nu_{max} \equiv R$ in all integrals should be chosen from the compromise provisions.

The first term derived in the linear in A_i, $(i = 1, 2)$ approximation is parameterized through the $a_2(J^P; I^G = 2^+; 1^-)$ -Reggeon exchange in the t-channel supplemented, in addition, by the real constant term, seemingly taking place [9] in the Ref_p and referred as the residue of the $j = 0$ fixed-pole in the complex angular momentum plane. Hence one should put $R \geq 1.5 \div 2.0$ GeV to apply the Regge-pole phenomenology with usually used parameters

$$\begin{aligned} Im[f_p(\nu) - f_n(\nu)] &= (\nu/4\pi)(\sigma_p^{tot} - \sigma_n^{tot}) = b_{a_2}\nu^{1/2} \\ Re(f_p(\nu) - f_n(\nu)) &= (1/4\pi)b_{a_2}(-\nu^{1/2}) + C_p - C_n \\ \sigma_p^{tot}(\nu) - \sigma_n^{tot}(\nu) &= 24.6/\nu^{1/2} \end{aligned} \qquad (10)$$

Following [9] we accept $C_p \simeq -3.0\mu b \cdot GeV$ and put the C_n-value rather arbitrary either $C_n = (2/3)C_p$ or $C_n = 0$ for the sake of further numerical estimations.
Due to the dominant scalar-isoscalar nature of the pionic operators we accept $S_\pi(p) \simeq S_\pi(n)$ while $S_\pi(A_i) \neq 0$ will disclose its essential nonlinear dependence on the atomic number A of real nuclei.

3 Numerical results and discussion

As an example of the generalized nuclear sum rule applications we choose a pair of lightest nuclei - the deuteron and ^3He. While in the deuteron case the total photoabsorption cross section is known well above our taken $\nu_{max} \simeq 1.6\ GeV$, the $\sigma_{tot}(\gamma^3He)$ is known to $.8\ GeV$ [10], hence, in this case we have to take $\nu_{max} = .8\ GeV$. The major purpose of the using these new type nuclear sum rules may be the extraction of information about the value of difference of the nuclear matrix elements: $\Delta\Sigma_\pi = \int d\vec{x}\frac{m_\pi^2}{2}[\frac{1}{A_1} < A_1|\vec{\phi}(x)\cdot\vec{\phi}(x)|A_1 > -\frac{1}{A_2} < A_2|\vec{\phi}(x)\cdot\vec{\phi}(x)|A_2 >]$.

The term $\Delta\Sigma_\pi$ can thus be extracted from experimentally measurable quantities to give useful information on the values closely related with the chiral symmetry characteristics in real nuclei. Of special interest is the situation when $Z_1N_2 - N_1Z_2 = 0$ in (8), as for the deuteron- and ^4He-pair, to mention. The contribution of the a_2-Reggeon is then absent and the optimal value of $\nu_{max} = R$ in dispersion integrals of cross sections could probably be taken at lower value. Qualitatively, this newly chosen R-value should provide a reasonable balance between the contribution of the same group of most important nucleon resonances into the real parts of nuclear Compton amplitudes represented by terms $S_\pi(A_i)$ and the respective imaginary parts entering into dispersion integrals in form of the corresponding nuclear photo-pion production cross sections. For arbitrary $A_1 = Z_1 + N_1$ and $A_2 = Z_2 + N_2$ our general sum rule reads

$$2\pi^2[\frac{f_{A_1}(\nu=0)+S_\pi(A_1)}{A_1} - \frac{f_{A_2}(\nu=0)+S_\pi(A_2)}{A_2} + \\ + \frac{Z_1N_2 - Z_2N_1}{A_1A_2}\cdot(\frac{2b_{a_2}\nu_{max}^{1/2}}{2\pi^2} - C_p + C_n)] = \frac{\sigma_0^{\nu_{max}}(\gamma A_1)}{A_1} - \frac{\sigma_0^{\nu_{max}}(\gamma A_2)}{A_2} \qquad (11)$$

where $f_{A_i}(\nu = 0) \simeq -(\alpha Z_i^2)/(A_i m_n)$ is the Thompson zero-energy amplitude, $S_\pi(A_i)$ is defined in Eq.(9) and the integration in $\sigma_0^{\nu_{max}}$ extends from the photodisintegration threshold to the upper bound ν_{max}. In the case of ^3He and deuteron the integration was carried out with the cross-sections tabulated in [10] up to $\nu_{max} = .8\ GeV$. The low-energy integrals up to the pion photoproduction thresholds $\nu_{\gamma\pi}$ were approximated by

$$\sigma_0^{\nu_{\gamma\pi}} = 60\frac{NZ}{A}(1 + \kappa_A^{exp})\ [\mu b \cdot GeV] \qquad (12)$$

where $\kappa^{exp}_{He-3(d)} = .75 \pm .10\ (.37 \pm .11)$ following [11]. To have an idea about the scale of the S_π for nuclei considered we confronted the calculated values of

$$(2\pi^2\alpha)/(3)[(1/3)S_\pi(^3He) - (1/2)S_\pi(d)] \simeq 7.75\ (1.17)\ [\mu b \cdot GeV]$$

for $C_p = -3, C_n = -2\ (0)$ with the value

$$60\cdot[(2/9)\kappa_{^3He} - (1/4)\kappa_d] = (1/3)\cdot 40\cdot(.75\pm.10) - (1/2)\cdot 30\cdot(.37\pm.11) \simeq 4.4\pm 2.1\ [\mu b\cdot GeV]$$

representing the "potential parts" in the difference of non-relativistic TRK sum rules

$$2\pi^2\alpha[(1/3) <^3 He|[D,[V_{NN}]]|^3He > -(1/2) < d|[D,[V_{NN}]]|d >]$$

The correspondence looks reasonable because the non-relativistic value is in between two values following from more general sum rule with the differing values of C_n. We also draw attention on the strong dependence of mentioned estimations on two chosen numerical values of C_n which emphasizes the significance of sum rule as a source of new interesting information.

4 Conclusion

In view of the carried out discussion the following is especially important:
($\star$) To extend measurements of the total photoabsorption on ^3He - and ^4He -nuclei at

least up to energy of photons $1.5 \div 2.0$ GeV.
($\star\star$) To continue calculation of $< A|[D[H,D]]|A >$, $A =^{3(4)} He$, with best modern potentials as well as with estimation of relativistic corrections.

Author wishes to express his deep gratitude to organizers for invitation and support during the EMIN-2006.

References

[1] M.Gell-Mann, M.L.Goldberger and W.Thirring, Phys.Rev.**95**(1954) 1612.

[2] S.B.Gerasimov, Phys.Lett., **5**(1963) 259.

[3] S.B.Gerasimov, Phys.Lett. **13**(1964) 240.

[4] S.B.Gerasimov, in Proc.Int.Conf. on Electromagnetic Interactions at Low and Medium Energies, AN USSR, Moscow, 1972, v.3, p.382.

[5] S.B.Gerasimov and J.Moulin, Nucl.Phys. **B98** (1975) 349.

[6] S.A.Kulagin, TRK 91-39, Uni. Regensburg, 1991.

[7] M.Ericson, M.Rosa-Clot, and S.A.Kulagin, Nuovo.Cim. **A111**(1998)75.

[8] M.Ericson, G.Chanfray, J. Delorm, and M.Rosa-Clot, Nucl.Phys. **A663& 664** (2000) 369c.

[9] M.Damashek and F.J.Gilman, Phys.Rev.**D1** (1970) 1319.

[10] M.MacCormick, *et al.*, Phys.Rev.**C 53** (1996) 41.

[11] D.Drechsel and Y.E.Kim, Phys.Rev.Lett.**40** (1978) 531.

Recent N* Results from Pion Electroproduction with CLAS

Kyungseon Joo

University of Connecticut, Storrs, CT 06269, U.S.A.

Abstract. Pion electroproduction in the resonance region has been studied as a means of exploring the physics underlying the structure of the nucleon. An extensive program with the CEBAF large acceptance spectrometer (CLAS) at Jefferson Lab, is currently underway to study electromagnetic transition form factors of nucleon low-lying excitation states and their dependence on the distance scale through pseudoscaler meson electroproduction, which we discuss in this report.

Keywords: QCD, Nucleon excitation, Electromagnetic scattering
PACS: 12.38.-t, 13.60.-r

INTRODUCTION

One of the fundamental questions in hadronic physics is "What is the structure of the nucleon?" We have learned that when probing the nucleon at short distances, the quarks and gluons of QCD are the fundamental degrees of freedom. At large distances, the answer is much less clear. This is, in part, due to the complexity of solving QCD in this regime and in part, due to the lack of relevant experimental information. An extensive program with the CEBAF large acceptance spectrometer (CLAS) at Jefferson Lab, is currently underway to provide answers to this basic question of hadronic physics by studying electromagnetic transition form factors of nucleon low-lying excitation states and their dependence on the distance scale through pseudoscaler meson electroproduction (π^0, π^+ and η channels) on protons for excitation energies up to 2 GeV. We discuss recent developments in the study of the transition amplitudes of $\gamma^*N \rightarrow \Delta(1232)$ and $\gamma^*N \rightarrow P_{11}(1440)$ through pion electroproduction on protons.

POLARIZED (5TH) STRUCTURE FUNCTION $\sigma_{LT'}$

We begin with our recent advancement in the beam spin asymmetry measurements to access the 5-th structure function $\sigma_{LT'}$ in the $\Delta(1232)$ resonance [1, 2] and the second resonance regions [3]. $\sigma_{LT'}$ measures the imaginary part of the interference of longitudinal and transverse amplitudes:

$$\sigma_{LT'} \propto Im(L^*T) = Im(L)Re(T) - Re(L)Im(T) \qquad (1)$$

where L and T represent the longitudinal and transverse amplitude, respectively.

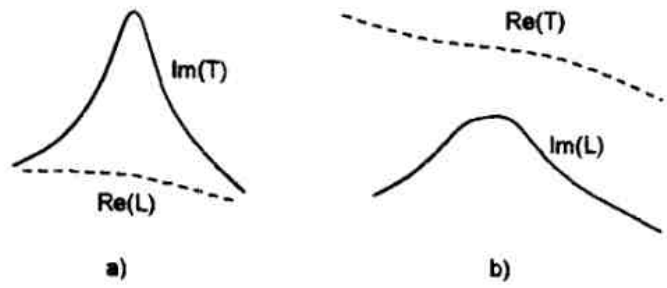

FIGURE 1. Illustration of sensitivity of $\sigma_{LT'}$ to different physics. a) Weak background $Re(L)$ buried under strong resonance $Im(T)$. b) Weak resonance $Im(L)$ buried under strong background $Re(T)$. In each case interference through Equation 1 allows the stronger amplitude to amplify the weaker amplitude, making the latter experimentally accessible.

Important information about multipole phases is available through this observable, which is important above the 2π threshold where unitarity constraints from Watson's Theorem no longer apply. Coupled channel calculations of resonance decays develop sign ambiguities which can be partially resolved using phase information. In addition, $\sigma_{LT'}$ can serve to amplify pion Born terms or other sources of non-resonant backgrounds, or to increase sensitivity to weak resonances such as Roper, as illustrated in Figure 1.

As shown in Figure 2, recent measurements of $\sigma_{LT'}$ in the $\Delta(1232)$ region [1, 2] indicate that largely real non-resonant multipoles are greatly amplified by the imaginary part of the dominant and well-determined M_{1+} resonant multipole as shown schematically in Figure 1 (a). In particular our measurement of the $\sigma_{LT'}(\pi^+ n)$ channel (Figure 2 (bottom)) was well described by several phenomenological unitary models, indicating that the dominant t-channel pion pole and Born terms are under control.

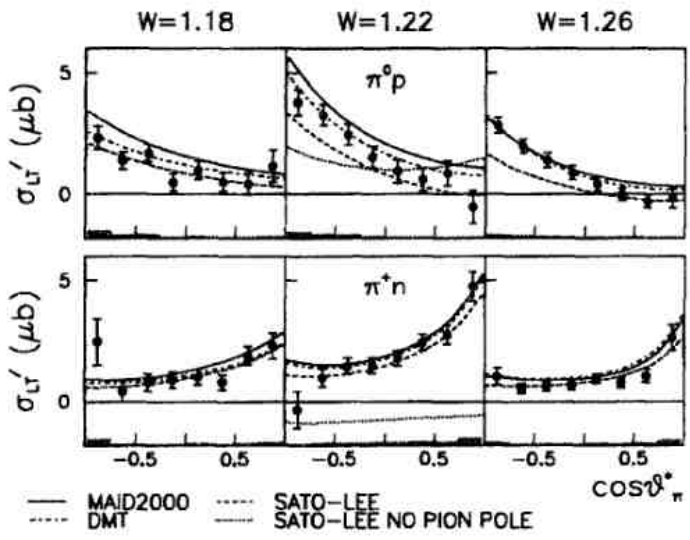

FIGURE 2. CLAS measurements of $\sigma_{LT'}$ versus $\cos\theta^*_\pi$ for the $\pi^0 p$ channel [1] (top) and for the $\pi^+ n$ channel [2] (bottom) extracted at Q^2=0.40 GeV^2 and $W = 1.18 - 1.26$ GeV. The curves show model predictions. The error bars are statistical and the shaded bars at the bottom of the figures show estimated systematic errors.

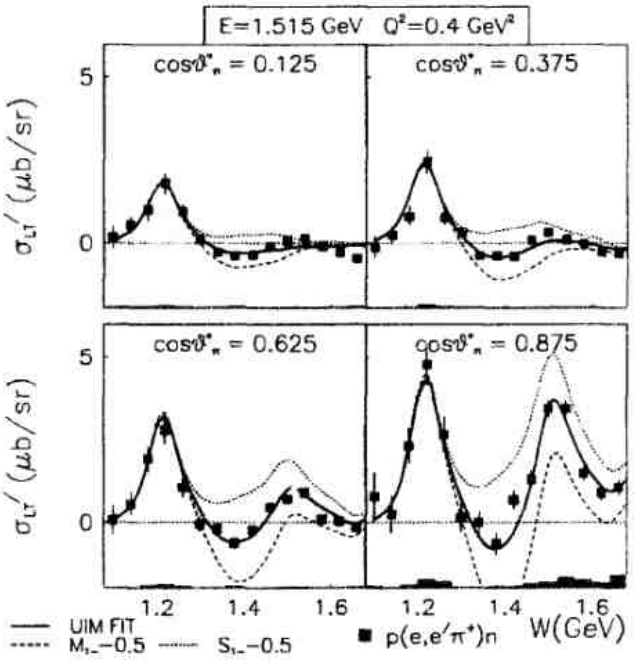

FIGURE 3. CLAS measurements of $\sigma_{LT'}$ versus W (GeV) for the π^+n channel extracted at Q^2=0.40 GeV^2 for different $\cos\theta_\pi^*$ points. The solid line shows the best fit using the Unitary Isobar Model of Aznauryan [4]. The sensitivity of $\sigma_{LT'}$ to the Roper resonance is demonstrated by the dashed and dotted curves where the Roper contributions to M_{1-} and S_{1-} are shifted by $-0.5\ \mu b^{1/2}$. The error bars are statistical and the shaded bars at the bottom of the figures show estimated systematic errors.

These contributions determine the real parts of the dominant non-resonant multipoles in the Roper resonance region and under the conditions illustrated in Figure 1 (b), the small Roper resonant multipoles, which are largely imaginary, can be greatly amplified by the well-determined non-resonant multipoles. The significance of this interference is illustrated in Figure 3, which shows the W dependence of $\sigma_{LT'}(\pi^+n)$ at $Q^2 = 0.4$ GeV^2 for different $\cos\theta_\pi^*$ bins, compared with the unitary isobar model (UIM) [4] developed at JLab. Figure 3 also shows the result of the UIM calculation after shifting the resonant part of each Roper multipole M_{1-} and S_{1-} by $-0.5\ \mu b^{1/2}$, leaving the other at the fitted value. This shift was comparable to the final fitted value of S_{1-}. It clearly shows that the sensitivity is larger in the W region where the imaginary part of the Roper multipoles is nonzero, and maximized in the forward direction due to the interference through the pion pole term.

THE $\gamma^*N \rightarrow \Delta(1232)$ TRANSITION FORM FACTORS

The first results [5] was published for the $N \rightarrow \Delta(1232)$ transition from CLAS data in the Q^2 range of 0.4 – 1.8 GeV^2 in 2002. The new results in the Q^2 range of 3.0 – 6.0 GeV^2 were recently published in Phys. Rev. Lett [6]. With extensive coverage over angles and energies and polarization observables, the pion electroproduction data from CLAS have allowed nearly model-independent determinations of $\gamma^*N \rightarrow \Delta(1232)$ transition form

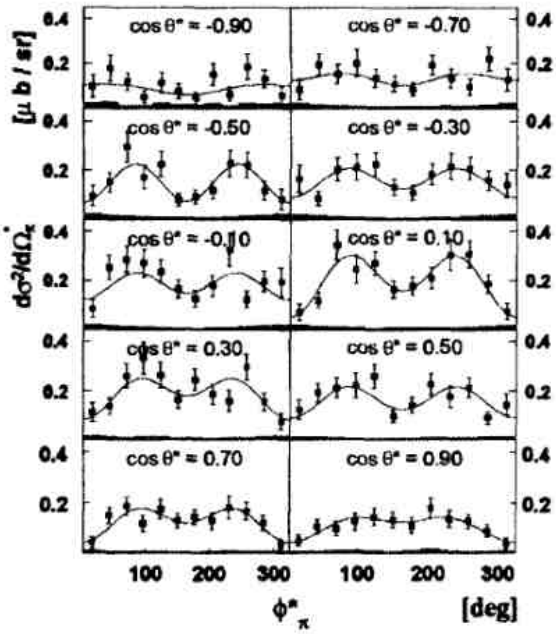

FIGURE 4. The extracted differential cross section of $\gamma^* p \to p\pi^0$ as a function of ϕ_π^* for each $\cos(\theta_\pi^*)$ bin in the center-of-mass system at W=1.25 GeV^2 and Q^2=4.2 GeV^2. The error bars are statistical, and the gray band at the bottom of each panel corresponds to the systematic. The solid curves represent the fit using UIM [4].

factors. Typical differential cross sections in $p\pi^0$ center-of-mass system are shown in Figure 4 for invariant energy W near the $\Delta(1232)$ peak.

In order to extract the $\Delta(1232)$ multipoles M_{1+}, E_{1+} and S_{1+}, the unitary isobar model (UIM) [4], developed at JLab, was used. This model incorporates the isobar approach as in Reference [8]. The non-resonant background consists of the Born term and the t-channel ρ and ω contributions. To calculate the Born term the latest available measurements of the nucleon and pion form factors are used. Underlying tails from resonances such as the $P_{11}(1440)$, $D_{13}(1520)$ and $S_{11}(1535)$, which are modeled as Breit–Wigner shapes, are also incorporated. The contributions of these resonances are evaluated according to information known from world data and the latest CLAS measurements. The dependence of the extracted results on uncertainties due to the non-resonant and higher resonance contributions is included in the systematic errors.

Figure 5(a) shows the extracted amplitude ratios $R_{EM} = E_{1+}/M_{1+}$ and $R_{SM} = S_{1+}/M_{1+}$. It can be seen that R_{EM} is small and negative over the entire Q^2 range, indicating strong helicity non-conservation while R_{SM} is negative and its magnitude increases as a function of Q^2. Our results suggest that the region of Q^2 where pQCD processes would be expected to be valid is higher than currently accessible. Adding to the controversy, Reference [9] has suggested that pQCD can possibly be invoked without strict helicity conservation if orbital angular momentum flips are included into the perturbative reaction mechanism. The prediction for R_{SM} of Reference [9] is shown in Figure 5(a) (lower panel). Figure 5(b) shows the extracted $G_M^*/3G_D$ ratio as a function of Q^2 where G_M^* is the $N \to \Delta$ form factor and $G_D = (1 + Q^2/0.71)^{-2}$. The most notable feature is that G_M^* decreases with Q^2 faster than the elastic magnetic

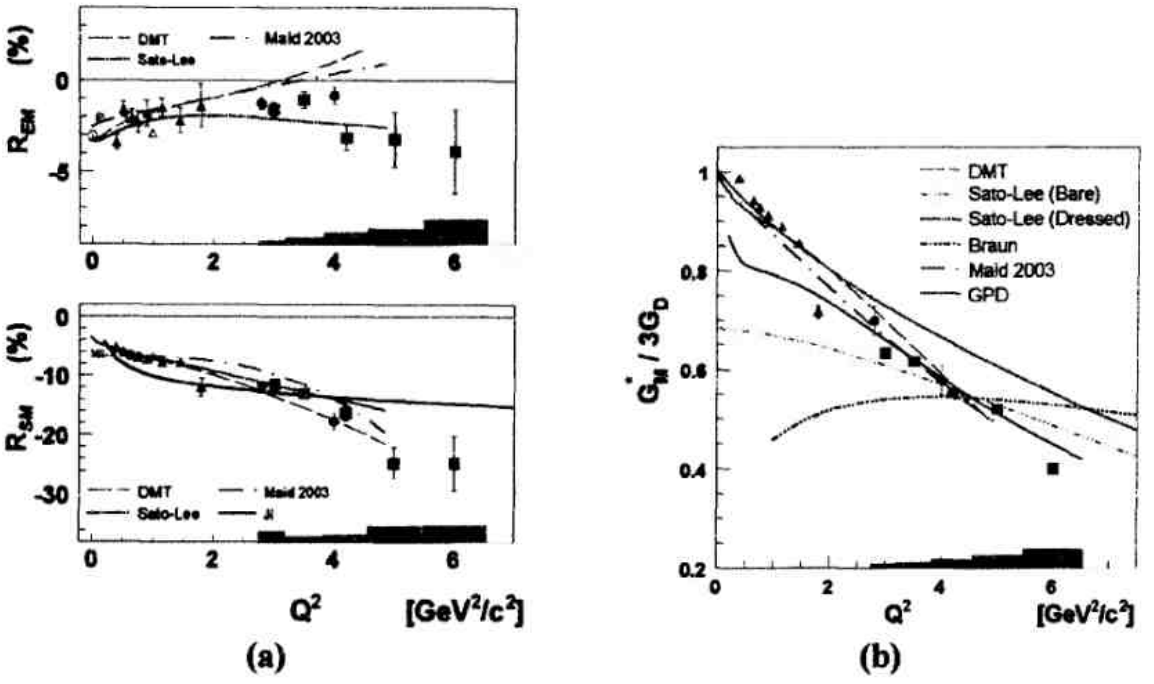

FIGURE 5. (a) Upper panel: the electric quadrupole amplitude relative to the magnetic dipole amplitude, $R_{EM} = E_{1+}/M_{1+}$. Bottom panel: the scaler amplitude relative to the magnetic dipole amplitude, $R_{SM} = S_{1+}/M_{1+}$. (b) The $N \rightarrow \Delta$ form factor $G_M^*/3G_D$. The errors shown are statistical, while estimated systematic errors are shown as gray bars at the bottom of the graph.

form factor. This is consistent with Reference [10], which pointed out that, through the application of chiral symmetry, G_M^* can be directly related to the isovector part of the nucleon elastic form factors. This idea was applied in the framework of Generalized Parton Distributions (GPDs) by Reference [11], and later by Reference [12], to suggest that the falloff of G_M^* is related to the falloff of G_E^p [13] through their common isovector form factor.

THE $\gamma^* N \rightarrow P_{11}(1440)$ TRANSITION FORM FACTORS

For the first time the amplitudes for the Roper resonance have been determined from pion electroproduction of both π^0 and π^+ channels. Especially, new results of the beam spin asymmetry measurements show a large sensitivity to the Roper amplitudes in the $n\pi^+$ channel through their interference with non-resonant backgrounds [3]. The $N \rightarrow P_{11}(1440)$ transition amplitudes $A_{1/2}^p$ and $S_{1/2}^p$ extracted from the global analysis of the UIM calculation [4] are shown in Figure 6, compared to recent quark model calculations of the Roper transition form factors [15, 16, 17, 18]. Also shown is a point at $Q^2 = 1.0$ GeV^2 from a recent Jefferson Lab/Hall A experiment by Laveissiere *et al.* [14] based on a MAID03 analysis of backward angle π^0 electroproduction. All the electroproduction points include model errors, and the plotted CLAS points are the average of UIM and dispersion relation fits [4]. The experimental result of a non-zero longitudinal coupling of the Roper appears to rule out the gluonic hybrid model [15] that

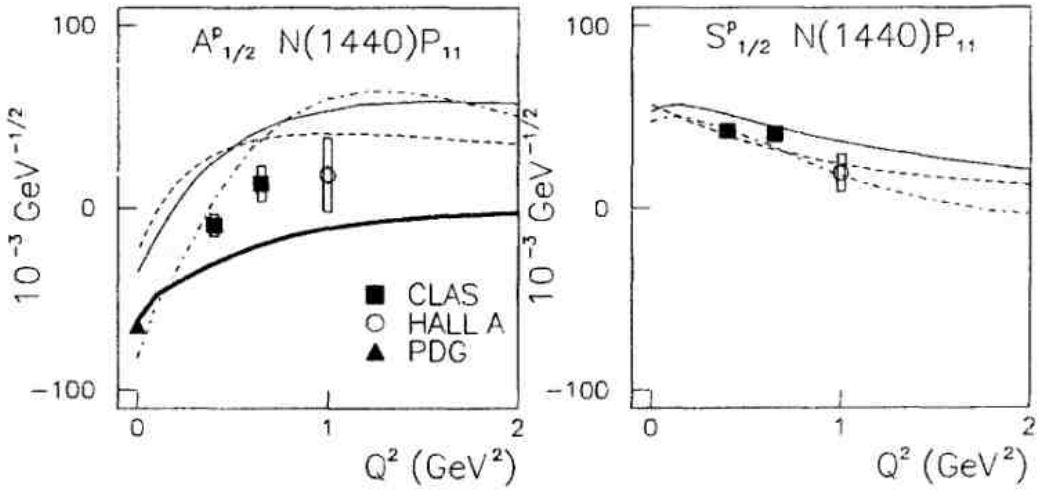

FIGURE 6. Summary of recent measurements showing the Q^2 dependence of the $P_{11}(1440)$ photocoupling amplitudes $A^p_{1/2}$ (left) and $S^p_{1/2}$ (right). The current measurement from CLAS includes model errors arising from the dispersion relations and UIM fits [4]. The data from Hall A [14] show the MAID03 fit model error. Quark model calculations are indicated by bold [15], solid [16], dashed [17] and dot-dashed [18] lines.

predicts the longitudinal amplitude to be identically zero.

SUMMARY

The recent effort of the CLAS collaboration in studying electromagnetic nucleon resonance transition form factors at increasingly short distances has resulted in a strong empirical evidence of large meson contributions to the resonance excitations at large and medium distances. This is particularly evident in the region of the $\gamma^* N\Delta(1232)$ transition where constituent quark models (CQM) are unable to explain the considerably larger strength of the magnetic dipole transition from what is predicted from quark contributions alone [19]. Also, the electric quadrupole transition moment usually expressed through the ratio $R_{EM} = E_{1+}/M_{1+}$ at the resonance pole, is much larger ($R_{EM} \approx 2-4\%$) than the predicted $R_{EM}^{CQM} < 0.5\%$. In the region of the Roper resonance $P_{11}(1440)$, the transverse transition amplitude $A_{1/2}(Q^2)$ shows a strong Q^2 dependence at small photon virtualities, even changing sign in the range $Q^2 = 0.5-1$ GeV^2 [4] as shown in Figure 6 (left). Moreover, the longitudinal transition amplitude $S_{1/2}$ is large at small Q^2, also indicating strong hadronic contributions to the resonance transition strength as shown in Figure 6 (right). This empirical information is best explained by large meson cloud effects. It is also supported by calculations within the chiral quark model [20] that discuss the role of these $q\bar{q}$ components in the wave function of the excited states, as well as of the nucleon.

REFERENCES

1. K. Joo *et al.*, Phys. Rev. **C68**, 033201 (2003).

2. K. Joo *et al.*, Phys. Rev. **C70**, 042201 (2004).
3. K. Joo *et al.*, Phys. Rev. **C72**, 058202 (2005).
4. I. Aznauryan *et al.*, Phys. Rev. **C71**, 015201 (2005).
5. K. Joo *et al.*, Phys. Rev. Lett. **88**, 122001 (2002).
6. M. Ungaro *et al.*, Phys. Rev. Lett. **97**, 112003 (2006).
7. H. Egiyan *et al.*, Phys. Rev. **C72**, 025204 (2006).
8. D. Drechsel, O. Hanstein, S.S. Kamalov and D. Drechsel, Nucl. Phys. **A645**, 145 (1999).
9. X. Ji, J.P. Ma and F. Yuan, Phys. Rev. Lett. **90**, 241601 (2003).
10. K. Goeke, M.V. Polyakov and M. Vanderhaegen, Prog. Part. Nucl. Phys. **47**, 401 (2001).
11. P. Stoler, Phys. Rev. Lett. **91**, 172303 (2003).
12. M. Guidal, M.V. Polyakov, A.V. Radyushkin and M. Vanderhaegen, Phys. Rev. **D72**, 054013 (2005).
13. O. Gayou *et al.*, Phys. Rev. **C64**, 038202 (2001).
14. G. Laveissiere *et al.*, Phys. Rev. **C69**, 045203 (2004).
15. Z. Li, V.D. Burkert and Z. Li, Phys. Rev. **D46**, 70 (1992).
16. S. Capstick and B.D. Keister, Phys. Rev. **D51**, 3598 (1995).
17. S. Simula, Proceedings of the Workshop on The Physics of Excited Nucleons, NSTAR 2001, p.135.
18. F. Cano and P. Gonzalez, Phys. Lett. **B431**, 270 (1998).
19. R.A. Arndt *et al.*, Phys. Rev. **C66**, 055213 (2002).
20. Q.B. Li and D.O. Riska, nucl-th/0605076.

PION POLARIZABILITIES

L.V. Fil'kov and V.L. Kashevarov
Lebedev Physical Institute, Leninsky Prospect 53, 119991 Moscow, Russia

1 Introduction

Pion polarizabilities are fundamental structure parameters characterizing the behavior of the pion in an external electromagnetic field. The dipole and quadrupole polarizabilities are defined [1, 2] through the expansion of the non-Born helicity amplitudes of the Compton scattering on the pion over t at the fixed $s = \mu^2$

$$\begin{aligned} M_{++}(s=\mu^2,t) &= \pi\mu\left[2(\alpha_1-\beta_1)+\frac{t}{6}(\alpha_2-\beta_2)\right]+\mathcal{O}(t^2), \\ M_{+-}(s=\mu^2,t) &= \frac{\pi}{\mu}\left[2(\alpha_1+\beta_1)+\frac{t}{6}(\alpha_2+\beta_2)\right]+\mathcal{O}(t^2), \end{aligned} \tag{1}$$

where s (t) is the square of the total energy (momentum transfer) in the $\gamma\pi$ c.m. system and μ is the pion mass. The dipole electric (α_1) and magnetic (β_1) pion polarizabilities measure the response of the pion to quasistatic electric and magnetic fields. On the other hand, the parameters α_2 and β_2 measure the electric and magnetic quadrupole moments induced in the pion in the presence of an applied field gradient. In the following the dipole and quadrupole polarizabilities are given in units 10^{-4}fm^3 and 10^{-4}fm^5, respectively.

The values of the pion polarizabilities are very sensitive to predictions of different theoretical models. Therefore, an accurate experimental determination of these parameters are very important for testing the validity of such models.

By now the values of the pion polarizabilities were determined by analysing processes $\pi^-A \to \gamma\pi^-A$, $\gamma p \to \gamma\pi^+n$, and $\gamma\gamma \to \pi\pi$. In the present work we mainly analyse the results obtained in recent works [2–5]

2 π^0 meson polarizabilities

At present the most reliable method of a determination of the π^0 meson polarizabilities is an analysis of the process $\gamma\gamma \to \pi^0\pi^0$ in the energy region up to ~ 2 GeV where the cross section of this process is very sensitive to the values of the π^0 polarizabilities. This process is described by the following invariant variables:

$$t=(k_1+k_2)^2, \quad s=(q_1-k_1)^2, \quad u=(q_1-k_2)^2, \tag{2}$$

where $q_1(q_2)$ and $k_1(k_2)$ are the pion and photon four-momenta. The cross section of the process $\gamma\gamma \to \pi^0\pi^0$ is expressed through the helicity amplitudes as follows

$$\frac{d\sigma_{\gamma\gamma\to\pi^0\pi^0}}{d\Omega}=\frac{1}{256\pi^2}\sqrt{\frac{(t-4\mu^2)}{t^3}}\left\{t^2|M_{++}|^2+\frac{1}{16}t^2(t-4\mu^2)^2\sin^4\theta^*|M_{+-}|^2\right\}, \tag{3}$$

where θ^* is the angle between the photon and the pion in the c.m.s. of the process under consideration.

In order to analyse the process $\gamma\gamma \to \pi^0\pi^0$ we constructed dispersion relations (DRs) at fixed t with one subtraction at $s = \mu^2$ for the helicity amplitude $M_{++}(s,t)$ [2]

$$ReM_{++}(s,t) = ReM_{++}(s=\mu^2,t) + \frac{(s-\mu^2)}{\pi} P \int\limits_{4\mu^2}^{\infty} ds'\, ImM_{++}(s',t) \left[\frac{1}{(s'-s)(s'-\mu^2)} - \frac{1}{(s'-u)(s'-\mu^2+t)} \right]. \quad (4)$$

Via the cross symmetry these DRs are identical to DRs with two subtractions. The subtraction function $ReM_{++}(s=\mu^2,t)$ was determined with the help of the DRs at fixed $s = \mu^2$ with two subtractions using the cross symmetry between the s and u channels

$$ReM_{++}(s=\mu^2,t) = M_{++}(s=\mu^2,0) + t\frac{dM_{++}(s=\mu^2,t)}{dt}\bigg|_{t=0} + \frac{t^2}{\pi}\left\{ P\int\limits_{4\mu^2}^{\infty} \frac{ImM_{++}(t',s=\mu^2)\,dt'}{t'^2(t'-t)} + \int\limits_{4\mu^2}^{\infty} \frac{ImM_{++}(s',u=\mu^2)\,ds'}{(s'-\mu^2)^2(s'-\mu^2+t)} \right\}. \quad (5)$$

The DRs for the amplitude $M_{+-}(s,t)$ had the same expressions (4) and (5) with substitutions: $M_{++} \to M_{+-}$ and $ImM_{++} \to ImM_{+-}$.

The subtraction constants were expressed through the sum and the difference of the electric and magnetic polarizabilities taking into account Eq. (1):

$$M_{++}(s=\mu^2,t=0) = 2\pi\mu(\alpha_1-\beta_1)_{\pi^0}, \quad \frac{dM_{++}(s=\mu^2,t)}{dt}\bigg|_{t=0} = \frac{\pi\mu}{6}(\alpha_2-\beta_2)_{\pi^0}, \quad (6)$$

$$M_{+-}(s=\mu^2,t=0) = \frac{2\pi}{\mu}(\alpha_1+\beta_1)_{\pi^0}, \quad \frac{dM_{+-}(s=\mu^2,t)}{dt}\bigg|_{t=0} = \frac{\pi}{6\mu}(\alpha_2+\beta_2)_{\pi^0}. \quad (7)$$

These DRs were used to fit the experimental data to the total cross section of the process $\gamma\gamma \to \pi^0\pi^0$. The DRs were saturated by the contribution of $\rho(770)$, $\omega(782)$, and $\phi(1020)$ mesons in the s channel and σ, $f_0(980)$, $f_0(1370)$, $f_2(1270)$, and $f_2(1525)$ in t channel. The polarizabilities $(\alpha_1 \pm \beta_1)_{\pi^0}$ and $(\alpha_2 \pm \beta_2)_{\pi^0}$ and parameters of the σ meson were considered as free parameters.

For the reaction under consideration the Born term is equal to zero and the main contribution in the energy region $\sqrt{t}$ =270–825 MeV is determined by S wave. So, this process gives a good possibility to search for the σ meson. The parameters of such a σ meson and the values of the dipole polarizabilities have been found from the fit to the experimental data [6] in the energy regions 270–825 MeV and 270–2000 MeV, respectively [3]. The values of the quadrupole polarizabilities have been determined from the fit to experimental data [6, 7] in the energy region 270–2250 MeV [2].

The result of the fit to the experimental data for the total cross section [6, 7] in the energy region from the threshold to 2250 MeV is presented in Fig. 1 by solid curve [2]. The dashed curve corresponds to the quadrupole polarizabilities calculated with the help of the dispersion sum rules (DSRs) from Ref. [2]. The full circles are data from Ref. [6] and the open ones are data from Ref. [7].

The following parameters of the σ meson have been determined in the Ref. [3]: $m_\sigma = 547 \pm 45$ MeV, $\Gamma_\sigma = 1204 \pm 362$ MeV, $\Gamma_{\sigma\to\gamma\gamma} = 0.62 \pm 0.19$ keV. This value of $\Gamma_{\sigma\to\gamma\gamma}$ differs strongly from the result of Ref. [8] [$\Gamma_{\sigma\to\gamma\gamma} = (3.8 \pm 1.5)$ keV]. It should be noted that the

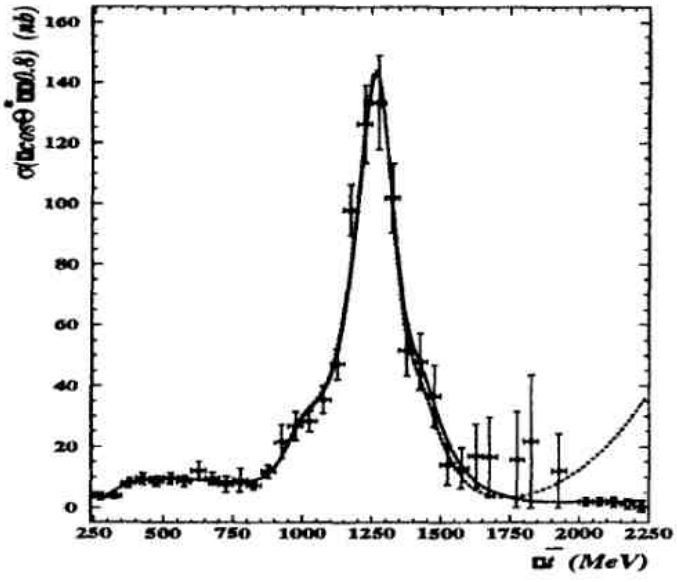

Figure 1: The total cross section of the reaction $\gamma\gamma \to \pi^0\pi^0$.

Table 1: The dipole and quadrupole polarizabilities of the π^0 meson

	fit	DSRs [2]	ChPT
$(\alpha_1 - \beta_1)_{\pi^0}$	-1.6 ± 2.2 [3] -0.6 ± 1.8 [9]	-3.49 ± 2.13	-1.9 ± 0.2 [11]
$(\alpha_1 + \beta_1)_{\pi^0}$	0.98 ± 0.03 [3] 1.00 ± 0.05 [10]	0.802 ± 0.035	1.1 ± 0.3 [11]
$(\alpha_2 - \beta_2)_{\pi^0}$	39.70 ± 0.02 [2]	39.72 ± 8.01	37.6 ± 3.3 [12]
$(\alpha_2 + \beta_2)_{\pi^0}$	-0.181 ± 0.004 [2]	-0.171 ± 0.067	0.04 [12]

use of the value of $\Gamma_{\sigma\to\gamma\gamma} = (3.8 \pm 1.5)$ keV in the analysis [2] leads to a strong deviation from the experimental data on the total cross section of the process under consideration.

The values of the dipole and quadrupole polarizabilities found in the fits [2,3] are listed in Table 1 together with results obtained in Refs. [9,10] and prediction of DSRs [2] and two loop calculations in the frame of ChPT [11,12]. The obtained values of the sum and difference of the dipole polarizabilities of π^0 and the difference of its quadrupole polarizabilities do not conflict within the errors with the predictions of DSRs and ChPT. However, there are very big errors in the experimental values for the difference of the dipole polarizabilities. Therefore, it is difficult to do a more unambiguous conclusion. As for the sum of the quadrupole polarizabilities of π^0, the DSR result agrees well with the experimental value, but the ChPT predicts a positive value in contrast to experimental result. However, as it was noted in Ref. [12], this quantity was obtained in a two-loop approximation, which is a leading order result for this sum, and one expects substantial corrections to it from three-loop calculations.

It should be noted that the values of the difference and the sum of the quadrupole polarizabilities found from the fit have very small errors. They are the errors of the fitting. This is a result of a very high sensitivity of the total cross section of the process $\gamma\gamma \to \pi^0\pi^0$ at $\sqrt{t} > 1500$ MeV to values of these parameters. In order to estimate real values of errors of these difference and sum, model errors should be added.

3 Measurement of the π^+ meson polarizabilities via the $\gamma p \to \gamma \pi^+ n$ reaction

The pion polarizability can be extracted from experimental data on radiative pion photoproduction, either by extrapolating these data to the pion pole [13–16], or by comparing the experimental cross section with the predictions of different theoretical models. The extrapolation method was first suggested in [17] and has been widely used for the determination of cross sections and phase shifts of elastic $\pi\pi$-scattering from the reaction $\pi N \to \pi\pi N$. For investigations of $\gamma\pi^+$-scattering this method was first used in [18, 19].

However, in order to obtain a reliable value of the pion polarizability, it is necessary to obtain the experimental data on pion radiative photoproduction with small errors over a sufficiently wide region of t, in particular very close to $t = 0$ [20, 21].

It should be noted that there is an essential difference in extrapolating the data of the processes $\pi N \to \pi\pi N$ and $\gamma p \to \gamma\pi N$. In the former case, the pion pole amplitude gives the main contribution in a certain energy region. This permits one to constrain the extrapolation function to be zero at $t = 0$ providing a precise determination of the amplitude. In the case of radiative pion photoproduction, the pion pole amplitude alone is not gauge invariant and we must take into account all pion and nucleon pole amplitudes. However, the sum of these amplitudes does not vanish at $t = 0$. This complicates the extrapolation procedure by increasing the requirements on the accuracy of the experimental data.

As the accuracy of the data [4] was not sufficient for a reliable extrapolation, the values of the pion polarizabilities have been obtained from a fit of the cross section calculated by different theoretical models to the data.

The theoretical calculations of the cross section for the reaction $\gamma p \to \gamma\pi^+ n$ showed that the contribution of nucleon resonances is suppressed for photons scattered backward in the c.m.s. of the reaction $\gamma\pi \to \gamma\pi$. Moreover, integration over φ and $\theta^{cm}_{\gamma\gamma'}$ essentially decreases the contribution of resonances from the crossed channels. On the other hand, the difference $(\alpha_1 - \beta_1)_{\pi^+}$ gives the biggest contribution to the cross section for $\theta^{cm}_{\gamma\gamma'}$ in the region of $140° - 180°$. Therefore, we considered the cross section of radiative pion photoproduction integrated over φ from 0° to 360° and over $\theta^{cm}_{\gamma\gamma'}$ from 140° to 180°,

$$\int_0^{360°} d\varphi \int_{-1}^{-0.766} d\cos\theta^{cm}_{\gamma\gamma'} \frac{d\sigma_{\gamma p \to \gamma\pi^+ n}}{dt ds_1 d\Omega_{\gamma\gamma}}, \tag{8}$$

where $s_1 = (q_1 + k_1)^2$ is the square of the total energy in c.m. system for the $\gamma\pi \to \gamma\pi$ reaction, $t = (p_p - p_n)^2 \simeq -2mT_n$ is the square of the momentum transfer for the $\gamma p \to \gamma\pi^+ n$ reaction and T_n is the kinetic energy of the neutron.

The cross section of the process $\gamma p \to \gamma\pi^+ n$ has been calculated in the framework of two different models. In the first model (model-1) the contribution of all the pion and nucleon pole diagrams was taken into account using pseudoscalar pion-nucleon coupling [22].

The second model (model-2) included the nucleon and the pion pole diagrams without the anomalous magnetic moments of the nucleons and in addition the contributions of the resonances $\Delta(1232)$, $P_{11}(1440)$, $D_{13}(1520)$, $S_{11}(1535)$, and σ meson.

The experiment on the radiative π^+ meson photoproduction was carrie out at the Mainz Microtron MAMI in the energy region 537 MeV< E_γ <817 MeV.

To increase our confidence that the model dependence of the result was under control we limited ourselves to kinematic regions where the difference between model-1 and model-2 did not exceed 3% when $(\alpha_1 - \beta_1)_{\pi^+}$ was constrained to zero. First, the kinematic region, where

the contribution of the pion polarizability is negligible, i.e. the region $1.5\mu^2 \leq s_1 < 5\mu^2$, was considered.

In Fig. 2, the experimental data for the differential cross section, averaged over the full

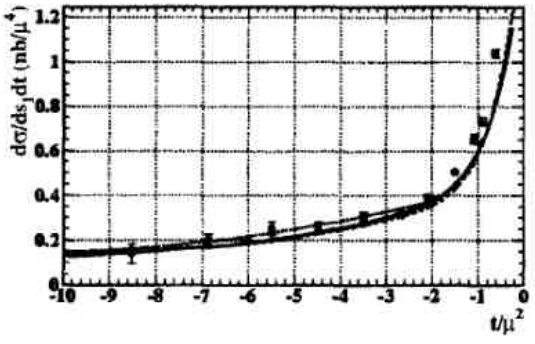

Figure 2: The differential cross section of the process $\gamma p \to \gamma\pi^+ n$ averaged over the full photon beam energy interval and over s_1 from $1.5\mu^2$ to $5\mu^2$

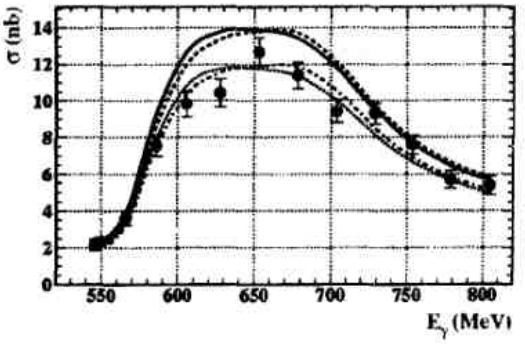

Figure 3: The differential cross section of the process $\gamma p \to \gamma\pi^+ n$ integrated over s_1 and t in the region, where the contribution of the pion polarizability is biggest.

photon beam energy interval from 537 MeV up to 817 MeV and over s_1 in the indicated interval, are compared to predictions of model-1 (dashed curve) and model-2 (solid curve). The dotted curve is the fit of the experimental data in the region of $-10\mu^2 < t < -2\mu^2$. As seen from this figure, the theoretical curves are very close to the experimental data. The small difference between the theoretical curves and the experimental data was used for a normalization of the experimental data.

Then we investigated the kinematic region where the polarizability contribution is biggest. This is the region $5\mu^2 \leq s_1 < 15\mu^2$ and $-12\mu^2 < t < -2\mu^2$. In the range $t > -2\mu^2$ the polarizability contribution is small and also the efficiency of the TOF is not well known here. Therefore, we have excluded this region. Fig. 3 presents the cross section of the process $\gamma p \to \gamma\pi^+ n$ integrated over s_1 and t in the region where the contribution of the pion polarizabilities is biggest end the difference between of the theoretical models does not exceed 3%. The dashed and dashed-dotted lines are the predictions of model-1 and the solid and dotted lines of model-2 for $(\alpha_1 - \beta_1)_{\pi^+} = 0$ and 14, respectively. As a result, the following value of the difference of the charged pion dipole polarizabilities has been obtained:

$$(\alpha_1 - \beta_1)_{\pi^+} = 11.6 \pm 1.5_{stat} \pm 3.0_{syst} \pm 0.5_{mod}. \quad (9)$$

4 Determination of the charged pion polarizabilities from the process $\gamma\gamma \to \pi^+\pi^-$

Attempts to determine the charge pion dipole polarizabilities from the reaction $\gamma\gamma \to \pi^+\pi^-$ suffered greatly from theoretical and experimental uncertainties. The analyses [9,23,24] have been performed in the region of the low energy ($\sqrt{t} < 700$ MeV, where t is the square of the total energy in $\gamma\gamma$ c.m.system). In this region values of the experimental cross sections of

the process under consideration [25–28] are very ambiguous. As a result, the values of $\alpha_{1\pi^\pm}$ found lie in the interval 2.2–26.3. The analyses of the data of Mark II [28] have given $\alpha_{1\pi^\pm}$ close to ChPT result. However, even changes of the dipole polarizabilities by more than 100% are still compatible with the present error bars in the energy region considered [24].

In the work [5] we constructed the DRs similar to those of Ref. [2] for the amplitudes of the process $\gamma\gamma \to \pi^+\pi^-$. But in this case the Born term does not equal to 0. Using the DRs allows one to avoid the problem of double counting and the subtractions in the DRs provide a good convergence of the integrand expressions of these DRs and, therefore, increases the reliability of the calculations. The DRs for the charged pions are saturated by the contributions of the $\rho(770)$, $b_1(1235)$, $a_1(1260)$, and $a_2(1320)$ mesons in the s channel and σ, $f_0(980)$, $f_0(1370)$, $f_2(1270)$, and $f_2(1525)$ in the t channel.

These DRs, where the charged pion dipole and quadrupole polarizabilities were free parameters, were used to fit to the experimental data for the total cross section [28–33] in energy region from the threshold to 2500 MeV. The best result of this fit is presented in Fig. 4 by the solid line. This solid curve well describes the experimental data in whole energy

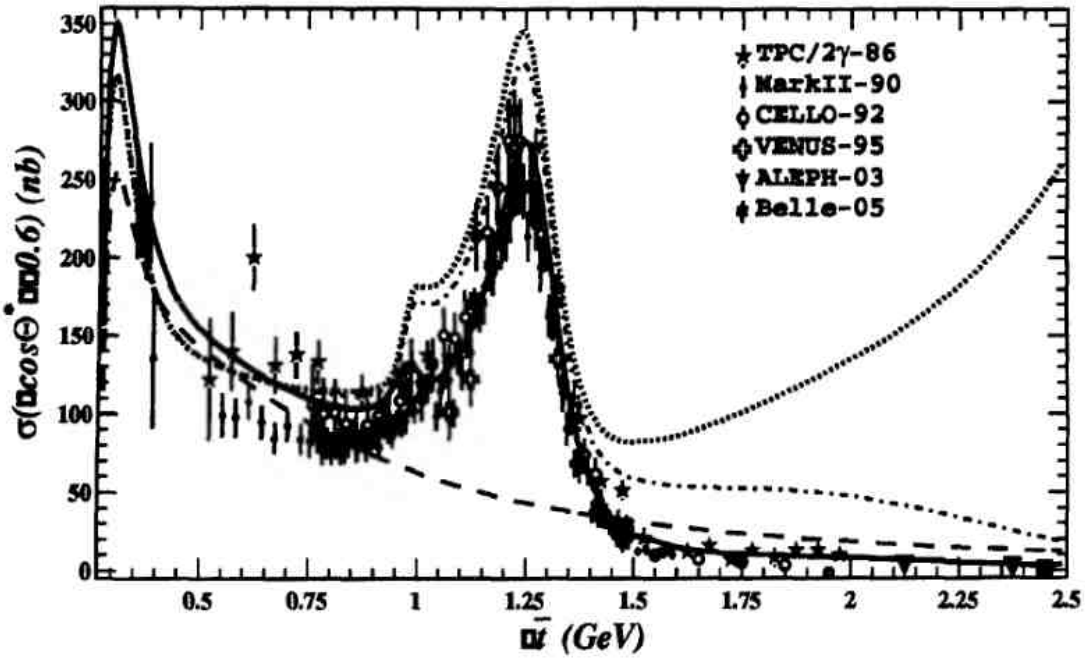

Figure 4: The total cross section of for the reaction $\gamma\gamma \to \pi^+\pi^-$ (with $|\cos\theta^*| < 0.6$).

region under investigation. As a result, we have found the dipole polarizabilities of the charged pions and determined their quadrupole polarizabilities for the first time. The values of the polarizabilities found in the work [5] and the predictions of DSRs [3] and two-loop ChPT [34] are listed in Table 2. The numbers in brackets correspond to the order p^6 low energy constants from Ref. [35]. As seen from this Table, the all values of polarizabilities found in Ref. [5] are in good agreement with the DSR predictions [2].

The dashed curve in Fig. 4 is the Born term contribution. The dotted curve is a result of calculations using the DRs when $(\alpha_2 - \beta_2)_{\pi^\pm}$ and $(\alpha_2 + \beta_2)_{\pi^\pm}$ equal to the respective values in Table 2. but the dipole polarizabilities are taken from ChPT calculations [36] as $(\alpha_1 - \beta_1)_{\pi^\pm} = 4.4$ and $(\alpha_1 + \beta_1)_{\pi^\pm} = 0.3$. The dashed-dotted curve presents a result of the fit to the experimental data when the quadrupole polarizabilities are the free parameters and the values of the dipole polarizabilities are fixed by ChPT calculations [36]. The both last

Table 2: The dipole and quadrupole polarizabilities of the charged pions.

	fit [5]	DSRs [2]	ChPT [34]	
			to one-loop	to two-loops
$(\alpha_1 - \beta_1)_{\pi^\pm}$	$13.0^{+2.6}_{-1.9}$	13.60 ± 2.15	6.0	5.7 [5.5]
$(\alpha_1 + \beta_1)_{\pi^\pm}$	$0.18^{+0.11}_{-0.02}$	0.166 ± 0.024	0	0.16 [0.16]
$(\alpha_2 - \beta_2)_{\pi^\pm}$	$25.0^{+0.8}_{-0.3}$	25.75 ± 7.03	11.9	16.2 [21.6]
$(\alpha_2 + \beta_2)_{\pi^\pm}$	0.133 ± 0.015	0.121 ± 0.064	0	-0.001 [-0.001]

curves are close to calculations in Ref. [24] in the energy region up to 700 MeV, however they differ strongly from all experimental data on the total cross section at higher energies.

The fits of the data to the total cross section for the separate works [28–31] were used to estimate the errors of the values of charged pion polarizabilities found.

The angular distributions of the differential cross section of the process $\gamma\gamma \to \pi^+\pi^-$ at different energies are shown in Fig. 5. The solid and dashed curves are the results of

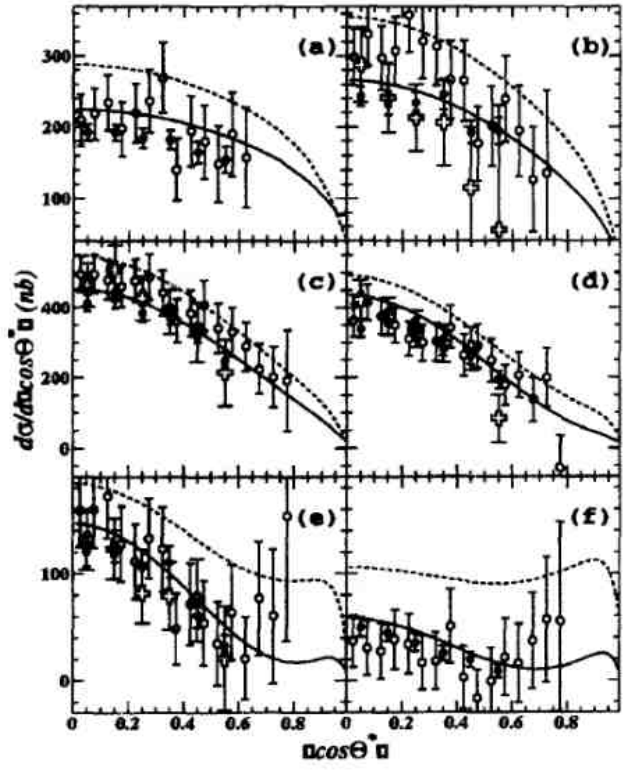

Figure 5: Angular distributions of the differential cross sections for the following energy intervals: (a) – 0.95–1.05 GeV, (b) – 1.05–1.15 GeV, (c) – 1.15–1.25 GeV, (d) – 1.25–1.35 GeV, (e) – 1.35–1.45 GeV, (f) – 1.45–1.55 GeV. The designations of the experimental data are the same as in Fig. 4.

calculations using our and the ChPT fits (the latter when the values of the dipole polarizabilities are fixed by ChPT [36]) to the total cross sections in Fig. 4, respectively. This figure demonstrates a good description of the angular distributions by the solid curves with the polarizability values found in the present work. On the other hand, the calculations with the dipole polarizabilities from ChPT [36] contradict these experimental data, particularly at higher energies.

6 Summary

We have reviewed and analysed the data on the pion polarizabilities obtained.

1. The values of the dipole and quadrupole polarizabilities of π^0 have been obtained from the fit of the experimental data [6,7] to the total cross section of the process $\gamma\gamma \to \pi^0\pi^0$ in the energy region from the threshold to 2250 MeV. The values of $(\alpha_1 \pm \beta_1)_{\pi^0}$ and $(\alpha_2 - \beta_2)_{\pi^0}$ do not conflict within the errors with the ChPT prediction. However, two-loop ChPT calculations have given opposite sign for the $(\alpha_2 + \beta_2)_{\pi^0}$.

2. The value of $(\alpha_1 - \beta_1)_{\pi^\pm}$ found in Ref. [5] from the fit of the all available at present experimental data to the total cross section (with $|\cos\theta^*| < 0.6$) of the process $\gamma\gamma \to \pi^+\pi^-$ in the energy region from the threshold to 2500 MeV is consisted with the results obtained at MAMI (2005) ($\gamma p \to \gamma\pi^+ n$), Serpukhov (1983) ($\pi^- Z \to \gamma\pi^- Z$), and Lebedev Physical Institute (1984) ($\gamma p \to \gamma\pi^+ n$). However, all these results are at variance with the ChPT calculations.

3. The values of the quadrupole polarizabilities $(\alpha_2 \pm \beta_2)_{\pi^\pm}$ found disagree with the present two-loop ChPT calculations.

4.All values of the pion polarizabilities found in Refs. [2–5, 18, 37] agree with DSR predictions.

This research is part of the EU integrated initiative hadronphysics project under contract number RII3-CT-2004-506078 and was supported in part by the Russian Foundation for Basic Research (Grant No. 05-02-04014).

References

[1] I. Guiasu and E.E. Radescu, Ann. Phys. **120**, 145 (1979); ibid. **122**, 436 (1979).

[2] L.V. Fil'kov and V.L. Kashevarov, Phys. Rev. C **72**, 035211 (2005).

[3] L.V. Fil'kov and V.L. Kashevarov, Eur. Phys. J. A **5**, 285 (1999).

[4] J. Ahrens *et al.*, Eur. Phys. J. A **23**, 113 (2005).

[5] L.V. Fil'kov and V.L. Kashevarov, Phys. Rev. C **73**, 035210 (2006).

[6] H. Marsiske *et al.*, Phys. Rev. D **41**, 3324 (1990).

[7] J.K. Bienlein, Crystal Ball Contribution to the 9th Intern. Workshop on Photon-Photon Collisions, San Diego, California, 22-26 March 1992.

[8] M. Boglione, M.R. Pennington, Eur. Phys. J. C **9**, 11 (1999).

[9] A.E. Kaloshin and V.V. Serebryakov, Z. Phys. C **64**, 689 (1994).

[10] A.E. Kaloshin, V.M. Persikov, and V.V. Serebryakov, Phys. Atom. Nucl. **57**, 2207 (1994).

[11] S. Bellucci, J. Gasser, and M.E. Sainio, Nucl. Phys. **B423**, 80 (1994); **B431**, 413 (1994).

[12] J. Gasser, M.A. Ivanov, and M.E. Sainio, Nucl. Phys. **728**, 31 (2005).

[13] L.V. Fil'kov, Proc. Lebedev. Phys. Inst. **41**, 1 (1967).

[14] T.A. Aibergenov *et al.*, Proc. Lebedev Phys. Inst. **186** 169 (1988)

[15] D. Drechsel and L.V. Fil'kov, Z. Phys. A **349**, 177 (1994).

[16] Th. Walcher, in Chiral Dynamics: Theory ans Experiment III, Proceedings from the Institute for Nuclear Theory, Vol. **11**, p.296.

[17] G. Gobel, Phys. Rev. Lett. **1**, 337 (1958); G.F. Chew and F.E. Low, Phys. Rev. **113**, 1640 (1959).

[18] T.A. Aibergenov *et al.* Sov. Phys.-Lebedev Inst. Rep. **6**, 32 (1984); Czech. J. Phys. B **36**, 948 (1986).

[19] T.A. Aibergenov *et al.*, Sov. Phys-Lebedev Inst. Rep. **5**, 28 (1982).

[20] J. Ahrens *et al.*, Few-Body Syst. Suppl. **9**, 449 (1995).

[21] J. Ahrens *et al.*, Preprint of Lebedev Phys. Inst. No. **52** (1996).

[22] Ch. Uhkmeir, PhD Thesis, Mainz University (2000).

[23] D. Babusci *et al.*, Phys. Lett. **B277**, 158 (1992).

[24] J.F. Donoghue and B.R. Holstein, Phys. Rev. D **48**, 137 (1993).

[25] PLUTO Collaboration (C. Berger *et al.*), Z. Phys. C **26** 199 (1984).

[26] DM1 Collaboration (A. Courau *et al.*), Nucl. Phys. B **271**, 1 (1986).

[27] DM2 Collaboration (Z. Ajaltoni *et al.*), Phys. Lett. **B194**, 573 (1987).

[28] Mark II Collaboration (J. Boyer *et al.*),Phys. Rev. D **42**, 1350 (1990).

[29] TPC/2γ Collaboration (H. Aihara *et al.*), Phys. Rev. Lett. **57**, 404 (1986).

[30] CELLO Collaboration (H.J. Behrend *et al.*), Z. Phys. C **56**, 381 (1992).

[31] VENUS Collaboration (Fumiaki Yabuki *et al.*), J. Phys. Soc. Jap. **64**, 435 (1995).

[32] ALEPH Collaboration (A. Heister *et al.*), Phys. Lett. B **569**, 140 (2003).

[33] Belle Collaboration (H. Makazawa *et al.*), Phys. Lett. B **615**, 39 (2005).

[34] J. Gasser, M.A. Ivanov, and N.E. Sainio, Nucl. Phys. B **745**, 84 (2006); hep-ph/0602234.

[35] J. Bijnens and J. Prades, Nucl. Phys. B **490**, 239 (1997).

[36] U. Bürgi, Nucl. Phys. B **479**, 392 (1997).

[37] Yu.M. Antipov *et al.*, Phys. Lett. **B121**, 445 (1983).

SEARCH FOR PENTAQUARKS IN HIGH-STATISTICS EXPERIMENTS AT CLAS

P. Rossi [a]
for the Jefferson Lab CLAS Collaboration

[a] *Laboratori Nazionali di Frascati - INFN, Via Enrico Fermi 40, 00044 Frascati, Italy*

Since the first evidence for a S=+1 baryon resonance appeared in early 2003 from the LEPS Collaboration, other experimental groups have confirmed this exotic state, dubbed the Θ^+. At the same time, a number of experiments, mostly at high energies, reported null results. In 2004 a second-generation experimental program has been undertaken at Jefferson Laboratory (JLab), to try to find a definite answer to whether the Θ^+ and other 5-quark baryons exist.
Here the results of CLAS high-statistics experiments are reported.

1. INTRODUCTION

Exotics, i.e. particles with more complex quark configurations than $q\bar{q}$ pairs (mesons) or 3-quarks states (baryons), have been proposed since the early 70's. The lack of experimental evidence did not stop the theoretical work on this subject, and in 1997 Diakonov, Petrov and Polyakov, in the framework of the Chiral Quark Soliton Model predicted an antidecuplet of 5-quarks baryons with $J^\pi = 1/2^+$ [1] . The lowest mass member is an isosinglet state, the Θ^+, with quark configuration ($uudd\bar{s}$) giving S=+1, mass $\sim$ 1.54 GeV and width $\sim$ 15 MeV.
Experimental evidence for a S=+1 baryon resonance, dubbed the Θ^+, has been reported for the first time by the LEPS Collaboration [2]. Evidence for an additional narrow exotic S=-2 state, called the Ξ^{--} with mass close to 1862 MeV was reported by the NA49 Collaboration [3]. Immediately after the LEPS announcement, several other groups analyzed old data, and found the exotic baryon Θ^+ in both pK^0 and nK^+ decay channels [4–12]. The relatively small statistical significance of every measurement, possibly explained by the fact that all the results come from the analysis of data taken for other purposes; the discrepancy in mass determination, which ranges from 1522 to 1555 MeV (varying by more than the uncertainties given for the individual experiments); and, above all, the null results reported by a similar number of high statistics and high energy experiments [13] have driven a second-generation experimental program in different laboratories, among those JLab.

2. THE CLAS PROGRAM AT JLAB

The superconducting electron accelerator at Jefferson Lab simultaneously delivers 100% duty-cycle electron beams to three different experimental Halls A, B and C. The maximum energy is 5.8 GeV and the maximum current is 200 μA.

Hall B is equipped with a tagged photon facility [14] and the CLAS detector [15]. The tagger system is able to tag photons in the energy range $(0.20 - 0.95)E_0$ with an energy resolution of 0.1% E_0. The CLAS spectrometer is built around six superconducting coils producing a toroidal magnetic field. The coils naturally separate the detector into six sectors each instrumented with 3 sets of multi-wire drift chambers for track reconstruction, one layer of scintillator counters for time-of-flight measurements, Cherenkov counters, and electromagnetic calorimeters for particle identification.

During the year 2004-2005, new dedicated experiments have been performed in Hall B with the aim of improving the statistical accuracy, by at least one order of magnitude, of the two positive published results [5,6] on the Θ^+ pentaquark obtained from existing CLAS data, and to look for the Ξ^{--} state found only by the NA49 Collaboration.

The CLAS pentaquark search experimental program is summarized in Table 1. Here I will discuss only the published results.

Table 1
The CLAS pentaquark program.

Exp	Target	Reaction	Comment		Egamma	Status
G10	**d**	$\gamma d \to pK^-\Theta^+ \hookrightarrow K^+n$	test of CLAS published data [5]	Θ^+	0.8-3.6	Published
		$\gamma d \to pK^-\Theta^+ \hookrightarrow K^0p$		"	"	In progress
		$\gamma d \to \Lambda(1116)\Theta^+ \hookrightarrow K^+n$	cfr LEPS-Spring8	"	"	Published
		$\gamma' n' \to K^-\Theta^+ \hookrightarrow K^+n$	cfr LEPS-Spring8 [2]	"	"	In progress
G11	**p**	$\gamma p \to K^0\Theta^+ \hookrightarrow K^+n$	test of SAPHIR data [7]	Θ^+	1.6-3.8	Published
		$\gamma p \to K^0\Theta^+ \hookrightarrow K^0p$		"	"	Published
		$\gamma p \to K^-\Theta^{++} \hookrightarrow K^+p$	cfr STAR in d+Au	Θ^{++}	"	Published
EG3	**d**	$\gamma d \to K^+K^+\Xi^{--}(p)$	test of NA49 data [3]	Ξ_5	4.0-5.4	In progress
SUPER G	**p**	$\gamma p \to K^-\pi^+\Theta^+ \hookrightarrow K^+n$	test of CLAS published data [6]	Θ^+	3.8-5.7	Data to be taken

2.1. G10 EXPERIMENT: SEARCH FOR PENTAQUARKS USING A DEUTEI TARGET

This experiment ran during spring 2004 using a 24 cm long liquid deuterium target, tagged photons in the energy range (0.8 - 3.59) GeV and the CLAS torus magnet at 2 different values. The run with lower magnetic field increased the acceptance for forward going negative particles (which allow us to perform an analysis similar to LEPS for inclusive reactions), while the one with higher magnetic field has the same geometrical acceptance and single track resolution as the published CLAS result on deuterium [5]. Under these conditions an integrated luminosity of 50 pb^{-1} was obtained (roughly shared between the two magnetic field configurations). This is a factor of 20 greater than for the published data [5]. Detector calibration and data quality checks have been carefully undertaken in order to achieve resolutions on the order of a few MeV for calculated invariant masses and on the order of $\sim$ 10 MeV for missing masses.

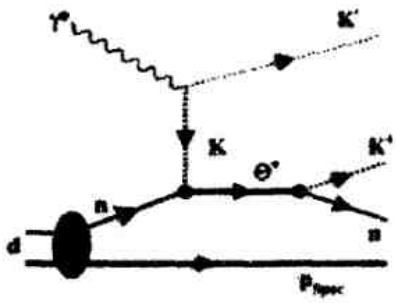

Figure 1. Production mechanism for the $\gamma d \to pK^-\Theta^+$ reaction.

2.1.1. The $\gamma d \to pK^-\Theta^+$ Reaction Channel

This reaction channel, schematically shown in Fig. 1, requires the detection of one proton, one K^+, and one K^-. The missing mass of the $\gamma d \to pK^-K^+X$ reaction was required to be within $\pm 3\sigma$ of the neutron mass and the missing momentum was required to be greater than 0.20 GeV/c in order to remove spectator neutrons. Events corresponding to ϕ-meson production were cut by requiring the K^+K^- mass to be above 1.06 GeV/c^2, and, similarly, events corresponding to the $\Lambda(1520)$ were cut by requiring 1.495 GeV/c^2 < $M(pK^-)$ < 1.545 GeV/c^2. The resulting invariant-mass spectrum of the nK^+ system, $M(nK^+)$, corrected for the CLAS detector acceptance and normalized by the luminosity, is shown in Fig. 2. These data show no evidence for a narrow peak near 1.54 GeV/c^2. The cross section spectrum of Fig. 2 was then fit with a third-degree polynomial, held fixed, and the excess (or deficit) above (or below) the curve was used to determine the cross section upper limit for the Θ^+. The integrated upper limit for the reaction $\gamma d \to pK^-\Theta^+$ is shown in Fig. 3 and is less than 0.3 nb in the mass range of 1.5-1.6 GeV/c^2. Fig. 4 shows upper limits for the differential cross section as a function of cosΘ^*, where Θ^* is the angle relative to the beam direction, of the Θ^+ in the center-of-mass frame. The solid line is the maximum upper limit in the mass range from 1.52 to 1.56 GeV/c^2 while the

dashed line is the upper limit at 1.54 GeV/c^2.

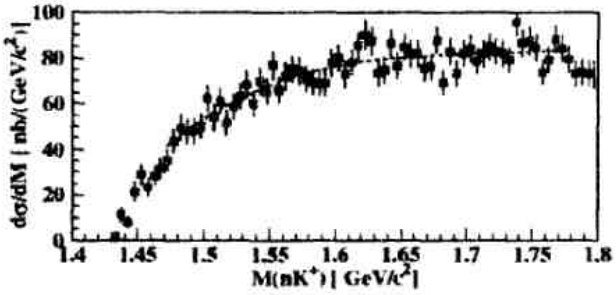

Figure 2. The cross section per mass bin of the $\gamma d \to pK^-\Theta^+$ reaction along with a polynomial fit.

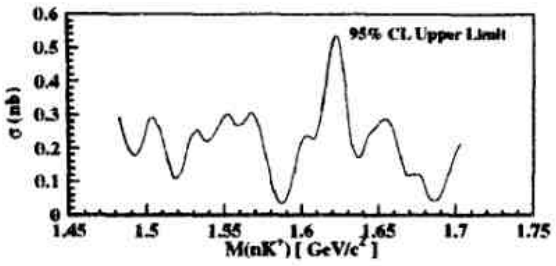

Figure 3. The 95% confidence level (C.L.) upper limit integrated cross section as a function of the M_{nK^+} invariant mass for the $\gamma d \to pK^-\Theta^+$ reaction.

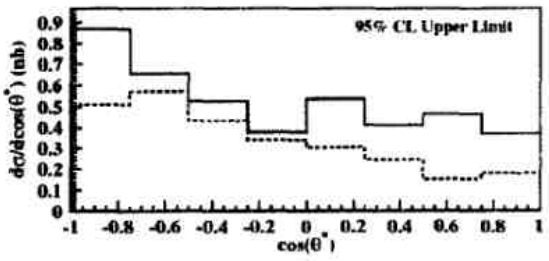

Figure 4. The 95% confidence level (C.L.) upper limit differential cross section of the $\gamma d \to pK^-\Theta^+$ reaction as a function of $cos\Theta^*$ for a mass range between 1.52 and 1.56 GeV/c^2 (solid line) and at 1.54 GeV/c^2 (dashed line).

The measured upper limits are for the $\gamma d \to pK^-\Theta^+$ reaction and not for the elementary cross section on the neutron. To find the connection between the two reactions a phenomenological approach to estimate the rescattering of the spectator nucleon using the t-channel symmetry between $\Lambda(1520)$ and Θ^+ production has been used [16]. This led to an upper limit for $\gamma n \to K^-\Theta^+$ which is a factor of 10 higher than those presented in Figs. 3 and 4.

2.1.2. The $\gamma d \to \Theta^+\Lambda$ Reaction Channel

The $\gamma d \to \Theta^+\Lambda$ reaction channel has very interesting features: *i)* the strangeness content of the final state is well-defined thanks to the presence of the Λ particle which has strangeness $S = -1$; *ii)* the presence of only one K^+ and no K^- in the final state allows us to identify it without the need of cutting on competing channels ($\phi, \Lambda(1520)$),

and *iii)* kinematical reflections in the NK invariant mass spectrum are excluded. The main reaction mechanism can be pictured as the two-step process of Fig. 5.

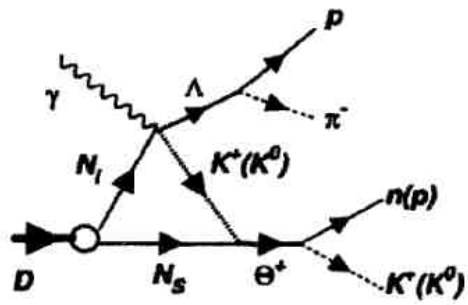

Figure 5. Production mechanism for $\Lambda\Theta^+$ in deuterium.

The following decay channels are detected in CLAS:
i) $\Lambda \to p\pi^-$, *ii)* $\Theta^+ \to pK^0$ and $\Theta^+ \to nK^+$, and *iii)* $K^0 \to \pi^+\pi^-$.
The final state is therefore $K^+np\pi^-$ for the nK^+ decay mode and $\pi^+\pi^-pp\pi^-$ for the pK^0 decay mode. The analysis of the pK^0 decay mode is still in progress, and only the result for $K^+np\pi^-$ is reported [17].
To analyze this channel, p, K, π were identified using momentum and time-of-flight information. After removing the background under the kaon mass peak due to p or π uncorrectly identified as K, exclusive $K^+n\pi^-p$ events were selected by computing the missing mass of the $K^+p\pi^-X$ system and choosing the events lying within $\pm 3\sigma$ around the neutron peak. The $K^+np\pi^-$ final state can also arise from the $\gamma d \to \Sigma^- pK^+$ channel when the Σ^- decays weakly into $n\pi^-$. In order to study this possible source of background, the distribution of the missing mass of the pK^+ system was studied. As expected, the Σ^- peak disappeared after applying the Λ selection cut on the $p\pi^-$ invariant mass.
After selecting the ΛnK^+ events, the Θ^+ signal was searched for in the invariant mass of the nK^+ system. The result obtained is shown in the top plot of Fig. 6. Since the nK^+ mass spectrum did not show any evident structure, further kinematical cuts have been applied, based upon the indications in [18], in order to try to increase a possible Θ^+ signal over the non-resonant nK^+ background: *i)* non-spectator-neutron cut (the non-resonant nK^+ background can be suppressed by removing the events in which the neutron is a spectator); and *ii)* photon-energy cut (according to the model [18], the $\gamma d \to \Lambda\Theta^+$ cross section decreases rapidly with increasing photon energy). Under these stringent kinematic conditions still no narrow peaks with statistical relevance were observed in the mass region around 1.54 GeV/c^2. An example is given in the bottom plot of Fig. 6, where the kinematic requirements $p_n > 0.2$ GeV/c and $E_\gamma < 1.6$ GeV are applied. Since no structures with relevant statistical significance appear in the nK^+ invariant mass for any of the kinematic cuts that have been studied, the upper limit on the cross section was calculated using the Feldman-Cousins method [19]. The acceptance was computed with the aid of a Monte-Carlo simulation that reproduces the response of the CLAS detector and was found to be on the order of 1-2%. The $\Lambda \to p\pi^-$ decay branching ratio (64%) was included in the calculation of the luminosity, as well as the Θ^+ decay branching ratio for the nK^+

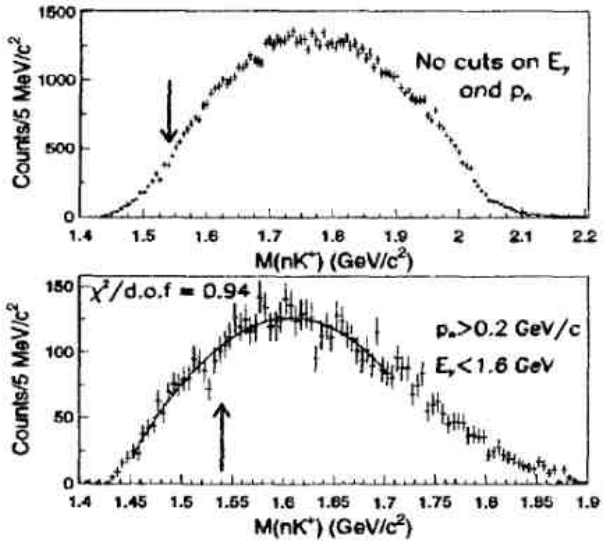

Figure 6. Invariant mass distribution of the nK^+ system for the $\gamma d \to \Lambda K^+ n$ reaction. Top plot: no kinematical cuts are applied. Bottom plot: the $E_\gamma < 1.6$ GeV and $p_n > 0.2$ GeV/c kinematical cuts are applied. The third-order polynomial fit used for the upper limit estimate is shown.

mode, which was assumed to be 50%. The resulting upper limit on the $\gamma d \to \Lambda\Theta^+$ total cross section is shown in Fig. 7 (top), as a function of $M(nK^+)$ for photon energies below 1.6 GeV. In the mass range between 1.52 and 1.56 GeV/c^2 it is 2-5 nb.

The upper limit on the $\gamma d \to \Lambda\Theta^+$ differential cross section as a function of the momentum transfer t, with $t = (p^\mu_\gamma - p^\mu_\Lambda)^2$, was also calculated. The data were divided into five t bins, as shown in the lower plot of Fig. 7. For each t bin, the upper limit on the cross section was extracted according to the procedure described above for the total cross section. The maximum value of the upper limit in the $M(nK^+) = 1.52 - 1.56$ GeV/c^2 range for each t bin was then used to get the upper limit on the differential cross section, as shown in the bottom plot of Fig. 7. It varies between less than 0.5 nb/(GeV/c)^2, at the highest values of $-t$, to 11 nb/(GeV/c)^2, as t approaches 0. The kinematic region around $t \simeq 0$, however, corresponds to the forward-most part of the CLAS detector, where its acceptance drops down to zero, and the dependence on the model used in the event generator becomes stronger. This explains the higher upper limit for the last bin in Fig. 7.

2.2. G11 EXPERIMENT: SEARCH FOR PENTAQUARKS USING A PROTON TARGET

The g11 experiment ran soon after g10 and finished taking data at the end of July 2004. Data were taken using a 40 cm length liquid hydrogen target and tagged photons in the energy range (1.6 - 3.8) GeV, produced by a 60 nA electron beam of $E_0 = 4.02$ GeV impinging on a gold foil of 8x10^{-5} radiation lengths thickness. Under these conditions an

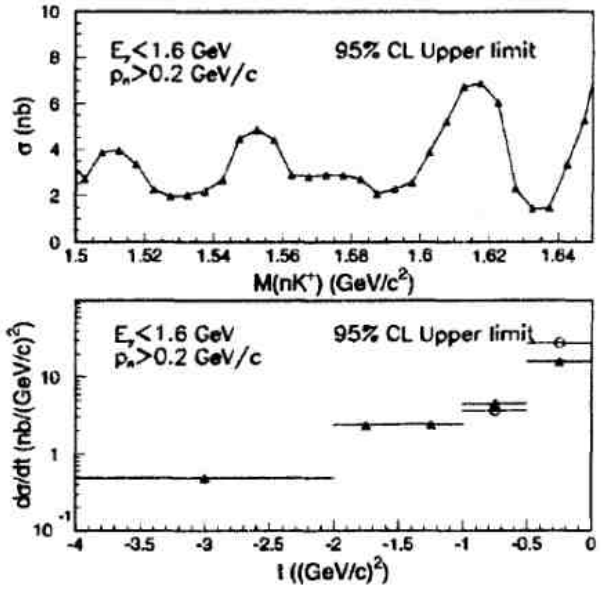

Figure 7. Top: 95% confidence level upper limit of the $\gamma d \to \Lambda\Theta^+$ reaction total cross section as a function of the nK^+ invariant mass. Bottom: 95% confidence level upper limit of the differential cross section $d\sigma/dt$ as a function of t, for $1.52 < M(nK^+) < 1.56\ GeV/c^2$. The triangles and the circles represent the results obtained using two different model for the acceptance calculation.

integrated luminosity of $\sim 70\ pb^{-1}$ was achieved.

2.2.1. The $\gamma p \to \bar{K}^0\Theta^+$ Reaction Channel

The exclusive reactions $\gamma p \to \bar{K}^0 K^+ n$ and $\gamma p \to \bar{K}^0 K^0 p$ were studied to look for evidence of the reaction $\gamma p \to \bar{K}^0\Theta^+$, where Θ^+ decays into pK^0 or nK^+ [20]. The reactions have been isolated by detecting the K^+ and proton directly, the neutral kaon via its decay $K_s \to \pi^+\pi^-$, and the neutron or neutral kaon via the missing mass technique. Reactions involving hyperon decays which contribute to the same final states were removed in the analysis. The most significant are $\gamma p \to K^+\Lambda^*(1520) \to K^+\bar{K}^0 n$, $\gamma p \to K^+\Sigma^+\pi^-$, and $\gamma p \to K^+\Sigma^-\pi^+$ for the $\gamma p \to \bar{K}^0 K^+ n$ reaction channel; and $\gamma p \to p\phi \to pK_lK_s$ and $\gamma p \to K^0\Lambda^*(1116)\pi^+ \to p\pi^+\pi^- K^0$ for $\gamma p \to \bar{K}^0 K^0 p$.

The resulting nK^+ and pK^0 invariant mass distributions are shown in Fig. 8 and Fig. 9, respectively. In both cases the spectrum is smooth and structureless. In particular, no evidence for a peak or an enhancement is observed at masses near 1540 MeV. For the reaction channel $\gamma p \to \bar{K}^0 K^+ n$ a comparison with the published results by the SAPHIR Collaboration [7] has been done. In this case, the analysis has been done using the same cuts reported in Ref. [7]. The resulting mass distribution is shown in the inset of Fig. 8. It remains smooth and structureless. Since no signal has been observed, an upper limit on the Θ^+ yield has been extracted and transformed to an upper limit on the production cross section in each reaction channel. For details of the followed procedure see Ref. [20].

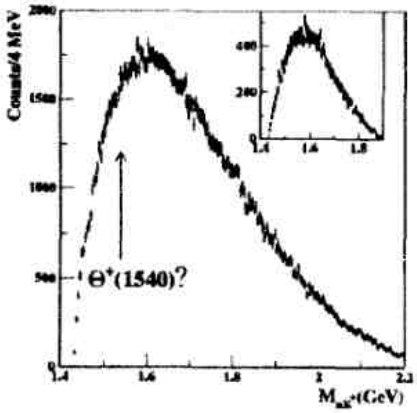

Figure 8. The nK^+ invariant mass distribution for the reaction $\gamma p \to \bar{K}^0 K^+ n$ after all cuts. The inset shows the nK^+ mass distribution with specific cuts to reproduce the SAPHIR analysis [7].

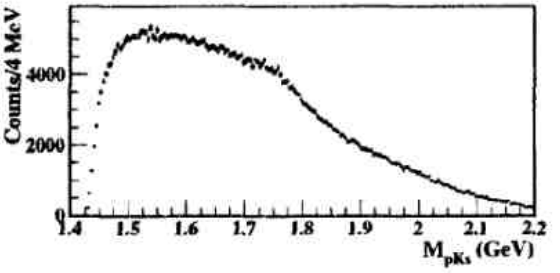

Figure 9. The pK_s invariant mass distribution for the reaction $\gamma p \to \bar{K}^0 K^0 p$ after all cuts, obtained by integrating over all measured photon energy and angles.

The final results are shown in Fig. 10 where the 95% confidence level upper limit on the Θ^+ cross section as a function of Θ^+ mass (top) and 95% confidence level upper limit on the differential cross section $d\sigma/\mathrm{dcos}\Theta^{CM}_{K^0}$ for a fixed Θ^+ mass of 1540 MeV (bottom) are reported. The results have been obtained combining the two channels $\gamma p \to \bar{K}^0 K^+ n$ and $\gamma p \to \bar{K}^0 K^0 p$. As it can be seen, the 95% confidence level upper limit on the total cross section for a resonance peaked at 1540 MeV is found to be 0.7 nb.

2.2.2. The $\gamma p \to \Theta^{++} p$ Reaction Channel

The existence of the Θ^{++} pentaquark is still controversial both from theoretical and experimental sides. In fact, if Θ^+ is an isovector state, one might expect to observe its isospin partners, in particular Θ^0 and Θ^{++}. On the experimental side the existence of a Θ^{++} has not been resolved. Experiments that observed the Θ^+ [6–8,12] reported no statistically significant Θ^{++} decaying to pK^+. On the other hand, a recent report by the STAR Collaboration [21] finds a positive signal for a candidate Θ^{++}.

The putative reaction $\gamma p \to K^- \Theta^{++} \to K^- p K^+$ was studied by the CLAS Collaboration [22] in two ways: in the first case, three final state hadrons, p, K^- and K^+ were detected while in the second case only a pK^+ pair were required and the K^- was identified by missing mass reconstruction. After that, cuts were applied in the pK^- and K^+K^- mass spectra to eliminate the contribution of the $\Lambda(1520)$ and $\phi(1020)$, respectively. The pK^+ mass spectra after all cuts were applied are shown for the first and second case in the upper and lower panels of Fig. 11. In neither case there is evidence for any narrow structures that could be interpreted as a Θ^{++} resonance. Also in this case, since no positive signal was observed, an upper limit for the cross section was determined. This was found to be of about 0.15 nb at 95% confidence level near 1.54 GeV/c^2, where a Θ^{++} might be expected.

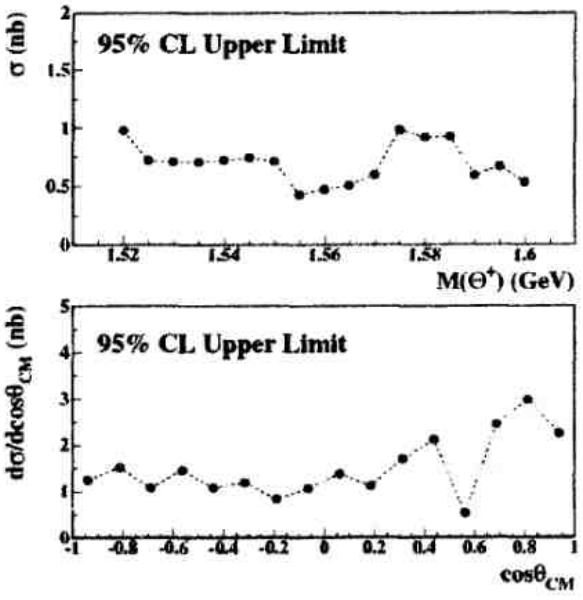

Figure 10. Top: 95% confidence level upper limit of the $\gamma d \to \bar{K}^0\Theta^+$ reaction total cross section as a function of the Θ^+ mass. Bottom: 95% confidence level upper limit of the differential cross section $d\sigma/\mathrm{dcos}\Theta^{CM}_{\bar{K}^0}$ for a fixed Θ^+ mass of 1540 MeV. The results have been obtained combining the two channels $\gamma p \to \bar{K}^0 K^+ n$ and $\gamma p \to \bar{K}^0 K^0 p$.

3. CONCLUSION

In the year 2004 a comprehensive program to search for pentaquarks in high statistics and high resolution experiments has been started by the CLAS Collaboration at Jefferson Lab. No evidence for pentaquark signals has been found in the photoproduction channels studied so far. From these results, CLAS sets upper limits on photoproduction cross sections from proton and neutron targets on the order of a few nb or less. The study of other reactions is in progress.

REFERENCES

1. D. Diakonv, V. Petrov, M.V. Polyakov, Z. Phys. A359, (1997) 305.
2. T. Nakano et al., Phys. Rev. Lett. 91, (2003) 012002.
3. C. Alt et al., Phys. Rev. Lett. 92, (2004) 042003.
4. V. Barmin et al., Phys. Atom. Nucl. 66, (2003) 1715.
5. S. Stepanyan et al., Phys. Rev. Lett. 91, (2003) 252001.
6. V. Koubarovsky et al., Phys. Rev. Lett. 92, (2004) 032001.
7. J. Barth et al., Phys. Lett. B572, (2003) 127.
8. A. Airapetian et al., Phys. Lett. B585, (2004) 213.
9. A.E. Asratyan, A.G. Dolgolenko, M.A. Kubantsev, Phys. Atom. Nucl. 67, (2004) 682.
10. A. Aleev et al., Phys.Atom.Nucl. 68 (2005) 974-981; Yad.Fiz. 68 (2005) 1012-1019.

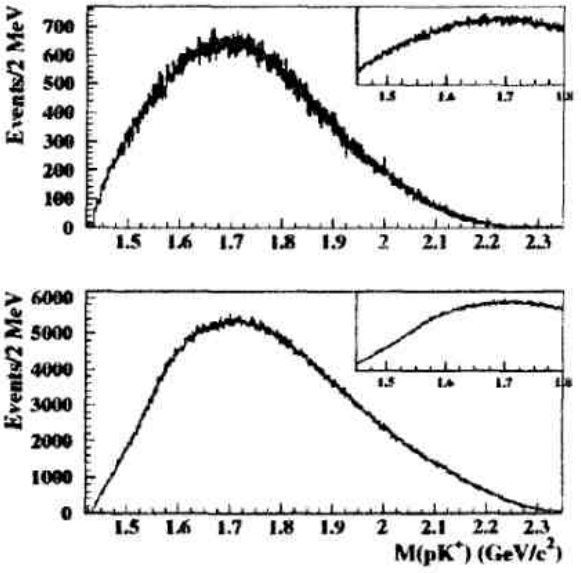

Figure 11. Top: The pK^+ mass spectra for the reaction $\gamma p \to pK^+K^-$ for the case that all three final state hadrons, p, K^- and K^+ are detected. Bottom: The pK^+ mass spectra for the case that only a pK^+ pair is detected and the K^- is identified from the missing mass. The inset in each panel expands the region where one might expect a peak due to the Θ^{++}.

11. M. Abdel-Bary et al., Phys. Lett. B595, (2004) 127.
12. S. Chekanov et al., Phys. Lett. B591, (2004) 7.
13. J.Z. Bai et al., Phys.Rev. D70 (2004) 012004. K.T. Knoepfle et al., J.Phys. G30 (2004) S1363-S1366; M.I. Adamovich et al., Phys.Rev. C70 (2004) 022201; C. Pinkeburg et al., Eur.Phys.J. C37 (2004) 91-104; BABAR, hep-ex/0408064; Yu.M. Antipov et al., Eur.Phys.J. A21 (2004) 455-468; S. Schaet et al., Phys. Lett. B 599, (2004); CDF, E690, LEP, Focus, HyperCP (QNP2004 conference presentation).
14. D.I. Sober et al., Nucl. Inst. & Meth. A440, (2000) 263.
15. B. Mecking et al., Nucl. Inst. & Meth. A503/3, (2003) 513.
16. B. McKinnon et al., Phys. Rev. Lett. 96, (2006) 212001.
17. S. Niccolai et al., Phys. Rev. Lett. 97, (2006) 032001.
18. V. Guzey, Phys. Rev. C 69, (2004) 173.
19. G.D. Feldman and R.D. Cousins, Phys. Rev. D 57, (1998) 3873.
20. M. Battaglieri et al., Phys. Rev. Lett. 96, (2006) 042001; R. De Vita et al., Phys. Rev. D 74, (2006) 032001.
21. Huan Z. Huang (STAR Collaboration), Int. J. Mod. Phys. A 21, (2006) 825.
22. V. Kubarovsky et al., Phys. Rev. Lett. 97, (2006) 102001.

RECENT STUDIES of $\pi^+\pi^-$ ELECTRO-PRODUCTION off PROTONS WITH CLAS.

G. FEDOTOV[a], V. BURKERT[b], H. EGIYAN[c], L. ELOUADRHIRI[b], B. ISHKHANOV[a], E. ISUPOV[a], V. MOKEEV[a,b], N. SHEVEDUNOV[a] and CLAS COLLABORATION.

[a] *Moscow State University, Vorob'evi gory, 119899 Moscow, Russia*

[b] *Thomas Jefferson National Accelerator Facility, 12000 Jefferson Avenue, Newport News, Virginia, 23606, USA*

[c] *University of New Hampshire Durham, New Hampshire 03824-3568 USA*

Abstract

We report new measurements of $ep \to e'p'\pi^+\pi^-$ reaction with the CEBAF Large Acceptance Spectrometer (CLAS) at Jefferson Lab. For the first time a complete sets of unpolarized single differential cross sections were obtained at photon virtualities $0.2 < Q^2 < 0.6$ GeV^2 and invariant masses of the final hadronic system $1.3 < W < 1.6$ GeV. Preliminary data analysis within the framework of JM05 phenomenological model clearly showed the possibility to determine Q^2 evolution of the electrocouplings for the $P_{11}(1440)$ and $D_{13}(1520)$ resonances at the kinematics area particularly sensitive to meson cloud contribution. Analysis also revealed possibility of extracting axial $p \to \Delta$ transition form factor.

1 Introduction

A comprehensive experimental program on nucleon resonance studies in various exclusive meson electroproduction channels off protons is now in progress in Hall B at Jefferson Lab [1, 2]. In this paper we report preliminary results, obtained in recent studies of double charged pion electroproduction off protons at $W < 1.6$ GeV and Q^2 from 0.2 to 0.6 GeV^2.

There are two major objectives for analysis of double charged pion production at low W and Q^2 :

- extraction of transition $p \to \Delta$ axial form factor;
- the studies of $P_{11}(1440)$ and $D_{13}(1520)$ electro- and poorly determined 2π hadronic coupling at the photon virtualities corresponded to the maximal contributions from meson cloud to N^* structure.

Current algebra [3] relates contact term in $\pi\Delta$ non-resonant production to the axial transition $p \to \Delta$ form factors. The contact term could be fitted to the data within the framework of isobar model JM05 [4–6]. This model was developed in collaboration between Jefferson Lab and Moscow University for description double charged pion production off protons in N^* excitation region. Successful description of all available world data on unpolarized observables in double charged pion photo and electroproduction was achieved with the framework of this approach [4]. Contact term has leading contribution to the double charged pion production at $W < 1.4$ GeV. Therefore, analysis of CLAS data at $W < 1.4$ GeV within the framework of model [4] enable us to extract contact term and through current algebra [3] to access $p \to \Delta$ axial transition form factor.

Analysis of recent CLAS data on single pion production by virtual photons at $Q^2 = 0.4$ and 0.65 GeV^2 [7] revealed compelling evidence for considerable contribution from meson cloud to the structure of $P_{11}(1440)$. It was found, that best description of the data on $P_{11}(1440)$ electrocouplings may be achieved within the framework of quark model, accounting for meson cloud contributions [8]. However, analysis [7] is restricted by just 1π electroproduction. Our 2π data complement single pion analyses. They cover Q^2 area from 0.2 to 0.6 GeV^2, corresponded to the maximal contributions from meson cloud effects. Δ resonance excitation in 2π electroproduction is not allowed. Therefore, the signal from $P_{11}(1440)$ in 2π exclusive channel is clean, and it is not contaminated by the Δ - tail as in the single pion production. The recent CLAS data on 2π electroproduction will allow to extend data on $D_{13}(1520)$ electrocouplings toward still unexplored area of low photon virtualities. They also further constraint poorly known $\pi\Delta$ and ρp hadronic couplings for $D_{13}(1520)$. Moreover, combined analysis of single and double charged pion production data from CLAS enables us to extract most reliable information on N* electrocouplings with essentially reduced systematic uncertainties, caused by phenomenological separation between resonant/background mechanisms.

New data on low-lying N^* electrocouplings will be particularly important for understanding of quark meson interactions. Considerable contribution from these interaction to N^* structure at distance scales of the order of hadron size is expected, based on fundamental phenomenon of chiral symmetry breaking [9].

2 Experiment

The measurement was carried out using the CEBAF Large Acceptance Spectrometer (CLAS) [10] at the Thomas Jefferson National Accelerator Facility (Jefferson Lab).. CLAS is a nearly 4π detector, providing almost complete angular coverage for the $ep \rightarrow e'p'\pi^+\pi^-$ reaction in the center-of-mass frame. It is well suited for conducting experiments witch require detection of two or more particles in the final state. Such detector and the continuous beam produced by CEBAF provide excellent conditions for measuring the $ep \rightarrow e'p'\pi^+\pi^-$ electroproduction cross section by detecting the outgoing electron, proton and pion in coincidence.

2.1 Apparatus

The major components of CLAS detector are shown on Fig. 1. The main magnetic field of CLAS is provided by six superconducting coils, which produce an approximately toroidal field in the azimuthal direction around the beam axis. The gaps between the cryostats are instrumented with six identical detector packages, also referred to here as "sectors", as shown in Fig. 1. Each sector consists of three regions (R1, R2, R3) of Drift Chambers (DC) [11] to determine the trajectories of the charged particles, Čerenkov Counters (CC) [12] for the electron identification, Scintillator Counters (SC) [13] for charged particle identification using the Time-Of-Flight (TOF) method, and Electromagnetic Calorimeter (EC) [14] used for electron identification and detection of neutral particles. The liquid-hydrogen target was located in the center of the detector on the beam axis. To reduce the electromagnetic background resulting from Møller scattering off atomic electrons, a second smaller normal-conducting toroidal magnet (mini-torus) was placed symmetrically around the target. This additional magnetic field prevented the Møller electrons from reaching the detector volume. A totally absorbing Faraday cup, located at the very end of beam line, was used to determine the integrated beam charge passing through the target. The CLAS detector provide $\approx$ 80% of 4π solid-angle coverage. The efficiency of detection and

reconstruction for stable charged particles in fiducial regions of CLAS is > 95%. The combined information from tracking in the DC and the TOF systems allows us to reliably separate protons from positive pions for momenta up to 3 GeV.

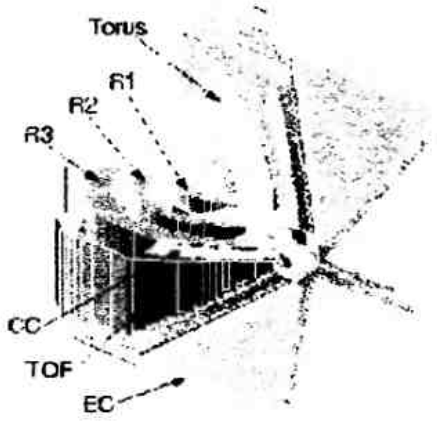

Figure 1: Three dimensional view of CLAS.

This analysis is based on the experimental data taken during 1999 e1c run period. The CEBAF 1.5 GeV electron beam was incident on a 5-cm long liquid hydrogen target at 20.5 K temperature. The data were taken at luminosities of $\sim 4 \times 10^{33}$ cm^{-2}s^{-1}. The CLAS event readout was triggered by a coincidence of signals from the electromagnetic calorimeter and the Čerenkov counters in a single sector, generating an events rate of $\sim$ 2 kHz. The total number of accumulated triggers at these detector settings was about 4.2×10^8. These data were further analyzed to extract the differential cross sections for the $ep \rightarrow e'p'\pi^+\pi^-$ reaction.

2.2 Evaluation of cross section.

The hardware trigger in CLAS was based on a coincidence between Čerenkov counter and electromagnetic calorimeter. So, first we identified electrons and, applying appropriate cuts, eliminated in part pion contamination. In the calorimeter, the electrons and pions have different energy deposition patterns. An electron produces an electromagnetic shower where the deposited energy is proportional to the electron momentum whereas a π^- loses a constant amount of energy per scintillator (2 MeV/cm) independently of its energy.

We identify as possible electron the first in time negative charged particle detected in calorimeter. To select among such particles true electrons, discussed above peculiarities in π^-/e^- energy losses were exploited. We isolate electrons applying the cut on the total energy deposited in calorimeter as a function of particle momentum. To improve π^-/e^- separation we also apply cut in number of photoelectrons in Čherenkov counter.

Using the momentum determined from the tracking and the timing information from the TOF scintillators, we identified protons and π^+. Eventually we selected events with identified electron, proton and π^+.

For these events we calculated π^-X missing mass squared $M^2_{\pi^-X}$. To select the exclusive process ($ep \rightarrow e'p'\pi^+\pi^-$) we applied cut over $M^2_{\pi^-X}$, isolating π^- peak. This so-called exclusivity cut is shown by arrows on Fig. 2.

After completion of selecting $\pi^-\pi+p$ exclusive channel, we have around 130 000 2π events. Fig. 3 show Q^2 versus W distributions for selected 2π events.

$\pi^-\pi^+p$ final state kinematics is determined unambiguously by the following set of 5 variables: invariant masses of π^+p, $\pi^-\pi^+$ final particles, solid angle of π^- in CM frame and the angle between two planes, composed by the final π^-p and $\pi^-\pi^+$ three-momenta. All selected events we binned

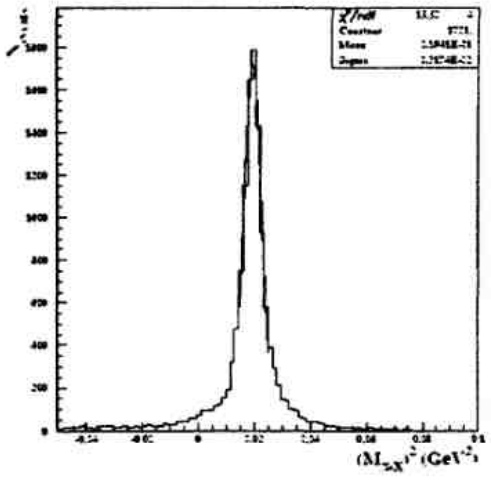

Figure 2: $M^2_{\pi^- X}$ (GeV^2) for selected $e'p'\pi^+$ events. Arrows show exclusivity cut.

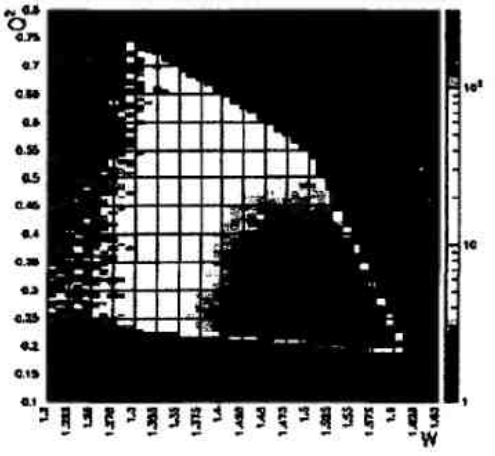

Figure 3: Q^2 (GeV^2) versus W (GeV) distribution for 2π events. Grid show binning used for cross section calculation.

in 7-dimensional grid, composed by mentioned above five variables plus invariant mass of the final hadronic system W and photon virtuality Q^2. Number of events in each 7-differential cell represent experiment input data to determine 7-differential cross sections for 2π electroproduction.

The Monte Carlo event generator and GEANT-based detector simulation package (GSIM) were used to estimate efficiency for particle registration. After that, using measured integrated luminosity, we estimated 7-differential cross section for $ep \to e'p'\pi^+\pi^-$ exclusive processes. Special procedures were developed for evaluation of 7-differential cross sections in the blinded areas of 7-dimensional phase space as well as to account for radiative corrections [15]. Applying standard virtual photon flux formalism [16], we estimated 5-differential virtual photon cross sections. After integration over 4 variables we get sets of single differential cross sections. After complete integration over 5 variables we determined integrated 2π cross sections as a function of W and Q^2.

Examples of differential and integrated cross sections obtained from recent CLAS 2π electroproduction data are shown on Fig. 4,5. For the first time most complete data on 2π electroproduction are available. In each (W&Q^2) bin we have 9 single differential cross sections, consisted of:

- $\pi^+\pi^-$, π^+p, π^-p mass distributions;
- 3 CM angular distributions for each final particle;
- 3 distributions over angle between two plains, composed by 3-momenta various pairs of the final particles.

3 Phenomenological analysis

Preliminary phenomenological analysis of our data was carried out with the framework of JM05 model [4]. For P11(1440) electrocouplings we used the values obtained in [8], while electrocouplings for other N^* were estimated interpolating world data into kinematics area, covered by our measurements (Fig. 3). Combined analysis of a complete set of $\pi^-\pi^+p$ unpolarized single differential cross section allowed us to establish for the first time the dynamics of direct 2π electroproduction mechanisms of JM05 model. We found that these mechanisms may be described as double exchange processes, shown on Fig. 6. Their amplitudes were derived from experimental data fit.

Implementing established in this way direct 2π mechanisms to JM05, we succeeded to describe complete set of unpolarized observables in entire kinematics area, covered by reported CLAS

measurements (see Fig. 3). We achieved reasonable data fit quality with χ^2 per d.p. less then 2.5 in major part of kinematics area. χ^2 per d.p. was always less than 3.2. Example of single

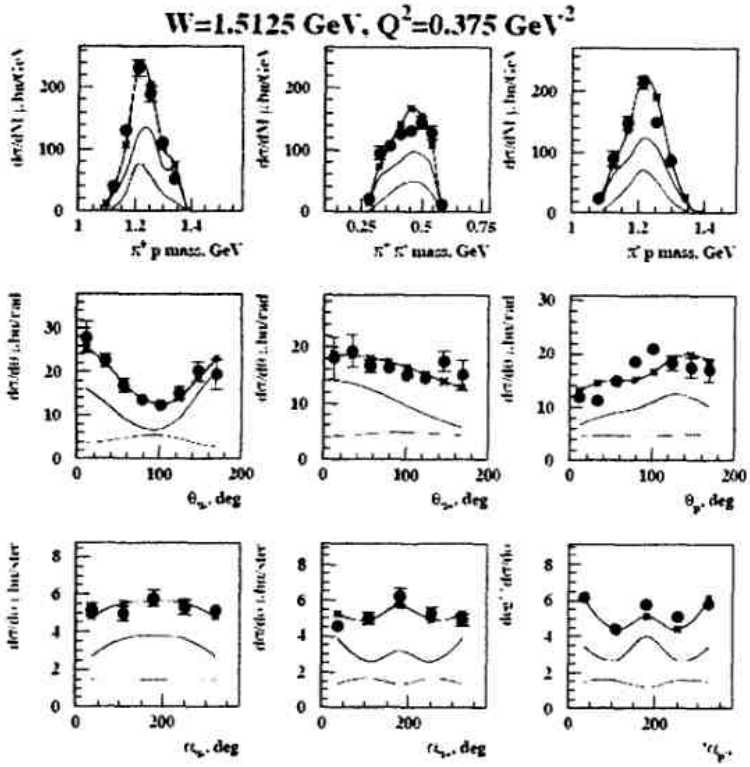

Figure 4: Complete set of single differential cross sections for 2π electroproduction measured with CLAS at $W = 1.51$ GeV and $Q^2 = 0.375$ GeV^2. The cross sections calculated within the framework of JM05 model [4] are shown by black lines, while the contributions from resonant and non-resonant parts are shown by blue and red lines respectively.

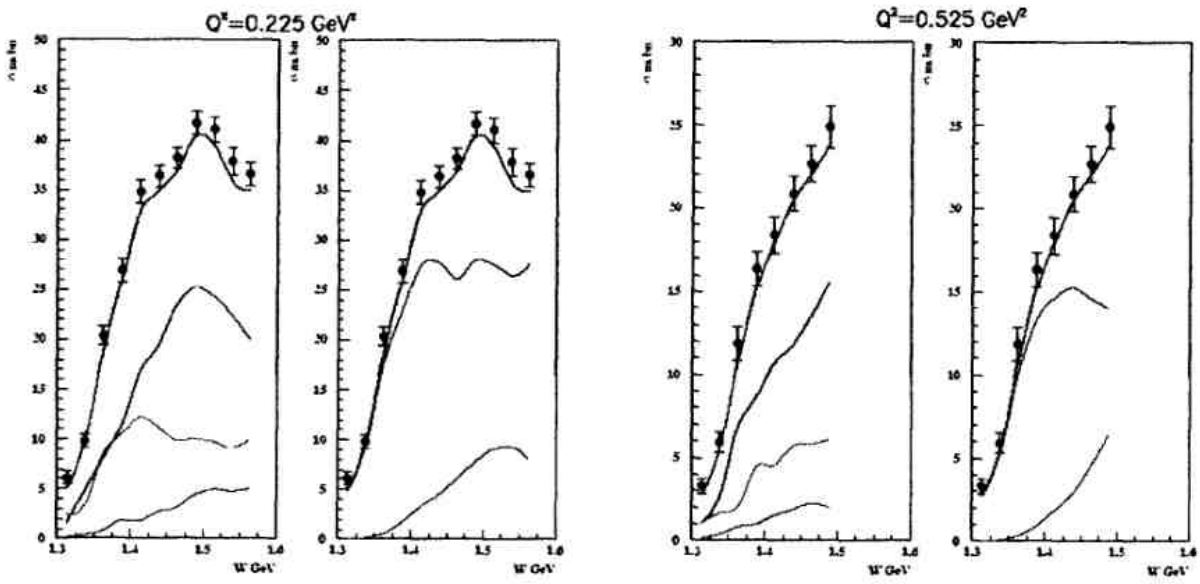

Figure 5: CLAS data on fully integrated 2π cross sections in comparison with fit within the framework of JM05 model [4] (black solid lines). The contributions from various mechanisms included to JM05 are shown on the left sides of plots: solid red, blue and dashed magenta lines correspond to $\pi^-\Delta^{++}$, $\pi^+\Delta^0$ isobar channels and direct 2π production respectively. The contributions from resonant and non-resonant parts of cross sections are shown on right sides of the plots by blue and red lines respectively.

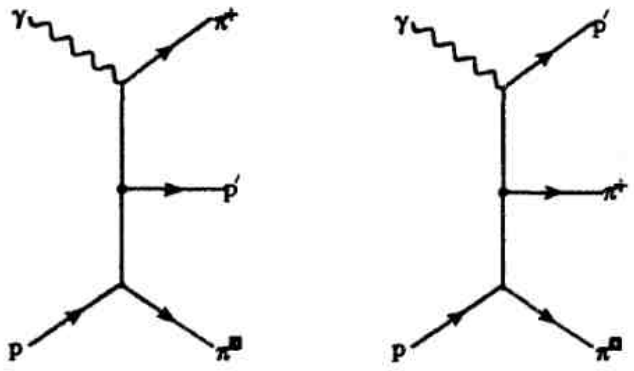

Figure 6: Direct 2π mechanisms, established in analysis of recent CLAS 2π electroproduction data.

differential cross section fit at $W = 1.51$ GeV and $Q^2 = 0.375$ GeV^2 is shown on Fig. 4.

The contributions from various isobar channels and from direct 2π production to fully integrated 2π cross section are shown on the left parts of plots on Fig. 5, while the contributions from non-resonant and resonant mechanisms are shown on right parts. The area $W < 1.4$ GeV is dominated by non-resonant contributions and will be used for extraction of axial $p \rightarrow \Delta$ transition form factor. Due to constraints imposed by gauge invariance $\pi\Delta$ entire non-resonant parts of $\pi\Delta$ channels are sensitive to axial transition form factor. Due to major contributions from non-resonant $\pi\Delta$ parts to the total 2π cross sections at $W < 1.4$ GeV, we have good possibility to extract axial transition form factor from combined analysis of a complete set of unpolarized 2π cross sections determined from recent CLAS data. The relative contributions from non-resonant parts of $\pi\Delta$ isobar channels increase with photon virtuality Q^2. Therefore, largest available Q^2 represent a preferable kinematics area for extraction axial $p \rightarrow \Delta$ transition form factor.

Resonant contributions to the total 2π cross sections increases with Q^2 from 20 % at smallest to 30 % at largest Q^2 (Fig. 5). However, for separation among resonant and non-resonant processes interference effects, which enhance influence of small resonant contributions, are also important. Influence of N^* part on full cross sections is determined also by ratio full over non-resonant part of cross section. These ratio turn out to be much larger than relative resonant contribution only, approaching almost factor 2. Furthermore, shapes for resonant and non-resonant parts of cross sections are very different in all kind of angular distributions of the final particles (Fig. 4). Both resonant and non-resonant processes have very different shapes in various single differential cross sections. From the other hand the manifestations of N^*/non-resonant process in various observables are highly correlated by reaction dynamics. Therefore, combined fit of most complete set of unpolarized observables in recent CLAS data opens up promising opportunity for extracting of $P_{11}(1440)$ and $D_{13}(1520)$ electrocouplings at Q^2 area particularly sensitive to the contributions from meson cloud effects.

4 Conclusions

- For the first time complete set of unpolarized single differential $\gamma_v p \rightarrow p\pi^+\pi^-$ cross sections was obtained from recent CLAS data in kinematics area $1.3 < W < 1.6$ GeV and Q^2 from 0.2 to 0.6 GeV^2.

- Reasonable description of all these data was achieved within the framework of JM05 model, implementing direct 2π production mechanisms with amplitudes, established in the data fit.

- Phenomenological analysis demonstrated sensitivity of measured cross sections to the contact terms in $\pi\Delta$ channels, related to the axial $p \rightarrow \Delta$ transition form factor. Analysis also

revealed good opportunity of determining $P_{11}(1440)$ and $D_{13}(1520)$ electrocouplings at area of photon virtualities particularly sensitive to meson cloud effects.

References

[1] V. D. Burkert, Prog. Part Nucl. Phys. 55, 108 (2005).

[2] V. Burkert, T. S.-H. Lee, Jnt. J. Mod. Phys. **E13**, 1035, (2004).

[3] T. Ebata, K. E. Lassia, Phys. Rev. **183**, 1425, (1969).

[4] V. I. Mokeev, V. D. Burkert, et.al., International Workshop on the Physics of Excited Baryons (NSTAR 05), Tallahassee, Florida, 10-15 Oct 2005, hep-ph0512164

[5] V. Mokeev, et. al. Phys. Atom. Nucl. **64**, 1292, (2001).

[6] V. Burkert ,et. al. Phys. Atom. Nucl. **67**, 1918, (2004).

[7] I. G. Aznauryan, et. al. Phys. Rev. **C71**, 015201, (2005).

[8] E.Cano, P.Gonzales, Phys. Lett. **B431**, 270 (1998).

[9] L. Ya. Glozman, hep-ph/0410194.

[10] B. Mecking et al., Nucl. Inst. and Meth. **A503**, 513, 2003.

[11] M. D. Mestayer et al., Nucl. Inst. and Meth. **A449**, 81, 2000.

[12] G. Adams et al., Nucl. Inst. and Meth. **A465**, 414, 2001.

[13] E. S. Smith et al., Nucl. Inst. and Meth. **A432**, 265, 1999.

[14] M. Amarian et al., Nucl. Inst. and Meth. **A460**, 239, 2001.

[15] G. Fedotov, et. al, CLAS Analysis Note.

[16] E. Amaldi, S. Fubini, G. Furlan, Springer Tracts in Mod. Phys. **V83**, 1989.

OBSERVATION OF QUASIBOUND Δ-NUCLEAR STATE IN $^{12}C(\gamma, \pi^- pp)$ REACTION

I.V.Glavanakov, Yu.F.Krechetov
Nuclear Physics Institute, Tomsk Politechnic University, Tomsk, Russia

The $(\gamma, \pi p)$ reaction for small energies and momenta transferred to the residual nucleus is similar in many respects to the (e, e'p) reaction and is satisfactorily explained in the quasifree approximation. Other situation is observed in the region of large momentum transfers. Two experiments were carried out at the Tomsk synchrotron in order to study this reaction in the last kinematic region. In the first experiment was measured the cross section for the neutral pion photoproduction in the Δ(1232) region [1]. The cross section for the negative pion photoproduction was measured in the similar experiment in the second resonance region [2]. The part of these experiments data is presented in Fig. 1.

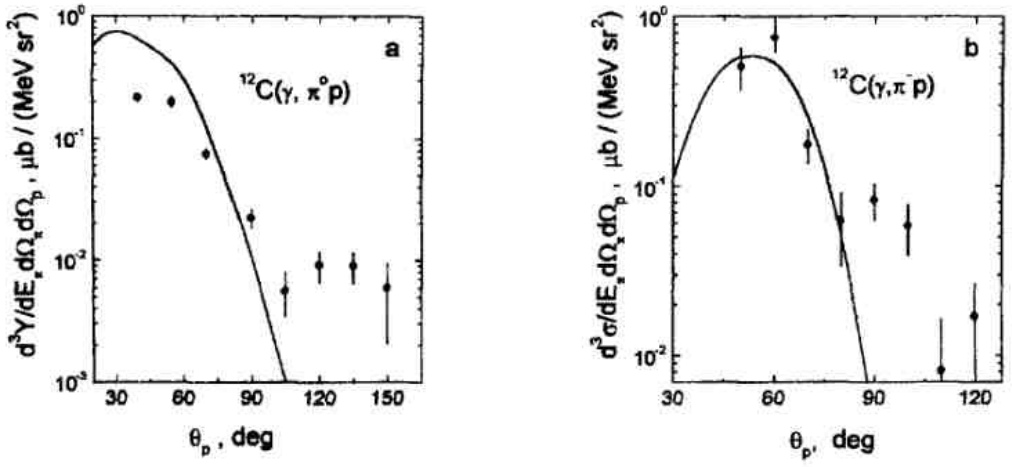

Fig. 1. Differential cross section versus polar angle of the proton emission: *a* – $^{12}C(\gamma, \pi^0 p)$ reaction, $E_{\gamma max} = 450$ MeV, $E_\pi = 300$ MeV, $\theta_\pi = 67°$, $T_p > 21$ MeV; *b* – $^{12}C(\gamma, \pi^- p)$ reaction, $E_{\gamma max} = 750$ MeV, $E_\pi = 541$ MeV, $\theta_\pi = 54°$, $T_p = 60 - 80$ MeV. The solid line – quasifree pion photoproduction.

The most interesting result of those works, which has not yet been finally interpreted, is the observation of a peak in the dependence of the reaction cross section on the proton emission angle in the region of large momentum transfers. This peak is absent in the experimental cross sections for the (e, e'p) reaction. In the present work, in order to analyze the mechanism of pion–proton pair photoproduction for high momenta of the residual nucleus, we study the reactions

$$^{12}C(\gamma, \pi^- p) \tag{1}$$

и

$$^{12}C(\gamma, \pi^- pp) \tag{2}$$

in overlapping kinematic regions [3].

The experiment was carried out in a bremsstrahlung beam from the Tomsk synchrotron at the maximum energy 500 MeV. The experimental setup, shown in Fig. 2, included a channel for detecting a negative pion and two channels for detecting protons in coincidence with a pion in complanar geometry.

Pions with a mean momentum of 224 MeV/c were detected by a strongly focusing magnetic analyzer, which was placed at an angle of 76°. Two proton channels are $(E, \Delta E)$ scintillation spectrometers. The first spectrometer detected protons in the angular range θ_p

= 40° to 140°. The second spectrometer was placed at an angle of 35° with respect to the photon beam axis in the half-plane of the pion channel.

The distribution of detected events over the kinetic energy T_p and the polar angle θ_p of the emission of the first proton is shown in Figs. 3*a* and 3*b* for reactions (1) and (2), respectively.

The dashed line in Fig. 3*a* bounds the region of the quasifree pion photoproduction. Nuclear reactions with emission two nucleons are associated usually with nucleon–nucleon correlations. The diagram shown in Fig. 4*a* illustrates an apparently dominant reaction mechanism where a pion is produced due to the interaction of a photon with the neutron of a correlated *np* pair. For such reaction mechanism distinctive low momentum of the residual nucleus and high relative momentum of the *np* pair.

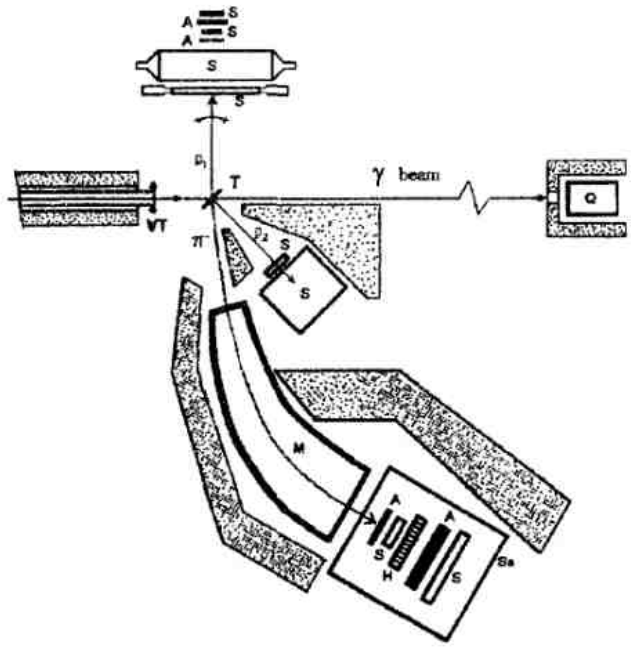

Fig. 2. Layout of the experimental setup, (VT) photon beam vacuum tube, (T) target, (Q) Gauss quantameter, (M) analyzing magnet, (S) scintillation counters, (H) hodoscope, (A) absorbers.

The solid line in Fig. 3*a* is the boundary of the region where the momentum of a correlated *np* pair is no more than the Fermi momentum and the relative momentum is higher than 450 MeV/c. Similar boundaries in Fig. 3*b* are calculated with the additional inclusion of the acceptance of the second proton spectrometer. According to Fig. 3, there are two groups of events, located in practically not overlapped kinematic regions. Founding on present data, we have drawn a conclusion that events of reactions $^{12}C(\gamma, \pi^- p)$ on the Fig. 3*a*, as well as on Fig. 3*b*, in the region of large proton-emission angles are attributable primarily to the two-nucleon knockout mechanism.

The measured yield $d^4Y/dE_p\,d\Omega_p\,dE_\pi\,d\Omega_\pi$ of the $^{12}C(\gamma,\pi^- p)X$ reaction is related to the differential cross sections $d^3\sigma_{\pi p}$ and $d^5\sigma_{\pi pp}$ for the $^{12}C(\gamma,\pi^- p)^{11}C$ and $^{12}C(\gamma,\pi^- pp)^{10}B$ reactions by the respective relations

$$\frac{d^4Y}{dE_p\,d\Omega_p\,dE_\pi\,d\Omega_\pi} = \frac{d^3\sigma_{\pi p}(E_\gamma)}{dE_p\,d\Omega_p\,d\Omega_\pi} f(E_\gamma) \left|\frac{\partial E_\gamma}{\partial E_\pi}\right| + \int dE_\gamma\,d\Omega_{p'} \frac{d^5\sigma_{\pi pp}(E_\gamma)}{dE_p\,d\Omega_p\,dE_\pi\,d\Omega_\pi\,d\Omega_{p'}} f(E_\gamma). \quad (3)$$

Here, E_γ and E_p are the photon energy and the total proton energy, respectively, and $f(E_\gamma)$ is the bremsstrahlung spectrum.

Figure 5*a* shows the differential yield of the $^{12}C(\gamma, \pi^- p)$ reaction as a function of the polar proton-emission angle. This yield is averaged over the range 60–140 MeV of the proton energy T_p. The dashed line in Fig. 5*a* is the theoretical yield of the $^{12}C(\gamma,\pi^- p)^{11}C$ reaction as calculated in the quasifree approximation. In the kinematic region under consideration, as the polar proton-emission angle θ_p increases in the range 40° – 140°, the mean momentum p_r of the residual ^{11}C nucleus in the ground state varies from 60 to 600 MeV/c. As is seen,

when the angle θ_p increases to 70° ($p_r \simeq 300$ MeV/c), the measured yield of the reaction decreases exponentially, in complete agreement with the calculation. However, with a further increase in θ_p, the behavior of the differential yield changes abruptly and a minimum is formed. The same qualitative angular dependence of the cross section was obtained in [1,2].

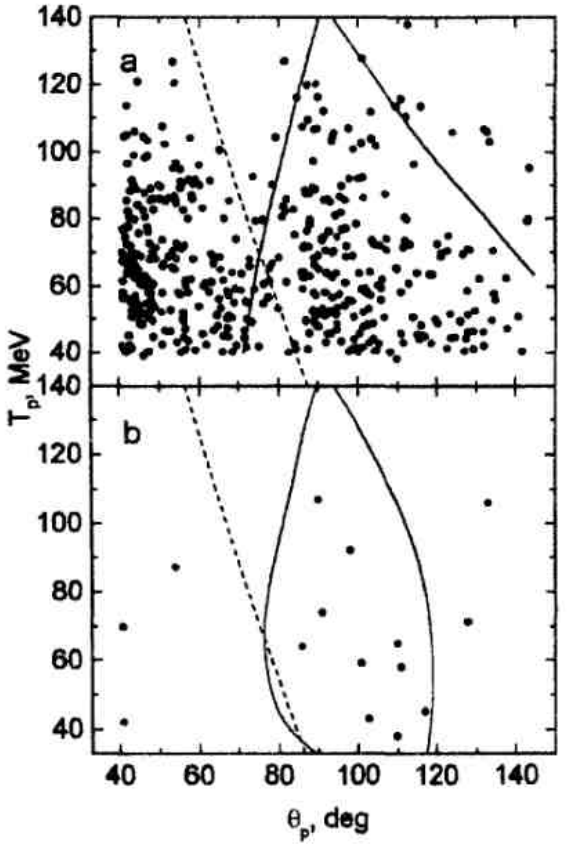

Fig. 3. Distribution of events over the polar emission angle и p of the proton and its energy T p for the (a) $^{12}C(\gamma,\pi^-p)$ and (b) $^{12}C(\gamma,\pi^-pp)$ reactions.

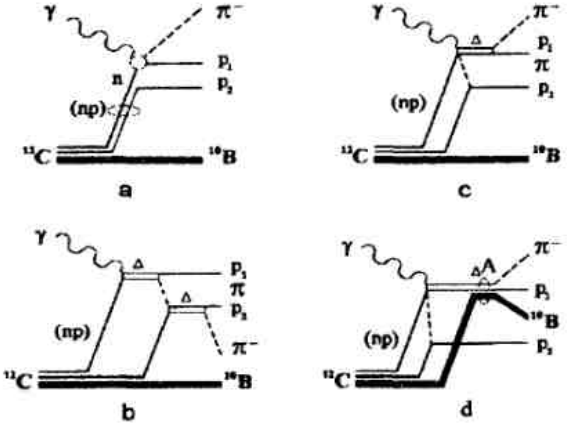

Fig. 4. Diagrams illustrating mechanisms of the $^{12}C(\gamma,\pi^-pp)^{10}B$ reaction.

The substantial properties of the differential cross section for multiparticle nuclear reactions are satisfactorily reproduced by phase-space models. The simplest model, which is shown by the dotted line in Fig. 5*a* and in which the amplitude of the $^{12}C(\gamma,\pi^-pp)$ reaction is constant over the entire range of its definition, cannot reproduce the angular dependence of the cross section.

The kinematic region separated in Fig. 3 by the solid line is traditionally associated with nucleon–nucleon correlations in the nuclear ground state. Since mechanisms of the manifestation of short-range correlations in the reactions of quasifree electron scattering and pion photoproduction are similar to each other, their possible contribution to the $^{12}C(\gamma,\pi^-p)^{11}C$ reaction for large proton-emission angles must be two or three orders of magnitude less than that in the quasifree peak. But results of our measurements are significantly more than this estimation. This difference can be explained by the contribution of additional mechanisms of the reaction that are associated with the specificity of particles involved in the reaction and by a closer connection of pion photoproduction with nucleon resonances. One such mechanism is shown in Fig. 4*b*, where nucleon–nucleon correlation is attributed to the final state interaction, the propagation of a Δ isobar in the nucleus.

The yield of the $^{12}C(\gamma,\pi^-pp)$ reaction calculated by this model is shown by the short dashed line in Fig. 5*a*. The reaction amplitude included the wavefunction of the nucleon pair in the momentum representation and takes into account the mass distribution of the Δ isobar. The normalization was performed using the data on the $^{12}C(\gamma,\pi^+p)$ reaction [4,5], whose yield for low momenta of the residual nucleus is attributed to the final-state rescattering. As is seen, according to this model, the reaction yield is concentrated primarily in the range of small θ_p angles. Two-proton events in Fig. 3*b* to the left of the dashed line bounding the region of the quasi-free production of

$\pi^- p$ pairs are possibly attributable to rescattering. However, it is impossible to explain the measurement data for large proton emission angles in the framework of this model.

The reaction mechanism that is represented by the diagram in Fig. 4*c* and in which two pions are formed, one of which is absorbed with the emission of a proton, was previously used in [6] to explain data on the photoproduction of single pions on the deuteron. The angular dependence of the yield according to this model is shown by the dashed–dotted line in Fig. 5*a*. The reaction amplitude is constructed similarly to the preceding model. The calculated yield well reproduces experimental data for large proton emission angles but overestimates the contribution of the two-nucleon reaction in the region of the quasi-free peak of the yield and does not reproduce the minimum in the angular dependence.

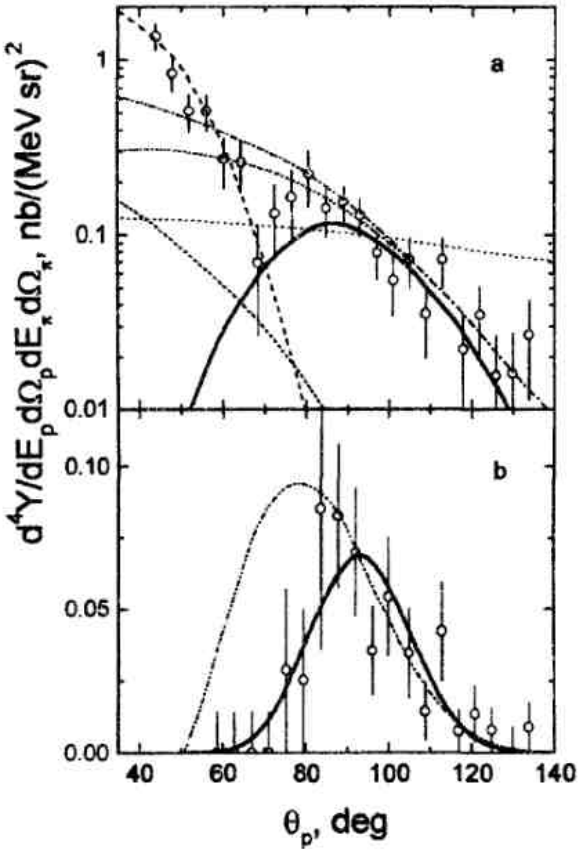

Fig. 5. Differential yield of the $^{12}C(\gamma,\pi^- p)$ reaction vs. the polar proton-emission angle for (a) $T_p > 60$ MeV and (b) $T_p > 60$ MeV and $p_p^* > 260$ MeV/c.

The minimum of the yield near $\theta_p \simeq 70°$ may result from the suppression of the reaction at small angles between the pion and proton scattering directions. If a detected pion–proton pair is a product of the decay of a Δ isobar, the strong angular correlation of the yield can be explained by mechanisms of the suppression of the formation of the isobar with a low mass or high momentum. One of possible suppression mechanisms is associated with the blocking of final states by the Pauli exclusion principle. The calculation that includes this factor and is shown by the dashed–double-dotted line in Fig. 5*a* does not significantly improve the agreement.

Another interpretation of the data is associated with the reaction mechanism represented by the diagram shown in Fig. 4*d*. Before the discussion of this model, we note that the second maximum in the reaction yield is observed for pion–proton scattering angles close to 180°. This maximum is located in the region where the total momentum of the pion–proton pair is minimal. Another remarkable feature of the reaction mechanism with the production of two pions is that a nucleon formed after the absorption of the pion can get a considerable part of the photon momentum. As a result, the Δ isobar is formed at rest with respect to the residual nucleus and is captured by the nucleus, with the formation of a short-lived bound state decaying with the emission of a pion and a proton.

The possibility of existing bound ΔN- and Δ-nuclear states was widely discussed in the 1970s [7–11]. Some works were stimulated by the results of the experiment in [12], where the $^4He(\gamma,\pi^- p)$ reaction was studied. Experimental data obtained in [12] for a residual nucleus momentum of 200 MeV/c could not be explained in the quasi-free approximation. The theoretical estimates of the possibility of such states existing are contradictory [10,11]. Since that time, conclusive experimental evidence of the existence or absence of such states has not been obtained. Our next model is based on the assumption that such states exist. The

solid line in Fig. 5a is the calculation in the model represented by the diagram shown in Fig. 4d. The reaction amplitude includes, in addition to the wavefunction of the neutron–proton pair, the momentum wavefunction of the Δ isobar bound in the nucleus. We suppose that baryons bounded in the nucleus cannot significantly change the spatial state over the isobar lifetime. For this reason, we take the nucleon oscillatory wavefunction for the ^{12}C nucleus as the radial wavefunction of the isobar. As is seen, the model of the reaction proceeding through an intermediate Δ nuclear bound state well reproduces the angular dependence of the yield. Since the isobar momentum depends on the opening angle between the pion and proton, the angular dependence of the reaction yield presents the momentum distribution of the isobar in the nucleus with a maximum at an opening angle close to 180°, where the isobar momentum is minimal.

Figure 5*b* shows the angular dependence of the yield for events in which the proton momentum in the c.m.s. of the pion–proton pair exceeds 260 MeV/c. This is the region of the high-energy slope of the isobar mass distribution. As is seen, in complete agreement with the proposed model, the angular distribution narrows and its center of gravity is shifted towards larger θ_p angles. In this kinematic region, the energy of both protons from the $^{12}C(\gamma, \pi^- pp)$ reaction is sufficiently high. Hence, the blocking of final states by the Pauli exclusion principle is inefficient. Angular-distribution narrowing that differs from the prediction of the model described by the diagram in Fig. 4*c* is attributed to the suppression of the formation of the isobar with a high momentum due to the dynamics of the isobar in the nucleus. Such behavior of the angular distribution of the reaction yield is additional evidence of the adequacy of the model with the intermediate Δ-nuclear bound state.

The basic results of this work are as follows. The $^{12}C(\gamma, \pi^- p)$ and $^{12}C(\gamma, \pi^- pp)$ reactions have been experimentally studied. The irregularity in the angular dependence of the differential yield of pion–proton pairs for large proton-emission angles has been explained. Analysis of the data provides evidence of the existence of a Δ-nuclear bound state (Δ nucleus) that decays with the emission of a pion and a nucleon.

This work was supported by the Russian Foundation for Basic Research (grant 02-02-17866).

Список литературы

[1] V. N. Eponeshnikov, Y. F. Krechetov, Pisma Zh. Eksp. Teor. Fiz., 29 (1979) 442.

[2] I. Glavanakov, Y. Krechetov, A.Moiseenko *et al.*, Phys. Atom. Nucl., 61 (1998) 2064.

[3] I. Glavanakov, Y. Krechetov, O. Saigushkin *et al.*, JETP Lett., 81 (2005) 432.

[4] V. M. Bystritsky, A. I. Fix, I. V. Glavanakov et al., Nucl. Phys., A 705 (2003) 55.

[5] M. Liang, D. Branford, T. Davinson *et al.*, Phys. Lett. B411 (1997) 244.

[6] J.M. Laget, Phys. Rev. Lett., 41 (1978) 89.

[7] L. Kondratyuk, I. Shapiro, Yad.Fiz., 12 (1970) 401.

[8] V. A. Karmanov, Pisma Zh. Eksp. Teor. Fiz., 14 (1971) 127.

[9] J.M. Laget, preprint, CEN Saclay, DPHN/HE (1973).

[10] H. Arenhovel, Nucl. Phys., A247 (1975) 473.

[11] V. B. Belyaev, K. Moller, and Y. A. Simonov, J. Phys., G5 (1979) 1057.

[12] P. E. Argan, G. Audit, N. D. Botton, et al., Phys. Rev. Lett, 29 (1972) 1191.

η PHOTOPRODUCTION FROM DEUTERON AT E_γ=0.7÷1.5 GeV

O. Bartalini[1,2], V. Bellini[3,4], J.P. Bocquet[5], M. Capogni[1,2], M. Casano[2], M. Castoldi[6], P. Calvat[5], A. D'Angelo[1,2], J.-P. Didelez[7], R. Di Salvo[1], A. Fantini[1,2], G. Gervino[8], F. Ghio[9], B. Girolami[9], M. Guidal[7], A. Giusa[3,10], E. Hourany[7], R. Kunne[7], V. Kouznetsov[11], A. Lapik[11], P. Levi Sandri[12], A. Lleres[5], D. Moricciani[1,2], A. Mushkarenkov[11], V. Nedorezov[11], L. Nicoletti[2], C. Perrin[5], D. Rebreyend[5], F. Renard[5], N. Rudnev[11], T. Russew[5], G. Russo[10], C. Schaerf[1,2], M.-L. Sperduto[3,10], M.-C. Sutera[10], A. Turinge[11]

[1] *Università di Roma "Tor Vergata", I-00133 Roma, Italy*

[2] *INFN Sezione di Roma "Tor Vergata", I-00133 Roma, Italy*

[3] *Università di Catania, I-95123 Catania, Italy*

[4] *INFN Laboratori Nazionali del Sud, I-95123 Catania, Italy*

[5] *IN2P3, Laboratoire de Physique Subatomique et de Cosmologie, 38026 Grenoble, France*

[6] *INFN Sezione di Genova, I-16146 Genova, Italy*

[7] *IN2P3, Institut de Physique Nucléaire d'Orsay, 91406 Orsay, France*

[8] *INFN Sezione di Torino, I-10125 Torino, Italy*

[9] *INFN Sezione di Roma I, I-00185 Roma, Italy*

[10] *INFN Sezione di Catania, I-95123 Catania, Italy*

[11] *Institute for Nuclear Research, 117312 Moscow, Russia*

[12] *INFN Laboratori Nazionali di Frascati, I-00044 Frascati, Italy*

Abstract

The preliminary results obtained in the GRAAL experiment on exclusive η-mesons photoproduction on the quasi-free proton and neutron are reported. Comparison with the MAID calculations and results of other experiments are presented.

1 Introduction

Study of η-mesons photoproduction on nucleon is particularly suitable due to isospin conservation in final state which selects resonances with isospin 1/2 only. Moreover, study of these reactions on neutron in conjunction with proton data provides information about isospin dependence of photoexcitation amplitudes. Deuteron is a most suitable neutron target for such study and it also opens possibility to study nuclear effects. Extensive studies of η-mesons photoproduction at $E_\gamma < 1$ GeV revealed strong dominance of S11(1535) resonance. (See [1, 2, 3] and reference therein). This result can be quite well explained by the MAID

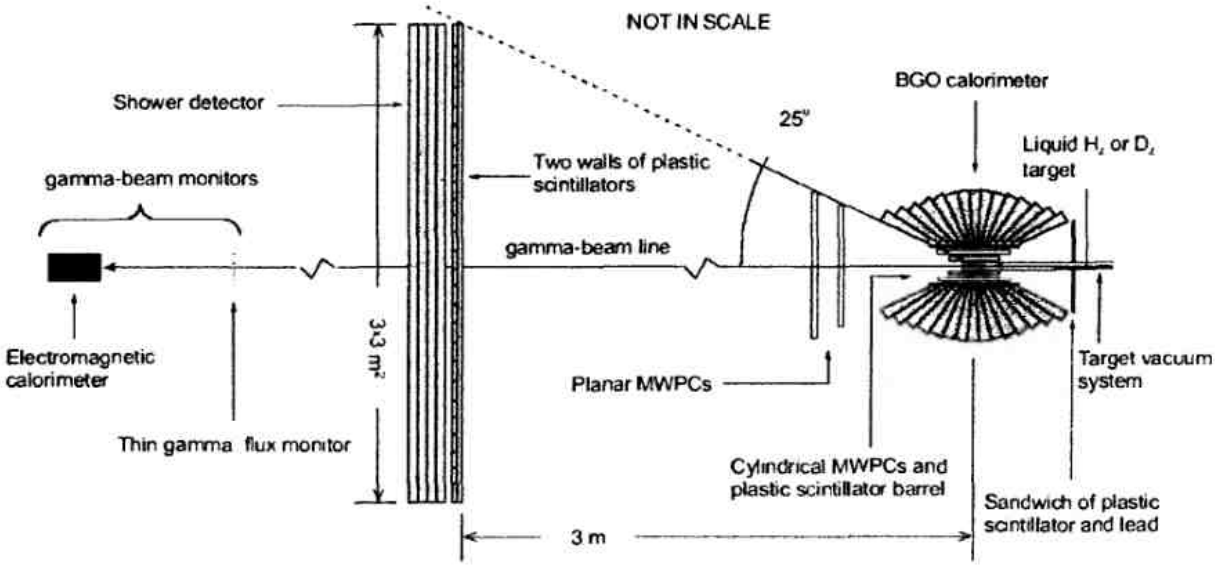

Fig. 1: Sketch of the GRAAL detection system.

analysis [4]. Recently, the energy region was extended for $E_\gamma > 1$ GeV [5, 6]. As well, the GRAAL and TAPSCB-ELSA collaborations reported the preliminary results on the beam asymmetry [7, 8] and the cross-sections [8] of η-mesons photoproduction on neutron (quasi-free from deuteron). The result from TAPSCB-ELSA experiment shows a bump structure in the neutron cross-section around the total c.m. energy $W = 1.675$ GeV which is not seen in the proton cross-section. At present time, this result is extensively discussed [9, 10]. There are two models which can qualitatively explain the neutron cross-section. First one is Isobar Model [11] which is used in the MAID calculations. This model explains the experimental result by the contribution of D15(1675) resonance imposing branching ratio $\Gamma_{\eta N}/\Gamma_{tot} = 17\%$. Alternatively, as it is suggested in work [12], the Chiral Soliton Model can also explain the neutron data by contribution of the narrow P11 resonance with mass around 1.7 GeV.

In the present work the preliminary results on the differential and total cross-sections of η-mesons photoproduction on the quasi-free proton and the quasi-free neutron at $E_\gamma = 0.7 \div 1.5$ GeV are reported. The data were obtained in the GRAAL experiment [13] with the use of a liquid deuterium target.

2 The setup

The beam of polarized tagged photons is produced by the backscattering of laser light on the 6.04 GeV electrons circulating in the storage ring of the ESRF (Grenoble, France). When using the green 514 nm and the ultraviolet 351 nm laser lines, the tagged spectrum covers the energy range $0.55 \div 1.5$ GeV. The tagging detector provides an energy resolution of 16 MeV(FWHM).

The detection system (Fig. 1) includes three main parts.

- The forward part in the angular range of $\theta \leq 25°$ which is covered by:
  1. two planar wire chambers for the tracking of charged particles;
  2. two walls of plastic scintillators consisting of 26 horizontal and 26 vertical bars, placed at 3 m from the target (They are designed for TOF, dE/dx, and angu-

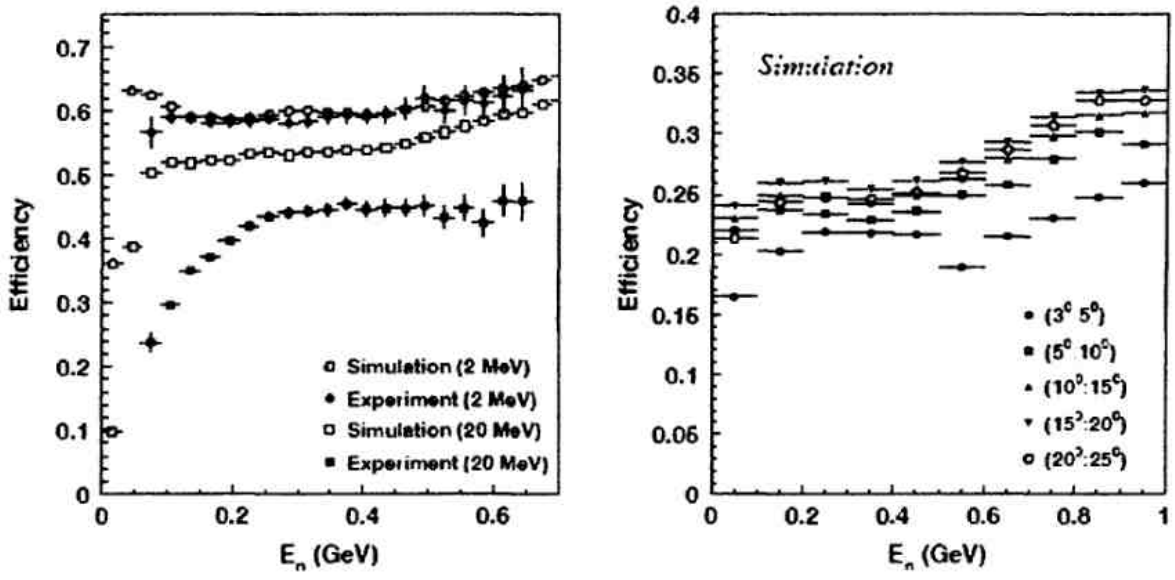

Fig. 2: The neutron detection efficiency in the BGO calorimeter (left) and the shower detector (right). See text for detailed explanation.

lar measurements of charged particles, as well as for particle identification and discrimination.);

3. the shower detector consisting of 16 vertical modules made of lead and plastic scintillator [14] (It provides TOF, dE/dx, and angular measurements, as well as the identification of both neutral (γ, neutron) and charged particles.);

- The central part, covering the angular range $25° \leq \theta \leq 155°$, which consists of:

  1. two cylindrical wire chambers for the tracking of charged particles;
  2. the barrel made of 5-mm-thick plastic scintillator bars for dE/dx measurement and the discrimination and identification of charged particles;
  3. the electromagnetic calorimeter made of 480 BGO crystals [15] (It is designed to measure energies and angles of gammas and low-energy protons up to 300 MeV/c, as well as the angles and ΔE response for charged pions and neutrons);

- The backward part within the angular range of $\theta \geq 155°$, which is covered by two plastic scintillator disks separated by a 1-cm-thick lead converter, which are sensitive to both neutral and charged particles (It is used as a veto detector).

The gamma-beam monitors are used in the determination of the γ-flux.

3 Neutron detection efficiency

The neutron detection efficiency was studied in simulation (with the GEANT3.21 package) and experiment for BGO calorimeter [15] and was simulated for the shower detector. Fig. 2 shows the neutron detection efficiency as a function of the neutron kinetic energy ((left) and (right) correspond to the BGO calorimeter and the shower detector, respectively). It was obtained a good agreement between the simulated and experimental data for a low (2 MeV) energy threshold of the BGO clusters (group of fired crystals) while for higher energy threshold (20MeV) there is discrepancy. Also, it was not obtained an angular dependence of the BGO efficiency. The simulated neutron detection efficiency of the shower detector

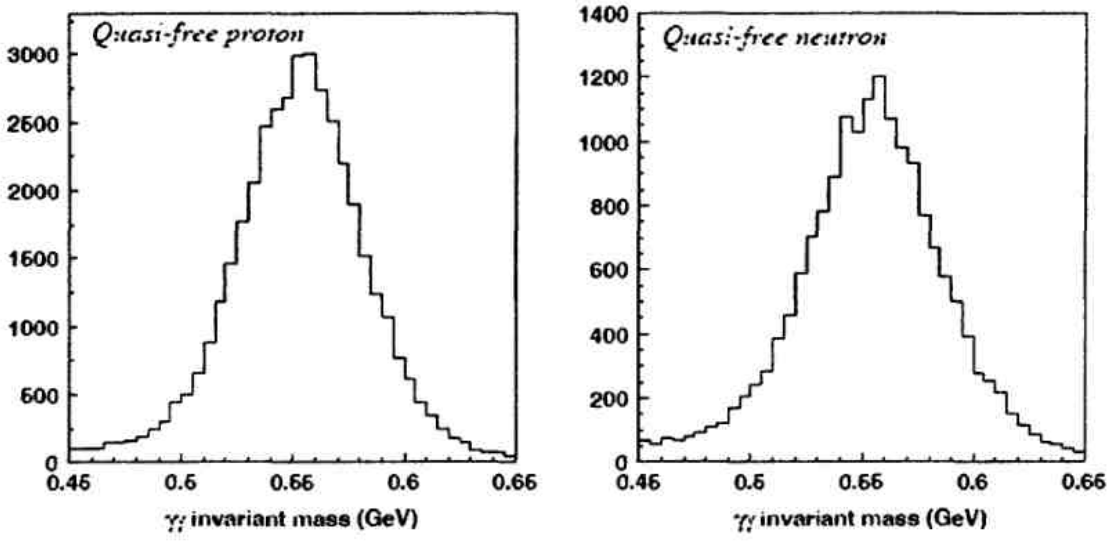

Fig. 3: Invariant mass of 2γ from η-mesons decay.

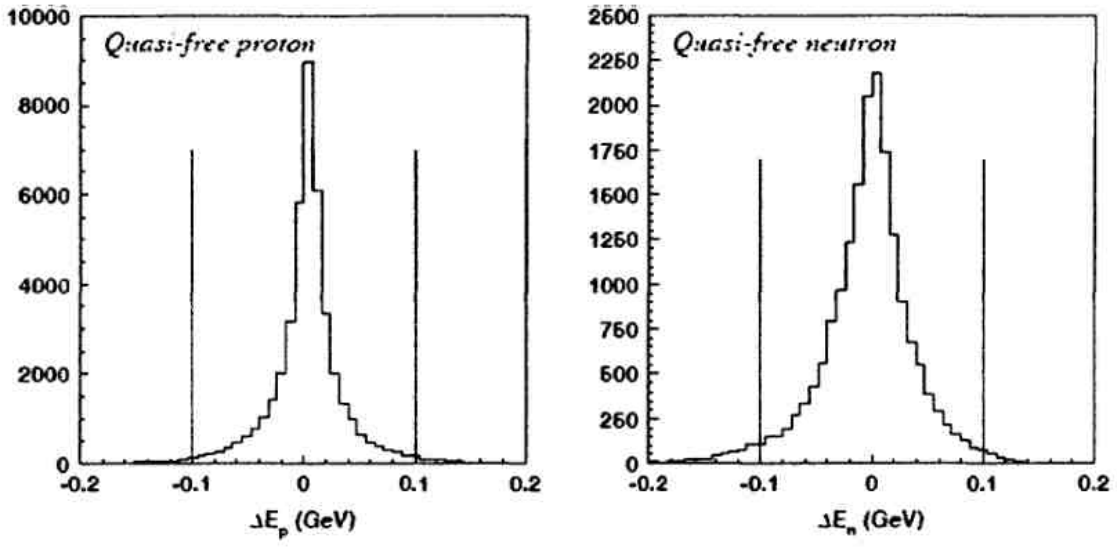

Fig. 4: Distributions of the difference between measured and expected energies of the recoil nucleons in the ηN c.m. frame.

is about twenty-five percents on average. Also it was obtained an angular dependence of this efficiency. Experimental study of the shower detector response for neutrons was not still done. Nevertheless, the information from this detector was used in the present analysis taking into account the simulated efficiency.

4 Event selection

In the present experiment two gammas from η decay and recoil nucleon (proton or neutron) were detected in coincidence. The η-mesons were identified via the standard invariant mass analysis of the two detected gammas (Fig. 3). Then, events which satisfy to the two-body kinematics of the quasi-free reactions, were selected via the missing energy analysis (Fig. 4), as well as the angles balance (Figs. 5 and 6).

The kinematic over-determination allows us to reconstruct the total c.m. energy W of the ηN system and to deduce the effective incident γ energy E_γ^* which is corresponded to

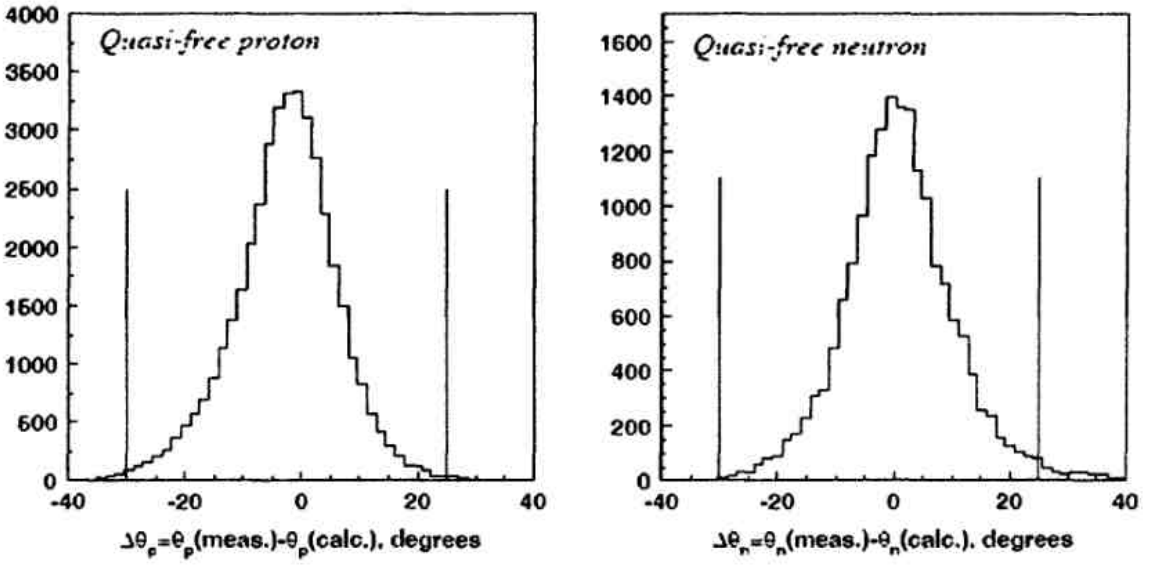

Fig. 5: The balance of the recoil nucleon polar angle.

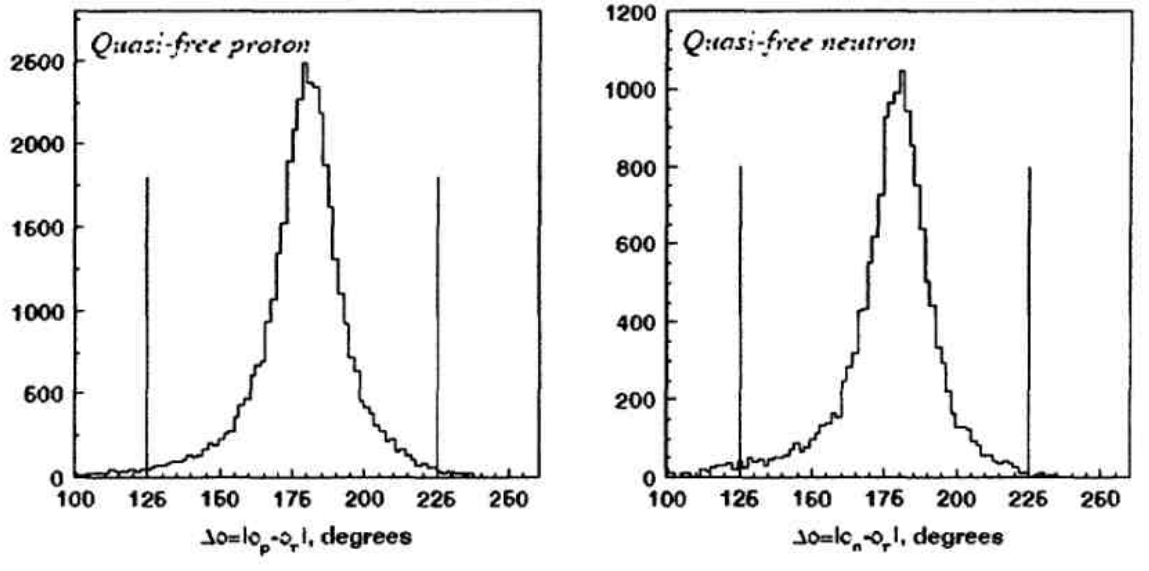

Fig. 6: The balance of the azimuthal angles.

the same c.m. energy for an target nucleon at rest:

$$W^2 = (E_\eta + E_N)^2 - (\vec{p}_\eta + \vec{p}_N)^2, \quad (1)$$

$$E_\gamma^* = \frac{W^2 - m_N^2}{2m_N}, \quad (2)$$

where E_η and $\vec{p}_\eta$ are the detected energy and momentum of η-meson, E_N and $\vec{p}_N$ are the recoil nucleon energy and momentum which are deduced from energy of the incident γ and E_η, m_N is mass of the recoil nucleon. In this way the Fermi smearing is eliminated from energy dependence of the cross-sections. As well, the cm polar angle θ^{cm} was calculated taking into account the Fermi momentum of target nucleon.

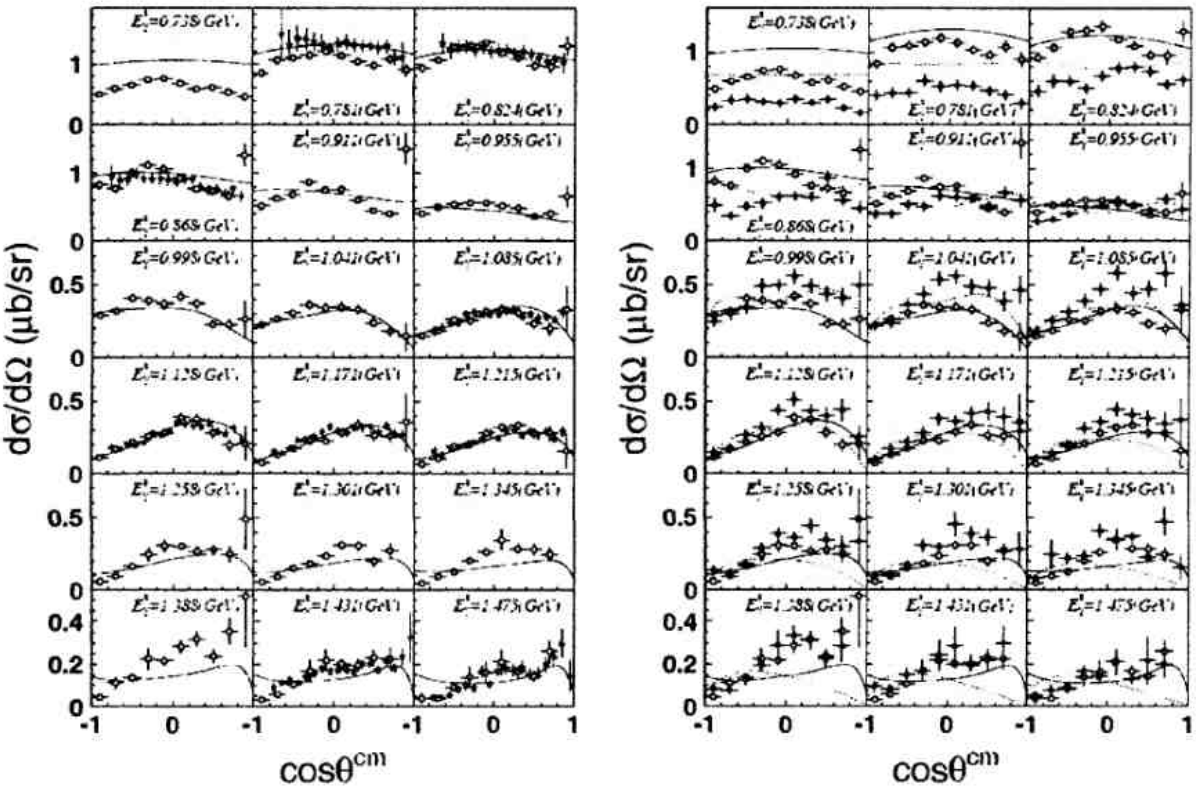

Fig. 7: The differential cross-sections of the η-mesons photproduction on the quasi-free proton (open circles) and the quasi-free neutron (full circles) in comparison with ETA-MAID2001 [4] predictions (solid and dashed lines correspond to $\gamma p \to \eta p$ and $\gamma n \to \eta n$, respectively). Stars show the data obtained in work [5] on free proton.

5 Results

5.1 Angular distributions

The differential cross-sections of the reaction $\gamma d \to \eta pn(spectator)$ are shown by circles on Fig. 7(left) as a function of $cos\theta_\eta^{cm}$. The data obtained in experiment CB-ELSA [5] on free proton as well as MAID calculations [4] are plotted for comparison by stars and solid line, respectively. One can see the data for free and quasi-free proton are in close agreement. Influence of the nuclear effects (e.g. FSI) seems to be negligible. It can indicate on the possibilities to extract the neutron data from the measurement on deuteron target without additional corrections. Also, it is seen that behavior of the angular distributions obtained in experiment and predicted by MAID are different at $E_\gamma > 1.25$ GeV.

The differential cross-sections of the reaction $\gamma d \to \eta np(spectator)$ are shown by filled circles on Fig. 7(right) in comparison with the data for the reaction $\gamma d \to \eta pn(spectator)$ as well as MAID predictions. One can see that the angular distribution in case of quasi-free proton and quasi-free neutron are different up to $E_\gamma \sim 1.13$ GeV. At higher energy, behavior of these angular distributions become very similar to each other. Additionally, the angular distributions of η photoproduction on quasi-free neutron poorly agree with MAID predictions.

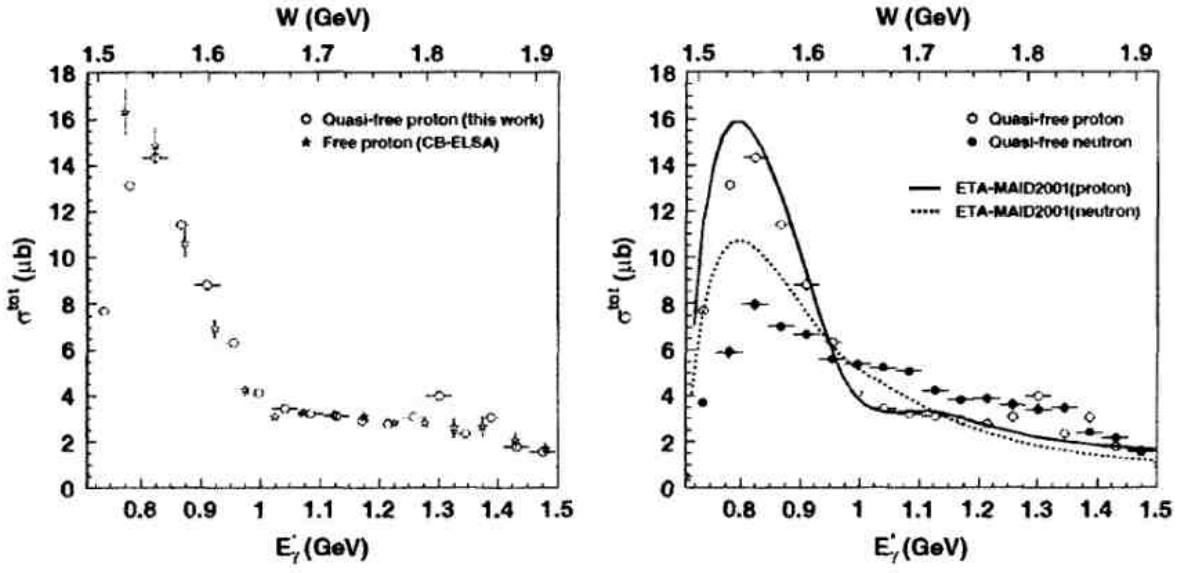

Fig. 8: The total cross-sections of η-meson photproduction on quasi-free proton and quasi-free neutron. All notations are identical to Fig. 7.

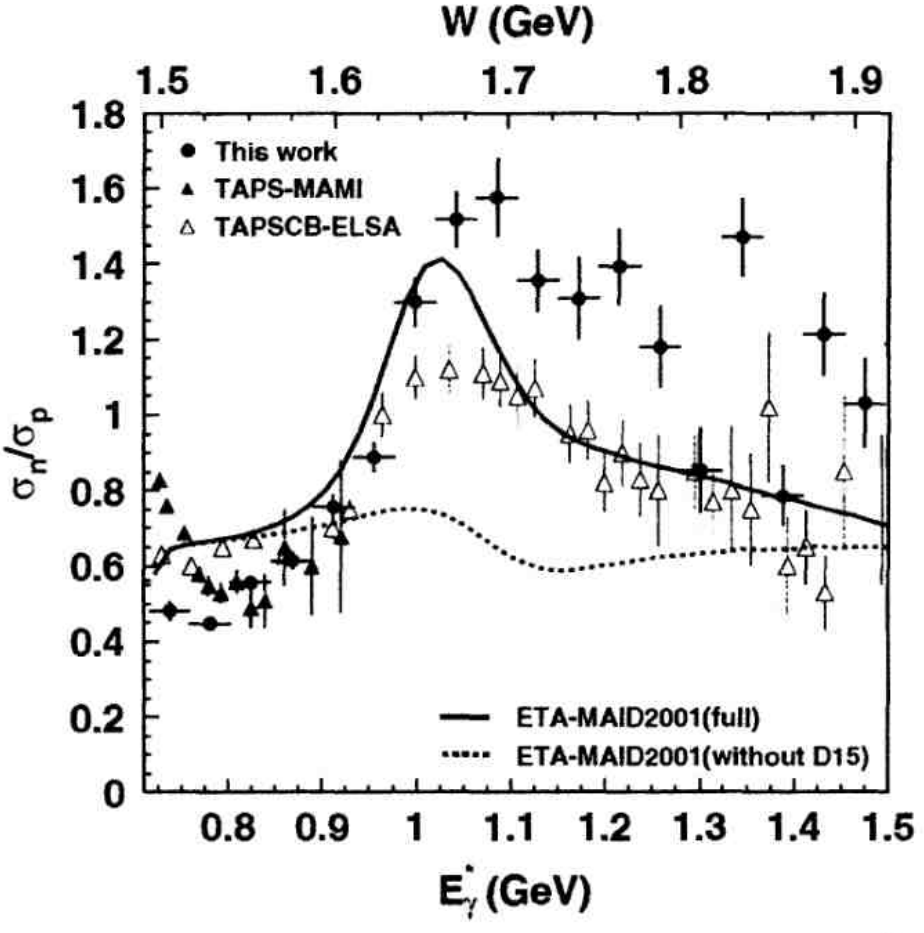

Fig. 9: The neutron/proton cross-sections ratio obtained in the present work (full circles) in comparison with TAPS-MAMI [1] (full triangles) and TAPSCB-ELSA [8] (open triangles) results. Solid line shows the calculation of the full MAID model, while the dashed line corresponds to the MAID calculation without the D15(1675) resonance contribution.

5.2 Total cross sections

The total cross-sections of η-meson photproduction on quasi-free proton and quasi-free neutron are shown on Figs. 8(left) and 8(right), respectively. All notations are identical to Fig. 7. Much as the differential cross-sections, the total cross-section on quasi-free proton is in good agreement with both the CB-ELSA data and MAID calculation for $E_\gamma < 1.25$ GeV. The difference seen at $E_\gamma \sim 0.740$ GeV is due to a systematic uncertainty, presumably.In case of the quasi-free neutron (Fig. 8(right)), the total cross-section has poorly agreement with respective MAID predictions. Moreover, the total cross-sections on quasi-free proton and quasi-free neutron have an opposite behavior in the region around $E_\gamma \sim 1.05$ GeV. The similar result was obtained in the TAPSCB-ELSA experiment [8].

Fig. 9 shows a ratio of the obtained total cross-sections σ_n/σ_p in comparison with the results from the previous experiments and MAID calculations. As it is seen, the MAID model qualitatively explains behavior the retion σ_n/σ_p. The restricted MAID calculations, in which the D15(1675) resonance is excluded, shows the important role of the D15(1675) resonance in the η-meson photoproduction on the neutron.

6 Summary

The preliminary results on exclusive η-mesons photoproduction on the quasi-free proton and neutron were reported. It was obtained close agreement between the quasi-free proton data and free proton data obtained earlier. At the same time, both these data are in disagreement with MAID prediction at $E_\gamma > 1.25$ GeV. The angular distributions of η photoproduction on the proton and neutron targets are different up to $E_\gamma \sim 1.13$ GeV and become very similar to each other at the higher energies. Additionally, the angular distributions of η photoproduction on quasi-free neutron poorly agree with MAID predictions. The neutron/proton cross-section ratio shows a rise up to ~ 1.5 at $E_\gamma \sim 1.05$ GeV. Behavior of the neutron/proton cross-section ratio agrees with results obtained earlier in the different experiments and can be qualitatively explained by the MAID analysis.

This work was supported by RFBR, grant no. 04-02-16996-a.

References

[1] J. Weiß et al., Eur. Phys. J. A 16, 275 (2003).

[2] F. Renard et al., Phys. Lett. B 528, 215 (2002).

[3] B. Krusche et al., Phys. Rev. Lett. 74, 3736 (1995).

[4] http://www.kph.uni-mainz.de/MAID/eta/etamaid.html

[5] V. Credé et al. Phys. Rev. Lett. 94, 012004 (2005).

[6] M. Dugger et al., Phys. Rev. Lett. 89, 222002 (2002).

[7] R. Di Salvo, MENU2004, August 29th -Sep 4th 2004, Beijing, China.

[8] I. Jeaglé, NSTAR2005, 12 - 15 October 2005, Tallahassee, Florida USA.

[9] L. Tiator, NSTAR2005, 12 - 15 October 2005, Tallahassee, Florida USA.

[10] L. Tiator, MESON2006, 9 - 13 June 2006, Kraków, Poland.

[11] W.-T. Chiang, S.-N. Yang, L. Tiator, D. Drechsel, Nucl. Phys. A 700, 429 (2002).

[12] M.V. Polyakov and A. Rathke, Eur. Phy. J A18 691 (2003).

[13] O. Bartalini et al., Eur. Phys. J. A 26 399 (2006).

[14] V. Kouznetsov et al., Nucl. Instr. and Meth. A 487 396 (2002).

[15] V. Bartalini et al., Nucl. Instr. and Meth. A 562 85 (2006).

MODERN DEVELOPMENTS IN CLUSTER PHOTODISINTEGRATION OF LIGHT NUCLEI

N.A. Burkova, K.A. Zhaksybekova

Al-Farabi Kazakh National University, Almaty, Kazakhstan

A modified cluster potential approach to a fragmentation of ^{7}Li, ^{7}Be and ^{9}Be nuclei has been developed. The analysis of observables for the whole set of two-cluster photodisintegration reactions was done. It was demonstrated that the given theory may not only explain practically all available experimental observables but gives also perspective predictions for future experiments.

Recently reported experimental data on the ground state and angular distributions of ^{9}Be(γ,p$_0$)^{8}Li, ^{9}Be(γ,t$_0$)^{6}Li, ^{9}Be(γ,^{3}He)^{6}He and ^{9}Be(γ,d$_0$)^{7}Li together with the cross section for the ^{9}Be(γ,d$_1$)^{7}Li reaction to the first excited state [1], gave rise for developing of new theoretical approach for treating of ^{9}Be nucleus fragmentation in two-cluster channels yielding lithium isotopes [2-4], what, in one's turn, allows to revaluate earlier experimental data [5,6].

Our approach is based on the modern $2\alpha n$ presentation of ^{9}Be nucleus in multicluster dynamic model with the Pauli projection (MDMP) [7]. In [2] the method of projecting of the $2\alpha n$ cluster wave functions (WFs) on to ^{9}Be$\rightarrow$^{8}Li+p, ^{7}Li+d and ^{6}Li+t (^{6}He+^{3}He) cluster channels was developed. For nuclei ^{8}Li, ^{6}Li, ^{6}He the MDMP three-body αtn [8] and αNN [9] functions have been used, as for the ^{7}Li nucleus the αt-cluster WF [10] was exploited.

As a first necessary step for check of obtained relative motion WFs the spectroscopic S-factors of p-, d-, and t-clusters separation from ^{9}Be have been calculated. Theoretical results reproduce the available experimental data quite good [11] and are not in contrast with calculations of one-particle shell model [12].

Then, the characteristics of the photodisintegration reaction ^{9}Be(γ,d$_{0+1}$)^{7}Li, as well as radiative capture process ^{7}Li(d,γ)^{9}Be, have been calculated within the developing approach [3]. Theoretical calculations fit the experimental data [1,13] both qualitatively and quantitatively.

Figure 1 shows how present theory reproduces the differential cross section $\frac{d\sigma}{d\Omega}(E_\gamma,\Theta)=\frac{d\sigma^{(S)}}{d\Omega}+\frac{d\sigma^{(D)}}{d\Omega}$ of the ^{9}Be(γ,d$_{0+1}$)^{7}Li process. It is important, that in our case weight of D-component in ^7Li-d relative motion function is $P_D \approx 68\%$. So, there is an essential difference between a *traditional approach* when (1a,b) amplitudes are taking into account only and *present one* leading to new transitions due to D-component (2a,b)

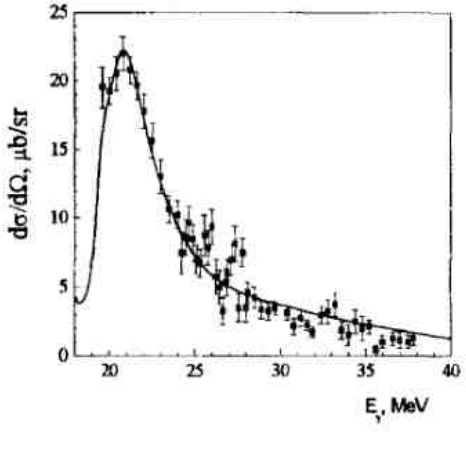

$$S(3/2^-) \xrightarrow{E1} p \quad (1a) \qquad D(3/2^-) \xrightarrow{E1} p+f \quad (2a)$$

$$S(3/2^-) \xrightarrow{E2} d \quad (1b) \qquad D(3/2^-) \xrightarrow{E2} s+d+g \quad (2b)$$

Fig. 1

Same calculation scheme was applied for the analyzing of $^7Li+\vec{d}\rightarrow{}^9Be+\gamma$ reaction measured at $E_d = 6\ MeV$ by *Schmid G.J.* et al [33]. Comparison of Fig. 2 and 3 shows the difference in results between the previous calculations and present approach.

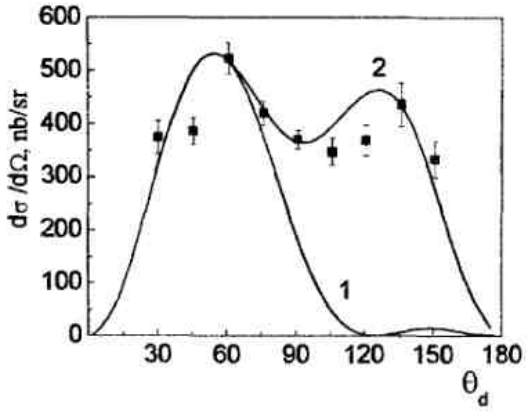

Fig. 2 Calculations by [33]

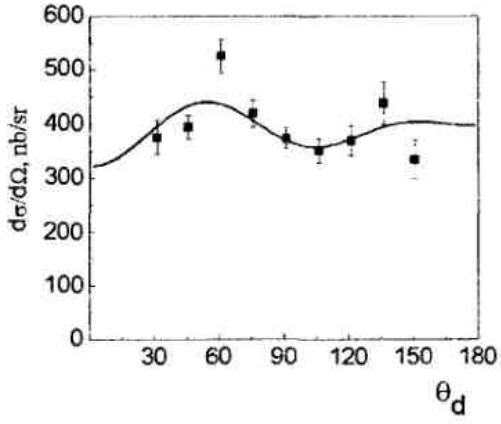

Fig. 3 Present calculations

1 – transitions to the S-state of ^{9}Be
2 – variation of 8 amplitudes and 7 relative phases

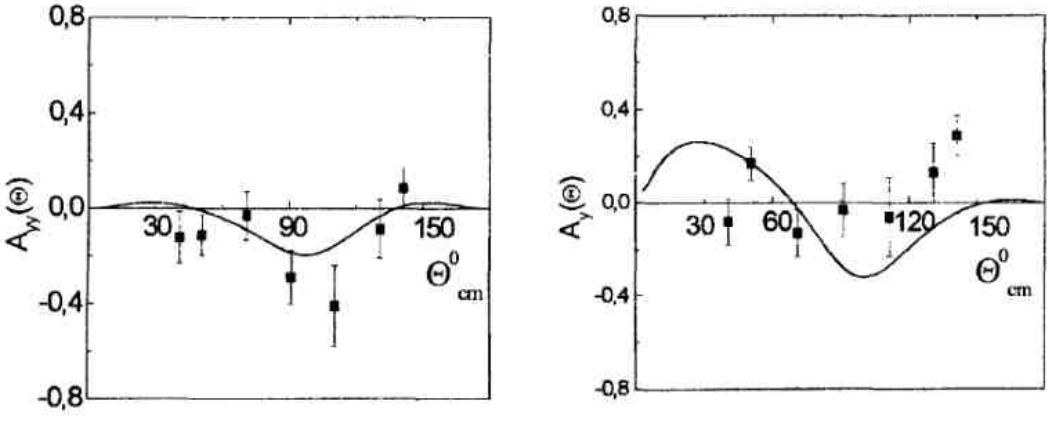

Fig. 4 Polarization observables in the $^{7}Li+\vec{d}\rightarrow{}^{9}Be+\gamma$ process.

Fig. 4 shows how the corresponding polarization observables A_{yy} and A_y are reproducing within the developed approach.

Actually, each of ^{8}Li, ^{7}Li, ^{6}Li nucleus has the pronounced cluster features which reveal individually in ^{9}Be photodisintegration channels. So, the promising results for (γ,d_{0+1}) reaction, make it natural to rise the trying level for our approach and continue with exploring of ^{9}Be$(\gamma,p)^{8}$Li reaction.

We based on two sets of exclusive experimental data on photo-proton emission from ^{9}Be. Shoda and Tanaka [1] measured the energy distribution for the (γ,p_0) process at $\theta_p=125^o$ in the energy interval $E_\gamma=20,5-27,5$ MeV (Q=16,8876 MeV), as well as angular distributions integrated by the energy range $E_\gamma=22-22,5$ MeV.

These data are complemented by Denisov [5] for (γ,p_{0+1}) differential cross section, when ^{8}Li is registered in the ground state $(j^\pi,t=2^+,1)$ and 1-st excited state $(j^\pi,t=1^+,1;\ E^*=0,9808$ MeV) at $\theta_p=90^o$, but in the energy range $E_\gamma=19,9-29,6$ Mev.

Both measurements show the pronounced resonance structure in $d\sigma/d\Omega(E_\gamma)$. The origin of this structure we clarify further.

Our preliminary results for investigation of (γ, p_0) process are presented in [15]. The differential cross sections at $\theta_p = 125^o$ and angular distributions of outgoing protons at $E_\gamma = 21,5 MeV$ have been calculated under assumption, that E1- and E2-multipoles are sufficient to fit the Shoda experimental data. Following amplitudes have been taken into account: $P \xrightarrow{E1} s(3/2^+) + d(1/2^-, 3/2^+, 5/2^+)$ and $P \xrightarrow{E2} p(1/2^-, 3/2^-, 5/2^-) + f(3/2^-, 5/2^-, 7/2^-)$. It was found that the resonance structure of differential cross sections is conditioned by the resonance behavior of $f(3/2^-, 5/2^-, 7/2^-)$ partial waves. M1-multipole was also estimated, it plays the minor role.

Analysis of (γ, p_{0+1}) experimental data by Denisov [5] shows that at $\theta_p = 90^o$ the energy dependence of cross section $d\sigma/d\Omega(E_\gamma)$ also has the pronounced resonance structure at $E_\gamma(E_{cm}) = 20,75(3,65)$; 21,66 (4,57) and 23,33(6,44) MeV. So, this structure should be interpreted as the resonance behavior of corresponding scattering waves, but not the result of somewhat interference effects. One more interesting moment appears while comparing of Shoda and Denisov data. Extending of energy interval in case of (γ, p_{0+1}) reaction to $E_\gamma(E_{cm}) = 29,6(12,7)\ MeV$ made observable one more resonance at $E_\gamma(E_{cm}) = 27,5(9,6)\ MeV$. Let us remark, that Shoda's data shows only a hint on such a resonance at the very edge of spectrum.

Thus, in addition to already treated E1 and E2 multipoles the E3-transition was included in consideration, i.e. the corresponding amplitudes $P \xrightarrow{E3} d(3/2^+, 5/2^+, 7/2^+) + g(5/2^+, 7/2^+, 9/2^-)$ were also taken into account. It should be mentioned, that in case of formation ^{8}Li in ground state $2^+,1$ the selection rules lead to channel spin s=3/2 only. But if ^{8}Li yields in 1-st excited state $1^+,1$ spin channel value may be both 3/2 and 1/2. Our calculations gave the negligible input of transitions to states with s=1/2. So, in present work all mentioned amplitudes are given for spin channel s=3/2.

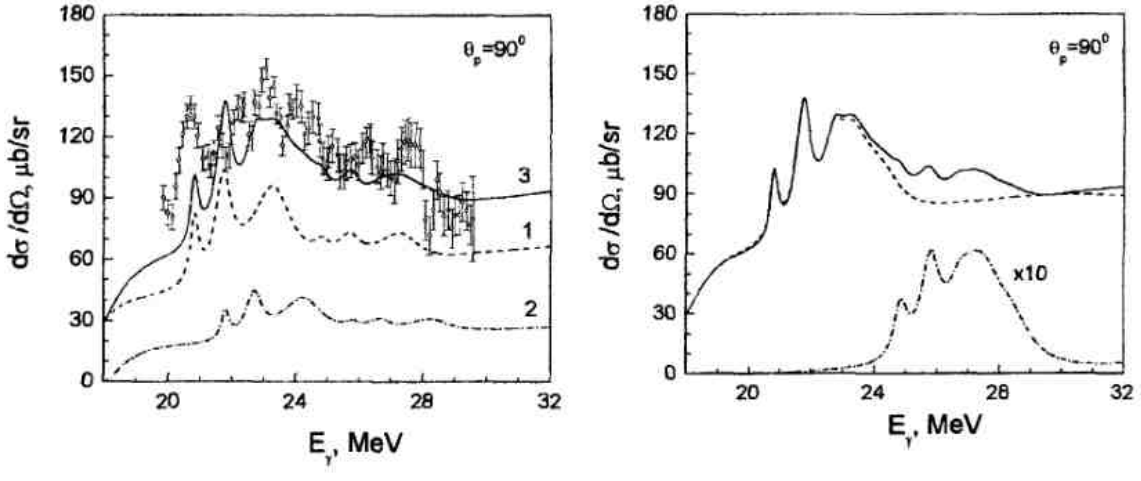

(a) *(b)*

Fig. 5 Differential cross sections of the process ^{9}Be$(\gamma, p_{0+1})^8$Li. Present calculations: a: curve 1 – (γ, p_0); curve 2 – (γ, p_1); curve 3 – total cross section. Experiment – [6]. b: dash – sum of E1 and E2 multipoles; dash-dot – partial cross section of E3 transition; solid curve – total cross section

Fig. 5a demonstrates the comparison of the theoretical calculations of $d\sigma/d\Omega(E_\gamma)$ cross section with experimental data. It is seen that both (γ, p_0) and (γ, p_1) cross sections have the resonance structure. The relative input of (γ, p_0) and (γ, p_1) channels corresponds approximately to the ratio of spectroscopic factors S_{1^-}/S_{2^+} =0,34/0,88≈0,39.

Fig. 5b illustrates the comparative input of E3-multipole on the ground of E1+E2-multipoles. It is clear that E1+E3 interference effects occurred at angle $\theta_p = 90^o$ play the most essential role at the edge of the treated energy range. The E3-multipole cross section has a resonance behavior correlated to the resonances in g-scattering partial waves.

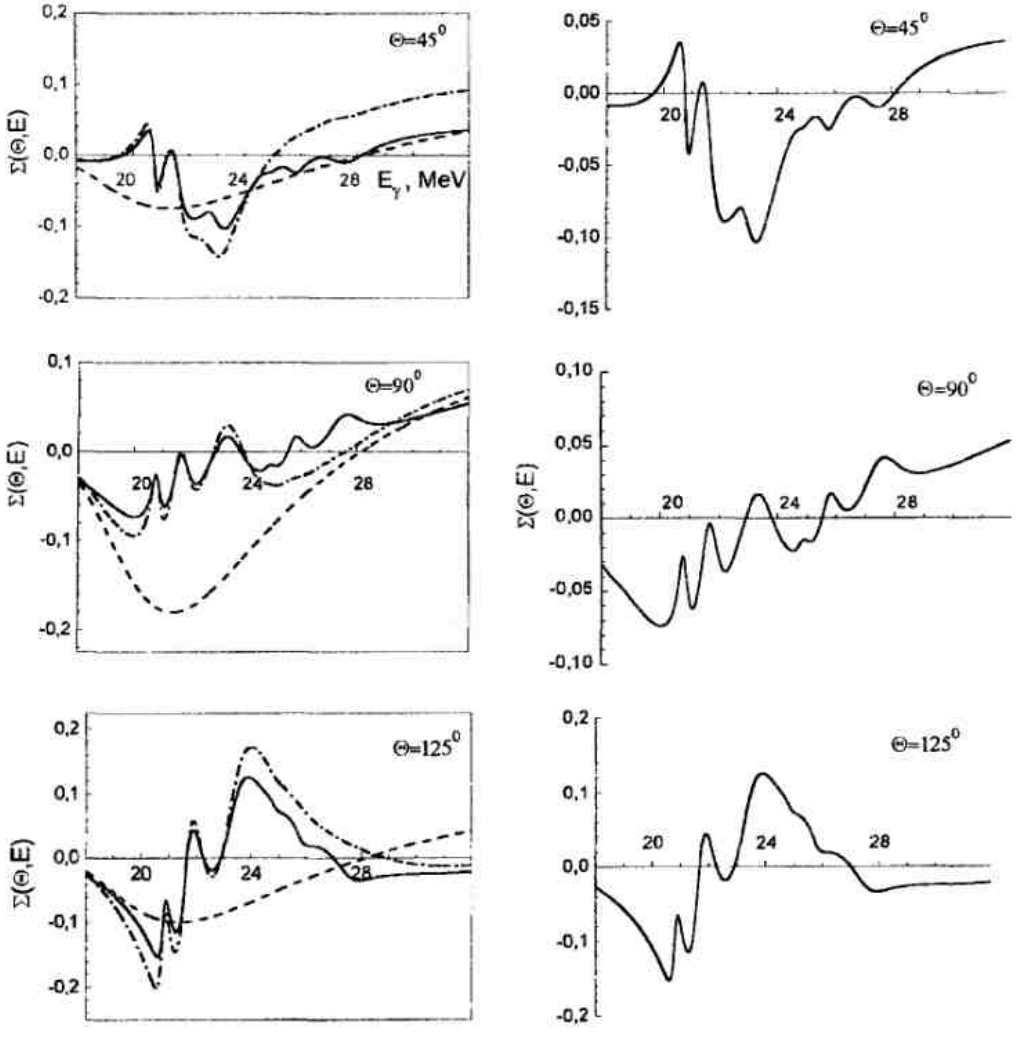

Fig. 6 Asymmetry in the process ${}^9Be(\vec{\gamma}, p){}^8Li$: dash curve – E1 multipole; dash-dot – E1+E2; solid curve – E1+E2+E3

To check our predictions on the strong E3-transition and the resonance structure observed in differential cross sections $d\sigma/d\Omega(E_\gamma, 90^\circ)$ and $d\sigma/d\Omega(E_\gamma, 125^\circ)$ at the energies $E_\gamma(E_{cm})$ =20,75(3,65); 21,66 (4,57); 23,33(6,44) and 27,5 (9,6) MeV we *proposed* for future measurements the asymmetry $\Sigma(E_\gamma, \theta)$ in the process ${}^9Be(\vec{\gamma}, p){}^8Li$ given in Fig. 6.

Further development of above theory concerns the calculation of the cluster fragmentation spectroscopy in $^7Li\{\alpha t\}\to{}^6 Li\{\alpha np\}+n$, $^7Li\{\alpha t\}\to{}^6 He\{\alpha nn\}+p$, $^7Be\{\alpha\tau\}\to{}^6 Li\{\alpha np\}+p$, $^7Be\{\alpha\tau\}\to{}^6 Be\{\alpha pp\}+n$ channels. Residual nuclei A=6 have been accounted both in ground state and excited states. Photoreactions $^7Li+\gamma\rightleftarrows{}^6 He+p$ and $^7Li+\gamma\rightleftarrows{}^6 Li+n$ have been examined, as well as polarization observables have been calculated.

For isobaric triplet $^6He-{}^6Li-{}^6Be$ MDMP functions have been used [9]. Isobaric doublet $^7Li-{}^7Be$ is described in a framework of $\alpha t-$ and $\alpha\tau-$cluster models based on the deep attractive potentials with excluded Pauli forbidden states [16]. It should be note, that in many particle shell model (MPSM) ^7Li and ^7Be nucleus are *indistinguishable*, but in cluster model they are *not identical*. Thus, it is not obvious, that ^7Li and ^7Be have one and the same spectroscopic characteristics as it follows from MPSM. This is a question for the following discussion.

It should be pointed, that in case of light nuclei *resultant isobars* $(Z-1,N+1)$ and $(Z+1,N-1)$ are unstable, but resemble the structure of a *parent* nucleus (Z,N). For example, ^6He is unstable long-live nucleus, $\tau_{1/2}=0{,}802$ s, ^6Be – unstable short-live nucleus, with life-time ~ 10^{-21} s. *Hence, it is a challenge to find a way for getting information on short-living isobar using the data on the stable parent nucleus or on the more stable isobaric partner.*

Here the virtual decays $^7Li\to{}^6 Li+n$, $^7Li\to{}^6 He+p$, $^7Be\to{}^6 Li+p$ and $^7Be\to{}^6 Be+n$ of isobar analogous channels are treated in details. Corresponding excitation levels E_x of $^6He-{}^6Li-{}^6Be$ triplet are pointed in Table 1. The relative motion wave functions (WF) in final channels have been obtained analytically as a result of overlapping integration and were used for the calculation of neutron S_n- and proton S_p-spectroscopic factors [17,18]. Residual nuclei $A=6$ have been treated both in ground and excited states. Projecting procedure of $\alpha t-$ and $\alpha\tau-$cluster functions assumes the using of structural WF of t and τ nucleus. It is possible to use the parametrization corresponding to free nuclei. In our case we are doing with translational invariant shell model (TISM) for t and τ, what allows to vary the oscillator parameter r_0 and, thus to simulate the deformation of three-body cluster.

Table 1

$^7Li\to{}^6 Li+n$, $^7Li\to{}^6 He+p$				
j^π,T	$0^+,1$		$2^+,1$	
A=6	^6Li	^6He	^6Li	^6He
E_x, MeV	3,56	*g.s.*	5,37	1,797
$S^{theor.}$ [12]	0,285	0,571	0,208	0,416
S^{theor} [19]		0,56		0,34
S^{exp} [11]	0,24	**0,48 ***	0,14	**0,28 ***
$S^{exp.}$ [20]	**0,31 ***	0,62	**0,165(0,16) ***	0,37 (0,32)
$S^{exp.}$ [21]	**0,21 ***	0,42(4)	**0,08 ***	0,16(2)
$S^{exp.}$ [22]	**0,3***	0,6	**0,2***	0,4
S^{theor}_{VMC} [21]		0,41		0,19

S^{theor}, r_0=1,3	0,2244	0,4611	0,1456	0,2913
S^{theor}, r_0=1,67	0,2855	0,5805	0,1688	0,3344
S^{theor}, r_0=2,36	0,2281	0,4563	0,1106	0,2189
$^7Be \to ^6 Li + p$, $^7Be \to ^6 Be + n$				
j^π, T	0^+,1		2^+,1	
A=6	^6Li	^6Be	^6Li	^6Be
E_x, MeV	3,56	*g.s.*	5,37	1,67
S^{theor}, r_0=1,6	0,2865	0,5333	0,1748	0,3320
S^{theor}, r_0=1,8	0,2963	0,5588	0,1725	0,3317

* – ***experimental data recalculated according model-independent ratio*** $S_p / S_n = 2$

The method of getting out the spectroscopic information on $^7Be \to ^6 Be + n$ virtual decay cluster channel was suggested basing on comparative analyses with $^7Li \to ^6 Li + n$ and $^7Li \to ^6 He + p$ channels [17], as well as with $^7Li \to ^6 Li + n$ and $^7Be \to ^6 Li + p$ ones [18].

It was shown in [17,18] that S-factors in $^7Li \to ^6 Li + n$ and $^7Li \to ^6 He + p$ channels are correlated by model independent ratio (MIR) $R = S_p / S_n$. In MPSM $R = 2$ exactly. In cluster models R is varying within 3-4% range. So, data on proton S_p-factors may be recalculated into data on neutron S_n-factors and vice versa (Table 1). In case of $^7Li \to ^6 Li + n$ and $^7Be \to ^6 Li + p$ channels MIR was also found and it equals $R = S_p / S_n \sim 1$ [18]. As it is seen from Table 1, a comparison of the calculated S – factors with available experimental data as well as with theoretical calculations done within a traditional many-particle shell model shows no radical discrepancies, and, even more, are in good agreement.

The developed approach was applied to treating of $^7Li + \gamma \rightleftarrows ^6 He + p$ processes. For direct photodisintegration reaction $^7Li(\gamma, p_{0+1})^6He$ two groups of experimental data on integral [23] and differential [24] cross sections measured from threshold up to E_γ~30 MeV more than 30 years ago are known. The problem is that these data are not in concordance. Exclusive data on $^7Li(\gamma, p_0)^6He$ in energy interval $E_\gamma \sim 50-140$ MeV are also available [25], but they are out of the frame of potential approach.

So, in present calculations we orient on radiative proton capture $^6He(p,\gamma_{0+1})^7Li$ data measured recently in inverse kinematics [26]. As in experiment transitions into g.s. of $^7Li(3/2^-)$ and 1-st exc. state $1/2^-$ (0,48 MeV) are indistinguishable, the following amplitudes have been taken into account in present calculations:

$$s(1/2^+) + d(3/2^+, 5/2^+) \xrightarrow{E1} P_{g.s.,3/2} \quad (3a) \qquad s(1/2^+) + d(3/2^+) \xrightarrow{E1} P_{exc,1/2} \quad (4a)$$

$$p(1/2^-, 3/2^-) + f(5/2^-, 7/2^-) \xrightarrow{E2} P_{g.s.,3/2^-}; \quad (3b) \qquad p(3/2^-) + f(5/2^-) \xrightarrow{E2} P_{exc,1/2^-} \quad (4b)$$

Fig. 7*a* shows a comparison of our calculations and those done [26] within the resonating group method (RGM). RGM calculations are normalized to the data and accounted only E1-multipole. One may recognize that our results reproduce the experiment better comparing RGM.

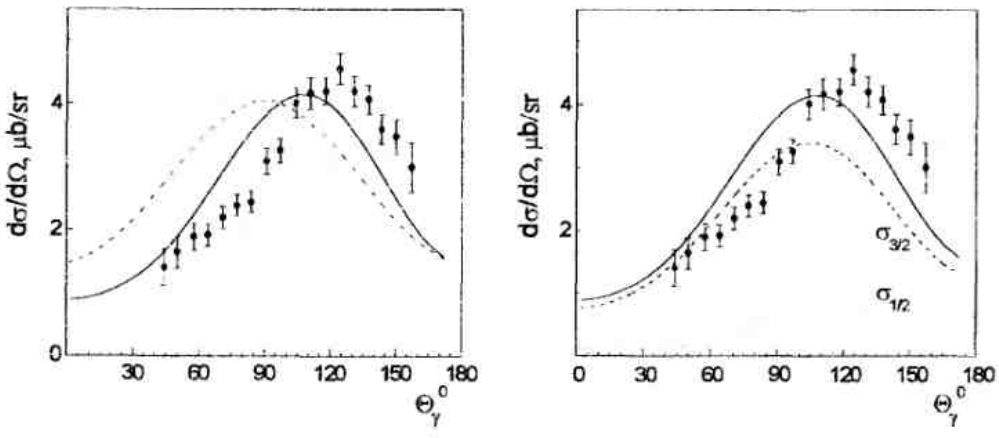

Fig. 7. Angular distributions in the process ${}^{6}He(p,\gamma_{0+1}){}^{7}Li$. Exp. – [26] . *a* – comparison of present (solid) and RGM [26,27] (dash) calculations; *b* – partial $\sigma_{3/2}$ and $\sigma_{1/2}$ cross sections, present work

One more essential difference of present work and RGM concerns estimations of relative input of partial cross sections $\sigma_{3/2}$ and $\sigma_{1/2}$ into angular distributions at $E_\gamma = 40$ MeV (Fig.7). According Table 2 from RGM calculations the ratio $\sigma_{1/2}/\sigma_{3/2} = 2,9$ follows. Authors [26] used this value for estimation of absolute value of experimental integral cross section $\sigma_{exp} = 35 \pm 2$ μb. Using data on photodisintegration ${}^{7}Li(\gamma,p_0){}^{6}He$ [25] via detailed balance consideration a value $\sigma_{3/2} = 9,6 \pm 0,4$ μb was obtained for transitions to ${}^{7}Li_{g.s.}$. Then, using factor 2,9 cross section $\sigma_{1/2}$ was calculated and final value $\sigma \sim 38$ μb was obtained. But, it should be noted that experimental data on ${}^{7}Li(\gamma,p_0){}^{6}He$ correspond to the photon energies $E_\gamma \geq 50$ MeV [25], thus it is not correct to use them in such a context.

Table 2

cross sections	$\sigma_{3/2}$, μb	$\sigma_{1/2}$, μb	σ, μb
theory [26]	15	44	59
present theory	31,08	6,0	37,08
exp. [25]	9,6± 0,4	-	~38
exp. [26]	-	-	35±2

Our estimations give $\sigma_{1/2}/\sigma_{3/2} = 0,19$ or inverse ratio $\sigma_{3/2}/\sigma_{1/2} = 5,2$, what differs from RGM. From Table 2 also well seen that our calculations reproduce the absolute value of the observed cross section very good. While $\sigma_{3/2}$ dominates, experimental data may be reproduced only if ~16% input of $\sigma_{1/2}$ cross section. That is why multipole analysis of both partial cross sections presented on Fig. 7 has a sense.

Fig. 8 shows "forward-backward" asymmetry of both cross sections, but in case of $\sigma_{1/2}$ it is more pronounced. The reason of such a behavior is due to E1-E2 interference. So, more accurate specifying of V_{p^6He} interaction potential for *even* scattering waves may improve the description of experiment.

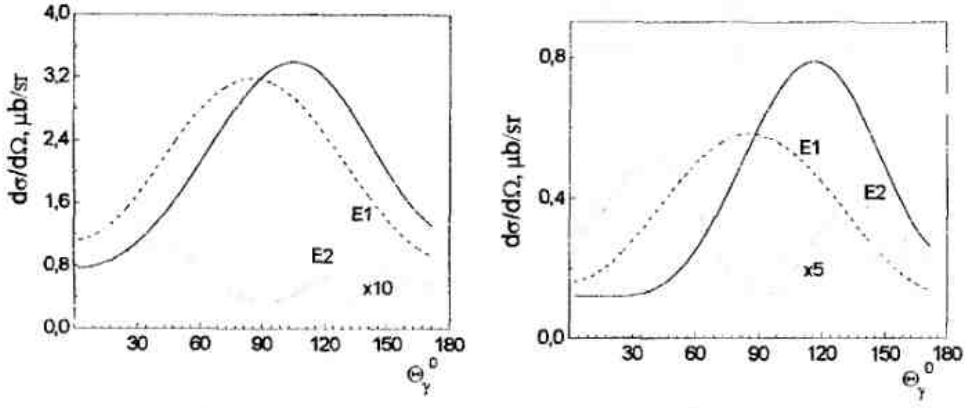

a *b*

Fig. 8 Multipole cross sections of radiative capture $^{6}He(p,\gamma_{0+1})^{7}Li$: *a* – transitions to g.s., $\sigma_{3/2}$; *b* – transitions to 0,48 state, $\sigma_{1/2}$

Basing on the same model, the calculation of integral cross section for the photodisintegration process $^{7}Li(\gamma,p_0)^{6}He$ was carried out, Fig. 9. Data sets (I and II refer to measurements with real photons corresponding to $E_{\gamma max}=28$ and 50 MeV, i. e. set II may include besides channel $^{7}Li(\gamma,p)$, Q=9,98 MeV, also channels $^{7}Li(\gamma,p2n)$, Q=10,95 MeV and $^{7}Li(\gamma,pn)$, Q=11,84 MeV [24].

Fig. 9

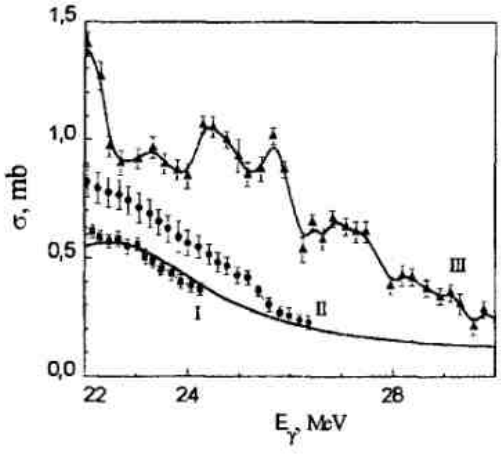

The upper experimental points (solid line for guidance only) on Fig. 9 (III) were measured with real photons also and related to the process $^{7}Li(\gamma,p_{0+1})^{6}He$ [23]. Well seen that set (III) reveals the resonance energy dependence contrary to sets (I) and (II). Our calculations are done for the $^{7}Li(\gamma,p_0)^{6}He$ reaction and may be compared with set (I) only – a coincidence of theory and experiment is quite well.

As both experimental (set I) and calculated cross sections of photoreaction $^{7}Li(\gamma,p_0)^{6}He$ show monotonous energy dependence, one may explain the resonance structure of data set (III) by additional contribution of (γ,p_1)-channel corresponding to formation of ^{6}He nucleus in 1-st excited state $2^{+},1$. According our estimations in fragmentation channel $^{7}Li_{gs}\rightarrow^{6}He(2^{+},1)+p$ states with channel spin $s_c=5/2$ dominate absolutely comparing those with $s_c=3/2$ [17,18]. This may lead to complicated final interactions $^{6}He(2^{+},1)+p$ what very likely was observed by *Denisov* [23]. Today there are no data on the high-spin states on proton fragmentation of ^{7}Li nucleus. Thus, new theoretic and experimental investigations of this problem are of great importance.

The developed approach for construction of ^6Li+n-channel by means of projecting procedure $\left\langle {}^6Li\{\alpha np\}, n \middle| {}^7Li\{\alpha t\}\right\rangle$, but the ***modified version***, was used for the calculation of $^7Li(\gamma,n)^6Li$ photodisintegration process at the energies E_γ~8-9 MeV. This energy range corresponds to (γ,n_0)-channel, i.e. experimental data might be recognized the exclusive ones [28,29]. Besides, there is an evidence of low-energy magnetic M1-resonace corresponding the $J_i^\pi, T_i = 5/2^-, 1/2$(7,456 MeV) level in ^7Li nucleus, which reveals also in continuous scattering ^6Li+n-channel as a resonant behavior of p-phase shift.

Let us comment the modifications appeared in our model. In case of *direct* projecting we obtained the radial relative motion $^6Li_{g.s}n$ bound state WF in a form

$$R^{(\kappa)}_{1^+,s_c}(R_{6n}) = \alpha_{[000,1]}P^2_{[000,1]} + \alpha_{[022,1]}P^4_{[022,1]} + \beta_{[022,1]}F^4_{[022,1]} \qquad (5)$$

Weight of each component equals the square root from the corresponding spectroscopic $S_{\kappa s_c}$-factor: $\alpha_{[000,1]} = 0,97$, $\alpha_{[022,1]} = 0,74\cdot10^{-2}$, $\beta_{[022,1]} = 0,26\cdot10^{-2}$. In (5): κ-relative angular momentum; $[\lambda lL,S]$- partial components of ^{6}Li MDMP function [9]; s_c-channel spin. It is clear, that direct transitions $P^2_{[000,1]} \xrightarrow{M1} p_{s_s=3/2}(1/2^-,3/2^-,5/2^-)$ to continuum with channel spin $s_s = 3/2$ are forbidden. Same problem met *Barker* [30], while performing the similar calculations basing on the ^{6}Lin-cluster model. But in our case it is possible to realize the modified scheme avoiding ***preliminary*** projection, but calculating the $\hat{\sigma}$-type matrix element $\left\langle {}^6Li\{\alpha np\}, n \middle| \hat{\sigma} \middle| {}^7Li\{\alpha t\}\right\rangle$ directly. As a result, in case of M1-multipole transitions into $[\lambda lL,S] = [000,1]$ state of ^{6}Li occurs and both spin channels s_c=1/2 and s_c=3/2 are allowed. Such a scheme gives rise for treating of ***magnetic*** disintegration $^7Li(\gamma,n)^6Li$ within the *direct mechanism* contrary to *Barker* approach, when Breit-Wigner formula for $\sigma_{res}(\gamma,n_0)$ cross section was used.

Besides M1-multipole convective electric E1- and E2-multipoles (channel spin is conserved $s_s = s_c$) are accounted. So, the corresponding amplitudes are

$$P^2_{[000,1]} \xrightarrow{E1} s(1/2^+) + d(3/2^+,5/2^+) \qquad (6)$$

$$P^2_{[000,1]} \xrightarrow{E2} p(1/2^-,3/2^-) + f(5/2^-,7/2^-) \qquad (7)$$

The results of present calculations and their comparison with available experimental data are presented on Fig. 10.

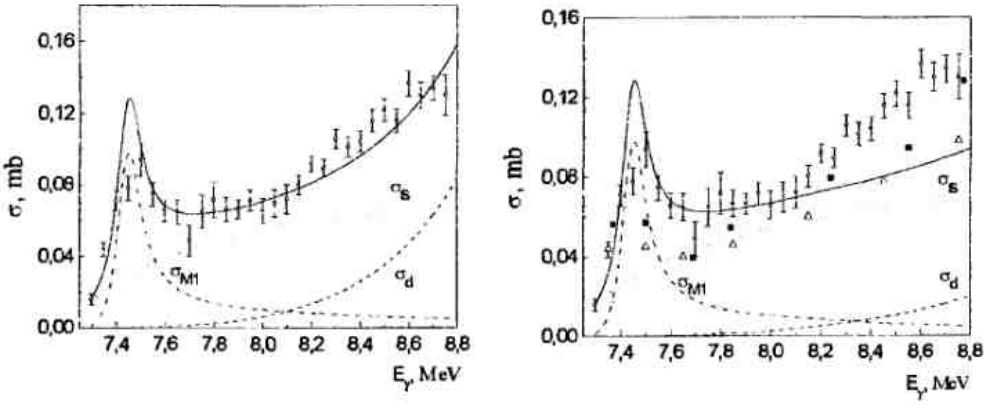

a *b*

Fig. 10. Cross sections of the $^7Li(\gamma,n_0)^6Li$. Experiment: ○ – [29], , – [31], △ - [32]. Theory: *a* – fit of data from [29], *b* – *realistic* calculations

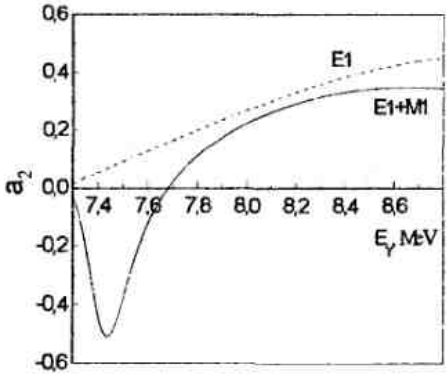

Fig. 11.

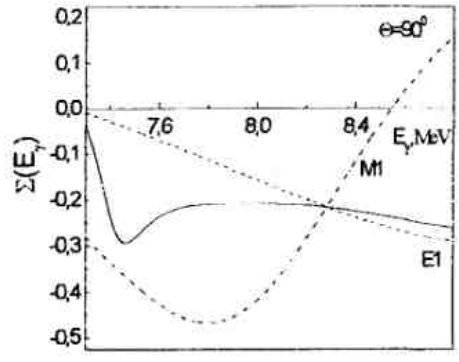

Fig. 12.

As it is seen from Fig. 10a we may fit the experimental data very accurately, but according our analysis more realistic calculations are presented at Fig. 10b, as preliminary treating of the higher E_γ-energies spectrum may be reproduced well with the parameters set for $V_{\epsilon_{Lm}}$ interaction potential corresponding Fig. 10b.

So, both *Barker*' and present report demonstrated that it is possible to *fit* the low-energy cross sections precisely, but the problem is that all experimental data being in qualitative coincidence differ quantitatively, and there is no independent criterion to make a reliable choice among them. *Thus, we suggest some additional characteristics for the possible new experimental investigations of the* $^7Li(\gamma,n)^6Li$ *process.*

As E2-multipole plays minor role within the treating energy interval, the angular distributions of the photoneutrons are determined by A_0 and a_2 coefficients in Legendre polynomial expansion. The corresponding energy dependence of a_2-coefficient presented on Fig. 11 shows specific illumination of M1-multipole on the background of E1-transition.

For comparison Fig. 12 illustrates the energy dependence of photoneutrons asymmetry $\Sigma(E_\gamma,\theta)$ in disintegration of ^7Li by linearly polarized photons $\vec{\gamma}$. It should be noted that E1- and M1-amplitudes do not interfere.

In conclusion, we want remark, that in present report we tried to show that there are new perspectives for developing of cluster model approach for description of low energy photonuclear physics.

References

1. Shoda K., Tanaka T. // Phys. Rev. C. 1999. V.59. № 1. P.239.
2. Burkova N. A., Grigorash S. S., Zhaksybekova K.A., Sagindykov Sh. Sh. // Vestnik KazNU. Ser. Fiz. 2004. № 1(16). P. 3.
3. Burkova N. A., Zhaksybekova K.A., Zhusupov M. A. // Izv. RAN. Ser. Fiz. 2004. V. 68. № 8. P. 1203.
4. Burkova N. A., Zhaksybekova K.A., Zhusupov M. A. // Physics of Particles and Nuclei, 2005. V. 36. № 4. P. 427.
5. Denisov V. P., Kul'chitskii L. A. // Sov. J. Nucl. Phys., 1966. V.3. P.192.
6. Clikeman F.M., Bureau A.J., Stewart M.G. // J. Phys., 1962. V. 126. P. 1822

7. Kukulin V. I., Vorontchev V. T., Pomerantcev V.N.// Few-Body Syst.,1995. V.18. P.191.
8. Zhusupov M. A., Sagindykov Sh. Sh., Sakhiev S. K. // Izv. RAN. Ser. Fiz. 2001.V.65. № 5. P.714.
9. Kukulin V.I. et al. // Nucl. Phys. A. 1986. V. 453. P. 356.
10. Dubovichenko S.B., Zhusupov M.A. // Yad. Fiz. 1984. T. 39. P. 1378.; Izv. AN Kaz. SSR. Ser. Fiz.-Mat. 1983. . №4. P. 44.
11. Ajzenberg-Selove F. // Nucl. Phys. A. 1988. V. 490. P. 11.
12. Boyarkina A.N. Structure of the 1p-Shell Nuclei. M. MGU.1973. 62 P.
13. Weller H.R., Lehman D.R. // Ann. Rev. Nucl. Part. Sci.1988. V. 38. P. 563.
14. Nemets O.F., Neudatchin V.G., Rudchik A.T., et al. Nucleon Clustering in Nuclei and Nuclear Reactions of Multinucleon Transfer. Kiev. Naukova Dumka. 1988. 488 P.
15. Burkova N.A. // Vestnic KazNU. Ser. Fiz. 2004. №3(18). C.13.; Vestnic KazNU. Ser. Fiz. 2004. №3(18). C.138.
16. S.B. Dubovichenko. Properties of light atomic nuclei in potential cluster model. Almaty, 2004. 247 p.
17. Burkova N.A., Zhaksybekova K.A. //Izv. NAN RK. Ser. Fiz.-mat. 2005. № 2(240). P.61; Vest. KazNU. Ser. fiz. 2005. №1(19). P. 11, ibid C.16; Izv. RAN. Ser. Fiz. 2006. № 2. P. 309; Vest. KazNU. Ser. fiz. 2006. №2(22). P. 14.
18. Zhaksybekova K.A. // Izv. NAN RK. Ser. Fiz.-mat. 2005. № 3(241). P.59; Vest. KazNU. Ser. fiz. 2005. №1(19).P.156.
19. Barker F.C.// Nucl. Phys.1966. V. 83. P. 418.
20. Brady F.P., King N.S.P., Bonner B.E. et al. // Phys. Rev. C. 1977. V.16. №1. P. 31.
21. Lapikas L., Wesseling J., and Wiringa R.B. // Phys. Rev. Lett. 1999. V.82. №22. P. 4404; Nucl. Phys. A. 2000. V. 663 & 664. P. 377c.
22. Sakuta S.B. et al . // Yad. Fiz. 2002. V. 65, №10. P. 1819.
23.Denisov V.P.,Kul'chitski L.A..// Yad. Fiz. 1966. V.3. P.192.
24. Junghans G., Bangert K. et al// Z. Physik A. 1979. V. 291. P 353.
25. Sene M.R. et al. // Nucl. Phys. A. 1985. V. 442. P. 215.
26. Sauvan E. et al. // Phys. Rev. Lett. 2001. V. 87, N 4. P.042501.
7. Arai K., Descouvemont P., Baye D. // Phys. Rev. C. 2001. V. 63. P. 044611.
28. Siddiqui S.A., Dytlewski N., Thies H.H. // Nucl. Phys. A. 1986. V. 458. P. 387.
29. Karataglidis S. et al // Nucl. Phys. A. 1989. V.501. P. 108.
30. Barker F.C. // Aust. J. Phys. 1980. V. 33. P. 159.
31. Bramblett R.L. et al// Proc. Int. Conf. Photonucl. React. Appl. California. 1973.V. 1. P .175.
32. Ferdinande H., Sherman N.K., Lokan K.H., Ross. C.K. // Can. J. Phys. 1977. V. 55. P.428.
3. Schmid G.J., Chasteler R.M., Weller H.R., and Tilley D.R. // Phys. Rev. C. 1993. V.48, No. 1. P.441.

THE OFF-SHELL VERIFICATION OF MOSCOW NN-POTENTIAL USING THE $d\gamma \to pn$ REACTION DATA AT PHOTON ENERGIES $E_\gamma = 2 \pm 0.5$ GEV SENSITIVE TO THE QUARK EFFECTS

N.A. Khokhlov,[1,*] V.A. Knyr,[1] and V.G. Neudatchin[2]

[1]*Pacific State University, 680035, Khabarovsk, Russia*

[2]*Institute of Nuclear Physics, Moscow State University, 119899, Moscow, Russia*

I. INTRODUCTION

Possible manifestations of quark degrees of freedom in nuclear reactions at intermediate energies attract attention of scientific community for a long time. It was noted [1] that the most suitable subject of research here is deuteron as the simplest nucleus where the secondary rescattering does not shadow the primary process so much.

The deuteron photodisintegration at intermediate photon energies above 1 GeV generates tremendous interest among experimentalists [1–4] and theoreticians [5–9] with the main emphasis on the properties of the NN-system which are just beyond the scope of realistic mesonic NN-potentials [6] and can be interpreted within quark concepts [5, 7]. First, it was shown in the papers by Khar'kov group [6] that starting from mesonic potentials it is possible to explain the $d\gamma \to np$ data at energy $E_\gamma \geq 1$ GeV only if the revision of electromagnetic part of the theory is done and instead of the ordinary electromagnetic nucleon form factors the essentially different ones are used with poles of third order. Second, the phenomenological theory of Regge poles was taken as a basis in Refs. [5] with selection of dominating poles according to the quark string model [10]. Third, the hard rescattering model was developed [7] within a semiempirical approach, when the photon is absorbed by a quark of one of the nucleons and then the hard rescattering of this quark by the second nucleon takes place. The wave function amplitude of the final np-state with large value of the mutual np-motion momentum is evaluated empirically by extrapolation of the corresponding np-scattering experimental data. Free parameters of these theories allow to describe the experimental data reasonably well.

In the present paper we show that the recent detailed deuteron photodisintegration experiment at E_γ values of $1.5 - 2.5$ GeV [4] gives direct confirmation of the Moscow NN-potential model (with the commonly used electromagnetic nucleon form factors). This potential has specific short-range part of the microscopical quark origin [11]. Its basic difference from the mesonic potentials is that it has not a core and the S- and P-radial wave functions have short-range nodes. So, Moscow potential (MP) is a deep attractive potential with forbidden S- and P-states. These forbidden states correspond to quark configurations $s^4p^2[42]_x$ and $s^3p^3[33]_x$ respectively. The history of MP appearance, details of its quark microscopics and discussion of related experimental data can be found in papers of our group [11, 12, 17, 18]. Originally, this concept was formulated in the seventies when we gave a

*Electronic address: khokhlov@fizika.khstu.ru

consistent description of singlet even NN-phase shifts up to $E_{lab} = 6$ GeV [11] on the basis of the generalized Levinson theorem (GLT). Subsequently, the first empirical attempt was made within this concept [12] to reconstruct the MP from phase shifts data for intermediate energies.

In the present paper the Moscow partial potentials are reconstructed from the NN-phase shifts data within the energy range $0 \leq E_{lab} \leq 3$ GeV [13]. This reconstruction is based on our method of solution of inverse-scattering problem for optical potentials [14]. The first step towards the off-shell verification of MP [11, 15, 16] was made in our papers [17, 18] where it was shown that the hard $pp \to pp\gamma$ bremsstrahlung at rather moderate energies ($E_{lab} \simeq 500$ MeV) is critical to the kind of potential (MP versus meson exchange potentials (MEP)). Unfortunately, the existing suitable experimental data at smaller energy of $E_{lab} = 280$ MeV [19] give only some preliminary indication of MP validity [18]. In this paper we make the next step. There is no competing potential model which is able to describe successfully both the elastic NN scattering and the modern experimental results on deuteron photodisintegration at photon energies of $1.5-2.5$ GeV with use of the ordinary electromagnetic form factors of nucleons.

The plan of the paper is as follows. In Sec. II, basing on our solution [14] of inverse scattering problem within the relativistic quasipotential approach [20, 21] we discuss the optical Moscow-type NN-potential and demonstrate description of phase shifts for the lowest L values within $0 < E_{lab} \leq 3$ GeV energy range including the manifestation of GLT. Namely, $^1S_0$-phase shift, all four $^{2S+1}P_J$-phase shifts are equal to π at zero energy; $^3S_1$-phase shift equals to 2π at zero energy. All the higher phase shifts ($L \geq 2$) are "small", they have zero values at zero energy. In Sec. III, the formalism of relativistic quantum mechanics for systems with a fixed number of particles [22] (point form dynamics [23, 24], RQM-PFD) is applied to the intermediate energy deuteron photodisintegration. The results and future prospects are discussed in the last fourth section.

II. RELATIVISTIC OPTICAL NN-POTENTIAL

We apply the inversion method to analysis of NN data up to energies where relativistic effects are essential. We take into account these effects in the frames of the relativistic quantum mechanics of systems with a fixed number of particles. A system of two particles is described by the wave function, which is an eigenfunction of the mass operator. In this case we may represent this wave function as a product of the external and internal wave functions. The internal wave function χ is also an eigenfunction of the mass operator and satisfies the Schrôdinger-like quasipotential equation [20] (the formally same equation may be deduced as a truncation of the quantum field dynamics [21]). In the considered case of two particles with equal masses ($m_1 = m_2 = m$, $m-$nucleon mass) it appears as

$$\left(\frac{\hat{\vec{q}}^2}{m} + V\right)|\chi_M\rangle = \frac{\vec{q}^2}{m}|\chi_M\rangle\,. \tag{1}$$

$$\vec{q}^2 = \frac{1}{4}(M^2 - 4m^2)\,, \tag{2}$$

where M is the relativistic mass of the system, V_{int} is some interaction operator acting only through internal variables (spins and relative momentum), $\hat{q}$ is a momentum operator of one of the particles in the center of masses frame (relative momentum).

So, introducing the quasicoordinate $\vec{r}$, $\hat{\vec{q}} = -i\frac{\partial}{\partial \vec{r}}$, $V = V(\vec{r})$ [18] we obtain description of the NN-system formally coinciding with the nonrelativistic one (but with relativistic Eq. (2)). In Ref. [14] we developed the method of reconstruction of optical potentials $W(\vec{r}) = (1 + i\alpha)V(\vec{r})$, where $V(\vec{r})$ is energy independent, and α depends on energy. This method is based on the solution of inverse scattering problem [25] when the elastic phase shift analysis (PSA) data are known within the reasonably broad energy range $0 \leq E_{lab} \leq 3$ GeV [13] (this is important to verify the realization of GLT) and constant α is energy dependent. Our calculations shows that final state interaction (FSI) in the S- and P-waves gives by far the largest contribution to the deuteron photodisintegration cross-section comparing with FSI in other waves.

The reconstructed potentials for S- and P-waves are presented in Fig. 1. All potentials and inelasticity multipliers (α's) can be accessed via a link to the website [26]. The forbidden states have the binding energies of $300 - 750$ MeV. Fig. 2 shows reproduction of the phase shifts. In Fig. 3 the energy dependence of parameter α and in Fig. 4 the corresponding description of inelasticities are shown.

It is interesting to learn from Fig. 2 that at present PSA by itself cannot provide us with definite conclusions. Say, $^1S_0$ and $^3P_2$ phase shifts running [13] corresponds to Moscow potential and to GLT (concerning $^1S_0$ phase shift see also Introduction) but $^3P_1$ phase shifts running does not within the energy range $E_{lab} = 2-3$ GeV. Of course, it would be important to refine PSA here using modern polarization data on pp-scattering at energies higher than 1 GeV. In this paper, we choose an independent complementing approach that is the off-shell verification of the MP when the existence of short range nodes in the $S-$ and $P-$wave functions is inspected by means of deuteron photodisintegration data analysis at photon energy $E_\gamma \simeq 2$ GeV. The MP S-wave node at $r \simeq 0.5$ fm replaces the core effect of meson potentials. For continuum $P-$waves the node radii equal to $0.6 - 0.9$ fm at the considered energies.

III. FORMALISM OF RELATIVISTIC QUANTUM MECHANICS AS APPLIED TO THE DEUTERON PHOTODISINTEGRATION PROCESS

Evaluation of the general expression for the differential cross section of a two-body reaction in the c.m. frame for $\gamma d \to np$ reaction yields

$$\frac{d\sigma}{d\Omega} = \frac{q_f}{64\pi^2 M_f^2 k_c} |\mathcal{A}_{if}|^2, \tag{3}$$

where q_f is the final asymptotic relative momentum, k_c is photon energy in c.m. frame. The $d\gamma \to np$ amplitude A_{if} is defined in the same manner as the $pp\gamma$ amplitude that we used in Ref. [18]

$$(2\pi)^4 \delta^4(P_i + k - P_f)\, A_{if} = \sqrt{4\pi} \int d^4x \, \langle P_f, \chi_f | \, \varepsilon_\mu \hat{J}^\mu(x) \, | P_i, \chi_i \rangle \, e^{ikx} \tag{4}$$

where P_i and P_f are initial and final 4-momenta of the NN-system correspondingly, ε^μ is the photon polarization vector. The deuteron wave function $|P_i, \chi_i\rangle$ is normalized as follows

$$\langle P_f, \chi_i | P_i, \chi_i \rangle = 2P_{10}\, \delta^3(\vec{P}_f - \vec{P}_i)\,. \tag{5}$$

The one particle wave functions of nucleons are normalized analogously. The current operator $\hat{J}^\mu(x)$ will be specified below.

The matrix element of the current operator appears especially simple [23] in the coordinate frame, where

$$\vec{G}_i + \vec{G}_f = 0\,, \quad \vec{G} = \vec{P}/M, \tag{6}$$

here

$$\langle P_f, \chi_f |\, \hat{j}^\mu(x)\, | P_i, \chi_i \rangle = 2\sqrt{M_i M_f}\, e^{i(P_f - P_i)x}\, \langle \chi_f |\, \hat{j}^\mu(\vec{h})\, | \chi_i \rangle \cdot \frac{1}{\sqrt{2}} (2\pi)^{3/2} \sqrt{M_f}. \tag{7}$$

In r.h.s. of Eq. (7) the internal initial deuteron $|\chi_i\rangle$ and final $|\chi_f\rangle$ np scattering states are normalized in the non-relativistic manner. The deuteron wave function is

$$|\chi_i\rangle = \frac{1}{r} \sum_{l=0,2} u_l(r)\, |l, 1;\, 1M_J\rangle\,, \qquad |l, S;\, JM_J\rangle = \sum_m \sum_\mu |S, \mu\rangle\, \mathcal{Y}_{lm}(\hat{n})\, C^{JM_J}_{lmS\mu}\,, \tag{8}$$

with normalization $\langle \chi_i | \chi_i \rangle = 1$. The internal final state continuum np wave function is

$$|\chi_f\rangle = \sqrt{\frac{2}{\pi}} \frac{1}{q_f r} \sum_{J=0}^{\infty} \sum_{l=J-S}^{J+S} \sum_{l'=J-S}^{J+S} \sum_{m=-l}^{l} i^{l'} u^J_{l,l'}(q_f, r) C^{JM}_{lmS\mu} \mathcal{Y}^*_{lm}(\hat{q}_f) |l', S; JM\rangle, \tag{9}$$

with normalization $\langle \chi_f(\vec{q}\,') | \chi_f(\vec{q}) \rangle = \delta(\vec{q}\,' - \vec{q})$. The corresponding plane wave $|\phi_f\rangle$ is characterized by spherical Bessel functions $j_l(q_f, r)$ instead of $u^J_{l,l'}(q_f, r)$ in formula (9).

Furthermore, following [18, 23] we use the dimensionless vector $\vec{h} = \vec{G}_f / G^0_f = -\vec{G}_i / G^0_i$ instead of the photon momentum $\vec{k}$, so that $\vec{h} = 2(M_i M_f)^{1/2} (M_i + M_f)^{-2}\, \vec{k}$, $|\vec{h}| = h = (M_i - M_f)/(M_i + M_f)$. We define a reduced amplitude $T_{fi} = \langle \chi_f |\, \varepsilon^{i*}_\mu \hat{j}^\mu(\vec{h})\, | \chi_i \rangle$. As a result the differential cross-section (3) can be rewritten as

$$\frac{d\sigma}{d\Omega} = \frac{\pi^2 q_f M_i}{6 k_c} \sum_i \sum_f |T_{fi}|^2\,. \tag{10}$$

where we average over photon polarizations, spin orientations of initial deuteron and sum over spin orientations of final nucleons. Using the transverse gauge

$$\varepsilon = (0, \vec{\varepsilon})\,, \qquad (\vec{\varepsilon}\,\vec{k}) = 0$$

we exclude the $j_0(\vec{k})$ component of the current.

In our calculations we approximate the above matrix element

$$\langle \chi_f |\, \hat{j}^\mu(\vec{h})\, | \chi_i \rangle \approx \langle \phi_f |\, \hat{j}^\mu(\vec{h})\, | \chi_i \rangle + \langle \chi_f - \phi_f |\, \hat{\tilde{j}}^\mu(\vec{h})\, | \chi_i \rangle\,. \tag{11}$$

The first term is a plain wave approximation and is calculated using the exact current operator (12). In this case the operator $\hat{\vec{q}}$ can be substituted by $\vec{q}_f$ and operator structure of $\hat{j}^\mu(\vec{h})$ can be presented as

$$\hat{j}^\mu(\vec{h}) = \sum_{i=1,2} \left(\vec{B}^\mu_{1i} + (\vec{B}^\mu_{2i} \cdot \vec{s}_2) + (\vec{B}^\mu_{3i} \cdot \vec{s}_1) + (\vec{B}^\mu_{2i} \cdot \vec{s}_2)(\vec{B}^\mu_{4i} \cdot \vec{s}_1) \right) I_i(\vec{h}) + \delta\vec{j}\,, \tag{12}$$

where $\vec{B}^\mu_{1i}$ and $\vec{B}^\mu_{ki}$, $k \geq 2$ are cumbersome vector and tensor functions of arguments $\vec{h}$ and $\vec{q}_f$ which we present in [29].

The use of $(\chi(\vec{r}) - \phi(\vec{r}))$ combination in the second term of r.h. side of Eq. (11) makes it possible to accelerate convergence of partial wave expansion. This term is nonzero due to the final state interaction (FSI) of neutron and proton. Its calculation is done with use of the first order in h approximation of the current operator (13). Basing on the technique exposed in Ref. [18] we present the action of the np 3-current $\hat{\vec{j}}(\vec{h})$ in first order in $\vec{h}$

$$\begin{aligned}\hat{\vec{j}}(\vec{h}) \approx \hat{\vec{j}}(\vec{h}) = \delta\vec{j} + \frac{\vec{q}}{w}\hat{g}_e^{pn} - \vec{h}\hat{G}_e^{pn} + \imath\left(\frac{m}{w}[\vec{S}\times\vec{h}] + \frac{1}{w(w+m)}[\vec{q}\times\vec{h}]\left(\vec{q}\cdot\vec{S}\right)\right)\hat{G}_m^{pn} + \\ + \imath\left(\frac{m}{w}[\vec{T}\times\vec{h}] + \frac{1}{w(w+m)}[\vec{q}\times\vec{h}]\left(\vec{q}\cdot\vec{T}\right)\right)\hat{g}_m^{pn} + \\ + \imath\left(\vec{h}\cdot[\vec{q}\times\vec{S}]\right)\vec{q}\left(\frac{\hat{G}_m^{pn}}{mw} + \frac{G_e^{pn}}{w(w+m)}\right) + \\ + \imath(\vec{h}\cdot[\vec{q}\times\vec{T}])\,\vec{q}\left(\frac{\hat{g}_m^{pn}}{mw} + \frac{g_e^{pn}}{w(w+m)}\right) - (\vec{h}\cdot\vec{q})\,\vec{q}\,\frac{\hat{G}_e^{pn}}{mw},\end{aligned} \tag{13}$$

$$\begin{aligned}\delta\vec{j} = -\left(1 - \frac{4w}{M_f+M_i} + h\right)\frac{\vec{q}}{w}g_e^{pn} + \\ + \imath h\left([\vec{q}\times\vec{T}]\left(\frac{G_m^{pn}}{m} - \frac{G_e^{pn}}{(w+m)}\right) - 2g_e^{pn}\,w\,\vec{r} + [\vec{q}\times\vec{S}]\left(\frac{g_m^{pn}}{m} - \frac{g_e^{pn}}{w+m}\right)\right)\ ,\end{aligned} \tag{14}$$

where $\vec{S} = \vec{s}_1 + \vec{s}_2$, $\vec{T} = \vec{s}_1 - \vec{s}_2$,

$$\hat{g}_m^{np} = G_m^p I_1(\vec{h}) - G_m^n I_2(\vec{h}), \quad \hat{G}_m^{pn} = G_m^p I_1(\vec{h}) + G_m^n I_2(\vec{h}), \tag{15}$$

$$\vec{d}_1 = \vec{q} - 2\vec{h}\,w, \quad \vec{d}_2 = \vec{q} + 2\vec{h}\,w, \quad w \equiv w(\vec{q}) = \sqrt{m^2 + \vec{q}^2}, \tag{16}$$

$$I_i(\vec{h})\chi(\vec{q}) = \begin{cases} \chi(\vec{q} - \dfrac{2\vec{h}}{1-h^2}\,(w - (\vec{h}\cdot\vec{q}))) \\ \chi(\vec{q} + \dfrac{2\vec{h}}{1-h^2}\,(w + (\vec{h}\cdot\vec{q}))) \end{cases} \approx \begin{cases} \chi(\vec{q} - 2\vec{h}w), & \text{when} \quad i = 1 \\ \chi(\vec{q} + 2\vec{h}w), & \text{when} \quad i = 2. \end{cases} \tag{17}$$

G_m^p, G_m^n, G_m^p, G_m^n are magnetic and electric neutron and proton formfactors parameterized according to [28]. Addend $\delta\vec{j}$ restores the current conservation equation according to assumptions of [18, 23]. This approximation is justified by estimation $h \approx 0.4$ for $E_\gamma \approx 2$ GeV. Other details of these cumbersome calculations will be published elsewhere [29].

IV. RESULTS AND FUTURE PROSPECTS

Our theoretical description of the differential cross-section of $d\gamma \to pn$ reaction is shown in Figs. 5 at a few energies around $E_\gamma = 2$ GeV value in comparison to recent experiment [4]. We do not use any free parameters in our calculations. However the values of electromagnetic form factors of nucleons are known within some errors [28] and we show two theoretical curves corresponding to lower and higher limits of form factors, respectively.

We see the good general correspondence of theory and experiment both in absolute values and in shape of angular dependence of differential cross-section at various energies.

The large absolute values of cross-sections in our theory in comparison with MEP results originate mainly in the nodal character of the deuteron S-wave functions (greater weight of the high momentum wave function components). The strong final state np–interaction plays the remarkable role via deep attractive optical Moscow potential. This FSI is taken into account properly in our theory.

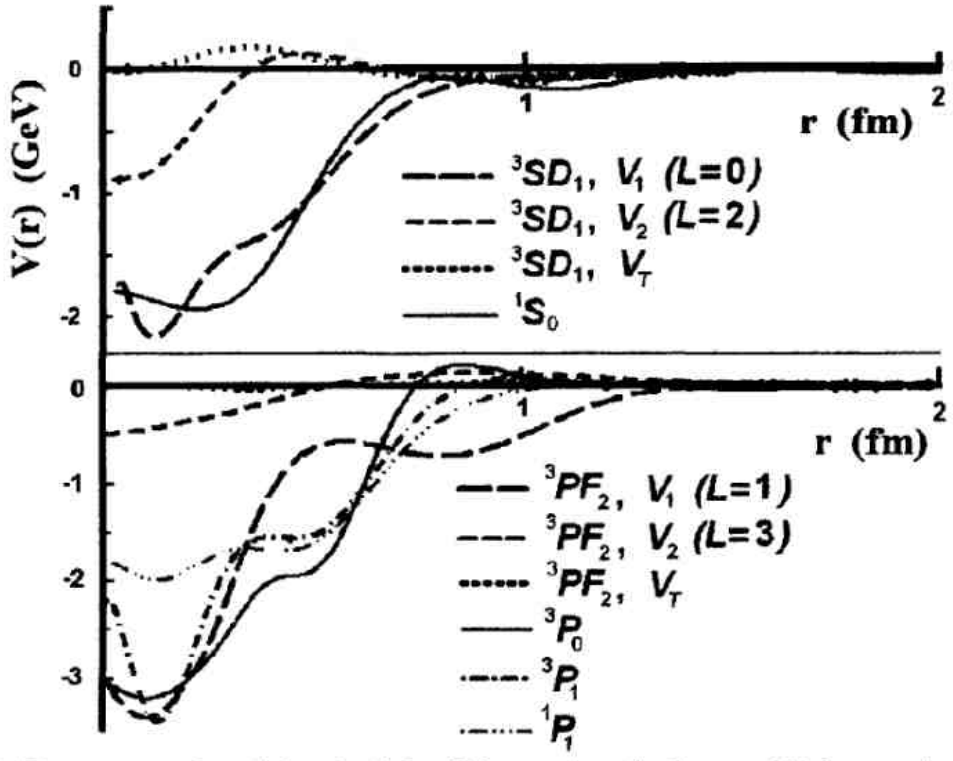

FIG. 1: Reconstructed partial potentials of Moscow type for lower orbital momentum (single and coupled channels).

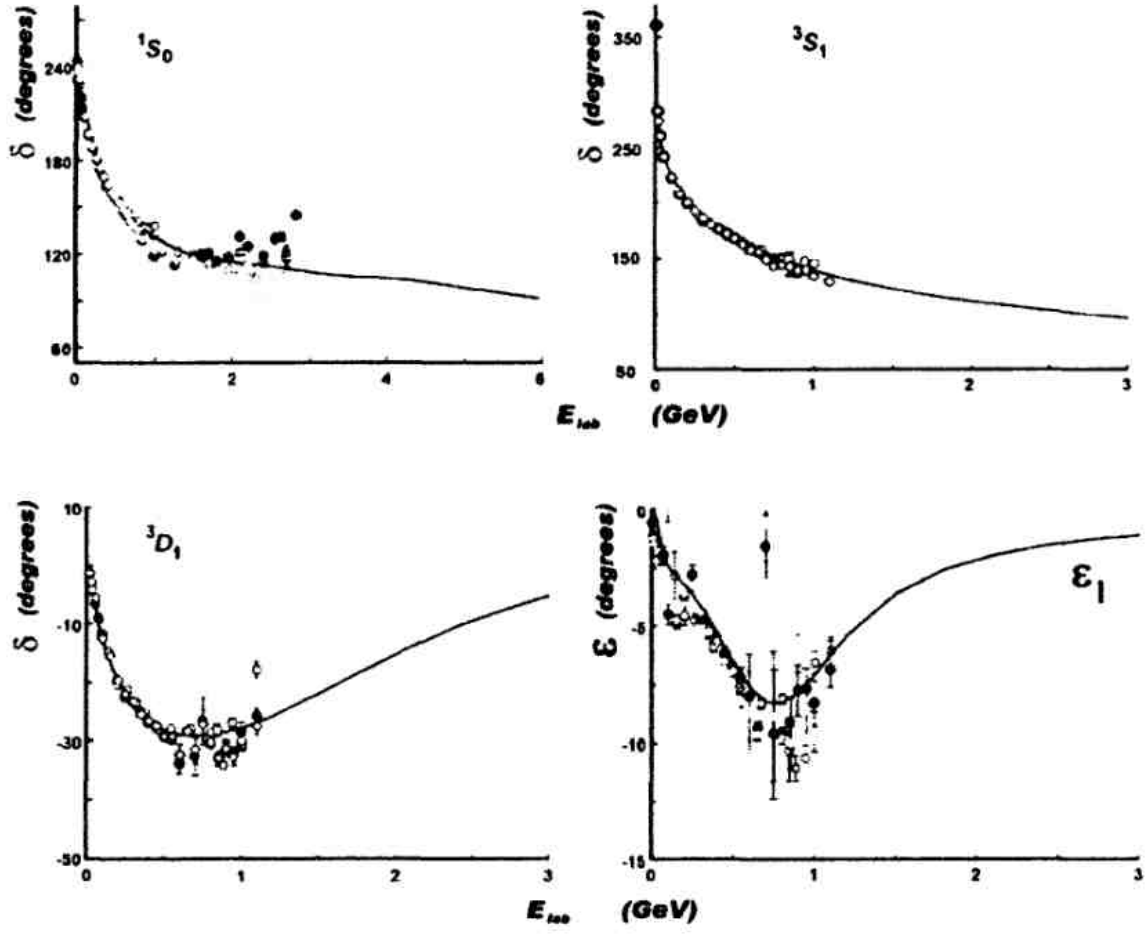

FIG. 2: Description of NN-phase shifts by the reconstructed potentials for $L = 0$ and 1 values.

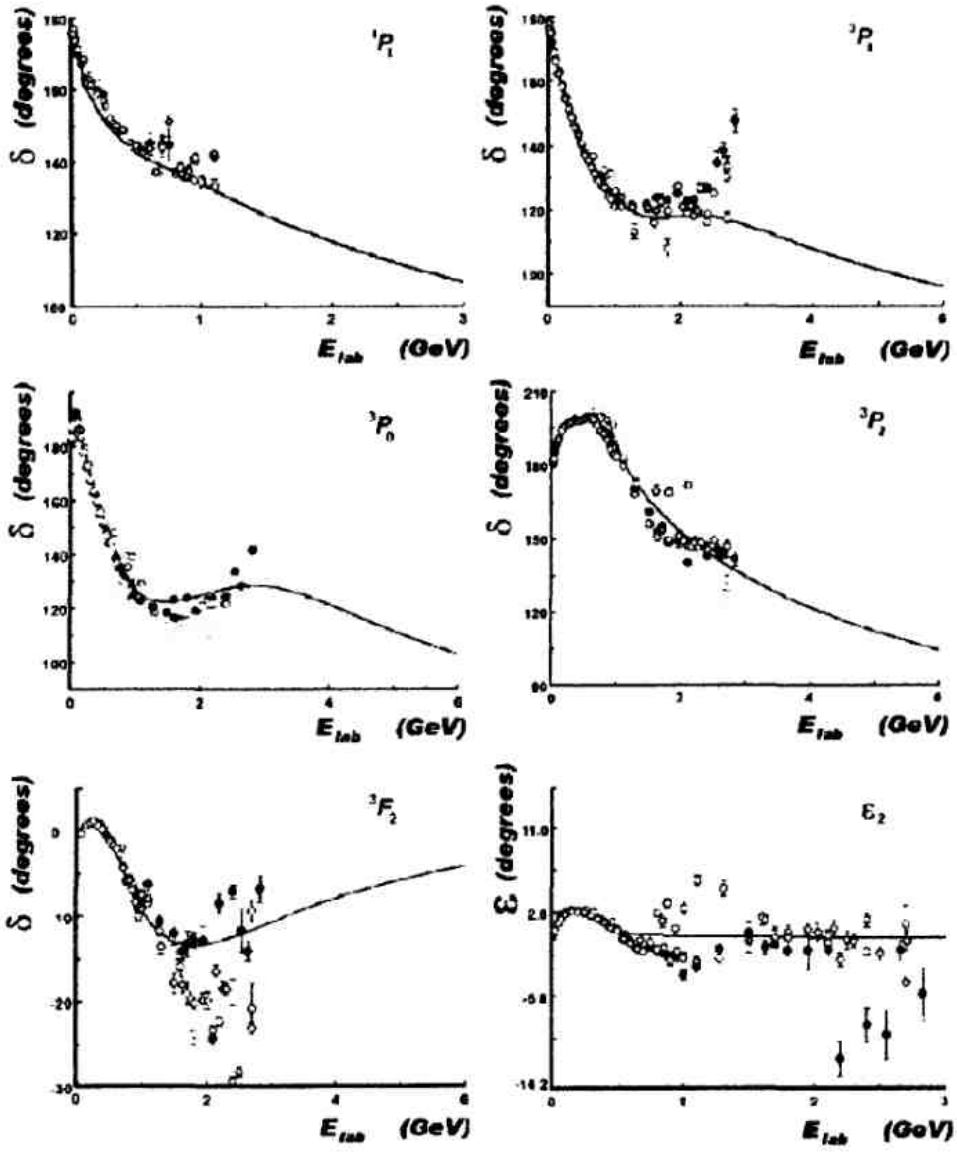

FIG. 2: (Continued).

The ability to describe both the absolute value and the angular dependence of differential cross-sections confirms the detailed algebraic structure of theory. We deal here with the interference of even and odd nucleon-nucleon partial waves in the final state. It produces the cross-section maximum of definite width at forward angles which moves to the left with increasing photon energy when the role of electric dipole excitation becomes more modest.

Meson exchange currents are of no importance at photon energies around 2 GeV.

To complete this line of our investigation we plan to make an analysis of polarization $d\gamma \to pn$ experiments and to consider the pionic radiative capture $pp \to d\pi^+$ at proper energies.

Other actual problems are outlined in Ref. [18]. The first of them concerns the microscopic theory of the MP. As we suppose, it is connected to the short-range quark exchange between nucleons accompanied by the excitation of color dipole states of two virtual baryons with the very strong attraction between them. This scenario is based on the quark configuration $s^4p^2[42]_x$ in deuteron.

As the concluding remark it should be stressed that usage of MP instead of MEP in

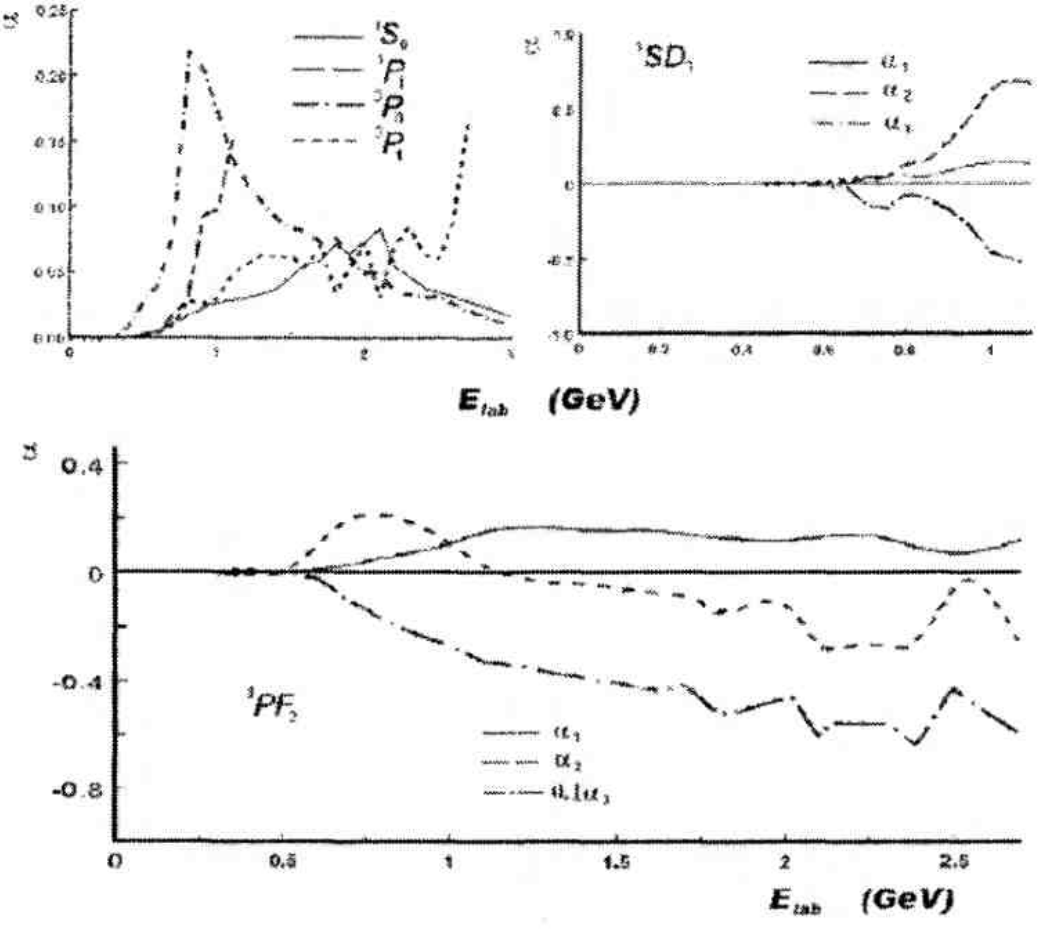

FIG. 3: Energy dependence of parameter α characterizing the imaginary part of optical NN-potentials of Moscow type.

the theory of complex nuclei demands accurate evaluation of $3N-$forces. Effect of these forces is much enhanced [14], as far as three nucleons without NN-hard core can overlap and form short-range $9q$-subsystems with large probability. Recent experiments [27] on the knock-out of nucleon from ^3He nucleus may clear this situation. In these experiments the missing momentum is great and recoil to $2N$-subsystem with large mutual momentum of two spectator-nucleons is observed.

Authors are grateful to Prof. V.I. Kukulin for useful remarks.

---

[1] R.J. Holt, Nucl.Phys. A **684**, 148c (2001), S. Strauch, Nucl.Phys. **A690**, 89c (2001).
[2] C. Bochna, B.P. Terburg, D.J. Abbott et al., Phys.Rev.Lett. **81**, 4576 (1998); E.C. Schutle, A. Afanasiev, M. Amarian et al., Phys.Rev. **C66**, 042201 (2002).
[3] K. Wijesooriya, A. Afanasiev, M. Amarian et al., Phys.Rev.Lett. **86**, 2975 (2001).
[4] M. Mirazita, F. Ponchetti, P. Rossi et al., Phys.Rev. **C70**, 014005 (2004).
[5] L.A. Kondratyuk, E. De Sanctis, P. Rossi et al. Phys.Rev. **C48**, 2491 (1993); V.Y. Grishina, L.A. Kondratyuk, W. Kassing et. al., Eur.Phys.J. **A19**, 117 (2004).
[6] A.E.L. Dieperink and S.I. Nagorny, Phys.Lett. **B456**, 9 (1999).
[7] L.L. Frankfurt, G.A. Miller, M.M. Sargsian, and M.I. Strikman, Nucl.Phys. **A663** and **A664**,

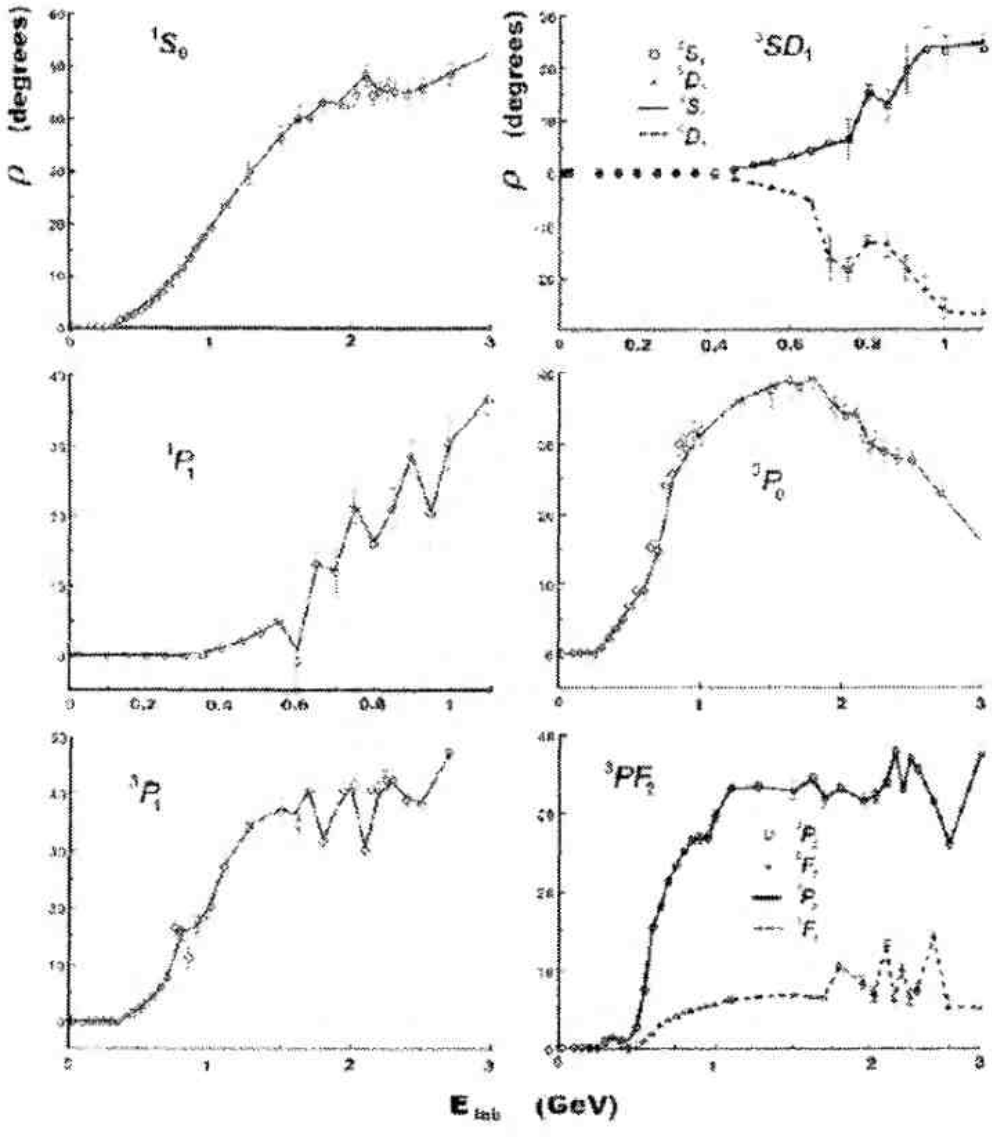

FIG. 4: Inelasticities parameters ρ for reconstructed optical potentials of Moscow type.

349[C] (2000); Phys.Rev.Lett. **84**, 3045 (2000).

[8] R. Gilman and F. Gross, J.Phys. **G28**, R37 (2002).

[9] K.Yu. Kazakov and S.F.Shirmovsky, Phys.Rev. **C65**, 064002 (2002).

[10] A.B. Kaidalov, Z. Phys. **C12**, 63 (1982).

[11] V.G. Neudatchin, I.T. Obukhovsky, V.I. Kukulin, and N.F. Golovanova, Phys.Rev. **C11**, 128 (1975); V.G. Neudatchin, I.T. Obukhovsky, and Yu.F. Smirnov, Fiz.Elem.Chastits At. Yadra (Sov.J.Part.Nucl.) **15**, 1165 (1984); V.I. Kukulin and V.N. Pomerantsev, Prog.Theor.Phys. **88**, 159 (1992); L.Ya. Glozman, V.G. Neudatchin, and I.T. Obukhovsky, Phys.Rev. **C48**, 389 (1993).

[12] V.G. Neudatchin, N.P. Yudin, Yu.L. Dorodnykh, and I.T. Obukhovsky, Phys.Rev. **C43**, 2499 (1991).

[13] R.A. Arndt, I.I. Strakovsky, and R.L. Workman, Phys.Rev. **C62**, 034005 (2000); http://lux2.phys.va.dwu.edu.

[14] N.A. Khokhlov, V.A. Knyr, Phys. Rev. **C73**, 024004 (2006).

[15] A.M. Kusainov, V.G. Neudatchin, and I.T. Obukhovsky, Phys.Rev. C **C44**, 2343 (1992).

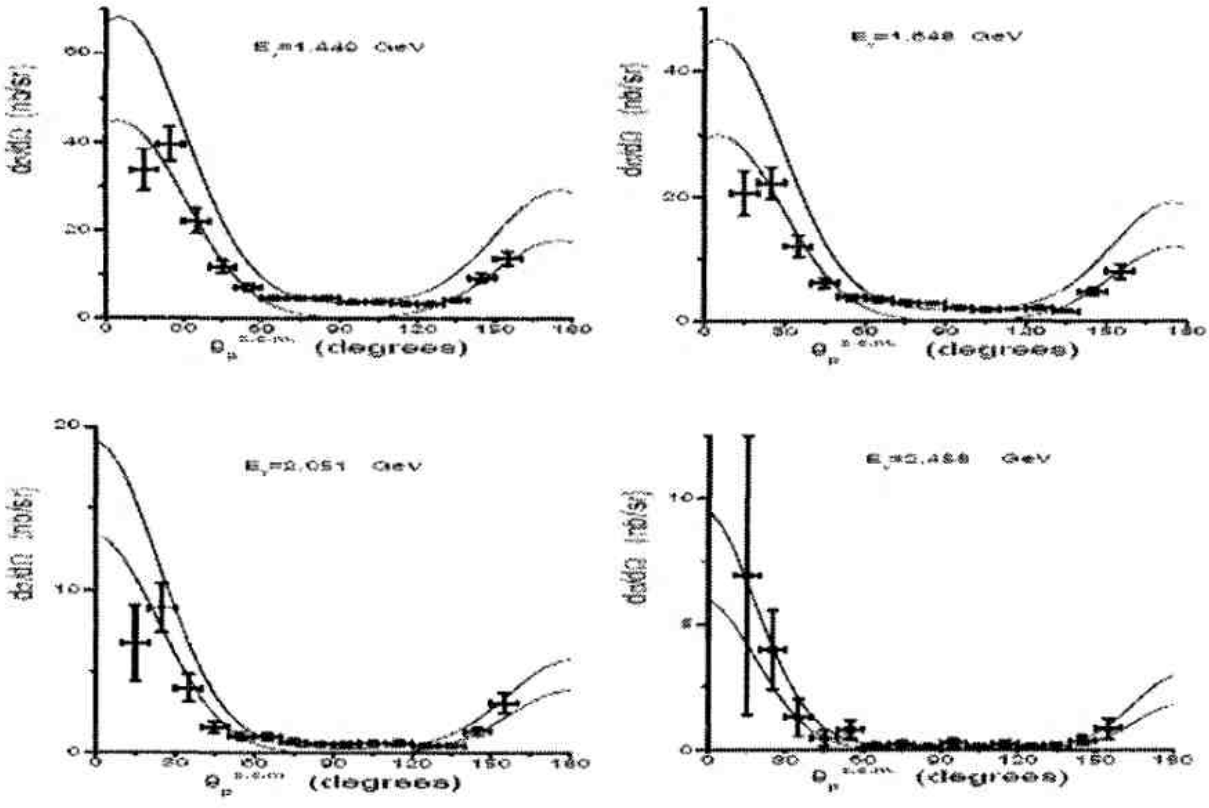

FIG. 5: Angular dependence of $d\gamma \to pn$ reaction differential cross-sections. Our theory is compared to experiment [4]. The theoretical result for the Nijmegen meson exchange potential (see text) is also shown (for $E_\gamma = 2.051$ GeV) for comparison (dashed curve).

[16] J.M. Sparenberg and D. Baye, Phys.Rev.Lett. **79**, 3802 (1997); H. Leeb, S.A. Sofianos, J.M. Sparenberg and D. Baye, Phys.Rev. **D62**, 064003 (2000).

[17] N.A. Khokhlov, V.A. Knyr, V.G. Neudatchin, and A.M. Shirikov, Phys.Rev. **C62**, 054003 (2000).

[18] N.A. Khokhlov, V.A. Knyr, and V.G. Neudatchin, Phys.Rev. **C68**, 054002 (2003).

[19] K. Michaelian, P. Kitching, D.A. Hutcheon et al., Phys.Rev. **D41**, 2689 (1990).

[20] B.D. Keister, W.N. Polyzou, in Advances in Nucl. Phys. V. 20, Ed. J. W. Negele and E. W. Vogt, Plenum Press 1991.

[21] A.A. Logunov and A.N. Tavkhelidze, Nuovo Cimento **29**, 380 (1963); I.T. Todorov, Phys.Rev. **D3**, 2351 (1971); A.P. Martynenko and R.N. Faustov, Theor.Mat.Fiz. **64**, 179 (1985); V.O. Galkin, A.Yu. Mishurov, and R.N. Faustov, Yad.Fiz. **55**, 2175 (1992).

[22] P.A.M. Dirac, Rev.Mod.Phys. **21**, 392 (1949); B.D. Keister and W. Polyzou, Ann. Phys. **21**, 225 (1991).

[23] F.M. Lev, Riv. Nouvo Cimento **16**, 1(1993); Nucl.Phys. A **657**, 979 (1994); hep-ph/9403222.

[24] T.W. Allen, W.H. Klink, and W.N. Polyzou, Phys.Rev. **C63**, 034002 (2001).

[25] K. Chadan and P.C. Sabatier, Inverse problem in Quantum Scattering Theory, second ed. (Springer, New York, 1989).

[26] `www.physics.khstu.ru`

[27] M. Holtrop, Nucl.Phys. **A755**, 171^c (2005).

[28] J.J. Keily, Phys. Rev. C **70**, 068202 (2004).

[29] N.A. Khokhlov, V.A. Knyr, and V.G. Neudatchin, sent to Phys.Rev. C.

Medium Modification of the nucleon-nucleon interaction

V. Tselyaev,[1,2] J. Speth,[1,3] F. Grümmer,[1] S. Krewald,[1] A. Avdeenkov,[1,4] S. Kamerdzhiev,[1,4] E.Litvinova,[4] and G. Tertychny[1,4]

[1]*Institut für Kernphysik, Forschungszentrum Jülich, 52425 Jülich, Germany*
[2]*Institute of Physics S.Petersburg University, Russia*
[3]*Institute of Nuclear Physics, PAN, PL-31-342 Cracow, Poland*
[4]*Institute of Physics and Power Engineering, 249020 Obninsk, Russia*

(Dated: 27. September)

Recent progress in nuclear structure physics relevant for astrophysical applications is reviewed. In order to predict the properties of neutron-rich nuclei, one has to determine the effective two-nucleon interaction in the nuclear medium. The effective Landau-Migdal interaction places strong empirical constraints on the effective interaction. We show that the study of low-lying dipole strength may provide information about the p-wave contributions of the Landau-Migdal force, provided the underlying many-body theory is pushed beyond the mean-field approximation. Evidence for isoscalar electric dipole strength below the particle emission threshold is found.

I. INTRODUCTION

The structure of neutron-rich nuclei is important for many applications in astrophysics. The rapid neutron-capture process, for instance, requires detailed knowledge of the properties of nuclei between the valley of stability and the neutron drip-line, such as neutron capture rates or photon-induced neutron emission cross sections. Progress in Nuclear Resonance Fluorescence photon scattering experiments has made possible studies of energetically low lying strength [1–4]. and to distinguish between 1^-, 2^+ and 1^+ states [2, 5]. Surprisingly, in the same region, appreciable isoscalar electric dipole strength was already detected some years ago with $(\alpha, \alpha'\gamma_0)$ experiments and reported in [6]. New data using the same technique have already been analyzed [7].

In analogy to the giant dipole resonance which exhausts the major part of the Thomas-Reiche-Kuhn sum rule, the low lying strength is called the *pygmy resonance*. Commonly, this strength is interpreted as an oscillation of the neutron halo against the nuclear core [8]. A collective model predicts the pygmy B(E1) strength to increase with the neutron excess [9].

For the electromagnetic dissociation of light nuclei with a one-neutron halo, Typel and Baur have developped a model independent approach that relies on only a few low-energy constants, e.g. the neutron separation energy. Coulomb dissociation is found to be dominated by the energetically low-lying electromagnetic dipole strength. While in experimentally known nuclei, the relevant low-energy constants can be obtained directly from the data, an extrapolation to unknown nuclei remains a challenge for many-body theory [10].

Several microscopic models have been applied to the pygmy resonances. The relativistic random-phase approximation is based on a Lagrangian which has the advantage that the extrapolation from the known stable nuclei to the nuclei near the drip line is well-defined. Theories of this kind are quite successful in reproducing the nuclear masses and radii, and also the collective excitation modes of nuclei, such as the giant dipole resonance, using the relativistic quasi-particle random phase approximation. A recent review is given in Ref. [11]. Quantitatively, relativistic approaches to the pygmy resonances do not compare too well with the experimental data. The theory obtains mean excitation energies of the pygmy strength consistently above the experimental strength. This appears to be a general phenomenon observed by several groups. Goriely and Khan [12] calculated within the QRPA the E1 strength distributions [12] for all nuclei with $8 \leq Z \leq 110$ between the proton and neutron drip lines using known Skyrme forces. In their calculation the low-lying E1 strength was located systematically higher by some 3 MeV compared with the available data.

Here, we want to point out that the discrepancy between the theoretical and experimental pygmy strength may be overcome by pushing the many-body approach beyond the mean field level.

The relativisic quasi-particle random phase approximation relies on a nuclear mean field which has been evaluated within the Hartree- or Hartree-Fock approximation. As most of the relativistic calculations employ effective masses well below unity, the corresponding single particle energies are more widely spread than the experimental separation energies. Therefore the relativistic approaches, in their present form, do not reproduce the experimental separation energies. A precise knowledge of the separation energies may be very important, however, as shown in Ref.[10].

In order to investigate this problem, we will rely on an extended version of the Landau-Migdal theory. Landau's theory shares two ideas with the modern effective field theories due to Weinberg: one has to identify the degrees of freedom relevant for the energy scale one is interested in and then can incorporate the physics of the larger energy scales in a few low-energy constants and one has to identify a small expansion parameter. What Landau's theory does not have, however, is an ordering scheme which allows to compute corrections systematically. The

single particle energies to be employed in Landau's theory are the experimental separation energies, a feature which turns out to be important in the light of Ref.[10].

In Landau's theory, the relevant degrees of freedom are called quasi-particles. The associated energy scale is of the order of the particle-hole gap, i.e. 16 MeV. On the other hand, there is another degree of freedom, the phonons, which corresponds to an energy scale of about 2 MeV to 8 MeV [13, 14]. In the Extended Theory of Finite Fermi Systems(ETFFS), the phonon degree is incorporated explicitly. The quasi-particles are dressed by the phonons, and it is the *dressed* quasi particle energy which has to be identified with the experimental separation energy. Details can be found in Ref.[15] (and references therein). A recent application of the quasi particle phonon model to the pygmy resonances is given in Refs.[16, 17].

II. EXTENDED THEORY OF FINITE FERMI SYSTEMS (ETFFS)

As in our previous calculations we used the effective particle-hole Landau-Migdal interaction:

$$F(\mathbf{r},\mathbf{r}') = C_0\,[f(r) + f'(r)\boldsymbol{\tau}_1\cdot\boldsymbol{\tau}_2 + (g + g'\boldsymbol{\tau}_1\cdot\boldsymbol{\tau}_2)\boldsymbol{\sigma}_1\cdot\boldsymbol{\sigma}_2]\;\delta(\mathbf{r}-\mathbf{r}') \qquad (2.1)$$

with the conventional interpolation formula, for example, for the parameter f

$$f(r) = f_{ex} + (f_{in} - f_{ex})\rho_0(r)/\rho_0(0) \qquad (2.2)$$

and similarly for the other r-dependent parameter $f'(r)$. Here $\rho_0(r)$ is the density distribution of the ground state of the nucleus under consideration and f_{in} and f_{ex} are the force parameters inside and outside of the nucleus. The standard values of the parameters, which have been used for all the nuclei under consideration [15], are as follows

$$f_{in} = -0.002,\; f_{ex} = -1.35,\; f'_{ex} = 2.30,\; f'_{in} = 0.76,\quad g_{in} = g_{ex} = 0.05,\; g'_{in} = g'_{ex} = 0.96. \qquad (2.3)$$

The parameters are given in units of $C_0 = 300$ MeVfm^3. For the nuclear density $\rho_0(r)$ in the interpolation formula we chose the theoretical ground state density distribution of the corresponding nucleus,

$$\rho_0(r) = \sum_{\epsilon_i \le \epsilon_F} \frac{1}{4\pi}(2j_i+1)R_i^2(r), \qquad (2.4)$$

Here $R_i(r)$ are the single-particle radial wave functions of the Woods-Saxon single-particle model. This is more consistent than the previously used phenomenological Fermi distribution. For that reason we had to readjust f_{ex} and obtained the value of f_{ex} = -1.7. For other details of the calculations, see [15].

III. LOW-LYING ELECTRIC DIPOLE STRENGTH

A. The isovector case

The giant electric dipole resonance (GDR) is one of the most collective states in nuclei. It exhausts a major part of the energy-weighted sum rule, the excitation energy is a smooth function of the mass number and the form of the GDR changes only little from nucleus to nucleus. Phenomenological collective models describe well the A dependence of the energy and the strength with only a few parameters. In microscopic models these collective states are coherent superpositions of many particle-hole states. The theoretical results of such models for the mean-energy and the total strength agrees in general very well with the data. The strength distribution, however, is reproduced by only a few very involved models, e.g. the here presented *ETFFS*.

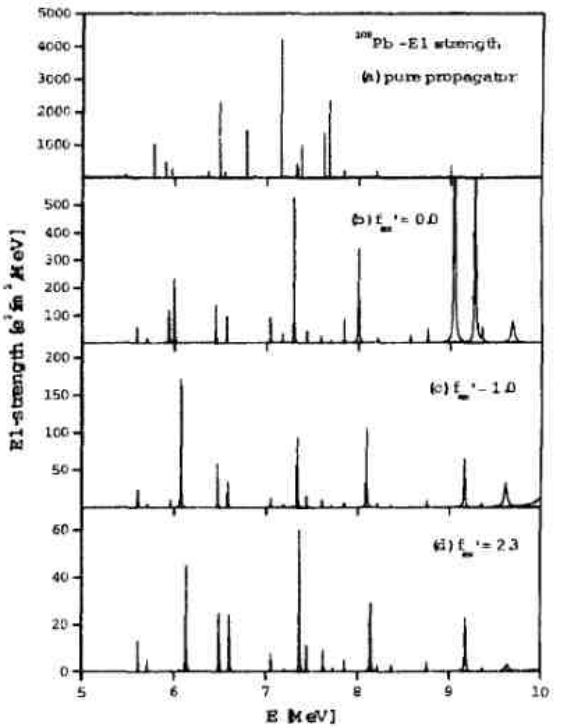

FIG. 1: Electromagnetic E1-strength calculated within the conventional 1p1h-RPA. In (a) we show the uncorrelated ph-matrix elements. In (b) the spurious state has been removed where we used our universal isoscalar interaction. For the results shown in (c) a reduced isovector force has been used, while (d) shows the results with the full interaction.

Here, we first investigate the question whether the

pygmy dipole resonances(PDR) are like the GDR collective states in the microscopic definition. That is, are they coherent superpositions of many particle-hole states. In order to answer this question we performed a series of calculations within the continuum RPA in which we varied the particle-hole interaction.

In Fig.1(a) the dipole distribution for the electromagnetic $E1$-operator is plotted, where the particle-hole interaction is zero i.e. the figure shows pure proton and neutron ph-matrix elements. The largest matrix elements are the ones between the ph states with the largest angular momenta which differ by one unit, the *stretched configurations*. The state at $E \approx 6.5MeV$ is the neutron $(1j_{13/2})(1i^{-1}_{13/2})$ configuration and the states at $E \approx 7.15MeV$ and $E \approx 7.70MeV$ are the proton configurations $(1i_{13/2})(1h_{11/2})^{-1}$ and $(1h_{11/2})(1g_{7/2})^{-1}$. The three largest transitions exhaust about 40 % of the total strength. Here, we have to bear in mind that the transitions shown here also include spurious components which give rise to the spurious isoscalar state at zero energy. This state corresponds to the translation of the whole nucleus. For that reason one has to remove the spurious components in each of the particle hole components. The method by Tselyaev [18] is used which brings the spurious state exactly to zero energy and removes completely the spurious strength in all excited states.

In Fig.1(b-d) the electromagnetic dipole strength is shown, where the spurious strength is removed.

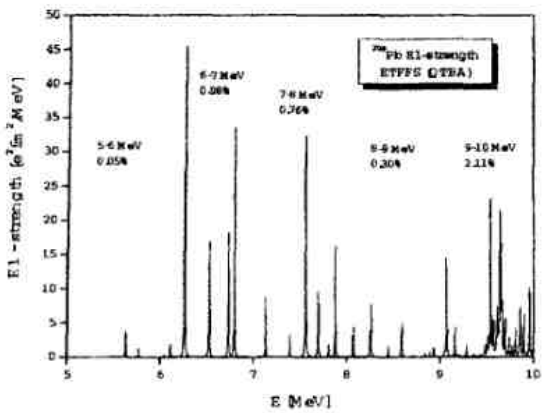

FIG. 2: Electromagnetic E1-strength calculated within the *ESFFS*. These results should be compared with the distribution shown in Fig.1(d).Note that the strength in the present figure is given in $[e^2fm^2]$.

To demonstrate the effect of the repulsive isovector interaction we have chosen three different values for the isovector force parameter f_0'. The isoscalar ph interaction is the same for all three cases. If we compare the completely uncorrelated strength distribution in Fig.1(a) with the results in Fig.1(b) where the spurious components are removed but the isovector force parameter $f_0' = 0$ one observes an appreciable shift of the B(E1) strength to higher energies. We notice thereby that if one removes the spurious strength one has to introduce correlations which give rise to this redistribution of the strength. With setting the isovector interaction to zero most of the B(E1)-strength (87%) lies below 10 MeV. If we increase the isovector interaction parameter to $f_0' = 1.0$ (Fig.1(c)) which is about half of the force parameter that reproduces the experimental data of the GDR, the dipole strength below 10 MeV reduces to 11%.

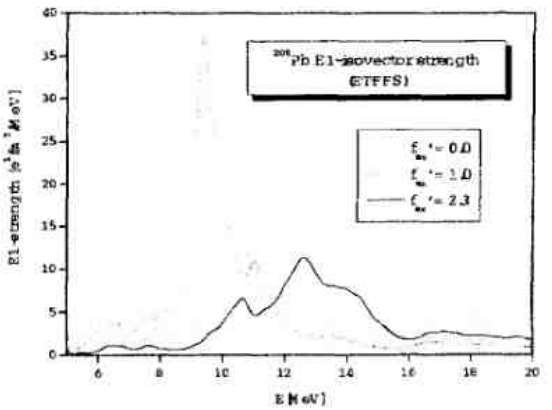

FIG. 3: Electromagnetic E1-strength from 5 to 20 MeV calculated in our *extended theory*. The thick line indicates the final result whereas the other lines are the results of calculation where the isovector force parameter has been varied as indicated in the figure

Finally in Fig.1(d), where we use our conventional force parameter - which reproduces nearly quantitatively the experimental data of the GDR - only 5.2% of the strength remain below 10 MeV. We observe that the major part of the E1-strength is shifted into the GDR region, where it creates a very collective resonance, in agreement with the data.

Within our model, in the electromagnetic E1-strength up to 9 MeV which is the region of the *pygmy resonance* we do not find a collective state where most of the low lying strength is concentrated but we find already in the 1p1h-RPA several states which energies essentially unchanged compared with the $f_0' = 0$ case. The E1-strength, however, is reduced by a factor of 10 due to the strongly repulsive isovector force which shifts the strength into the GDR region and produces a collective resonance. Such a behavior is expected from the schematic model by Brown and Bolsterli [21].

In Fig.2 we present the results of the *ETFFS* calculation where in addition to the single-particle continuum the effect of the phonons is also included. The result

in Fig.2 has to be compared with the results in Fig.1(d). One observes a further fragmentation of the strength and a small shift of the two strongest states to higher energies. Whereas the calculated strength distribution between 7 and 8 MeV is in good agreement with the data we obtain too little strength below 6 MeV and to much between 6-7 MeV, compared with the present data. A shift of the two neutron states $1j_{13/2}$ and $1i^{-1}_{13/2}$ improves the agreement between theory and experiment.

In Fig.3 the electromagnetic E1-strength distribution calculated within the *ETFFS* is shown up to 20 MeV with a smearing parameter $\Delta = 250keV$ and 3 different f'_0 parameters. It is interesting to see how the strength is shifted to higher energies with increasing interaction. For our conventional value $f'_0 = 2.30$ the theoretical distribution in the GDR region agrees quantitatively with the experimental data. In connection with the previous discussion, the energy range between 6-8 MeV is of special interest. With no isovector interaction, but the spurious components removed, one obtains some concentration of strength around 6.2 MeV and 7.5 MeV. The latter is considered as the PDR region. With increasing isovector force this strength gets reduced. For the full force the reduction is a factor of 5 compared to $f'_0 = 0$. This behavior is just the opposite of a collective structure, where with increasing force the collectivity is enhanced.

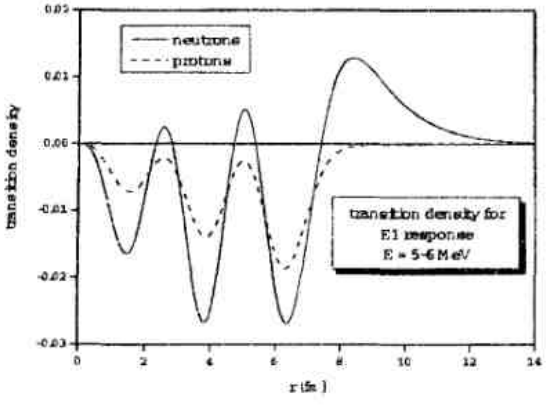

FIG. 4: Summed transition densities for the electric dipole response shown in Fig.2 from 5 to 6 MeV

In Figs.4-6 the transition densities between 5-6 MeV, 6-7 MeV and 7-8 MeV of the electric dipole response are plotted for transitions shown in Fig.2. In all three cases protons and neutron are in phase which indicates strong isoscalar components. This at first glance surprising behavior has been found also by other authors. It can be understood immediately in our microscopic model. As discussed in the next section, the isoscalar force is attractive and give rise to a collective structure around 22 MeV. Due to this attractive force, some of the high-lying

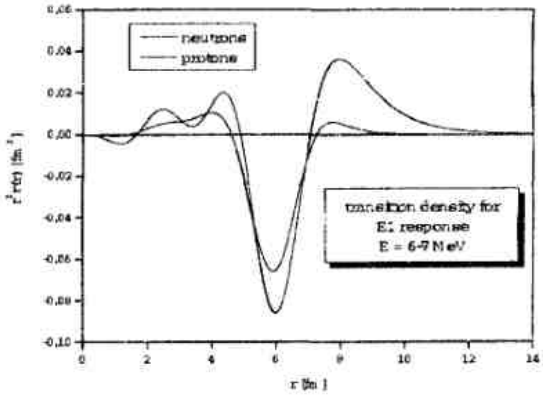

FIG. 5: Summed transition densities for the electric dipole response shown in Fig.2 from 6 to 7 MeV

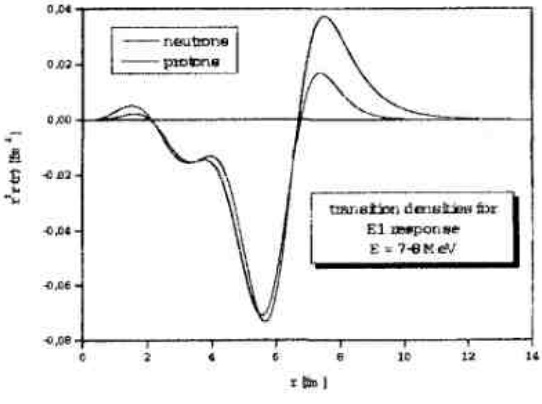

FIG. 6: Summed transition densities for the electric dipole response shown in Fig.2 from 7 to 8 MeV

strength couples also to the low-lying states, whereas simultaneously the strong repulsive isovector force shifts the isovector strength from these configurations into the GDR region.

B. The isoscalar case

For the electric isoscalar dipole states we have a special situation because the lowest isoscalar resonance is the spurious state corresponding to the translation of the whole nucleus. In self-consistent calculations this state appears (at least in principle) at zero energy and carries all the spurious strength.

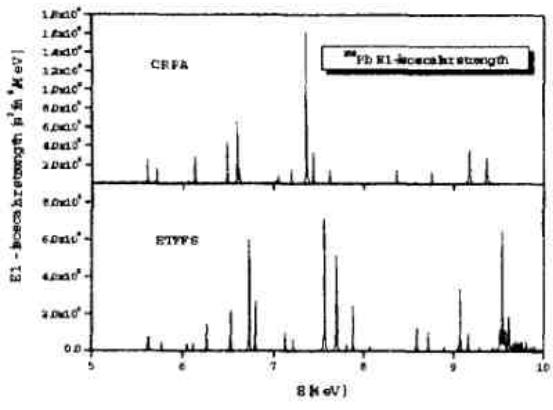

FIG. 7: E1-isoscalar strength distribution in ^{208}Pb from 5-10 MeV for the transition operator $r^3Y_{1,\mu}$. Here we compare the results derived from the CRPA with the results obtained with the *extended theory*

In shell model approaches like the present one, the spurious state has to be removed explicitly. Here we use the procedure developed in [18] to obtain the energy of the spurious E1 state exactly at zero energy, with no spurious components in the excited state. As the isoscalar electric dipole strength distribution depends on the isoscalar parameter f_0 we test the force by calculating the isoscalar monopole resonance - the breathing mode. With our universal value of $f_0 = -1.35$ we reproduce the mean energy as well as the width of the resonance. In Fig.7 the results of our calculation for the isoscalar dipole operator $r^3Y_{1,\mu}$ up to 10 MeV are presented. Here we compare the *CRPA* with the *ETFFS* results. In the *CRPA* we obtain one strong state near 7.4 MeV and several somewhat weaker states at lower energies. Due to the phonon coupling the strength of the strongest state is fragmented and shifted to slightly higher energies. Those isoscalar states have been investigated experimentally with the $(\alpha, \alpha', \gamma_0)$ reaction. So far the experimental data from ^{208}Pb are not given in the form of cross sections but only in counts [6]. The data show a very strong signal around 5.6 MeV and a somewhat weaker signal around 6.7 MeV. As the isoscalar strength distribution in Fig.7 is calculated with the operator r^3Y_{10} a comparison with these data is not directly possible as the (α, α') reaction is sensitive to the tails of the isoscalar distributions and the γ_0 is proportional the isovector admixture. Unfortunately analyzing programs where microscopic transition densities can be used do not exist so far [20]. The transition densities shown previously are the same for the isoscalar and isovector case. Only the transition strength is different as the corresponding operators weight the transition densities differently.

IV. HIGH LYING ELECTRIC DIPOLE STRENGTH

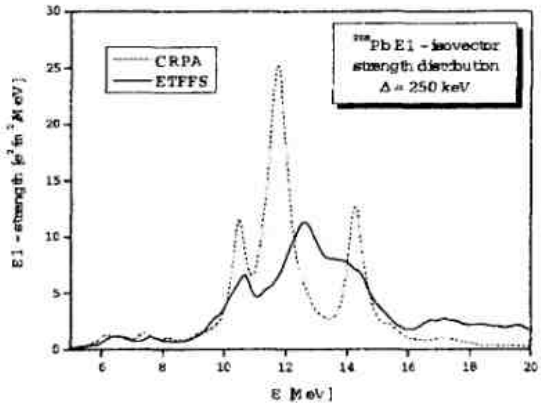

FIG. 8: E1 isovector strength from 5 to 20 MeV. We compare here the results of the continuum RPA with the *extended theory* the width and the mean energy of the latter one agrees quantitatively with the experimental result.

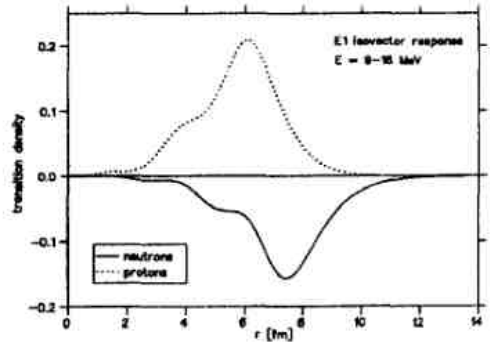

FIG. 9: Transition density of the isovector giant dipole resonance.

The GDR was calculated with our universal parameters given in eq.(2.1) and the result is shown in Fig.8. The mean energy and the width of the resonance agree with the data within the error bars. The escape and spreading widths are included in our microscopic model. In addition we consider a *smearing* parameter $\Delta = 250keV$, which corrects for more complex configurations that have not be considered in our approach. Here we point out again that the low-lying and high-lying E1 strength is calculated within the same model with exactly the same single-particle energies and force parameters. This differs from some *self-consistent* approaches where the single-

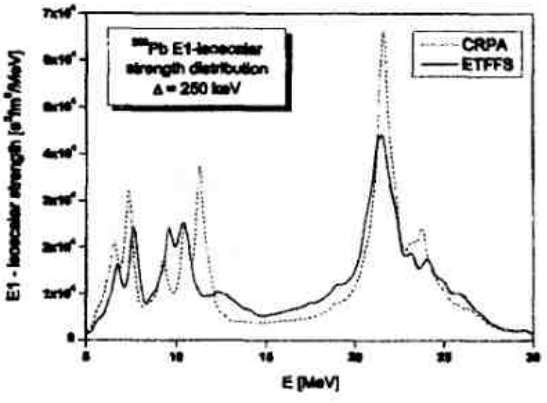

FIG. 10: Isoscalar E1 strength from 5 to 30 MeV.

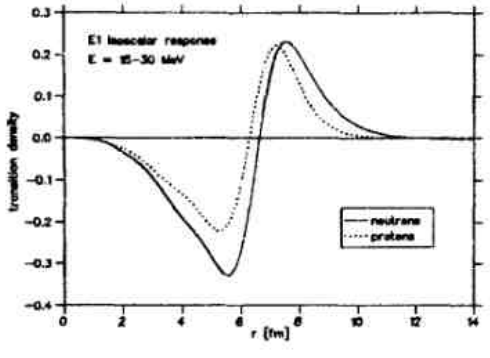

FIG. 11: Transition density of the isoscalar giant dipole resonance.

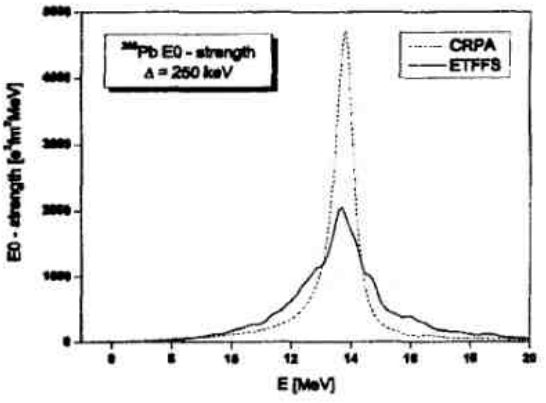

FIG. 12: Isoscalar E0 strength from 5 to 20 MeV calculated in the continuum RPA and *the extended theory*. Mean energy and width of the latter one agrees with the data.

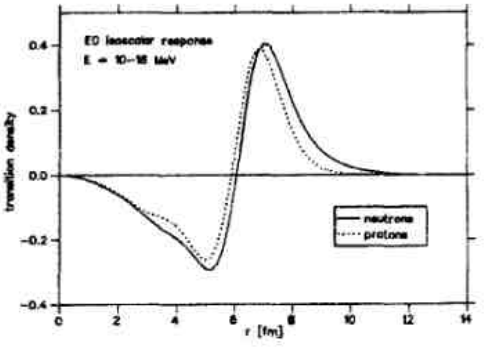

FIG. 13: Transition density of the breathing mode.

particle spectrum is modified in order to fit the low-lying spectrum.

In Fig.9 the corresponding transition density is plotted. It is surface peaked and protons and neutrons are out of phase. As we have 50% more neutrons than protons, the neutron density has *not* only a stronger and longer tail than the proton density, but it is also peaked further outside. For that reason we also have some admixture of isoscalar E1-strength – even in the isovector giant dipole region, as one can see from the isoscalar E1-strength distribution in Fig.10. The form of the transition density agrees with surface peaked phenomenological models.

In Fig.10 the theoretical isoscalar E1-response from 5-30 MeV is plotted. One realizes, that in addition to the low-lying strength, we obtain a strong collective structure above 20 MeV, which represents the isoscalar electric dipole resonance. As the strength is well concentrated these giant resonance could be seen in a (α, α') reaction. The corresponding transition density is given in Fig.11. It has the form of a compression mode and for that reason we have shown –finally - in Fig.12 and Fig.13 the isoscalar monopole strength and the corresponding transition density. These calculations are performed for purpose of consistency because the isoscalar monopole and isoscalar dipole depend both on the isoscalar parameters f_0 and have, in addition, a very similar structure, as can be seen in the transition densities. In the monopole case the radial integral over the transition density has to be zero; in the electric dipole case the transition density multiplied by the radial coordinate r must vanish.

V. DISCUSSION

The center of our investigations is the origin and the structure of the pygmy resonances. We have chosen in ^{208}Pb a nucleus with an excess of 44 neutrons, which

means that we have 50% more neutrons than protons. The structure of this double magic nucleus as well, as the neighboring odd mass nuclei, is well known and all microscopic models and microscopic theories – self-consistent and non-self-consistent– work best for this case. Our calculation shows first of all that we obtain isovector as well as isoscalar electric dipole states below 10 MeV. This is obvious, as the ph-interaction has isoscalar as well as isovector components. Here we point out that all the spurious components are removed i.e. the expectation value of the translation operator $rY_{1\mu}$ in all the excited states is zero. The isoscalar strength is due to the $3\hbar\omega$ and higher ph components. In the present shell model approach one is able to remove the spurious strength without performing a full RPA calculation, as it has to be done in self consistent approaches. Here it is only necessary to use the appropriate isoscalar force parameter f_0; the isovector force parameter f_0' can be independently varied. This allows one to investigate the influence of the isovector interaction on the low-lying isovector dipole strength in detail. We have shown in Fig.1 and Fig.3 that if one starts with the experimental single-particle energies then with increasing isovector force the isovector dipole strength is shifted to higher energies and one is finally left with a small fraction of the sum rule in a couple of states that are only slightly shifted with respect to the unperturbed ph energies. There is no indication in the present model of a low-lying collective state which is built up by the isovector interaction. The theoretical electromagnetic strength below 8 MeV is 1.94 $[e^2fm^2]$ compared with the experimental strength of 1.32 $[e^2fm^2]$. The distribution of the theoretical strength agree in the range between 7-8 MeV with the current data. The calculated strength between 6-7 MeV, however, is too large and the strength below 6 MeV too small compared with the experimental values. On the other hand the width and the mean energy of the GDR is reproduced quantitatively in our model.

It is obvious that if one changes the single particle spectrum one is always able to improve the agreement with the data. In the present calculation we only consider the lowest order in the expansion of the Migdal interaction as it is done in nearly all calculations. The next-to-leading order in Migdal's interaction depends on the momenta through $\boldsymbol{p} \cdot \boldsymbol{p}'$ with the isoscalar force parameter f_1 and the isovector force parameter f_1'. The sign and magnitude of the two parameters can be estimated from the effective mass of the nucleus and the orbital part of the effective magnetic operator [19]. From this consideration it follows that both parameters are negative, with the f_1' parameter slightly larger in magnitude. These parameters would gives rise to an attractive velocity dependent isoscalar and isovector ph-interaction. A small effective mass, as it is used in relativistic RPA calculations, would increase the magnitude of both of the parameters. A strong isovector, velocity dependent force could be the explanation of the collective states with large vorticities which are found in relativistic RPA calculations [11]. In this approach two phonon states will give rise to a fragmentation which should explain the E1 data between 5.5-9 MeV. Unfortunately, the lowest two phonon states are at 6.7 and 6.9 MeV whereas the lowest experimental 1p1h states are more then one MeV lower. We therefore consider the present result, where the E1 strength between 5,5-9 MeV lies essentially at the unperturbed ph-energies and the major part of the isovector E1 strength is shifted into the GDR , to be the more physical one. More over such a collective phenomena has not been found in self-consistent calculations in which one starts with effective forces from the Skyrme type.

VI. CONSEQUENCES FOR SELF-CONSISTENT CALCULATIONS

The present calculation is not self-consistent in the sense that one starts with an effective Lagrangian and Hamiltonian, respectively, the numerous parameters of which are –in general– adjusted to gross properties of nuclei. These parameters can not be determined in a unique way and therefore there exists numerous sets of parameters which reproduce the gross properties equally well but could give quite different results for excited states. If we consider, as a specific example effective forces of the Skyrme type, we find parameterizations that, e.g. give rise to effective masses from $m^*/m = .6$ to $m^*/m = 1$. For nuclear structure calculations the effective mass is of special importance because the spacing of the single particle spectrum is inversely proportional to it; a smaller m^*/m expands the single particle spectrum and a larger one compresses the spectrum. The experimental single particle spectrum in the neighboring odd mass nuclei of ^{208}Pb correspond to an effective mass of roughly one. If one describe the spectrum in the odd mass nuclei correctly one simultaneously reproduces the non-collective states in ^{208}Pb. The collective states, on the other hand, depend not only on the ph-spectrum but also on the residual ph interaction. It seems always possible to find, under the numerous sets of Skyrme parameters, one set that reproduces the collective states in which one is interested in.

In our calculations we investigated simultaneously the E1 spectrum between 5-8 MeV and the high-lying spectrum. Our calculations show that the E1 spectrum below 8 MeV is very similar to the unperturbed experimental ph spectrum, whereas the high-lying collective states depends sensitively on the (universal) Migdal parameters. This is not an exception; rather, it is the general experience. In the low energy spectrum of ^{208}Pbone finds some collective states with natural parity which are collective (e.g. $3^-, 5^-, 2^+$ ect.)but the majority of the states –especially the low lying unnatural ones – are energetically at the experimental ph energies. Therefore, if one is looking for an unified description of the structure of even-even nuclei one has also to consider the spectra of the neighboring odd mass nuclei.

VII. SUMMARY

The *extended theory of finite Fermi systems* has been applied to the low-lying and high-lying E1-spectrum of ^{208}Pb as an example of a neutron rich nucleus. In the present approach the low-lying electromagnetic E1 spectrum is non-collective but we find in the low-lying E1 states strong isoscalar admixtures. The theoretical results for GDR as well as the breathing mode agree quantitatively with the data. We also find in our calculation well localized isoscalar E1 resonance a about 21 MeV which could be dedected in (α, α') scattering.

From the present investigation one may draw important conclusions for self-consistent calculations. We have seen that the inclusion of the phonons give rise to a shift of the single particle spectrum of about 1MeV for neutron and nearly 2 MeV for protons. In the present *extended theory* one has to determine *bare* single particle energies which give the experimental ones if one includes the phonons. Self-consistent approaches determine the *bare* spectrum which we have to use as input in our *extended theory*. Therefore one has to chose a parametrization which give rise to a *bare* spectrum which agrees with the experimental one if one includes the phonons. From this point of view, a self-consistent calculation for excited states at the level of 1p1h RPA is not appropriate.

VIII. ACKNOWLEDGEMENT

One of as (JS) thanks Stanislaw Drozdz for many discussions and the Foundation for Polish Science for financial support through the *Alexander von Humboldt Honorary Research Fellowship*. The work was partly supported by the DFG and RFBR grants Nos.GZ:432RUS113/806/0-1 and 05-02-04005 and by the INTAS grand No.03-54-6545.

[1] R. Palit, P. Adrich, T. Aumann, et al., Nucl. Phys. A731 (2004) 235.
[2] U. Kneisl, H.H. Pilz, and A. Zilges, Progr. Part. Nucl. Phys. 37 (1996) 349.
[3] T. Hartmann, J. Enders, P.Mohr, et al., Phys. Rev. C 65 (2002) 034301.
[4] T. Hartmann et al., Phys. Rev. Lett. 93 (2004) 192501.
[5] R.M.Laszewski, P.Rullhusen, S.D.Hoblit and S.F.LeBrun, Phys. Rev. Lett. 54 (1985) 530.
[6] M.N. Harakeh and A.van der Woude, Giant Resonances (Clarendon Press, Oxford, 2001).
[7] A.Zilges, private communication.
[8] Y. Suzuki, K. Ikeda, and H. Sato, Progr. Theor. Phys. 83 (1990) 180.
[9] P. Van Isacker, M. A. Nagarajan, and D. D. Warner, Phys.Rev.C45(1992)R13
[10] S.Typel and G.Baur,Phys.Rev.Lett.93(2004)142502
[11] D. Vretenar, A.V. Afanasjev, G.A. Lalazissis, and P.Ring, Phys. Rep. 409 (2005) 101.
[12] S. Goriely, E. Khan, Nucl.Phys. A 706 (2002) 217.
[13] V.G. Soloviev, Theory of Complex Nuclei (Pergamon Press, Oxford, 1976) [Russ. original, Nauka, 1971]
[14] V.G. Soloviev, Theory of Atomic Nuclei: Quasiparticlws and Phonons (Institute of Physics , Bristol and Phyladelphia, USA, 1992)
[15] S. Kamerdzhiev, J. Speth and G. Tertychny, Phys. Rep. 393 (2004) 1. N. Ryezaeva, T. Hartmann, Y. Kalmykov, et.al., Phys. Rev. Lett. 89 (2002) 272502.
[16] N. Tsoneva, H. Lenske, Ch. Stoyanov, Phys. Lett. B 586 (2004) 213.
[17] D.Sarchi, P.F. Bortignon, G. Colo, Phys. Lett. B 601 (2004) 27.
[18] S.Kamerdzhiev,R.J.Liotta,E.Litvinova and V.Tselyaev, Phys.Rev.C 58 (1998) 172
[19] J.Speth,E.Werner,W.Wild,Phys.Rep.33(1977)127
[20] A.Zilges,private communication
[21] G.E.Brown and M.Bolsterli, Phys.Rev.Lett.3(1959)472

LARGE-SCALE NO-CORE SHELL MODEL STUDIES OF SPECTRA OF *s* AND *p* SHELL NUCLEI WITH HIGH-QUALITY NON-LOCAL INVERSE SCATTERING NUCLEON-NUCLEON INTERACTION

A.M.Shirokov,[1] J.P.Vary,[2] A.I.Mazur,[3] and T.A.Weber[2]

[1]*Skobeltsyn Institute of Nuclear Physics, Moscow State University, Moscow 119992, Russia*

[2]*Department of Physics and Astronomy, Iowa State University, Ames, Ia 50011-3160, USA*

[3]*Pacific National University, 136 Tikhookeanskaya, Khabarovsk 680035, Russia*

High-quality nucleon-nucleon interaction is constructed in the J-matrix inverse scattering approach. The interaction is of the form of a matrix in the oscillator basis in each of the NN partial waves. The matrix ranks are small, nevertheless the interaction reproduces the NN scattering data with the accuracy of the best modern realistic NN interactions. Phase-equivalent transformations, i.e. transformations that do not affect the scattering data, are used to get a high-quality description of binding energies and spectra of all stable nuclei up through $A = 16$ without the use of three-nucleon forces. The large-scale nuclear structure calculations are performed in the framework of the fully-microscopic no-core shell model where all nucleons are spectroscopically active.

One of the modern nuclear structure theory mainstreams is the development of *ab initio* microscopic approaches, i.e. approaches that make no use of various model assumptions like, e.g., the inert core. A number of *ab initio* methods was recently introduced and tested, in particular, Faddeev approach in few-body physics, hyperspherical method, Green's function Monte Carlo, coupled cluster approach, and no-core shell model (NCSM). At the moment, *ab initio* studies are limited to light enough nuclei ($A \lesssim 16$) by the modern computer resources. In our microscopic studies, we make use of NCSM [1] which we expect to have a better perspective among other *ab initio* approaches to be extended to heavier nuclear systems with evolving computational facilities.

Nucleon-nucleon interaction is the only input information for *ab initio* calculations. There is a number of high-quality realistic interactions on the market perfectly describing NN scattering data and deuteron properties. Most of the modern realistic NN potentials like CD-Bonn [2], Argonne V18 [3] and Nijmegen [4], were obtained within the meson-exchange theory. A new realistic interaction was obtained within the chiral perturbation theory [5]. All these realistic NN potentials fail to describe binding energies of the lightest nuclei ^{3}H, ^{3}He and ^{4}He which are calculated now with high accuracy by various methods. There are other drawbacks of modern realistic NN forces, for example, they produce $(J^\pi T) = (1^+0)$ ^{10}B ground state contrary to the experimental (3^+0) [6]. These shortcomings are conventionally eliminated by introducing three-nucleon forces. This approach has been proven to be very successful (see, e.g., [7–13]). However the use of the three-nucleon interactions results in emerging computational complexity, especially in nuclei with $A > 10$. With modern computer facilities, the three-body forces restrict the possibility to extend *ab initio* studies to heavier nuclei and the range of available model spaces, i.e. the reliability of the microscopic

TABLE I: JISP16 deuteron property predictions in comparison with the ones obtained with various modern realistic potentials.

Potential	E_d, MeV	d state probability, %	rms radius, fm	Q, fm^2	As. norm. const. $\mathscr{A}_s$, fm$^{-1/2}$	$\eta = \frac{\mathscr{A}_d}{\mathscr{A}_s}$
JISP16	−2.224575	4.136	1.964	0.2886	0.8629	0.0252
Nijmegen-II	−2.224575	5.635	1.968	0.2707	0.8845	0.0252
AV18	−2.224575	5.76	1.967	0.270	0.8850	0.0250
CD–Bonn	−2.224575	4.85	1.966	0.270	0.8846	0.0256
Nature	−2.224575(9)	—	1.971(6)	0.2859(3)	0.8846(9)	0.0256(4)

predictions.

This hassle motivated us to introduce an approach that simultaneously minimizes the role of three-nucleon forces in nuclei while providing more rapid convergence of *ab initio* calculations with a pure nucleon-nucleon force. We develop a new class of NN potentials that provide accurate descriptions of available nucleon-nucleon data together with a broad range of observed properties of nuclei without three-nucleon forces. We are supported by the work of Polyzou and Glöckle who demonstrated [14] that a realistic NN interaction is equivalent at the $A = 3$ level to a realistic $NN + NNN$ interaction where the new NN force is related to the initial one through a phase-equivalent transformation (PET). The net consequence is that properties of nuclei beyond $A = 3$ become dependent on the freedom within the transformations at the $A = 3$ level. It seems reasonable then to exploit this freedom and work to minimize the need for the explicit introduction of three and higher body forces.

Recently we suggested a J-matrix inverse scattering approach to construct high-quality NN potentials [15]. The obtained charge-independent NN interaction provides an excellent description of the NN scattering data with χ^2/datum = 1.03 for the 1992 np data base (2514 data), and 1.05 for the 1999 np data base (3058 data) [16]. To compare, χ^2/datum = 1.08, 1.03 and 0.99 (the 1992 np data base) and 1.07, 1.02 and 0.99 (the 1999 np data base) [2] for respectively Argonne AV18, CD-Bonn potentials and the Nijmegen phase shift analysis utilized in the J-matrix inverse scattering approach to construct the NN interaction. We used PET suggested in Ref. [17] and discussed in detail in Refs. [15, 18] to get the perfect description of the deuteron properties (see Table I) by the J-matrix inverse scattering NN potential (JISP) [15, 19, 20]. Next we used PETs in various NN partial waves to provide description of various heavier nuclei properties with the JISP interaction. The first version of the interaction, JISP6 [19], was fitted to the binding energies and spectra of nuclei with $A \leq 6$. However we found out that JISP6 overbinds nuclei with $A \geq 10$. To eliminate this deficiency, we exploited PETs to modify the JISP6. The resulting interaction JISP16 [20] was fitted to the spectra and bindings of stable $A \leq 16$ nuclei. Our fitting procedure was one of 'trial-and-error' where we worked with only a few partial waves that we deemed important for these nuclei. We fitted only the excitation energies of few lowest ^{6}Li levels and the ^{6}Li and ^{16}O binding energies. To save time, we performed the NCSM calculations in small enough model spaces (up to $10\hbar\omega$ for ^{6}Li and up to $4\hbar\omega$ for ^{16}O). After obtaining a reasonable description of these observables, we checked that the binding energies and spectra of all the rest s and p shell nuclei are well-described in small model spaces. The results presented below are obtained in the *ab initio* NCSM calculations with the JISP16 NN interaction in

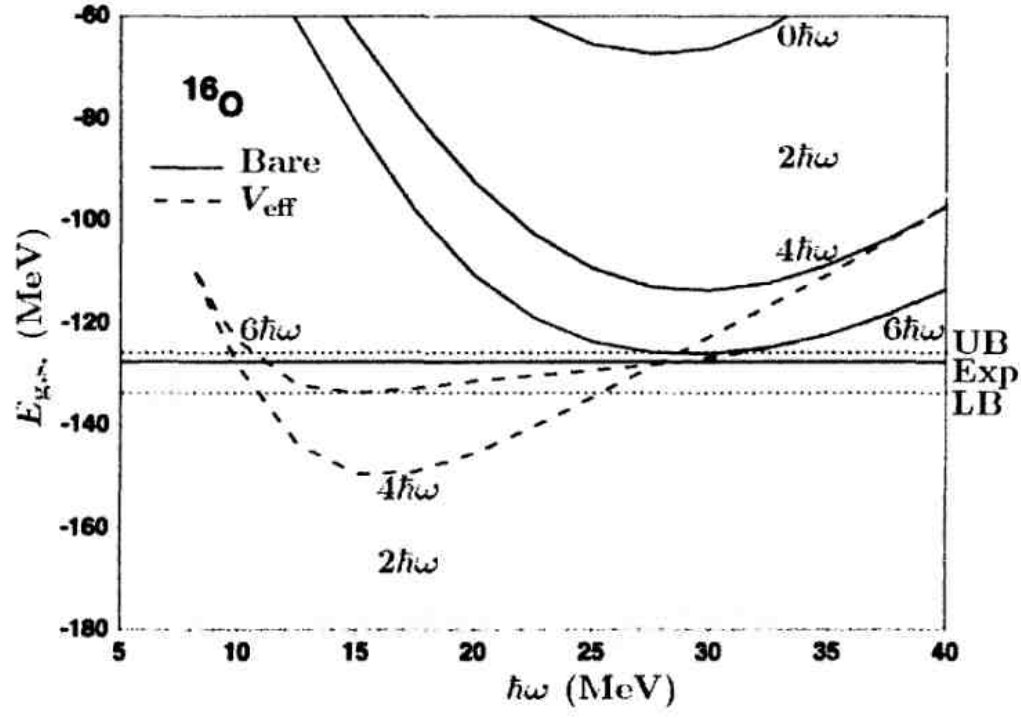

FIG. 1: The $\hbar\omega$ dependence of the ^{16}O ground state energy obtained with the bare JISP16 and the effective interaction based on JISP16 in a sequence of $N_{max}\hbar\omega$ model spaces up to $N_{max} = 6$; the lines marked as Exp., UB and LB show the experimental ground state energy, the upper bound and the suggested lower bound for the NCSM ground state energy predictions.

larger model spaces. This description of the binding energies is somewhat worse than the one obtained during the fit in smaller model spaces, however it is still very reasonable. In a future effort, we will perform a thorough search through the space of possible PETs that should further improve the description of nuclear properties while retaining the excellent description of the NN data.

We illustrate our approach to the description of the binding energies within NCSM by Figs. 1 and 2 where we present the $\hbar\omega$ dependence of the ground state energies $E_{\rm g.s.}$ of ^{16}O and ^{4}He.

The convergence of the NCSM calculations with conventional realistic potentials is pure, therefore the calculations are usually performed with the effective NN interaction obtained from the parent realistic ('bare') NN interaction by the Lee–Suzuki transformation [1]. However, the JISP interaction provides a rapid convergence within NCSM and it is worthwhile to perform also calculations with the bare JISP interaction. The variational principle holds for the bare interaction results; hence the upper bound (UB) for the ground state energy is the minimum of its $\hbar\omega$ dependence in the largest available model space ($6\hbar\omega$ model space in the case of ^{16}O and $14\hbar\omega$ model space in the ^{4}He case). There is no variational principle for the calculations with the effective interaction which is different in different model spaces. The quoted NCSM result is conventionally associated with the minimum of the ground state energy $\hbar\omega$ dependence obtained in the effective interaction calculations. This minimum is seen from Figs. 1–2 to ascend with increasing model space. Similar trends are found for all s shell and most of the p shell nuclei. The minimum obtained with the effective interaction in the largest available model space for a given nucleus is a suggested lower bound (LB) for the ground state energy. The difference between these upper and lower bounds is our estimate for the 'error bars' of our predictions. These error bars are seen to be very small in the ^{4}He case suggesting that a very good convergence is attained. A remarkable flatness

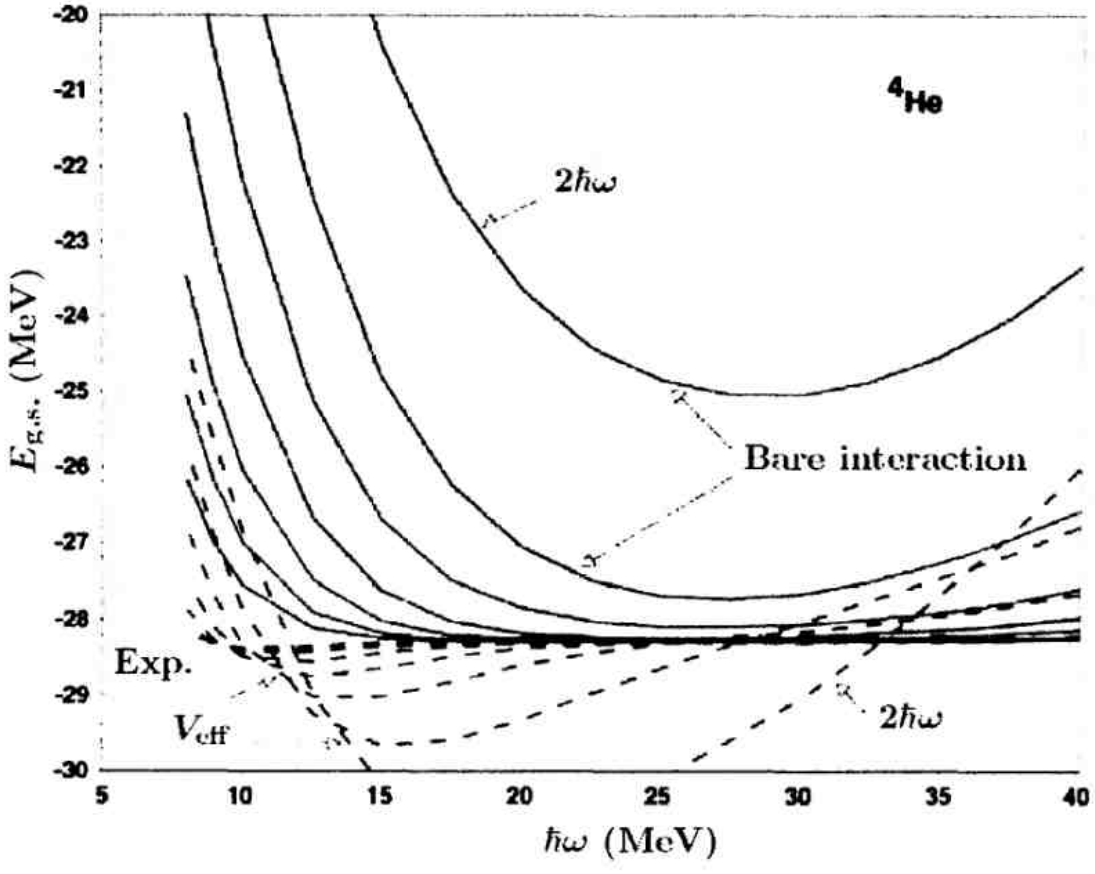

FIG. 2: The $\hbar\omega$ dependence of the ^{4}He ground state energy. See Fig. 1 for details.

of the $\hbar\omega$ dependence in large enough model spaces in a wide range of $\hbar\omega$ values is another indication of the excellent convergence of the ^{4}He calculations. The convergence in the ^{16}O case is seen to be somewhat worse that is not surprising since the largest available NCSM model space for this nucleus is $6\hbar\omega$ while $14\hbar\omega$ model space is attainable for ^{6}He.

We present in Table II binding energies obtained with both bare and effective interactions of all nuclei where bare and effective bindings converge from opposite sides. We also quote the $\hbar\omega$ values providing the minimum with the effective interaction. The difference between the given result and the result obtained with the same $\hbar\omega$ in the next smaller model space is presented in parenthesis to give an estimate of the convergence of the calculations. We quote our differences in significant figures from the rightmost figure of the stated result, omitting decimal points to save space.

The ground state energy of $A = 6$, 7 and 8 nuclei converges uniformly from above with both the bare and effective interactions. We present in Table II only the effective interaction results for these nuclei due to their superior convergence features. For these nuclei, an extrapolation based on the fit by a constant plus exponential function for different $\hbar\omega$ values may be useful. For ^{6}Li, this extrapolation results in a binding energy of 31.70(17) MeV where the value in parenthesis is the uncertainty of the fit. A similar extrapolation for ^{6}He results in a binding energy of 28.89(17) MeV which is bound with respect to the $\alpha + n + n$ threshold. We note that the ^{6}He binding energy presented in the Table II is smaller than the ^{4}He binding energy, i.e. ^{6}He seems to be unbound with respect to the $\alpha + n + n$ threshold in our calculations. However this quasi-unbinding is only an indication of a moderate convergence in the case of weakly-bound ^{6}He nucleus as is elucidated by the above extrapolation. We note also that the bare interaction results for $A = 6$ nuclei are very close to the effective interaction ones demonstrating a remarkable softness of the JISP16 interaction: the ^{6}Li and

TABLE II: Binding energies (in MeV) of nuclei obtained with bare JISP16 and effective interaction generated by JISP16.

Nucleus	Nature	Bare	Effective	$\hbar\omega$ (MeV)	Model space
^{3}H	8.482	8.354	8.496(20)	7	$14\hbar\omega$
^{3}He	7.718	7.648	7.797(17)	7	$14\hbar\omega$
^{4}He	28.296	28.297	28.374(57)	10	$14\hbar\omega$
^{6}He	29.269		28.32(28)	17.5	$12\hbar\omega$
^{6}Li	31.995		31.00(31)	17.5	$12\hbar\omega$
^{7}Li	39.245		37.59(30)	17.5	$10\hbar\omega$
^{7}Be	37.600		35.91(29)	17	$10\hbar\omega$
^{8}Be	56.500		53.40(10)	15	$8\hbar\omega$
^{9}Be	58.165	53.54	54.63(26)	16	$8\hbar\omega$
^{9}B	56.314	51.31	52.53(20)	16	$8\hbar\omega$
^{10}Be	64.977	60.55	61.39(20)	19	$8\hbar\omega$
^{10}B	64.751	60.39	60.95(20)	20	$8\hbar\omega$
^{10}C	60.321	55.26	56.36(67)	17	$8\hbar\omega$
^{11}B	76.205	69.2	73.0(31)	17	$6\hbar\omega$
^{11}C	73.440	66.1	70.1(32)	17	$6\hbar\omega$
^{12}B	79.575	71.2	75.9(48)	15	$6\hbar\omega$
^{12}C	92.162	87.4	91.0(49)	17.5	$6\hbar\omega$
^{12}N	74.041	64.5	70.2(48)	15	$6\hbar\omega$
^{13}B	84.453	73.5	82.1(67)	15	$6\hbar\omega$
^{13}C	97.108	93.2	96.4(59)	19	$6\hbar\omega$
^{13}N	94.105	89.7	93.1(62)	18	$6\hbar\omega$
^{13}O	75.558	63.0	72.9(62)	14	$6\hbar\omega$
^{14}C	105.285	101.5	106.0(93)	17.5	$6\hbar\omega$
^{14}N	104.659	103.8	106.8(77)	20	$6\hbar\omega$
^{14}O	98.733	93.7	99.1(92)	16	$6\hbar\omega$
^{15}N	115.492	114.4	119.5(126)	16	$6\hbar\omega$
^{15}O	111.956	110.1	115.8(126)	16	$6\hbar\omega$
^{16}O	127.619	126.2	133.8(158)	15	$6\hbar\omega$

^{6}He binding energies are 30.94(44) and 28.23(41) MeV respectively, the extrapolations of the bare interaction bindings produce 31.33(12) MeV for ^{6}Li and 28.61(12) MeV for ^{6}He.

The nuclear Hamiltonian based on the NN interaction JISP16, is seen to be realistic and reproduces well the binding energies of nuclei with $A \leq 16$ in *ab initio* NCSN calculations. The lowest state of natural parity has the correct total angular momentum in each nucleus studied. The experimental binding energies of all nuclei presented in Table II either lie within error bars of our predictions or are close to our suggested LB based on the effective interaction calculations. Generally JISP16 slightly underbinds only nuclei in the middle of the p shell. In other words, we see underbinding of nuclei where the $p_{3/2}$ subshell is filled. Most probably, this indicates that the JISP16 NN interaction produces an underestimated

TABLE III: Ground state energy $E_{\rm g.s.}$ and excitation energies E_x (in MeV), ground state point-proton rms radius r_p (in fm) and quadrupole moment Q (in $e \cdot \mathrm{fm}^2$) of the ^{6}Li nucleus; $\hbar\omega$ = 17.5 MeV.

Interaction Method	Nature	JISP16 NCSM, $12\hbar\omega$	AV8'+TM' NCSM, $6\hbar\omega$ [12]	AV18+UIX GFMC [8, 11]	AV18+IL2 GFMC [9, 11]
$E_{\rm g.s.}(1^+_1,0)$	−31.995	−31.00	−31.04	−31.25(8)	−32.0(1)
r_p	2.32(3)	2.151	2.054	2.46(2)	2.39(1)
Q	−0.082(2)	−0.0646	−0.025	−0.33(18)	−0.32(6)
$E_x(3^+,0)$	2.186	2.529	2.471	2.8(1)	2.2
$E_x(0^+,1)$	3.563	3.701	3.886	3.94(23)	3.4
$E_x(2^+,0)$	4.312	5.001	5.010	4.0(1)	4.2
$E_x(2^+,1)$	5.366	6.266	6.482		5.5
$E_x(1^+_2,0)$	5.65	6.573	7.621	5.1(1)	5.6

spin-orbit splitting in the p shell. The difference between UB and LB is small suggesting that JISP16 provides good convergence. However, our error bars increase as binding energy decreases in a chain of isobars (for example, compare the results for ^{13}O and ^{13}N).

We present in Tables III and IV spectra and ground state properties of ^{6}Li and ^{10}B which are known [8, 10–12] to be sensitive to the three-nucleon interaction. Our JISP16 NN interaction alone provides a good description of ^{6}Li and ^{10}B. The JISP16 ^{6}Li spectrum is seen to be competitive with those of realistic $NN + NNN$ potential models. We note a good description of the ^{6}Li quadrupole moment Q that is a recognized challenge due to a delicate cancellation between deuteron quadrupole moment and the d wave component of the α–d relative wave function. We observe that Q and the point-proton rms radius r_p have a more prominent $\hbar\omega$ dependence than the binding energy.

A complicated ^{10}B spectrum is a recognized challenge in nuclear structure studies. The ^{10}B ground state spin and the level ordering in the ^{10}B spectrum were never described microscopically with pure two-nucleon realistic interactions (see, e. g., [10, 12]). However the ^{10}B properties are seen from Table IV to be well-described with the JISP16 NN interaction. We note that the ^{10}B spectrum depends on $\hbar\omega$ at $N_{max} = 8$ but not so strongly as to alter our main conclusions. For example, the minimum of the ^{10}B ground state corresponds to $\hbar\omega = 20$ MeV while the minimum in the first excited state energy occurs at $\hbar\omega = 15$ MeV. We present in Table IV the ^{10}B properties obtained with $\hbar\omega = 15$ MeV, i.e. with the $\hbar\omega$ value corresponding to the minimum of the first excited state since it has a more pronounced $\hbar\omega$ dependence than the ground state. We observe that our description of the ^{10}B spectrum is somewhat better than the one obtained with the Argonne AV8' NN potential and Tucson–Melbourne TM' NNN force. In particular, we reproduce the ordering of ^{10}B levels except for the $(3^+_2,0)$ state. We note that the $(3^+_2,0)$ state is also too high with the AV8' + TM' interaction.

We see that our JISP16 NN interaction gives rise to a realistic many-body nuclear Hamiltonian providing a good description of various properties of nuclei up through ^{16}O. This Hamiltonian opens a path for extending realistic microscopic theory to heavier nuclei, to achieve better convergence and to obtain improved agreement with experiment.

In constructing JISP interactions [15, 19, 20] and the JISP16 interaction in particular [20] we adopted only the accepted symmetries of the NN interaction and neglected explicit con-

TABLE IV: Same as in Table III but for the ^{10}B nucleus; $\hbar\omega = 15$ MeV.

Interaction Method	Nature	JISP16 NCSM, $8\hbar\omega$	AV8'+TM' NCSM, $4\hbar\omega$ [12]	AV18+IL2 GFMC [10]
$E_{gs}(3_1^+,0)$	−64.751	−60.14	−60.57	−65.6(5)
r_p	2.30(12)	2.168	2.168	2.33(1)
Q	+8.472(56)	6.484	+5.682	+9.5(2)
$E_x(1_1^+,0)$	0.718	0.555	0.340	0.9
$E_x(0^+,1)$	1.740	1.202	1.259	
$E_x(1_2^+,0)$	2.154	2.379	1.216	
$E_x(2_1^+,0)$	3.587	3.721	2.775	3.9
$E_x(3_2^+,0)$	4.774	6.162	5.971	
$E_x(2_1^+,1)$	5.164	5.049	5.182	
$E_x(2_2^+,0)$	5.92	5.548	3.987	
$E_x(4^+,0)$	6.025	5.775	5.229	5.6
$E_x(2_2^+,1)$	7.478	7.776	7.491	

straints such as the long-range behavior from meson-exchange theory or another microscopic theory of the NN interaction. However, this does not mean that the JISP NN interactions are inconsistent with meson-theoretical forms of the NN interaction. On the contrary, it is well-known that the one-pion exchange (OPE) dominates the NN interaction in higher partial waves and the long-range behavior of NN interaction in lower partial waves. In this context, we showed in Ref. [15] that our scattering wave functions in higher partial waves are nearly indistinguishable from those of the Nijmegen-II OPE potential. Also, in lower partial waves, our wave functions are very close to those of Nijmegen-II at large distances and a small difference is seen only at higher energies. Finally, we introduced the PETs of JISP6 and JISP16 only in lower partial waves and only in a few lowest oscillator components of the potential with a large value of $\hbar\omega = 40$ MeV. As a result, PETs reshape the wave functions at short distances ($\lesssim 1$ fm). Thus, the JISP16 interaction appears to be consistent with the well-established OPE tail as embodied in the Nijmegen-II NN interaction.

We propose our JISP16 as a realistic NN interaction since it describes the two-body observables with high precision. In addition, it provides a reasonable and economic description of properties of many-body nuclear systems in the microscopic NCSM approach. Economy arises from the softness of the interaction represented in a separable oscillator form. Short distance phase-equivalent transformations adjust the off-shell properties successfully to reduce the roles of multi-nucleon interactions. The particular mechanism of this reduction is not clear at the present time. However, our results as well as the success of the approach of Ref. [21], clearly demonstrate that such a mechanism exists and should be studied in detail. We plan to study this with explicit NNN interactions.

This work was supported in part by the Russian Foundation of Basic Research grant No 05-02-17429, by US NSF grant No PHY-007-1027 and under the auspices of the US Department of Energy by the University of California, Lawrence Livermore National Laboratory under contract No. W-7405-Eng-48 and under US DOE grants DE-FG-02 87ER40371 and DE–AC02–76SF00515.

[1] P. Navrátil, J. P. Vary, B. R. Barrett, Phys. Rev. Lett. **84** (2000) 5728; Phys. Rev. C **62** (2000) 054311.
[2] R.Machleidt, Phys. Rev. C **63** (2001) 024001.
[3] R.B.Wiringa, V.G.J.Stoks, R.Schiavilla, Phys. Rev. C. **51** (1995) 38.
[4] V.G.J.Stoks, R.A.M.Klomp, C.P.F.Terheggen, J.J. de Swart, Phys. Rev. C **49** (1994) 2950.
[5] D.R.Entem, R.Machleidt, Phys. Rev. C. **68** (2003) 041001.
[6] E.Caurier, P. Navrátil, W.E.Ormand, J. P. Vary, Phys. Rev. C. **66** (2002) 024314.
[7] A.Nogga, H.Kamada, W.Glöckle, Phys. Rev. Lett. **85** (2000) 944.
[8] B.S.Pudliner, V.R.Pandharipande, J.Carlson, S.C.Pieper, R.B.Wiringa, Phys. Rev. C **56** (1997) 1720.
[9] S.C.Pieper, V.R.Pandharipande, R.B.Wiringa, J.Carlson, Phys. Rev. C **64** (2001) 014001.
[10] S.C.Pieper, K.Varga, R.B.Wiringa, Phys. Rev. C **66** (2002) 044310.
[11] S.C.Pieper, R.B.Wiringa, J.Carlson, Phys. Rev. C **70** (2004) 054325.
[12] P.Navrátil, W.E.Ormand, Phys. Rev. C **68** (2003) 034305.
[13] A.Nogga, P.Navrátil, B.R.Barrett, J.P.Vary, Phys. Rev. C **73** (2006) 064002.
[14] W.N.Polyzou, W.Glöckle, Few-Body Syst. **9** (1990) 97.
[15] A.M.Shirokov, A.I.Mazur, S.A.Zaytsev, J.P.Vary, T.A.Weber, Phys. Rev. C **70** (2004) 044005.
[16] R. Machleidt, private communication.
[17] Yu.A.Lurie, A.M.Shirokov, Izv. Ros. Akad. Nauk, Ser. Fiz. **61** (1997) 2121 [Bull. Rus. Acad. Sci., Phys. Ser. **61** (1997) 1665].
[18] Yu.A.Lurie, A.M.Shirokov, Ann. Phys. (NY) (2005) 96.
[19] A.M.Shirokov, J.P.Vary, A.I.Mazur, S.A.Zaytsev, T.A.Weber, Phys. Lett. B **621** (2005) 96.
[20] A.M.Shirokov, J.P.Vary, A.I.Mazur, T.A.Weber, Nucl-th/0512105 (2005).
[21] P. Doleschall and I. Borbély, Phys. Rev. C **62**, 054004 (2000).

THE PROCESS OF COULOMB DISSOCIATION OF WEAKLY BOUND RELATIVISTIC NUCLEI AND HYPERNUCLEI WITHIN THE TWO-CLUSTER MODEL

V.L.Lyuboshitz and V.V.Lyuboshitz†

Joint Institute for Nuclear Research,
141980 Dubna, Moscow region, Russia
† *E-mail: Valery.Lyuboshitz@jinr.ru*

1. Introduction

The process of dissociation of nuclei in the Coulomb field of fast charged particles has been discussed repeatedly (see, for example, [1-3]). In the recent years the interest to this electromagnetic process was revived in connection with the creation of beams of relativistic nuclei and the problem of identification of relativistic hypernuclei [4,5]. In the paper [6] the process of excitation and disintegration of relativistic nuclei and hypernuclei was investigated using the direct analogy with the problem of ionization and excitation of atoms at the propagation of relativistic charged particles through matter [7]. In this work (see also [8]) we will discuss the application of the results of [6] to the weakly bound deuteron-like systems consisting of two compact clusters (charged and neutral), the distance between which essentially exceeds the sizes of clusters themselves and the target nucleus radius R. The sharp increase of the cross-section of Coulomb dissociation at the decrease of binding energies allows one to determine experimentally these binding energies in the case of weakly bound nuclei and hypernuclei, studying their disintegration at ultrarelativistic velocities. We will investigate also the role of the finite sizes of the target nucleus.

2. Excitation and disintegration of relativistic nuclei in the Coulomb field of a point-like charge

It was shown in the paper [6] that the total cross-section of excitation and dissociation of a relativistic nucleus in the field of an immovable Coulomb centre with the charge Ze can be presented in the following form:

$$\sigma = \frac{4\pi(Z\alpha)^2}{v^2}\int\left(\mathbf{q}_\perp^2+\frac{\epsilon_{n0}}{\gamma^2v^2}\right)^{-2}\sum_{n\neq 0}\overline{\left|\langle n|\mathbf{j}|0\rangle\left(\frac{\mathbf{q}_\perp}{\epsilon_{n0}}-\frac{\mathbf{v}}{\gamma^2v^2}\right)\right|^2}\,d(\mathbf{q}_\perp^2)\,, \qquad (1)$$

Here $\hbar = c = 1$, $\alpha = e^2 = 1/137$ is the electromagnetic constant, $\mathbf{q}_\perp$ is the transverse momentum transferred to the nucleus, $v = |\mathbf{v}|$ is the velocity of the projectile nucleus in the rest frame of the Coulomb centre (i.e. in the *laboratory* frame), $\langle n|\mathbf{j}|0\rangle$ is the vector of the current of transition from the ground state $|0\rangle$ of the projectile nucleus to the excited state of the continuous or discrete spectrum $|n\rangle$, ϵ_{n0} is the excitation energy. The summation in Eq.(1) is performed over all quantum numbers of final states including spin and angular variables, and the upper bar denotes the averaging over polarizations of the initial ground state of the projectile nucleus, which is assumed to be unpolarized [1] .

[1] At the first glance, the formula (1) for the cross-section of Coulomb dissociation corresponds to the one-photon exchange, i.e. to the approximation $Z\alpha \ll 1$. However, the analysis shows that even at large

At small transverse and longitudinal momenta transferred to the projectile nucleus ($|\mathbf{q}_\perp| \ll 1/R_{\rm pr}$, $q_\parallel = \epsilon_{n0}/v \ll 1/R_{\rm pr}$, where $R_{\rm pr}$ is the radius of the projectile nucleus) the transition current is expressed directly through the matrix element of the dipole moment:

$$\langle n|\mathbf{j}|0\rangle = -i\epsilon_{n0}\langle n|\sum_p \mathbf{r}_p|0\rangle\,. \tag{2}$$

In Eq.(2) the summation is performed over the coordinates of all the protons in the projectile nucleus. In accordance with the rule of multiplication of matrices, taking into account the equality $\langle 0|\sum_p \mathbf{r}_p|0\rangle = 0$, that arises due to the space parity conservation, the following relation holds:

$$\sum_{n\neq 0} |\langle n|\sum_p \mathbf{r}_p|0\rangle|^2 = \langle 0|(\sum_p \mathbf{r}_p)^2|0\rangle\,. \tag{3}$$

Finally, dividing the integration range into two intervals corresponding to very small and larger $\mathbf{q}_\perp^2$, the following formula for the cross-section of the Coulomb dissociation emerges, after all transformations [6]:

$$\sigma = \frac{4\pi(Z\alpha)^2}{3v^2}\langle 0|\left(\sum_p \mathbf{r}_p\right)^2|0\rangle\left[\ln\left(\frac{\gamma^2 v^2}{\epsilon_{\rm bin}^2\langle 0|\left(\sum_p \mathbf{r}_p\right)^2|0\rangle}\right) - 2A + B - v^2\right]. \tag{4}$$

Here $\epsilon_{\rm bin}$ is the binding energy of the projectile nucleus, the constant

$$A = \ln\frac{\epsilon}{\epsilon_{\rm bin}} = \frac{\sum_{n\neq 0}\langle n|\sum_p \mathbf{r}_p|0\rangle|^2 \ln(\epsilon_{n0}/\epsilon_{\rm bin})}{\langle 0|\left(\sum_p \mathbf{r}_p\right)^2|0\rangle} \tag{5}$$

involves the dependence of the minimal momentum transfer, at the transition to excited states $|n\rangle$, upon the excitation energy $\epsilon_{n0} > \epsilon_{\rm bin}$ ($\epsilon = \epsilon_{\rm bin}e^A \ll 1/R_{\rm pr}$); the constant B describes the contribution of *comparatively large* transfers of transverse momentum. Calculations lead to the expressions:

$$B = -3\int_0^\infty \ln y \frac{d}{dy}\left(\frac{G(y)}{y}\right)dy\,, \qquad y = \mathbf{q}_\perp^2\langle 0|\left(\sum_p \mathbf{r}_p\right)^2|0\rangle\,. \tag{6}$$

Taking into account the completeness condition,

$$G(y) = \sum_{n\neq 0} |\langle n|\sum_p \exp(-i\mathbf{q}_\perp\mathbf{r}_p)|0\rangle|^2 =$$

$$= \langle 0|\,|\sum_p \exp(-i\mathbf{q}_\perp\mathbf{r}_p)|^2|0\rangle - |\langle 0|\sum_p \exp(-i\mathbf{q}_\perp\mathbf{r}_p)|0\rangle|^2\,. \tag{7}$$

At $y \ll 1$ the function $G(y) \approx y/3$, at $y \gg 1$ the function $G(y) \to z$, where z is the number of protons in the projectile nucleus. For the projectile nucleus with the unity charge we have: $G(y) = 1 - F^2(y)$, where

$$F(y) \equiv F(\mathbf{q}_\perp^2) = \langle 0|\exp(-i\mathbf{q}_\perp\mathbf{r}_p)|0\rangle$$

is the electromagnetic formfactor of the ground state.

---

values of Z, when $Z\alpha \sim 1$, the corrections to this formula still remain small. That is connected with the fact that the considered result can be justified in the framework of the impulse approach with the amplitude of the Coulomb scattering; in doing so, the exact amplitude of the Coulomb scattering in the region of small transferred momenta, where the *main* contribution into σ is provided, differs from the amplitude obtained within the Born approximation only by phase.

3. Contribution of finite sizes of the target nucleus

Taking into account that the target nucleus is not point-like, one should subtract the correction term ΔB from the constant B in Eq. (4):

$$\Delta B = 3\int_0^\infty \frac{G(y)(1-H(y))}{y^2}\,dy\,. \tag{8}$$

Here $G(y)$ is determined by Eq. (7) as before, and

$$H(y) = \frac{1}{Z^2}|\,\langle 0'|\sum_p \exp(-i\mathbf{q}_\perp \mathbf{r}'_p)\,|0'\rangle\,|^2 \tag{9}$$

is the square of the electromagnetic formfactor of the ground state of the target nucleus $|0'\rangle$; in doing so, $\mathbf{r}'_p$ is the coordinate of a proton in the target nucleus. For the uniform distribution of protons over the volume of the target nucleus

$$H(y) = 9\left(\frac{\sin x}{x^3} - \frac{\cos x}{x^2}\right)^2, \tag{10}$$

where

$$x = \sqrt{y}\frac{R_{tag}}{\sqrt{\langle 0|(\sum_p \mathbf{r}_p)^2|0\rangle}}, \tag{11}$$

R_{tag} is the radius of the target nucleus. It is clear that $H(0) = 1$.

Let us note that Eq. (8) describes the influence of finite sizes of the target nucleus on the process of Coulomb dissociation of the projectile nucleus *without* the excitation and breakup of the target nucleus. When the quantum state of the target nucleus is not fixed and transitions into all excited states are taken into account, the function $H(y)$ is replaced by the expression [6]

$$\widetilde{H}(y) = \frac{1}{Z^2}\langle 0'|\,|(\sum_p \exp(-i\mathbf{q}_\perp \mathbf{r}'_p)|^2\,|0'\rangle\,. \tag{9a}$$

It is easy to show that at the uniform distribution of the charge Z the functions $\widetilde{H}(y)$ and $H(y)$ are connected by the relation

$$1 - \widetilde{H}(y) = [1 - H(y)]\frac{Z-1}{Z}; \tag{9b}$$

thus, in the case of heavy target nuclei the corrections ΔB and $\widetilde{\Delta B} = [1 - (1/Z)]\Delta B$ practically coincide.

It is clear from Eq.(4) that in the case of relativistic nuclei with small binding energies the principal contribution into the cross-section of the Coulomb dissociation is conditioned by the logarithmic term being proportional to $\ln[\gamma^2 v^2/(\epsilon^2_{bin}\langle 0|(\sum_p \mathbf{r}_p)^2|0\rangle)]$. At ultrarelativistic energies of the projectile nucleus ($v \to 1$, $\gamma \gg 1$) the cross-section of the Coulomb dissociation of this nucleus, irrespective of the relation between radii of the projectile and target nuclei, has the structure:

$$\sigma = a\ln\gamma + b, \quad a = \frac{8\pi(Z\alpha)^2}{3}\langle 0|(\sum_p \mathbf{r}_p)^2|0\rangle\,. \tag{12}$$

4. Weakly bound systems. Two-cluster model

Now we will consider the Coulomb disintegration of the "friable", deuteron-like nuclei consisting of two clusters (charged and neutral), the average distance between which is significantly larger than the radius of the force action and the sizes of the clusters themselves. In this case the excited bound states are absent, and the normalized wave function of the ground state, corresponding to the zero orbital momentum, has the following form:

$$\phi_0(r) = \frac{1}{\sqrt{2\pi\rho}} \frac{\exp(-r/\rho)}{r}, \tag{13}$$

where $r = |\mathbf{r}|$ is the distance between the clusters,

$$\rho = \left(2\frac{m_1 m_2}{M}\epsilon_{\text{bin}}\right)^{-1/2}. \tag{14}$$

Here m_1 and m_2 are the masses of the charged and neutral clusters, respectively, $M = m_1 + m_2$ is the mass of the deuteron-like nucleus, $\epsilon_0 = (-\epsilon_{\text{bin}})$ is the energy of its bound state. In the given case the quantity $\langle 0|(\sum_p \mathbf{r}_p)^2|0\rangle$ can be explicitly determined:

$$\langle 0|(\sum_p \mathbf{r}_p)^2|0\rangle \approx 4\pi z^2 \left(\frac{m_2}{M}\right)^2 \int_0^\infty \phi_0^2(r) r^4 dr =$$

$$= z^2 \left(\frac{m_2}{M}\right)^2 \frac{\rho^2}{2} = \frac{1}{4} z^2 \frac{m_2}{m_1 M \epsilon_{\text{bin}}}, \tag{15}$$

where z is the number of protons in the charged cluster.

Using Eqs. (7) and (13), we obtain the analytical expression for the function $G(y)$:

$$G(y) = z^2 \left(1 - \left|\int \phi_0^2(r) \exp\left(-i\mathbf{q}_\perp \mathbf{r}\frac{m_2}{M}\right) d^3\mathbf{r}\right|^2\right) =$$

$$= z^2 \left(1 - \frac{2z^2}{y}\left[\arctan\left(\sqrt{\frac{y}{2z^2}}\right)\right]^2\right). \tag{16}$$

Here, according to Eq. (15),

$$y = \frac{1}{4}\mathbf{q}_\perp^2 z^2 \frac{m_2}{m_1 M \epsilon_{\text{bin}}}. \tag{17}$$

According to Eq.(14), at very small binding energies the effective radius ρ of the projectile nucleus considerably exceeds the target radius R ($\rho \gg R$). In so doing, we may, in the first approximation, take $H(y) = 1$, considering the target nucleus as a point-like Coulomb centre. Substituting Eq.(16) into Eq.(6), we obtain the following value for the constant B:

$$B = -3z^2 \int_0^\infty \ln y \frac{d}{dy}\left(\frac{1}{y} - \frac{2z^2}{y^2}\left[\arctan\left(\sqrt{\frac{y}{2z^2}}\right)\right]^2\right) dy = \ln 2z^2 + C, \tag{18}$$

where [6]

$$C = 6\int_0^\infty \ln u \left(\frac{1}{u^3} + \frac{\arctan u}{u^4(1+u^2)} - \frac{2}{u^5}(\arctan u)^2\right) \approx 0.316. \tag{19}$$

Meantime, taking into account that at small binding energies all excited states belong to the continuous spectrum, for a two-cluster system with the wave function $\phi_0(r)$ (see Eq. (13)) the constant A, determined by Eq. (5), is given by the integral:

$$A = \frac{16}{\pi}\int_0^\infty \frac{t^{3/2}}{(1+t)^4}\ln(1+t)dt \approx 1.218\,. \tag{20}$$

Finally, Eq. (4) leads to the following result for the total cross-section of Coulomb disintegration of the *weakly bound two-cluster nuclei*, taking into account also the correction term $\Delta B(Z)$ connected with the finite size of the target nucleus:

$$\sigma = \frac{\pi}{3}(Z\alpha)^2 z^2 \frac{m_2}{v^2 M m_1 \epsilon_{\rm bin}}\left[\ln\left(\frac{8\gamma^2 v^2 M m_1}{m_2 \epsilon_{\rm bin}}\right) - (2A - C) - v^2 - \Delta B(Z)\right]. \tag{21}$$

Here $2A - C \approx 2.12$; the quantity $\Delta B(Z)$ in Eq.(21) is determined according to Eq.(8).

It is well seen from Eq.(21) that in the limit of very small binding energies $\epsilon_{\rm bin}$ the cross-section of Coulomb disintegration increases inversely proportionally to $\epsilon_{\rm bin}$; in so doing, the logarithmic term inside the square brackets essentially exceeds the other ones. Measuring experimentally the Coulomb dissociation cross-section σ for weakly bound nuclei and hypernuclei, one can determine, in principle, the value of the binding energy $\epsilon_{\rm bin}$ for these nuclei.

5. Projectile nuclei with small binding energies: corrections due to the finite radius of the target nucleus

Due to the correction term $\Delta B(Z)$, the cross-section of Coulomb dissociation σ decreases as compared with the case of the point-like target ($\Delta\sigma < 0$). Substituting Eqs. (16) and (10) into Eq.(8), we obtain the quantity $\Delta B(Z)$ in the case of two-cluster projectile nuclei as the integral

$$\Delta B(Z) = \int_0^\infty \frac{s^2 - (\arctan s)^2}{s^5}\left[1 - 9\left(\frac{\sin x}{x^3} - \frac{\cos x}{x^2}\right)^2\right] ds\,, \tag{22}$$

where, in accordance with Eqs. (11) and (17),

$$s = \frac{1}{z}\sqrt{\frac{y}{2}}, \quad x = \chi s, \quad \chi = 2\frac{R_{\rm tag}}{\rho}\frac{M}{m_2} = 2\sqrt{2}\,R_{\rm tag}\sqrt{\frac{M m_1}{m_2}\epsilon_{\rm bin}}\,. \tag{23}$$

It should be emphasized that, owing to the dependence of the quantity ΔB upon the radius of the target nucleus ($R_{\rm tag} = 1.1\,A^{1/3}$, where A is the total number of nucleons in the nucleus; for heavy nuclei $R_{\rm tag} \approx 1.5\,Z^{1/3}$) the total cross-section of Coulomb dissociation σ gets a certain deviation from the pure dependence $\sim Z^2$. However, according to our calculations, the dependence of the total cross-section of Coulomb disintegration of weakly bound nuclei and hypernuclei upon Z *cannot be presented* as $\sim Z^{2-\delta}$ with a small *constant* δ, contrary to the statements in the papers [9,10].

The dependence of the correction term ΔB on the parameter χ is presented in Fig.1 and Fig.2. The corresponding correction to the Coulomb dissociation cross-section is

$$\Delta\sigma = -\frac{\pi}{3}(Z\alpha)^2 z^2 \frac{m_2}{v^2 M m_1 \epsilon_{\rm bin}}\Delta B(Z)\,, \tag{24}$$

As shown by the analysis, the quantity $\Delta B(Z)$ tends to zero with the decrease of the ratio R_{tag}/ρ as $\Delta B \sim \chi^2 \ln \chi$. Let us note that, for a given projectile nucleus, at charges of target nuclei in the interval $Z = 50 \div 100$ the dependence of ΔB on χ is almost linear ($\Delta B \approx b_{\text{pr}}\chi$). As a result, the quantities ΔB, $\Delta\sigma$ are proportional, respectively, to the factors $Z^{1/3}$, $Z^{7/3}$: $\Delta B \sim Z^{1/3}$, $\Delta\sigma \sim Z^{7/3}$. In so doing, the "effective" charge, determining the cross-section of the Coulomb dissociation, is $Z_{\text{eff}} = Z(1 - a_{\text{pr}}Z^{1/3})^{1/2}$. The coefficients b_{pr} and a_{pr} depend on the concrete projectile nucleus.

6. Calculations of the cross-section of Coulomb dissociation for the hypernuclei $^3H_\Lambda$ and $^6He_\Lambda$

1. Let us consider the process of Coulomb dissociation of the hypernucleus $^3H_\Lambda$ into the deuteron and the Λ-particle:

$$^3H_\Lambda + Z \to d + \Lambda + Z$$

($z = 1$, $M = M(^3H_\Lambda) = 2993.6$ MeV/c^2: $m_1 = m_d = 1878$ MeV/c^2; $m_2 = m_\Lambda = 1115.7$ MeV/c^2). According to the experimental data, the binding energy of the Λ hyperon in the hypernucleus $^3H_\Lambda$ is $\epsilon_{\text{bin}}^{(\Lambda)} = (0.01 \pm 0.07)$ MeV [11], or $\epsilon_{\text{bin}}^{(\Lambda)} = (0.15 \pm 0.07)$ MeV [12]. Taking $\gamma = 6$ and $\epsilon_{\text{bin}}^{(\Lambda)} \approx 0.08$ MeV, we obtain:

$$\chi \approx 0.43Z^{1/3}; \quad \Delta B \approx 0.63\chi; \quad Z_{\text{eff}}^2 = Z^2(1 - 0.02Z^{1/3}).$$

In particular, for the tin target ($Z = 50$):
$\sigma_0 = 1.88$ barn; $\Delta\sigma = -0.14$ barn; $\sigma = 1.74$ barn.
For the uranium target ($Z = 92$):
$\sigma_0 = 6.38$ barn; $\Delta\sigma = -0.58$ barn; $\sigma = 5.8$ barn.

Here σ_0 is the cross-section calculated for the point-like Coulomb centre, $\Delta\sigma$ is the correction to the cross-section due to the finite radius of the target nucleus.

2. Now let us consider the process of Coulomb dissociation of the hypernucleus $^6He_\Lambda$ into $^5He_\Lambda$ and the neutron:

$$^6He_\Lambda + Z \to {}^5He_\Lambda + n + Z$$

($z = 2$, $M = M(^6He_\Lambda) = 5.78$ GeV/c^2, $m_1 = m(^5He_\Lambda) = 4.84$ GeV/c^2, $m_2 = m_n = 939$ MeV/c^2).
The data on the binding energies of the Λ-hyperon in the hypernuclei $^6He_\Lambda$ and $^5He_\Lambda$ [12] and on the masses of their nucleon bases (ordinary nuclei ^5He and ^4He [13]) lead to the following estimation of the binding energy of the *neutron* in the hypernucleus $^6He_\Lambda$: $\epsilon_{\text{bin}}^{(n)} = (0.23 \pm 0.13)$ MeV. Taking $\gamma = 6$ and $\epsilon_{\text{bin}}^{(n)} \approx 0.15$ MeV, we have:

$$\chi \approx 1.43Z^{1/3}; \quad \Delta B \approx 0.5\chi: \quad Z_{\text{eff}}^2 \approx Z^2(1 - 0.05Z^{1/3}).$$

In the case of the tin target ($Z = 50$): $\sigma_0 = 0.74$ barn; $\Delta\sigma = -0.14$ barn; $\sigma = 0.6$ barn.
For the uranium target ($Z = 92$): $\sigma_0 = 2.50$ barn; $\Delta\sigma = -0.54$ barn; $\sigma = 1.96$ barn.

So, for the considered cases (especially – for $^6He_\Lambda$) the correction $\Delta\sigma$ to the Coulomb dissociation cross-section, emerging due to the finite size of the target, proves to be rather essential.

7. Summary

1. The process of Coulomb dissociation of weakly bound relativistic nuclei and hypernuclei has been studied within the two-cluster "deuteron-like" model. Explicit expressions for the total effective cross-section of Coulomb disintegration, taking into account the corrections conditioned by the finite size of the target nucleus, are obtained.

2. The experimental measurement of the Coulomb dissociation cross-section for weakly bound nuclei and hypernuclei enables one to determine the value of the binding energy for these systems.

This work is supported by Russian Foundation for Basic Research
(Grant No. 05-02-16674) and by INTAS (Grant No. 03-51-6417) .

REFERENCES

1. A.I. Akhiezer and I.Ya.Pomeranchuk, *Some topics of nuclear theory* (in Russian) (Gostekhteorizdat, Moscow, 1950), §13
2. C.I. Mullin and E. Guth, Phys. Rev. **82**, 141 (1951)
3. S.T. Butler and C.A. Pirson, Nuovo cimento **19**, 1266 (1961)
4. S.A. Avramenko et al., Pis'ma v Zh. Exp. Teor. Fiz. (JETP Lett.) **48**, 474 (1988)
5. S.A. Avramenko et al., Nucl. Phys. **A585**, 91c (1995)
6. V.L. Lyuboshitz, Yad. Fiz. **51**, 1013 (1990) [Sov. Jour. Nucl. Phys. **51**, 648 (1990)]
7. V.B. Berestetsky, E.M. Lifshitz and L.P. Pitaevsky, *Kvantovaya elektrodinamika (Quantum Electrodynamics)* (in Russian) (Nauka, Moscow, 1980), §82
8. V.L. Lyuboshitz and V.V. Lyuboshitz, Proceedings of XVIII International Workshop on High Energy Physics and Quantum Field Theory (QFTHEP'2004) (Max Press, Moscow, 2005), p.425
9. M.V. Evlanov, A.M. Sokolov and V.K. Tartakovsky, Yad. Fiz. **60**, 444 (1997)
10. M.V. Evlanov et al., Nucl. Phys. **A632**, 624 (1998)
11. G. Bohm et al., Nucl. Phys. **B4**, 412 (1968)
12. M. Juric' et al., Nucl. Phys. **B52**, 1 (1973)
13. H.A. Bethe and Ph. Morrison, *Elementary nuclear theory* (John Wiley & Sons, Inc., New York - London, 1956), Appendix

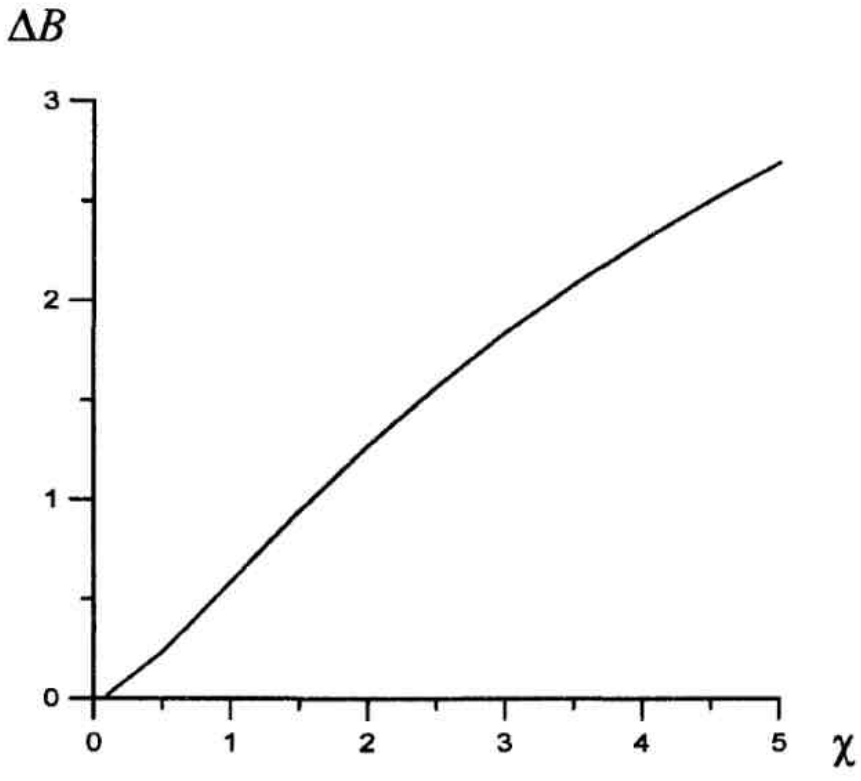

Fig. 1. Dependence of the correction term ΔB (22) upon the parameter χ (23) .

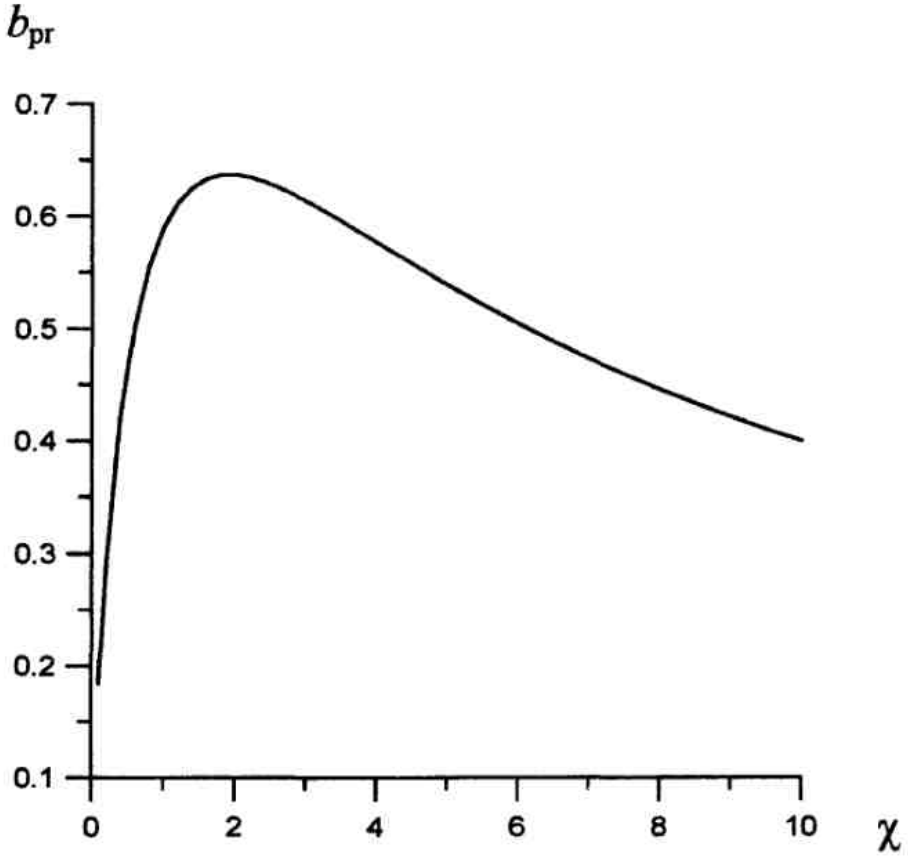

Fig. 2. Dependence of the coefficient $b_{pr} = \Delta B / \chi$ upon the parameter χ .

Two–photon exchange and elastic scattering of electrons/positrons on the proton.

(Proposal for the experiment at VEPP-3.)

J. Arrington[a], V.F. Dmitriev[b], R.J. Holt[a], D.M. Nikolenko[b], I.A. Rachek[b], Yu.V.Shestakov[b], V.N. Stibunov[c], D.K. Toporkov[b], H.de Vries[d].

[a] *ANL, Argonne, IL 60439-4843, USA,*
[b] *BINP, 630090 Novosibirsk, Russia,*
[c] *NPI at TPU, 634050 Tomsk, Russia,*
[d] *NIKHEF, P.O. Box 41882, 1009 DB Amsterdam, The Netherlands*

1 Introduction.

The study of the electromagnetic form factors of the proton – important properties of this fundamental object – allows increased understanding of the nature of the proton, as well as the nature of interactions of its constituents - the quarks. Until recently, the electric ($G_E(Q^2)$) and magnetic ($G_M(Q^2)$) form factors, which describe the distribution of charge and current inside the proton, were determined by the separation of longitudinal and transversal contributions to the electron–proton scattering cross section. Differential cross section of the elastic scattering in one–photon approximation, assuming $P-$ and $T-$invariance, can be written [1] as:

$$\frac{d\sigma}{d\Omega} = \sigma_{Mott}\left[\frac{G_E^2+\tau G_M^2}{1+\tau} + 2\tau G_M^2 \tan^2\frac{\theta}{2}\right],$$

where σ_{Mott} is the Mott cross section, θ is electron scattering angle, Q is transfered four-momentum, and $\tau = Q^2/4M_p^2$. Introducing the longitudinal virtual photon polarization, $\epsilon = (1+2(1+\tau)\tan^2(\theta/2))^{-1}$, one can re-write the above formula as:

$$\frac{d\sigma}{d\Omega} = \frac{\tau\sigma_{Mott}}{\epsilon(1+\tau)}\left[G_M^2 + \frac{\epsilon}{\tau}G_E^2\right] .$$

The two form factors can be disentangled by measuring scattering cross sections at different initial electron energies and scattering angles while keeping momentum transfer (Q) the same. Such a procedure is called Rosenbluth separation or Rosenbluth technique. As is seen from the last formula, the contribution of the electric form factor to the cross section drops down with increasing Q^2. Therefore it becomes difficult to measure G_E using the Rosenbluth method at high Q^2.

In the mid-nineties, it became possible to use polarization transfer experiments to study nucleon electromagnetic form factors. Through such measurements contributions

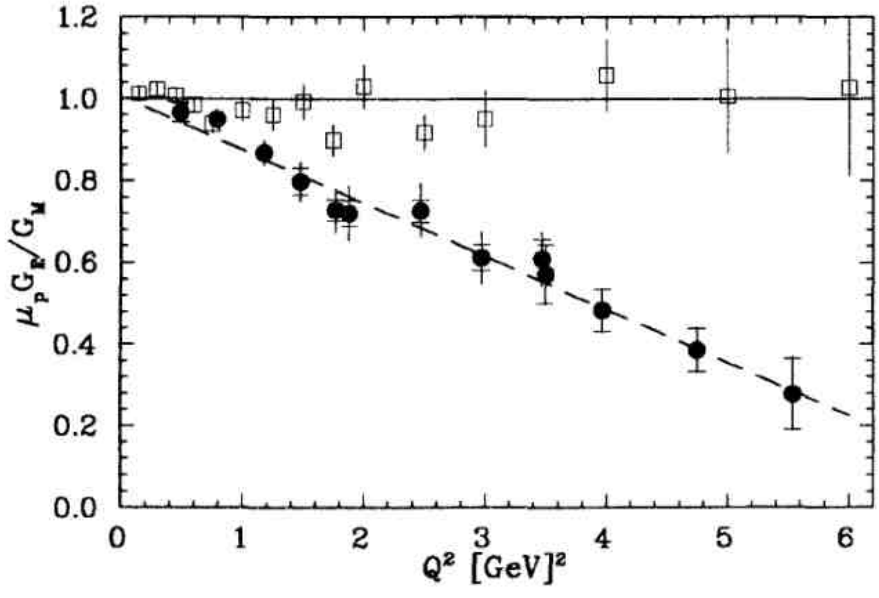

Figure 1: From [3]: comparison of form factors ratio, obtained by Rosenbluth technique (hollow squares) with data of polarized measurements (full circles).

of interference terms into the scattering cross-section become accessible, hence the contribution of the small form factors can be enhanced resulting in increased accuracy of their determination. A series of precise measurements of the ratio of proton form factors $G_E(Q^2)/G_M(Q^2)$ for a wide range of transfered momentum was carried out recently at TJNAF [2]. In these experiments a ratio of transverse (P_t) and longitudinal (P_l) polarization of recoil protons from elastic scattering of longitudinally polarized electrons on an unpolarized hydrogen target was measured. In such a case the ratio of proton form factors can be extracted directly from the ratio of P_t and P_l:

$$\frac{G_E}{G_M} = -\frac{P_t}{P_l}\frac{(E+E')}{2M_p}\tan\frac{\theta}{2} ,$$

where E, E' are the electron energy before and after scattering and M_p is the proton mass. These polarization experiments yielded unexpected results, indicating that the ratio $\mu G_E/G_M$ depends strongly on Q^2, while before it had been assumed to be nearly constant, close to unity (see Fig. 1). A thorough reanalysis of the available unpolarized experimental data [3], as well as new precise unpolarized measurements done at TJNAF [4] have clearly shown that these two methods deliver contradictory results.

2 Two–photon exchange.

A number of authors [5] - [10] argue that the possible origin of these discrepancies is the failure of the one–photon approximation to precisely describe the results of unpolarized experiments. Indeed, with increasing Q^2 the cross section of elastic scattering and especially the contribution of electric form factor drops down substantially. In such a case the contribution of two–photon exchange (TPE), which depends weakly on Q^2, can become considerable. Thus it was shown in [8] that allowing for the TPE in Rosenbluth technique,

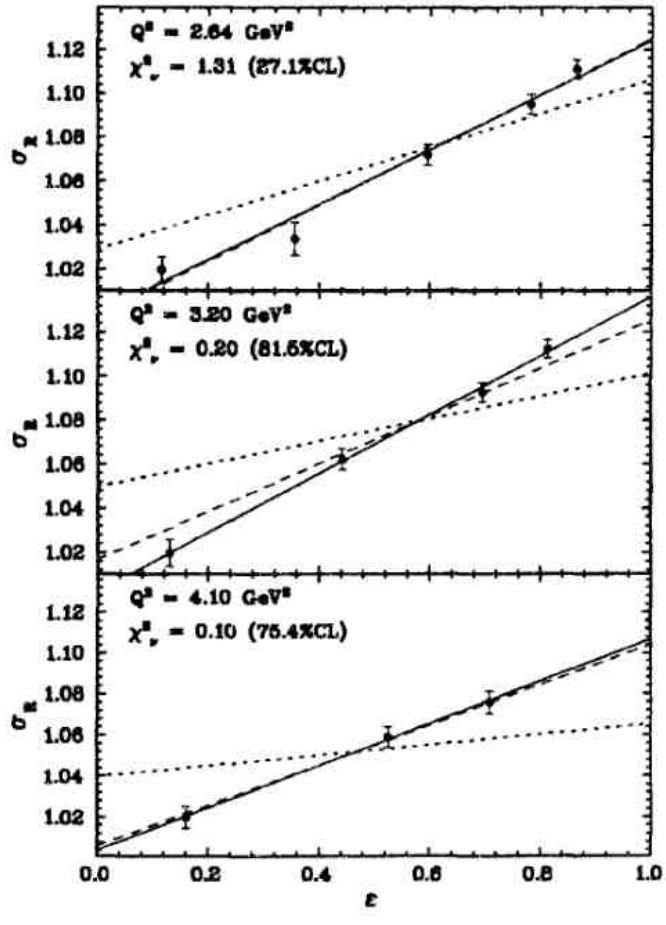

Figure 2: From [4]: comparison of the results of a new measurement of the proton form factors ("reduced" cross section $\sigma_R \propto \tau G_M^2 + \epsilon G_E^2$ is presented, scaled to yield $\sigma_R \approx 1$ at $\varepsilon = 0$) obtained by the Rosenbluth technique (points – data, solid lines – best linear fit) with the world "unpolarized" data (dashed lines are linear fit to these data) and with the "polarized" results (dotted lines show best liner fit to these data). One can see that old and new "unpolarized" data are compatible, while they both contradict the polarization measurements.

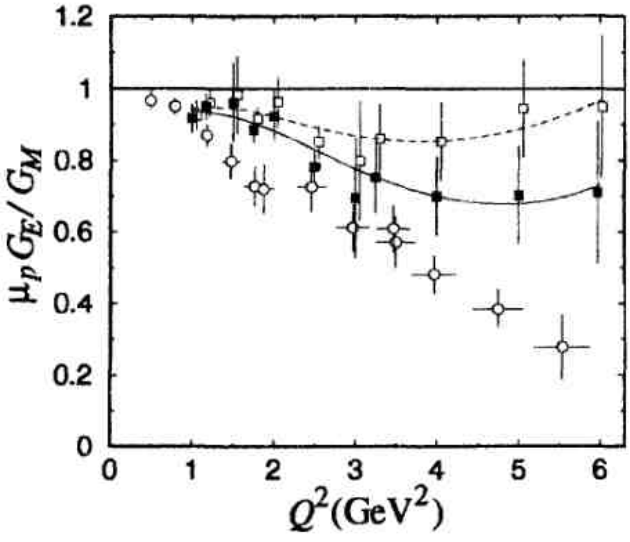

Figure 3: From [8]: The ratio of proton form factors obtained by the Rosenbluth technique: before (hollow squares) and after (full squares) the TPE corrections, and the data of polarized measurements (hollow circles).

using a simplified model (which does not include nucleon excitations in the intermediate state), leads to a substantial change of form factors ratio, despite the small contribution of the TPE to the cross section (Fig. 3). This results from a strong dependence of the TPE contribution on electron scattering angle for a fixed Q^2 [8].

Complications arising in the calculation of the TPE corrections are connected with difficulties in accounting for proton excitations in the intermediate state. The intermediate state contributions have been treated in a recent calculation at the quark-parton level, using generalized parton distributions to [10].

The Born amplitude is proportional to the lepton charge, e_l, while the TPE amplitude is proportional to e_l^2. The Born cross section is proportional to e_l^2, while the interference term to the cross section goes like e_l^3. Hence the interference term, which is the dominant part of the TPE contribution (since the TPE amplitude is small compared to the Born amplitude) changes sign with respect to the Born cross section and can therefore be determined by comparing electron–proton and positron–proton scattering.

Attempts to measure the TPE contribution were made in the 1960s, but either the accuracy of the measurements was insufficient: $\delta R/R \sim 5\%$, where $R = \sigma(e^+)/\sigma(e^-)$, or scattering angles were too small and therefore $\epsilon \approx 1$ – where most theories predict $R \approx 1$, see Fig.4.

3 Experiment at VEPP–3.

We propose to perform a measurement of R at the VEPP–3 storage ring at an energy of electron/positron beams of 1.6 GeV and at electron/positron scattering angles approximately 25^o, 65^o (corresponding to $\epsilon \approx 0.90$, 0.45 and $Q^2 \approx 0.3$, 1.5 GeV^2/c^2)

There are several necessary preconditions for a successful realization of this experiment:

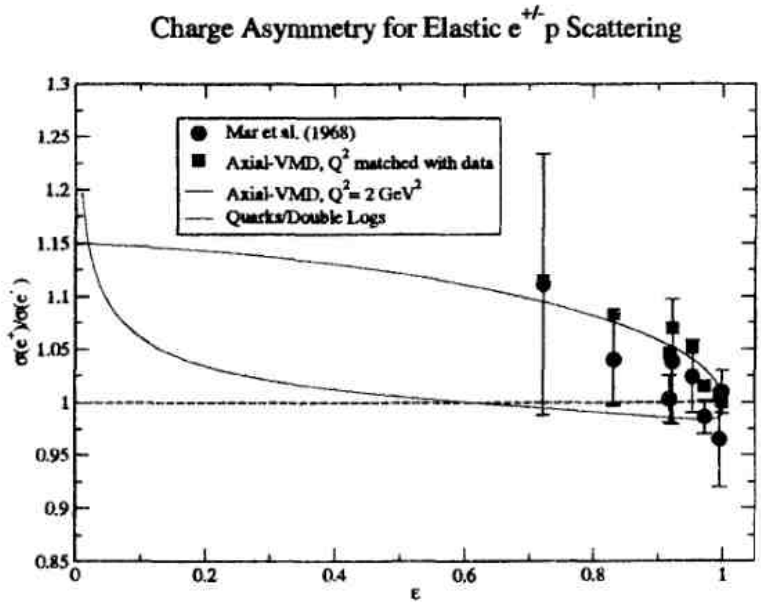

Figure 4: From [12]: theoretical predictions from [9] (square points and curves) and experimental data from [11] (circles) for the ratio $R = \sigma(e^+)/\sigma(e^-)$ as a function of ϵ.

- the injector delivering positrons at a rate 50 μA/s (measured in VEPP–3 current);
- the storage ring where electrons or positrons move in the same direction;
- the experimental straight section with quadrupole lenses (to compress the beam) and with an internal gas target;
- mean experimental luminosity (defined by positrons) can be rather high: $L = I \cdot t = 0.009 \cdot 6 \cdot 10^{18} \cdot 10^{15} = 5 \cdot 10^{31}$, here t – target thickness, I – positron current averaged over a working cycle which includes storage phase, energy ramping phase, production phase and return-to-storage-mode phase. Storage phase for electrons is much less, as a result the cycle length is about a factor 1.6 smaller than that for positrons and the luminosity is larger by the same factor.
- the equipment used at the previous experiment – particle detectors, data acquisition system, detector and target infrastructure, readout and slow control software as well as a large experience of conducting internal target experiments at VEPP–3 provides with a good basis for developing new target and detector and performing the measurements.

4 Target.

In previous experiments at VEPP–3 a polarized deuterium target was used. The luminosity was restricted by maximum achievable polarized target thickness of $t \approx 10^{14}$at/cm^2, while electron beam current was limited (by large current effects) at a level of $I_{max} \approx 140$ mA. Mean luminosity was $L \approx 5 \cdot 10^{31}$.

In the new target we are going to utilize a similar storage cell: having elliptical cross section 13×24 mm, length 400 mm, cooled by liquid nitrogen. Hydrogen flux directed to

the cell is going to be restricted at a level of $\sim 10^{18}$ at/sec, providing a target thickness of $\sim 10^{15}$at/cm^2. Note that gas density profile along the cell has a triangle shape with a maximum $\sim 5 \times 10^{13}$at/cm^3 in the cell center and a base equal to the cell length (40 cm). With these target parameters two upper limits are reached simultaneously: first, with a higher gas flux the available vacuum pumps might not be able to maintain a required vacuum in the storage ring, second, for a thicker target the detector singles rates might become too high.

Let us also note that e.g. doubling the target thickness would result in only 30% increase of an average luminosity, because it is the time of positrons storing that takes up the main part of experimental time–cycle.

Gas flux to the storage ring vacuum chamber can be made about factor two lower (while retaining target thickness the same) by decreasing the temperature of the cell (down to $\sim 20^{\circ}K$). This can be done using an appropriate cooler, but at present it is not available and has to be purchased.

A storage cell placed in the VEPP–3 ring would prevent beam injection into VEPP–4 and this may become a serious obstacle. That is why we are going to modify the design of the coupling between the cell and the straight section in order to be able to remove easily the cell from the aperture of VEPP–3 during VEPP–4 operations.

Optimal relation between beam storage time and data taking time in a timing cycle for positrons is shown in Table 1. Positron beam current will be changing from 50 mA down to 9 mA during the data taking phase. To decrease the systematic errors we are going to keep electron beam in the same range. But since the timing cycle for electrons is substantially shorter we will run two "electron" cycles for each "positron" cycle.

Table 1: Timing scheme for positron/electron working cycles (in seconds).

phase	positrons	electrons
storage	1630	10
energy ramping	300	300
production	1920	1920
return to storage mode	300	300
sum for a single beam cycle	4150	2530
duration of a total cycle, which includes 3 beam cycles: $\{e^-/e^+/e^-\}$	9190	

5 Detector, event rate.

As was mentioned above, the detector for the measurement of (e^+p) and (e^-p) elastic scattering will be build on the basis of the detector used in the experiment that measured the deuteron form factors. Scattered electron and recoil proton will be detected in coincidence, which allows us to use kinematical correlations between their emission angles and energies, characteristic of two–body reactions. This is important for separation of the events from the process under study from those of various background processes.

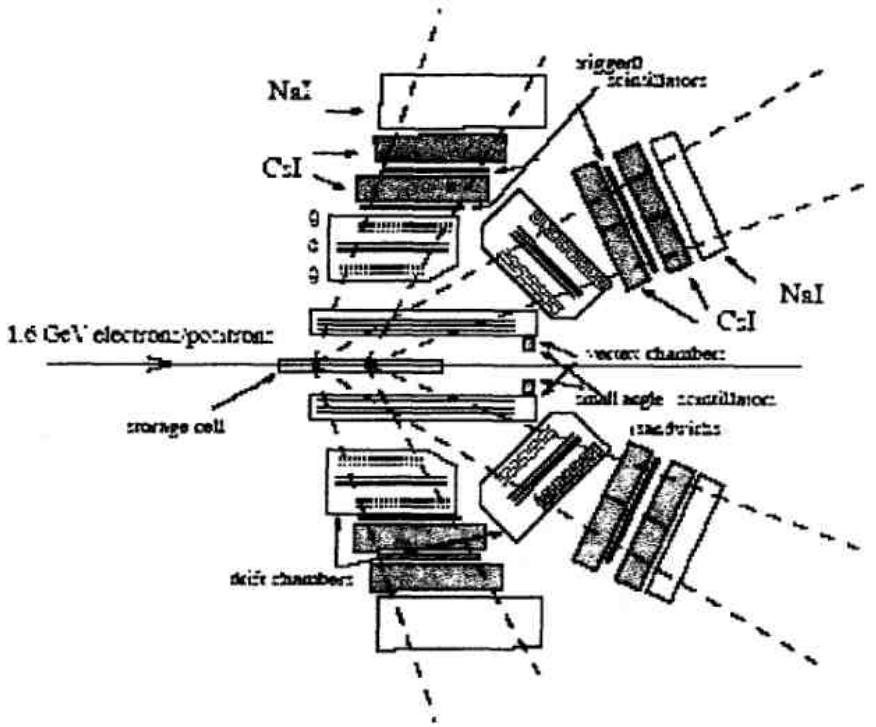

Figure 5: Schematic side view of the particle detection system.

The detector (Fig. 5) is comprised of two identical systems placed symmetrically with respect to the storage ring median plane. Azimuthal angle acceptance of each system is 60^o. Total ϕ–acceptance is $\Delta\phi = 120^o$, because particles can be detected either by upper or by lower system. Regarding the polar angles – electrons/positrons scattered at angles close to 12^o, 25^o, 65^o will be detected. These three θ–ranges are denoted later on as Small Angles (SA), Medium Angles (MA) and Large Angles (LA).

Electrons/positrons scattered at SA are detected by small scintillators (sandwiches). Recoil protons in this case are detected by LA–arms, where their trajectories and energies are measured. Here only part of extended target is "visible" to the detectors. Scattering at SA will be used as a luminosity monitor — as it was pointed out at small Q^2 and θ_e the ratio R should be very close to unity, i.e. $\sigma(e^+) \approx \sigma(e^-)$. Application of two detector systems (upper and lower) not only increases the detecting solid angle but also allows to suppress systematic errors related to instability of the electron/positron beam position.

When electrons/positrons scatter to MA–arms, protons hit LA–arm detectors. For these events tracks and energies are measured for both particles. The experience obtained at previous experiments allows us to be sure that the information gathered by such detectors will be quite sufficient for a reliable event identification for scattering both at SA and at MA.

In addition, we plan to equip the LA–arms with electromagnetic calorimeters (there were no calorimeters here earlier). This is needed in order to measure the energy of electrons/positrons scattered at those angles, to separate the elastic electron/positron from pions or inelastic events. Note that in this case recoil protons are detected by MA–arm detectors. A minimal configuration of the calorimeters that can be assembled using CsI and NaI crystals, which we have at our disposal, is shown in Fig. 5.

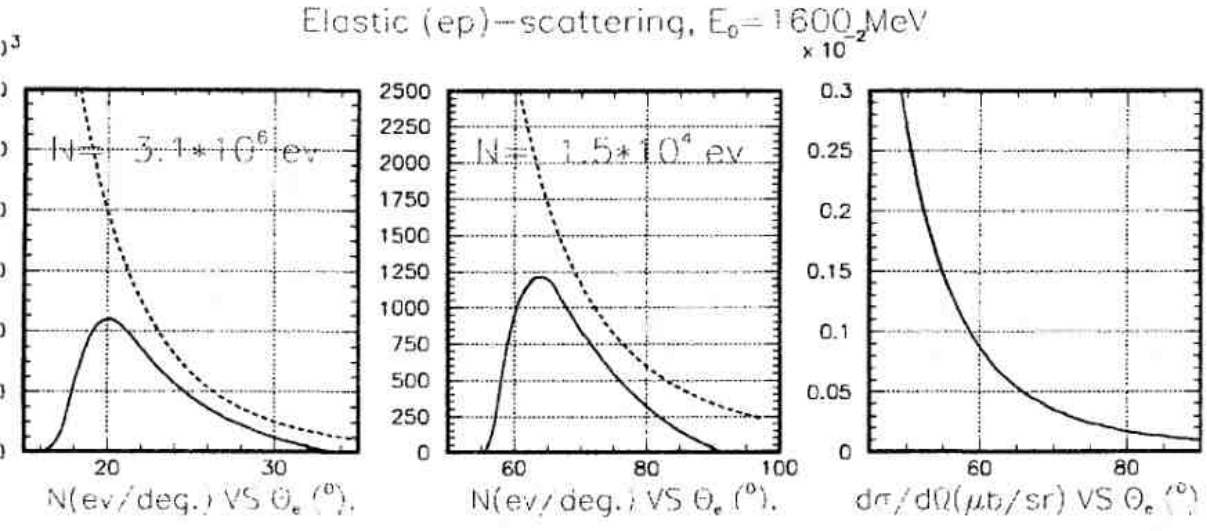

Figure 6: Left and middle panels: solid lines show number of events (in a $\Delta\theta_e = 1^o$ bins) detected by *MA*–arm (left panel) and by *LA*–arm (middle panel) as a function of θ_e for a luminosity integral $\int Ldt = 10^{15}\text{at/cm}^2 \cdot 12\text{kQ}$ (or during 30 days run). Total number of events detected by *MA*–arm is $3.1 \cdot 10^6$ and by *LA*–arm is $1.5 \cdot 10^4$. Dashed curves demonstrate the event counts that would be in case of a point–like target. The right panel shows differential cross section of the elastic (ep)–scattering.

Cross section of (e^+p),(e^-p) elastic scattering at *LA* is two orders of magnitude lower than that for *MA*. However, as it shown below, selection of the elastic scattering events can be done in this case as well, by measuring trajectories of both particles and electron energy at an accuracy provided by the calorimeters ($\sigma \approx 50$ MeV, see Fig. 7).

6 Background estimation.

As it was mentioned above, difficulties in event selection may come out only for scattering at *LA*, where the cross section of elastic scattering becomes small ($\sim 0.2 - 1$ nb/sr, see Fig. 6). Here we present an estimation of a background level from the processes which seem to be the most dangerous, namely electro- and photoproduction of pions.

Differential cross section of pion electroproduction can be written as [13]:

$$\frac{d\sigma}{dE'\, d\Omega_e\, d\Omega_\pi} = \Gamma \frac{d\sigma}{d\Omega_\pi} ,$$

where Γ is a flux of virtual photons, defined as:

$$\Gamma = \frac{\alpha}{2\pi^2} \frac{E'}{E} \frac{W^2 - M_p^2}{2M_p Q^2} \frac{1}{1-\epsilon} .$$

Here W is an invariant mass of the hadron system.

From Fig 8 one can see that after applying even a loose cut on scattered electron energy (e.g. $E' > 400$ MeV) a total flux of virtual photons would not exceed 10^{-5} of a

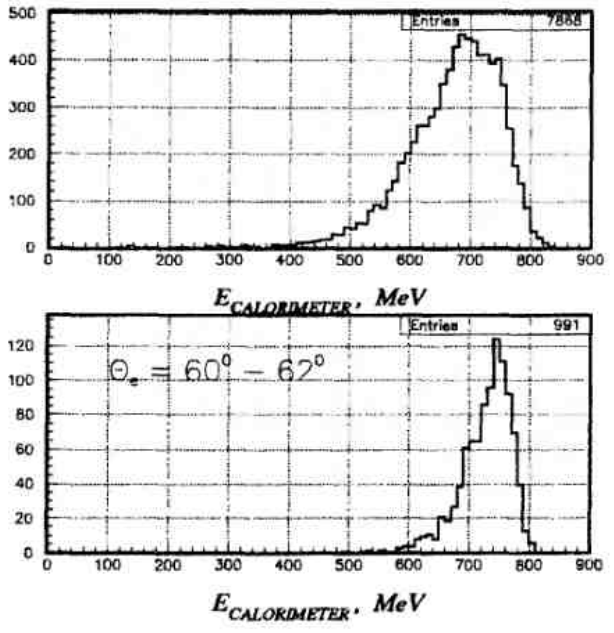

Figure 7: Electron energy spectra measured by LA–arm calorimeter (Monte Carlo simulation) for events with the proton detected by MA–arm. Upper histogram – all events, lower histogram – for quasi-monochromatic electrons ($\theta_e = 60 - 62^o$).

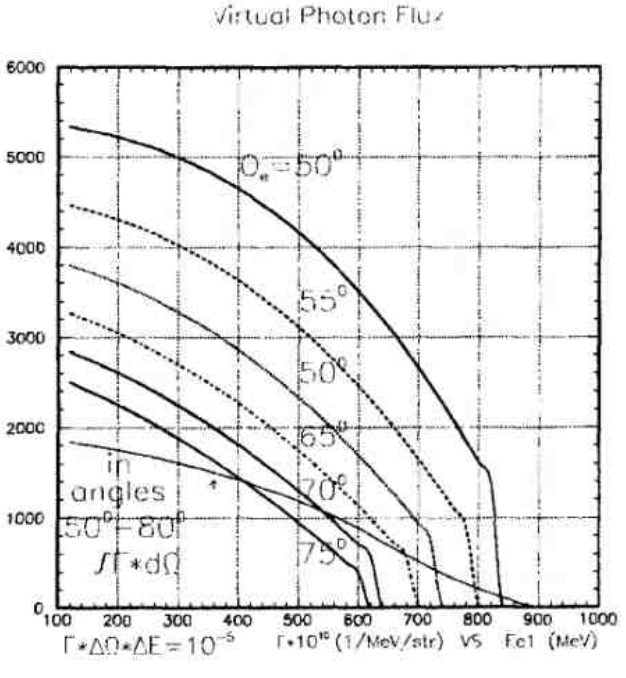

Figure 8: Virtual photon flux Γ as a function of energy of scattered electrons for various θ_e (specified in the figure). A gently sloped curve shows an integral of Γ over solid angle of the LA–arm.

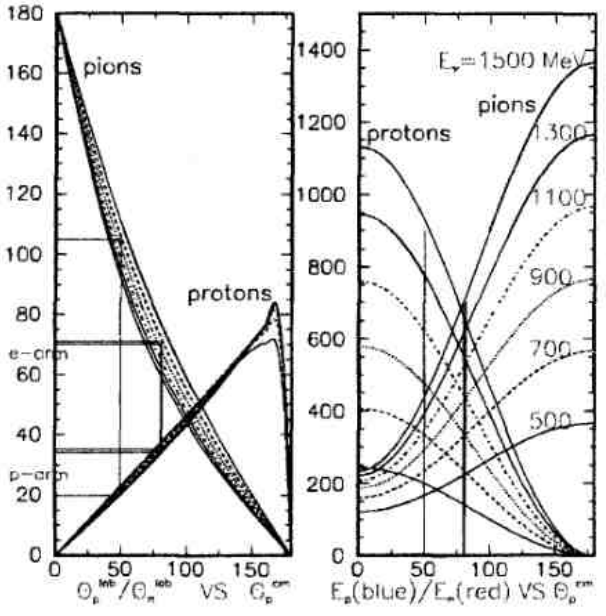

Figure 9: Pion production kinematics. Left panel: emission angles of protons (blue curves) and pions (red curves) in Lab system as a function of proton C.M.–angle for various photon energies (legend for curves is shown in the right panel). Right panel: kinetic energy of protons (blue curves) and pions (red curves) in Lab system as a function of proton C.M.–angle for various photon energies.

number of electrons deposited on the target. The cross section $d\sigma/d\Omega_\pi$ of the reaction $ep \to e\pi^+ n$ is estimated to be $\approx 10\mu b/sr$, using data from [14, 15]. The cross section of the reaction $ep \to e\pi^o p$ is about the same. Therefore $\Gamma \cdot d\sigma/d\Omega_\pi$ should not exceed $0.1nb/sr$. This is close to elastic scattering cross section, but applying cuts on the angular correlations specific to elastic scattering allows one to further decrease this background by two orders of magnitude.

Electron scattering at forward angle with pion production is usually considered as a process of pion photoproduction by equivalent photons. In this case there is only one charged particle (besides the undetected electron), therefore in order to get hits in tracking systems of both arms (from e.g $\gamma p \to \pi^o p$ reaction) it is required that a gamma-quantum from pion decay to be converted to a charged particle in materials on its way to wire chambers. Probability of such conversion (K_{con}) is small, estimated as $\sim 10^{-2}$.

As one can see in Fig. 9, when a proton hits the MA–arm a π^o is emitted in the direction of LA–arm and can be detected, providing the conversion occurred. A number of equivalent photons emitted by a beam's electron (in energy intervals ΔE_γ ± 100 MeV) is shown in Table 2 (second column) for various photon energies (first column). Cross section of pion photoproduction does not exceed $5\mu b/sr$ [16]. Taking into account small K_{con} one gets an event rate about the same as for elastic scattering (the last column in Table 2). However here again the background can be greatly reduced by applying angular correlation cuts.

It is also worth noting that a requirement to have a large energy deposition in LA–arm calorimeter is important to avoid confusing large–angle and medium–angle scattering

events.

Table 2: Estimation of neutral pion photoproduction background.

E_γ	N_γ^{eq}	K_{con}	$d\sigma_\pi/d\Omega$ (μb/sr)	$N_\gamma^{eq} \cdot K_\gamma^{con} \cdot d\sigma/d\Omega$ (nb/sr)
500	0.0058	0.01	5	0.29
700	0.0034	0.01	5	0.17
900	0.0022	0.01	5	0.11
1100	0.0016	0.01	5	0.08
1300	0.0012	0.01	5	0.06
1500	0.0010	0.01	5	0.05

7 Experiment duration. Estimation of accuracy.

The experiment is divided into three phases, each requiring either VEPP–3 hall access or VEPP–3 operation:

1. during shutdown of the VEPP–3 the following should be completed: installation of the straight section with gas target, obtaining the vacuum, commissioning the target, assembling and commissioning detectors, data acquisition system and target control system ;

2. beam tuning: finding/restoring regimes of positron/electrons beam operation at VEPP–3, minimizing background — 7 days in total;

3. data taking run: to obtain high statistical accuracy in measuring R (see Table 3) it is required approximately 300 full time-cycles (as defined in Table 1) corresponding to $\approx$30 days of continuous operation of the storage ring.

Expected statistical accuracy in measuring R is shown in Table 3. Below several possible sources of systematic errors are listed.

- Unequal beam energy for electrons and positrons.
  It is assumed that this difference can be made 1 MeV or less. Then $\Delta R/R$ for three angle intervals will not exceed 0.1%, 0.2%, 0.2%. Using *SA*–arm data for normalization one can reduce this error by factor two.

- Different beam positions for electrons and positrons.
  Sensitivity of $\Delta R/R$ is estimated as 5.6%/mm, 1.4%/mm, 0.9%/mm for *SA*-, *MA*-, *LA*-scattering respectively. Beam positions will be monitored by current pick–up sensors with accuracy $\sim$ 0.1mm for relative position of electron/positron beams. Moreover already existing system for beam position stabilization can keep the beams orbit near the experimental straight section sable with same accuracy. Besides, one can see that *SA*–arms are very sensitive to the beam position, hence their count rates can be served as a beam position monitor. Finally since we have symmetrical arm pairs therefore by averaging count rates of up-arm and down-arm this effect can be suppressed in first order. Here an accuracy of $\Delta R/R \sim 0.1\%$ can be achieved.

- Time instability of detectors efficiency.
  This effect (like the previous one) is suppressed in first order because data collection with electron and positron beams will be alternated regularly. We expect that detectors efficiency would not change by more than $\sim 1\%$ during one time cycle. Assuming that this instability has a random character, one would get a reduction of this error by averaging over many cycles. For 300 time-cycles the reduction will be $1/\sqrt{300}$, i.e. by over an order of magnitude.

- Drift of the target thickness in time. Special efforts will be devoted to achieve a stable gas flow during the whole experiment. And again using data rate of SA–arms as a monitor, and averaging over many cycles one should get a contribution of this effect to the systematic error of R to be 0.1% or less.

Combining the above uncertainties, the total systematic error for the largest Q^2 bin is expected to be constrained below $\Delta R/R \sim 0.3\%$. Therefore the measurement accuracy will be defined by statistical error.

Table 3: Expected accuracy of the measurement of the ratio $R = \sigma(e^+) \ / \ \sigma(e^-)$. It is assumed that $N_- = 2N_+$.

θ_e (°)	Q^2 (GeV^2)	ϵ	N_+ (events)	$\Delta R/R$ % (stat)	$\Delta R/R$ % (sys)
10–12	0.08–0.11	0.98–0.98	$8.7 \cdot 10^6$	—	0.30
19–27	0.26–0.47	0.94–0.88	$3.1 \cdot 10^6$	0.07	0.30
60–80	1.40–1.76	0.51–0.32	$1.5 \cdot 10^4$	1.00	0.30

Calculations of the TPE effects indicate that the Q^2-dependence of the TPE correction is weak at large Q^2 values. Analyses of the discrepancy between Rosenbluth and polarization transfer form factors also indicate a weak Q^2-dependence, and a change in the ϵ-dependence of 5–7% for Q^2 >1–2 GeV^2 [3, 6, 17]. Figure 10 shows the projected ratio and uncertainty, assuming an ϵ-dependence of roughly 5% in the electron cross section, yielding a slope of ≈10% in the ratio of positron to electron yield.

This work is supported in part by the U.S. Department of Energy, Office of Nuclear Physics, under contract W-31-109-ENG-38

References

[1] M. N. Rosenbluth, Phys. Rev. **79** (1950) 615.

[2] M. K. Jones *et al.*, Phys. Rev. Lett. **84** (2000) 1398; O. Gayou *et al.*, Phys. Rev. Lett. **88** (2002) 092301.

[3] J. Arrington, Phys. Rev. **C 68**, (2003) 034325 and arXiv:nucl-ex/0305009.

[4] J. Arrington, "New measurement of G_E/G_M of the proton," International Workshop EEP03, 14-17 October 2003, Grenoble, France, arXiv:nucl-ex/0312017.

[5] M. P. Rekalo and E. Tomasi-Gustafsson, arXiv:nucl-th/0312030.

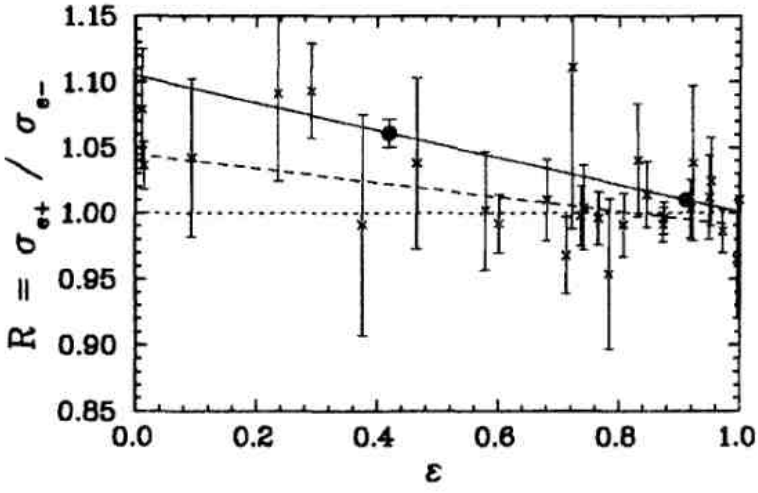

Figure 10: Projected uncertainty (combined statistical and systematic) for the proposed measurement (blue circles), compared to previous data (red "x" - Ref. [7] and refs. therein). Note that the previous measurements have an average Q^2 value of approximately 0.5 GeV^2 for the data below $\epsilon = 0.5$, and thus should have a smaller TPE contribution than the proposed measurement. The dashed line is a linear fit to the combined worlds data on R, and yields a slope of $-(5.7 \pm 1.8)\%$

[6] P.A.M. Guichon and M. Vanderhaeghen, Phys. Rev. Lett. **91** (2003) 142303 and arXiv:hep-ph/0306007.

[7] J. Arrington, Phys. Rev. **C 69**, (2004) 032201 and arXiv:nucl-ex/0311019.

[8] P. G. Blunden, W. Melnitchouk and J. A. Tjon, Phys. Rev. Lett. **91** (2003) 142304 and arXiv:nucl-th/0306076.

[9] A. Afanasev, S. Brodsky and C. Carlson, presented by A.Afanasev at the DNP Meeting, Tucson, AZ, Oct. 2003.

[10] Y. C. Chen, A. Afanasev, S. J. Brodsky, C. E. Carlson, and M. Vanderhaeghen, arXiv:hep-ph/0403058.

[11] J. Mar *et al.*, Phys. Rev. Lett. **21** (1968) 482.

[12] K. Joo *et al.*, "Two-photon exchange from a precise comparison of e+p and e-p elastic scattering in CLAS," Letter of Intent to PAC 25, TJNAF, 2004.

[13] F.Foster, and G.Hughes, "Electroproduction of nuclear resonances", Rept. Prog. Phys. **46** (1983) 1445.

[14] V.V.Frolov *et al.*, Phys. Rev. Lett. **82** (1999) 45.

[15] Hovanes.Egiyan, Ph.D. Thesis, The College of William and Mary in Virginia,(2001) (unpublished).

[16] B. Krusche *et al.*, Eur. Phys. J. **A 6** (1999) 309.

[17] J. Arrington, Phys. Rev. **C 69** (2004) 022201 and arXiv:nucl-ex/0309011.

DECAY MODES OF MULTIPOLE GIANT RESONANCES AT LIGHT AND MEDIUM NUCLEI (A≤ 64)

B.S. Dolbilkin
Institute for Nuclear Research RAS, Moscow, Russia

The knowledge of decay properties of multipole giant resonances (MGR) is actual for understanding of fundamental modes of nuclear excitation. A study of nucleon decay to ground- and low-lying hole states is a source of an direct information of a coupling between collective and single particle excitations. In this field a lot of experimental and theoretical works have been done for last years. Different probes, as with electromagnetic interactions (photons, electrons), which is well known, and nuclear ones (nucleons, deuterons, α - particles, heavy ions) were used. After putting into operation a new generation of accelerators with continuous beam, coincidence technique experiments for study reactions (e,e'x), where $x = p,n,d,\alpha$, would be possible with essentially more information about reaction mechanism and nuclear structure.

The diagram of the coincidence $A_1(e,e'x)A_2$ reaction for the electromagnetic interaction in the first order Born approximation is shown on Fig.1. For relativistic calculations of the coincidence cross section, the one-photon exchange and plane-wave Dirac wavefunctions for electrons were used, what is reasonable for light nuclei [1,2].

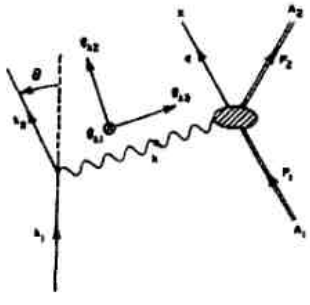

Fig.1. The diagram of the coincidence $A_1(e,e'x)A_2$ reaction in the first order Born approximation. θ - the angle of the electron scattering. The initial and final electron 4- momenta are $k_1^\mu = (e_1,\vec{k}_1)$ and $k_2^\mu = (e_2,\vec{k}_2)$ Four-momentum transfer to a nucleus is given by $k^\mu = (k_1 - k_2)^\mu = (\omega,\vec{k})$, $\hat{e}_{ki}$ - unit vectors. The initial and final 4-momenta for the nucleus is defined by $p_1^\mu = (E_1,\vec{p}_1)$ and $p_2^\mu = (E_2,\vec{p}_2)$ with masses M_1 and M_2.

A large amount of data has been come from $(e,e'p)$ and $(e,e'\alpha)$ reactions. In addition to dependence of a cross-section from the energy excitation of a nucleus-target in photo-reactions [3], in inelastic electron scattering an impulse, giving to a nucleus, is changed, what gives an opportunity, to study different multipolarities, except the isovector dipole excitations in photodisintegration. An example of an $(e,e'p)$ reaction is illustrated in Fig.2 for the $O^{16}(e,e'p)$ experiment [4]. It shows new advantages of coincidence technique, using

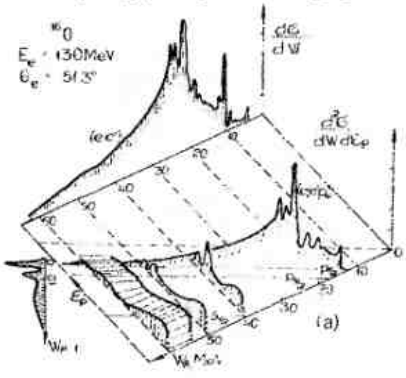

Fig.2. Projections of the $^{16}O(e,e'p)$ reaction cross-section $d^2\sigma/dWd\varepsilon_p$ on the plane (W_A,ε_p). It is shown also (e,e') cross-section and a population of ^{15}N nuclear states [4].

which an valuable information about MGR is obtained.

An actual question, how, after MGR collective excitation in the continuum, the energy dissipates and decay is divided between the escape width $\Gamma\uparrow$, formed from coupling to the

continuum,($1p-1h$ configurations), and the spreading width $\Gamma\downarrow$, due to more complex $np-nh$ configurations. In the former case the decay is connected with MGR microscopic structure. The next stage is a loss of coherence at moving to more complex configurations. The classification of a decay contains direct, semi-direct, pre-equilibrium and statistical processes[5]. The direct reaction is a knock-out type, which is described by the initial and final nuclear wave functions and the free nucleon one. This process is not connected with an excitation GR and not considered here. Schematically the excitation and decay of different stages is shown on Fig.3. After an excitation by an photon or electron of the electrical GR in the

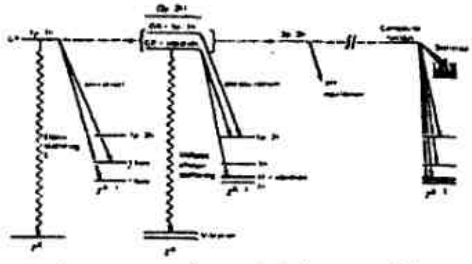

Fig.3. Schematic representation of MGR decay modes.

continuum, preferential decay of the coherent GR to particular 1-hole states in the residual nucleus is called semi-direct. GR acts as a doorway state, through which an probe causes the emission of a nucleon (or more complicated particles). The process leaves the nucleus in states, which are dominantly single nucleon holes. There are nuclear decays intermediate between semi-direct and statistical ones, i.e. $1p-1h$ states in nuclear time proceeds to the compound nucleus through a sequence of $2p-2h$ states, which either emit nucleons or mix with $3p-3h$ states and so on, until equilibrium states are reached. For example, the pre-equilibrium process would give rise to a nucleon emission to vibrational states and/or nucleon decay to states, which correspond to a nucleon hole coupled with a surface vibration.

There are a hope, that a better knowledge of decay properties MGR, first of all, dipole GR which can be thought of as more easily understood, since small amplitude vibrations, can help to use theoretical approaches to describe deep inelastic heavy ion reactions. It is important also to study a damping mechanism for better understanding of deep inelastic collisions.
An example of GR decay to 1- hole states of residual nuclei for ^{58}Ni nucleus is shown on Fig.4.

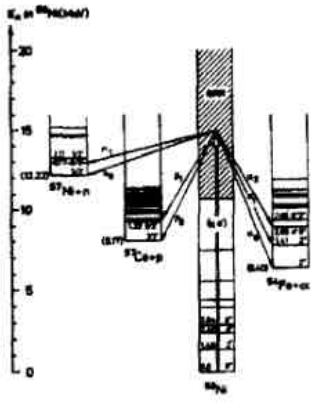

Fig.4. An illustration of an excitation by electrons of ^{58}Ni GR region in the continuum and the main GR channels, proton, neutron and alpha, decay, to the ground and low-lying states of daughter- nuclei $^{57}Co, ^{57}Ni, ^{54}Fe$.

1. Kinematics and cross sections.

The cross-section of the $(e,e'x)$ reaction is given[2]:

$$d^5\sigma / d\omega d\Omega_e d\Omega_x = \sigma_M \cdot (v_L W_L + v_T W_T + v_{LT} W_{LT} \cdot \cos\phi_x + v_{TT} W_{TT} \cdot \cos 2\phi_x), \qquad (1)$$

where W_L, W_T, W_{LT}, W_{TT} - nuclear response functions of longitudinal or perpendicular type and their combinations, the first two are connected with charge- , the next ones with current- operator.

ν_{ab} - kinematical factors:

$$\nu_L = (Q^2/q^2)^2 \qquad \nu_T = -(Q^2/2q^2) + \tan^2(\theta_{e'}/2)$$

$$\nu_{LT} = (Q^2/q^2)\cdot[-Q^2/2q^{2)} + (1/2)\tan^2(\theta_{e'}/2)]^{1/2} \qquad \nu_{TT} = (Q^2/q^2)$$

Nuclear excitation functions depend from 4 Lorentz- invariant scalars $\{Q^2, Q\cdot P_i, P_x\cdot P_i, Q\cdot P_x\}$ or in laboratory frames (q,ω,p_x,θ_x) and do not depend from azimuthal angle ϕ_x.

In principle it is possible, using Rosenbluth method to define all W_{ik} at expression (1).

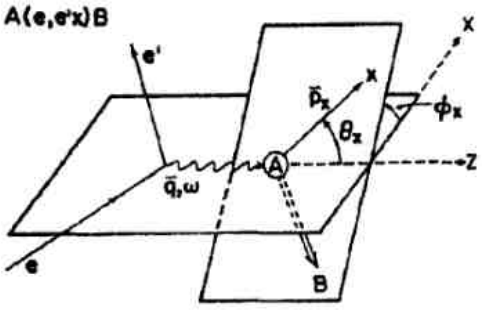

Fig.4. The kinematics of the $(e,e'x)$ reaction. (θ_k,φ_k) - polar coordinates of an emitted particle x in the center of mass of the decaying nucleus. Scattering of electrons is going in the (x,z) plane. The momentum transfer is directed along the z - plane [2].

In experiments described here small scattering angles were used ($\leq 40^0$), on this reason perpendicular and interference terms has been neglected in the limit of data errors. The angle between the planes of scattering and reaction ϕ_k has been chosen equal 45^0, so the last term in (1) was absent. In this approximation the longitudinal excitation of MGR is denoted as C_L, commonly also used E_L

2. Multipole decomposition analysis.

From the beginning in the analysis of (e,e') experiments, later in coincidence $(e,e'x)$ reactions, Goldhaber- Teller(GT), Steinwedel-Jensen(SJ) collective models were used for an GDR description, Tassie model – for GR other multipolarities. Since an essential difference between GT and SJ models, it was difficult to define the real value of parameters MGR under investigation.

A new, in principle, model-independent multipole analysis has been developed for $(e,e'x)$ coincidence cross sections of all measured decay channels [6,7], which is based on equations for the total cross sections, $\sigma(q_j,\omega_k)$. For each decay channel form factors $F(q_j,\omega_k) = \sigma(q_j,\omega_k)/\sigma_{Mott}$, measured at few (usually 3) momentum transfers q_j are expressed as linear combination of longitudinal multipole coefficients:

$$\left.\begin{matrix}\sigma_{exp}(q_1,\omega_k)/\sigma_{Mott}\\ \sigma_{exp}(q_2,\omega_k)/\sigma_{Mott}\\ \sigma_{exp}(q_3,\omega_k)/\sigma_{Mott}\end{matrix}\right\} = a_{E1}(\omega_k)\cdot\left\{\begin{matrix}|F_{E1}(q_1)|^2\\ |F_{E1}(q_2)|^2\\ |F_{E1}(q_3)|^2\end{matrix}\right. + a_{E2/E0}(\omega_k)\cdot\left\{\begin{matrix}|F_{E2/E0}(q_1)|^2\\ |F_{E2/E0}(q_2)|^2\\ |F_{E2/E0}(q_3)|^2\end{matrix}\right.$$

In an analysis the next assumptions have been made:

1. E0,E1,E2 excitations only contribute
2. E2 and E0 form factors are identical
3. Form factors in the region GR 10 – 25 MeV are constant for the definite multipolarity.

The last assumption leads from I independent systems of 3 linear equations for each energy ω_k to a single system of $3I$ nonlinear equations with $2I+4$ unknown quantities $a_{E1}(\omega_k), a_{E2/E0}(\omega_k)$ and $|F_{E1}(q_j)|^2, |F_{E2/E0}(q_j)|^2$, which is overdetermined for $I > 4$ and solved by the least-squared fit procedure. During the analysis it was shown, that for these equations many solutions exist, and a link between form factors should be introduced to get an unique solution[7]

3.Proton decay of p,sd,sf - shell nuclei.

3.1. p - nuclei: $^{12}C,^{16}O$.

The $^{12}C(e,e'p_0)$ angular distributions at excitation energies of the maximum GDR, 22.5 MeV, shoulder (25.5 MeV) at momentum transfers q = 0.24-0.61 fm^{-1} (right), and the integrated cross sections at the same q (left) are shown on Fig.5[8]. A pure longitudinal form factor is symmetric relatively $\theta_p = 90^0$ with maxima at 0 and 180^0, whereas a transverse one has the maximum at 90^0. The transverse to longitudinal ratio at a small momentum transfer in the long wavelength limit (Siegert's theorem) is given

$$T_\lambda / C_\lambda = -[(\lambda+1)/\lambda]^{1/2} \cdot \omega / q$$

An admixture of the transverse form factor shifts the angular correlation function (ACF) of longitudinal one to larger decay particle angles.

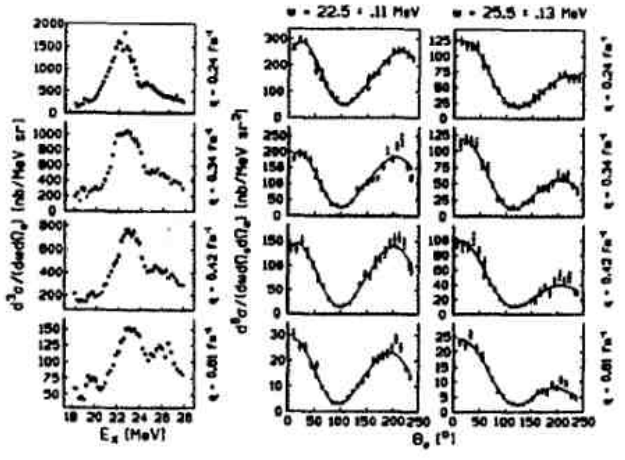

Fig.5. Angular distributions of $^{12}C(e,e'p_0)$ reaction at 22.5 and 25.5 MeV (right) and integrated p_0-cross sections vs excitation energy 18-28 MeV (left) at momentum transfer 0.24-0.61 fm^{-1} [8].

At all measured momentum transfers (Fig.5) a minimum is seen near 90^0, what is proved the GDR longitudinal excitation. The 2nd resonance is more asymmetric. The shape of total cross sections (left) for lower q is analogical to photonuclear ones.

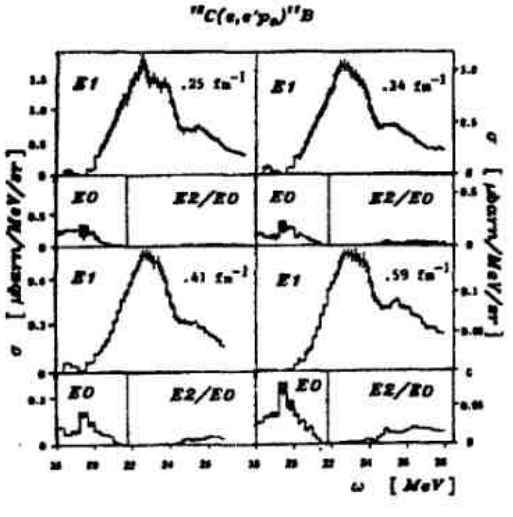

The $^{12}C(e,e'p_0)$ reaction multipole decomposition at four momentum transfer for E1 and E2(E0) multipolarities from the data on Fig.5 is presented on Fig.6. According the assumptions, made above, E2 and E0 form factors have an identical q- dependence (it is correct at least at the first maximum region), they could not been expanded by the method used here [6,7].

Fig.6. Electric E1 distribution and E2/E0 admixtures in $^{12}C(e,e'p_0)$ reaction for the momentum transfers q= 0.25-0.59 fm^{-1}.

The decay of the $^{12}C(e,e'p)$ cross section is dominated by the p_0-channel to the ^{11}B ground state, meanwhile transitions to $p_1, p_{2,3}$ excited states is only ~ 20%[8]. The semi-direct (in the next – direct) decay part of this reaction is (93 ± 5) %.

The multipole decomposition of $^{16}O(e,e'p_0)$ reaction is shown on Fig.7 for 4 momentum transfer. At lower q an E2(E0) contribution is neglible, what decreases parameter numbers of the fit.

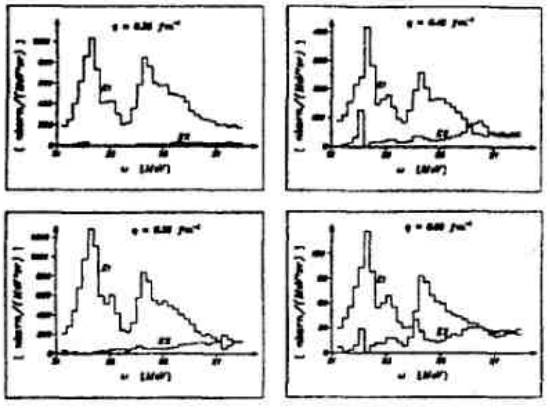

Fig.7. Electric GDR distributions (E1) with E2(E0) admixtures in $^{16}O(e,e'p_0)$ reaction vs the excitation energy at momentum transfer 0.25-0.6 fm^{-1} [6].

The $^{16}O(e,e'p)$ reaction decay to the ground and 3rd excited states of ^{15}N is presented on Fig.8. Decay proton cross section is dominated by p_0 and p_3 channels, which have nearly the same strength. But their energy distribution is quit different. At the p_0- cross section there are

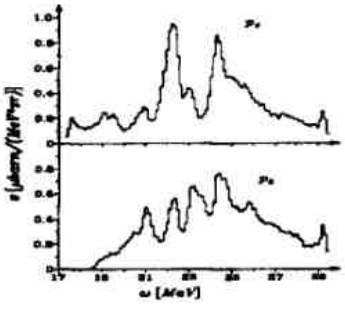

Fig.8.The 4π integrated $^{16}O(e,e'p_i)$ cross sections, $p_i = p_0$ (upper), p_3 (lower) vs the excitation energy ^{16}O for the momentum transfer $q = 0.25$ fm^{-1}.

two dominating resonances at 22.3 and 24.5 MeV as in the total absorption and (γ,p) reactions. The p_3-spectrum has four nearly equally strong resonances, two of them coincide with p_0-maxima. The direct part of $^{16}O(e,e'p)$ reaction is ~ (90 ± 5) %.

3.2. *sd*-nuclei: ^{28}Si, Ca.

The $^{28}Si(e,e'c)$ cross sections, where $c = p_i, \alpha_i$ is presented [6] on Fig.9 in comparison with decay channels of the E1 GR $^{28}Si(\gamma,c_i)$ reaction [9]. An estimate of the $^{28}Si(e,e'p)$ reaction direct part is (85 ± 10) %. The photonuclear cross sections at Fig.9 were converted to the $(e,e'c)$ ones by use of an identical normalization for all decay channels c_i.

The absolute E1 strength of both reactions is agreed within the 20 % accuracy. The nice agreement is observed in shapes of the shown E1 decay channels in spite of strongly structured cross sections what confirms the used here multipole decomposition method.

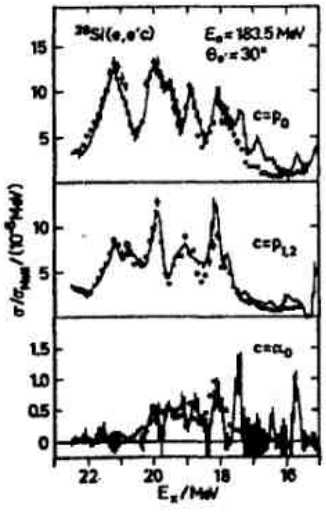

Fig.9. The $^{28}Si(e,e'c)$ reaction cross sections at the momentum transfer $q = 0.36$ fm^{-1} for decay channels p_0, p_{12}, α_0 of the E1 Giant Resonance are presented. Dots are the normalized $^{28}Si(\gamma,c)$ cross sections [6]

Integral E1 and E2 form factors, deduced by this method are agreed with respective predictions of the collective GT for E1 excitations and Tassie models for E2 ones, calculated in DWBA after adjustment of the half-density radius c_0. For the E1 the fit is resulted to $c = 1.1c_0$, for E2 – to $c = 0.9c_0$. Steinwedel-Jensen (SJ) model predictions have worse agreed with the data (Fig.10).

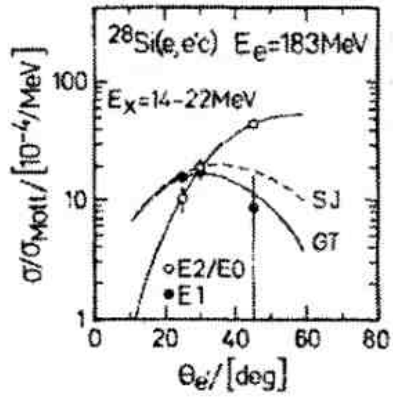

Fig.10. The comparison of the integrated E1 and E2(E0) form factor DWBA predictions of GT, SJ models for E1 excitation and Tassie for E2(E0) ones with experimental form factors (black circles- E1, open- E2(E0)).

The $^{40}Ca(e,e'p_0)$ reaction at the momentum transfer q=0.35 fm^{-1} is compared with $^{39}K(p,\gamma_0)$ ones on Fig.11[6]. An fair agreement is observed at the GDR region. The lower 18 MeV an contribution of E2(E0) GR is seen. The semi-direct part of p_0, p_1- decay channels estimate is an order of 80%, the p_3~ 50%, in total $(e,e'p)$ reaction ~(60 ± 10)%.

^{40}Ca is a double-magic nucleus, in which a contribution of the $^{40}Ca(e,e'p_0)$ is essentially more, than in $^{42,44}Ca$ isotopes and equal 13% of the classical dipole sum rule, for ^{44}Ca - 3%

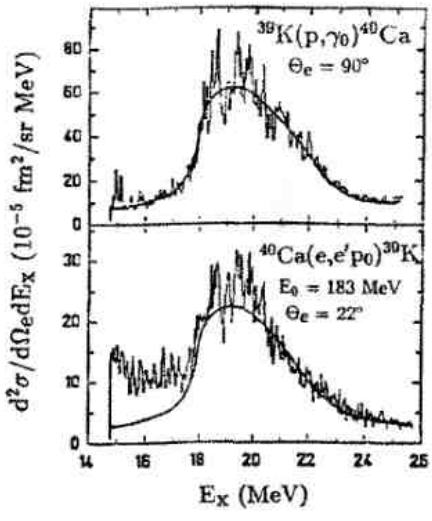

Fig.11. Comparison of the $^{40}Ca(e,e'p_0)$ (bottom) and $^{39}K(p,\gamma_0)$ (top) reactions. The solid line is an average fit of the E1 GR. At E_x=15-18 MeV an E2 contribution is seen.

Dynamics of (γ,p_0) reaction in $^{40-42-44}Ca$ isotopes is shown on Fig.12. $^{40,42}Ca(\gamma,p_0)$ cross sections are presented, derived from (p,γ_0) reactions by the detailed balance method. From the Fig. it is seen a broadening and decrease of σ_{max}, while couple of additional neutrons are added to the double-magic ^{40}Ca. The p_0- channel part is quickly decreased with mass number A. For isotopes with A= 42,44 isospin effects are also observed: GDR is splitted into the $T_>$ and $T_<$ components. Parameters are numerically shown in Table1.

In contrast to ^{40}Ca neutron decay dominates in $^{48}Ca(e,e'n)$ reaction. Its direct part in comparison with statistical calculation HF is estimated to be ~ 40% [22]

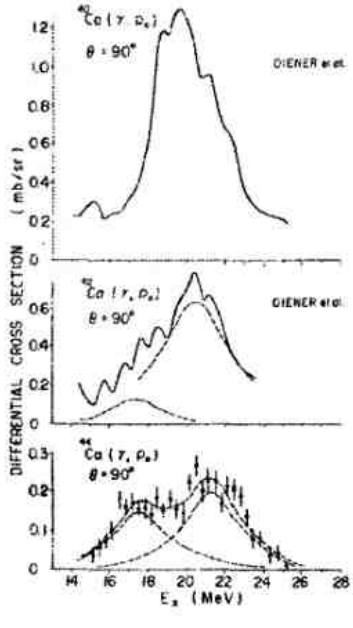

Fig.12. E1 GR is in the $^{40-42-44}Ca(\gamma,p_0)$ cross sections vs the energy excitation nucleus-target at 90^0. Dashed curves are estimates $T_<$ and $T_>$ branches of GDR[10].

Table1. Experimental parameters of the (γ, p_0) reaction on Ca isotopes [10].

	T	$\int\sigma_{p_0}dE$ (mb · MeV)	$\int\sigma_{p_0}dE$ [a] CDSR (%)	$\frac{\sigma^{>}_{-1}(\gamma,p_0)}{\sigma^{<}_{-1}(\gamma,p_0)}$	$\frac{\sigma^{>}_{-1}}{\sigma^{<}_{-1}}$ (theory)	$E^{>}_R$ (MeV)	$\Gamma^{>}_R$ (MeV)	$E^{<}_R$ (MeV)	$\Gamma^{<}_R$ (MeV)	$E^{>}_R - E^{<}_R$ (MeV) exp.	theory[b]
^{40}Ca	0	77	13								
^{42}Ca	1	52	8	6.7	0.78	20.4	4.4	17.4	3.3	3.0	2.9
^{44}Ca	2	18±3	3	1.3±0.3	0.34	21.3	3.5	17.5	3.5	3.8	4.1

[a]) CDSR shows classical dipole sum rule limit given by 60 NZ/A mb · MeV.

3.3. Medium nuclei: $^{58,60}Ni$, ^{64}Zn

Complex research were made for nuclei f-shell, ^{58}Ni with Z=28, filled proton subshell plus 2 neutrons, ^{60}Ni with 2 additional neutrons, ^{64}Zn with +2 protons and 2 neutrons [11,12].

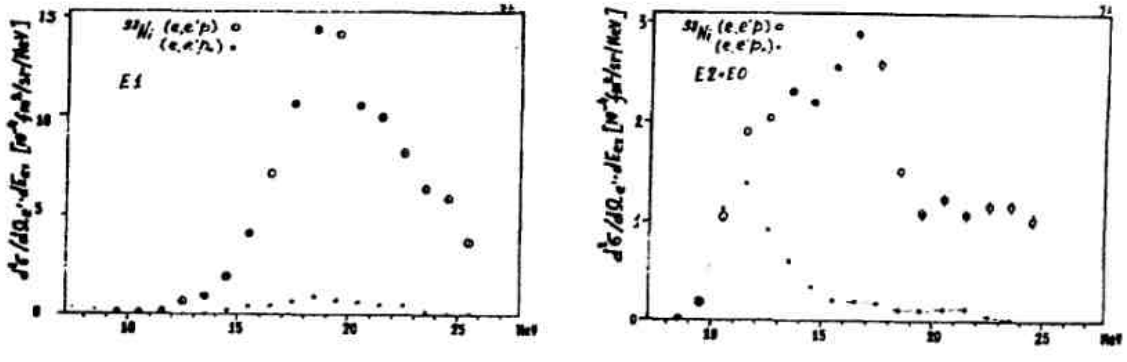

Fig.13. The E1(left) and E2(E0) (right) GR $^{58}Ni(e,e'p,p_0)$ vs. the excitation energy 9-26 MeV at the momentum transfer 0.27 fm^{-1}.

The shape of decay to the total proton and p_0 channels are quit different for E1 and E2(E0) multipolarity GR. The p and p_0 - reactions at E1 GR have almost similar energy dependence, maximum is near 19 MeV, their ratio is (7±2)%. E2(E0) GR is asymmetric with a maximum ~16.5 MeV and a shoulder in the 20-25 MeV region, its p_0-branch has a maximum at 11.5 MeV and the ratio-(20±5)% [see Fig.13for ^{58}Ni]. Their parameters are presented at Table 2.

Table 2. The experimental E1,E2(E0) GR parameters for p, p_0 -decay channels of ^{58}Ni.

Multipolarity	E1			E2+E0		
Channels	E_{max},MeV	σ_{max},mkb/srMeV	Γ,MeV	E_{max},MeV	σ_{max},mkb/srMeV	Γ,MeV
p	19±0.2	15±0.6	~7.5±0.3	16.5±0.2	2.9±0.2	~8.0
p_0	19±0.3	0.8±0.1	~7.0±0.3	11.5±0.2	1.4±0.1	~3.5

The change of E1 and E2(E0) GR $^{58}Ni(e,e'p_0)$ reaction value at the increase of the momentum transfer to 0.47 fm^{-1} is shown at Fig.14. Although $\int d^2\sigma(e,e'p_0)$ is nearly constant (~ 10 mkb/sr), the E1 contribution is lower at the last one to ~ 15%.

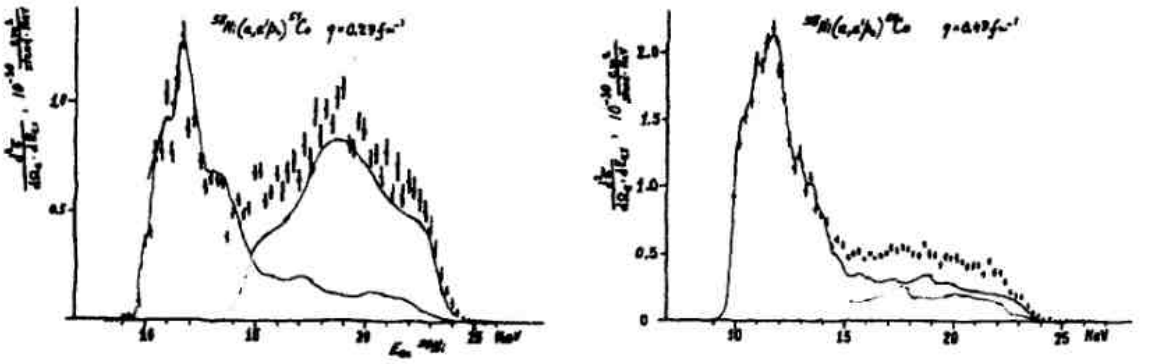

Fig.14. Comparison of E1 (right curve) and E2(E0) (left one) GR in the $^{58}Ni(e,e'p_0)$ reaction at the momentum transfers $q = 0.27$ and 0.47 fm^{-1}. The full curves- fit to experimental points.

The E1 energy dependence of $^{58}Ni(e,e'p_0)$ reaction is practically coincided with the shape of $^{58}Ni(\gamma,p_0)$ reaction, extracted from the inverse one, as for α_0-channel, is shown on Fig.15[13].

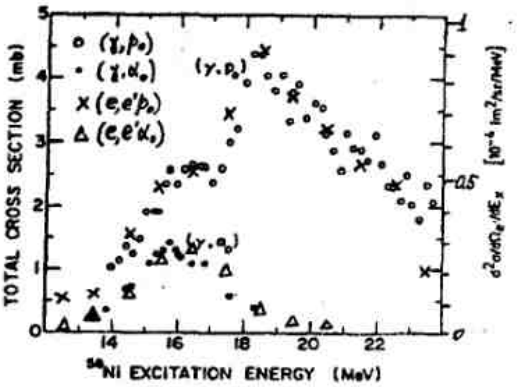

Hence the experimental $^{58}Ni(e,e'p_0)$ cross section can be compared with $^{58}Ni(\gamma,p_0)$ theoretical calculations[14]. The result is presented on Fig.16.

Fig.15. Comparison of $^{58}Ni(e,e'c_0)$, $c_0 = p_0$ (crosses), α_0 (triangles), cross sections with (γ,p_0)- open circles, and (γ,α_0)-dots.

At calculations isospin was assumed to be a good quantum number. A satisfactory agreement is seen. It is better for the full curve. The experimental $(e,e'p_0)$ curve was normalized to the theoretical one at the maximum ~8 mb, although the peak value of $^{58}Ni(\gamma,p_0)$ is ~ 4 mb. The analogical agreement is observed for $^{60}Ni(\gamma,p_0)$ calculations.

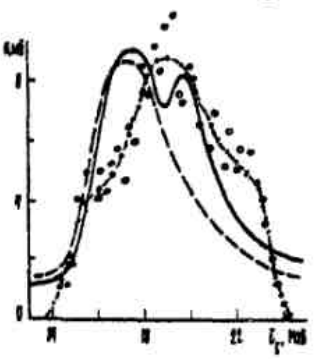

Fig.16. Comparison of the experimental $^{58}Ni(e,e'p_0)$ reaction (open dots, fit: dot-dashed curve) with theoretical calculations (full curve–the total amplitude $|M_{\lambda m}|^2$, dotted- without contribution $|M^{\sim}_{\lambda m}|^2$).

The population ^{57}Co p_i-states from decay of ^{58}Ni GR is shown on Fig.17.

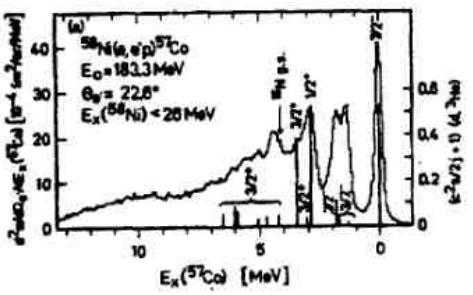

Fig.17. The $^{58}Ni(e,e'p)$ cross section vs the excitation energy of ^{57}Co in comparison with spectroscopic factors from the $^{58}Ni(d,^3He)^{57}Co$ pickup reaction

The strength distribution of $^{60}Ni(e,e'p)$ to ^{57}Co residual states from energy intervals ^{60}Ni GR is presented in Table 3 for the momentum transfer $q = 0.27$ fm^{-1}

Table.3. The $^{60}Ni(e,e'p)$ strength distribution to ^{57}Co states from excitation energies of ^{60}Ni.

		E_p	0	1	2	3	4	5	4+5	6	7	6+7
		j^{-1}	$1f^{-1}_{7/2}$	$2p^{-1}_{3/2}$	$1f^{-1}_{7/2}$	$2s^{-1}_{1/2}$	$1d^{-1}_{3/2}$			$1d^{-1}_{5/2}$		
		E_p^{min}	0	0,7	1,6	2,5	3,7	4,9		6,5	8,2	
N	E_x(MeV)	E_p^{max}	0,7	1,6	2,5	3,7	4,9	6,5		8,2	9,4	
1	10,0-12,5		0	0	0	0	0	0	0	0	0	0
2	12,5-14,0		50	26	6	16	0	0	0	0	0	0
3	14,0-16,0		12	40	10	26	11	1	12	0	0	0
4	16,0-17,5		8	21	7	34	20	10	30	0	0	0
5	17,5-19,0		8	10	5	27	25	23	48	3	0	3
6	19,0-20,0		9	7	3	19	18	36	54	8	0	8
7	20,0-22,0		5	6	3	14	10	35	45	23	1	24
8	22,0-24,0		9	4	2	11	6	21	27	33	13	46
9	24,0-25,5		5	6	2	13	5	10	15	22	38	60
10	10,0-25,5		9	12	4	20	14	22	36	14	5	19

An estimate of the E1 direct decay from $^{58,60}Ni, ^{64}Zn$ GR has been made by comparison with Hauser-Feshbach statistical calculations: (33 ± 3)% of experimental cross sections [11,12].

4. α-decay.

4.1. p-shell nuclei

The isovector GR's are eliminated at α-decay channels, except an amount depended on an isospin mixing. From comparison of $(\alpha,\gamma_0),(\alpha,\alpha'\alpha),(e,e'\alpha)$ reactions on $^{12}C, ^{16}O$ it was concluded [15,16], that α-decay cross sections is mainly consistent with the isoscalar giant quadrupole resonance (IsGQR). Angle correlations were measured for both nuclei at q-interval 0.25-0.6 fm^{-1}. In addition, especially for these p-shell nuclei with α-particle structure, the α-reactions are dominated by $\alpha_0 + \alpha_1$ channels. An example for $^{16}O(e,e'\alpha_0,\alpha_1)$ reactions is shown on Fig.18. The α_1-cross section to the 1st excited state in ^{12}C is larger ~ 1.5-2 times. Both channels have a strong resonance at $\omega = 18.8$ MeV. The 2nd resonance is clearly seen at α_0-reaction at 20.8 MeV and as a bump at α_1-one. In the last reaction more strengths with some structure is seen higher 21 MeV. At higher q a fast rise of E3 multipolarity was noticed.

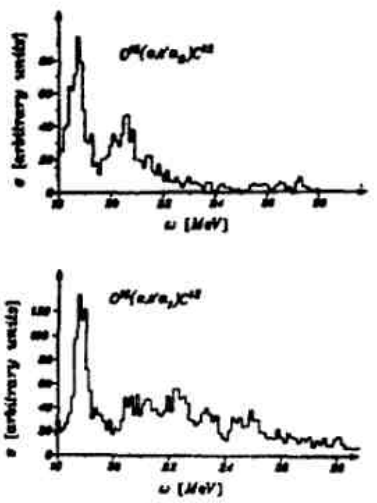

Fig.18. α_0 (top) and α_1 (bottom)- decay cross sections in arbitrary units vs the ^{16}O excitation energy.

The total $^{12}C(e,e'\alpha_0)$ reaction has a main maximum at $\omega = 21.6$ MeV and resonance structures at 18.5 MeV and ~24 MeV. The E2/E0 contribution at the interval 18-28 MeV is ~ 10%. In the total α-channel the estimated E2 strength value is ~ 37% EWSR, E0 ~10%, the isovector E1- inside of an statistical accuracy.

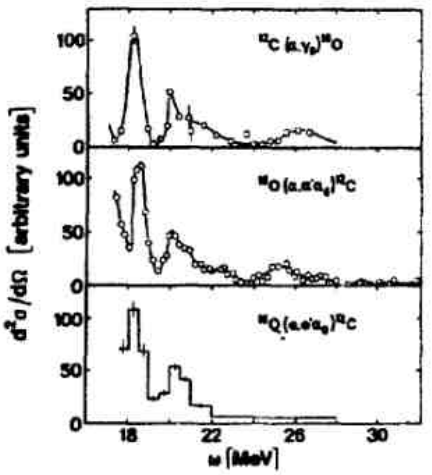

At $^{16}O(e,e'\alpha)$ reaction angular distributions were measured at the angle range from -10 to 240^0, i.e. so called the total angular correlations, which were extracted cross sections from. Comparison of three different E2 reactions in ^{16}O is presented on Fig.19[15]. There are small amounts of other multipoles ($\leq 10\%$).

Fig.19. The E2 GR in the α_0-channel from $^{12}C(\alpha,\gamma_0)$ (top), $^{16}O(\alpha,\alpha'\alpha_0)$ (middle) and $^{16}O(e,e'\alpha_0)$ (bottom) vs the ^{16}O excitation energy 17.5-28 MeV at the momentum transfer q=0.25 fm^{-1}.

The structure at ~ 18, 20 MeV is similar for all three reactions. The $^{16}O(e,e'\alpha_0)$ IsGQR integral strength in the energy interval 17.5-28 MeV of $(3.6\pm0.7)\%$ is lower than $(5.0\pm1.3)\%$ from $^{12}C(\alpha,\gamma_0)$ and 13% from $^{16}O(\alpha,\alpha'\alpha_0)$ reactions [16].

An extension of Is.E2 strength has been made for the $(\alpha_0+\alpha_1)$ sum, which is practically the total α-channel, under assumption, that the ratio Is.E2 in both channels is independent from q.

As a result it was found, that the $^{16}O(e,e'\alpha_1)$ channel exhausts $(15\pm3)\%$ of EWSR, or 4.2 times more then $(e,e'\alpha_0)$ one. It means, for total α-channel is exhausted ~20% of EWSR. The fraction ~50% EWSR from $(\alpha,\alpha'\alpha_i)$ - channels[17] seems to be too large.

4.2. *sd*-shell nuclei: ^{26}Mg, ^{40}Ca

An energy excitation spectrum of $^{26}Mg(e,e'\alpha)^{22}Ne$ reaction is shown on Fig.20[18]. It looks similar to ^{12}C, ^{16}O α-cross sections, consist from two sharp resonances, α_0 and α_1-decay channels, and weak structured tail higher 2 MeV. Except it, α_1 value here is smaller of α_0 decay branch.

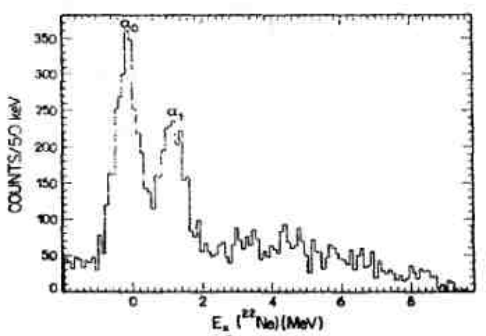

Fig.20. The relative $^{26}Mg(e,e'\alpha)$ reaction cross section for $\theta_\alpha = 20^0$ and the ^{26}Mg excitation energy ω=20.1 MeV at the momentum transfer q= 0.35 fm^{-1}.

Angular correlation functions (ACF) of $^{26}Mg(e,e'\alpha_0)$ reaction at the momentum transfer 0.35 fm^{-1} are presented in Fig.21. ACF were measured at two energy intervals with $\Delta\omega$ = 0.2 MeV. The E0,E1,E2 strengths are extracted for every interval. Their value are shown on Fig.21

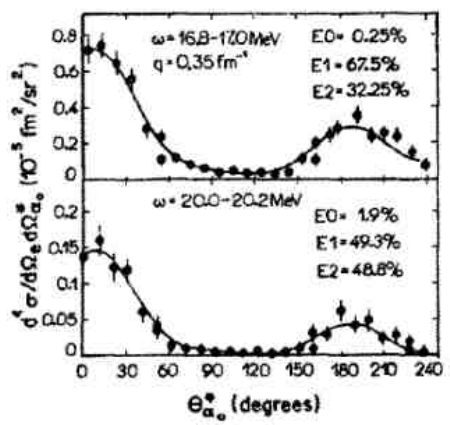

Fig.21 Angular correlation functions for $^{26}Mg(e,e'\alpha_0)$ reaction at the momentum transfer q=0.35 fm^{-1}. Dots-experimental points in the θ_{α_0} = 0-240^0 range. Curves – results of fitting with a Legendre polynomial series[18]

Comparison of the isospin splitting in ^{26}Mg partial channels is shown on Fig.22, where $^{26}Mg(e,e'p_{01})$ (bottom), $^{26}Mg(e,e'p_2)$ (middle) and $^{26}Mg(e,e'\alpha_0)$ (top) reactions.

In the $^{26}Mg(e,e'\alpha_0)$ cross section just one bump, splitted into two peaks, is observed in the 15-18 MeV range, the right bump is absent. The reason is, that only $T_<$ is an isospin allowed in the α_0-decay. GDR splitting in $^{26}Mg(\gamma,n)$ cross section is also connected with isospin.

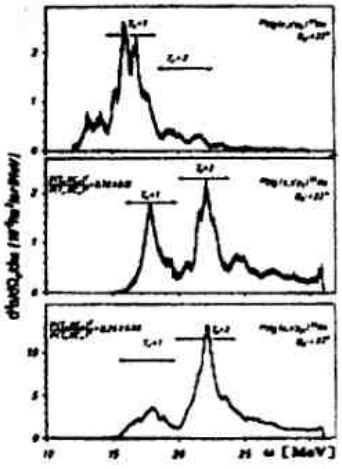

At p_1- channels $T_>$ and $T_<$ GR components are presented with the peak energies ~17.5 and 22 MeV and the maxima splitting ~ 4.5 MeV. Ratio of $T_</T_>$ is ~ 0.8 in the p_2- decay and 0.25 in p_{01} one (difference of p_0 and p_1 states is only 0.09 MeV). The branching ratios are 5.8 for p_{01}/α_0 and 1.2 for p_2/α_0.

Fig.22. The 4π integrated cross sections of α_0 (top), p_2 (middle) and p_{01} (bottom) channels of ^{26}Mg E1 GR.

The E2 $^{26}Mg(e,e'\alpha_0)$ cross section at the momentum transfer $q = 0.35$ fm^{-1} is shown on Fig.23 (bottom) together with E2 $^{26}Mg(\gamma,\alpha_0)$ reaction (top), obtained from the inverse reaction. Both reactions have a bump around 14-18 MeV with some structure inside. The IsGQR systematic gives the maximum energy $\sim 63 \cdot A^{-1/3}$ MeV, i.e. 22 MeV in ^{26}Mg, but this cross section maxima has essentially lower energies. The strengths of both resonances were evaluated to be for E1- 0.45%, for E2-1.4% EWSR. The E0 fraction of 0.2% EWSR is at the same energy interval 14-18 MeV. The total α_0-channel takes only ~ 2% of the total IsGQR strength.

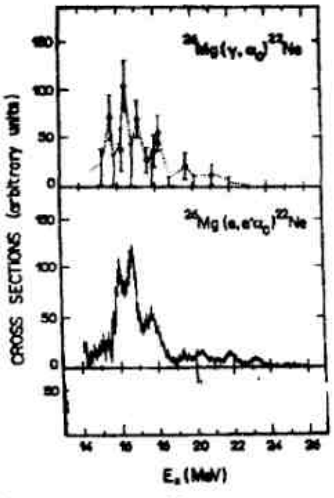

Fig.23. The E2 cross section part, obtained from the inverse $^{22}Ne(\alpha,\gamma_0)$ reaction (top), and $^{26}Mg(e,e'\alpha_0)$ one (bottom) vs the excitation energy ^{26}Mg.

^{28}Si is close to ^{26}Mg, but with equal numbers of protons and neutrons and isotopspin $T = 0$. The E2 $^{28}Si(e,e'\alpha_0)$ strength, extracted from ACF[6], is compared with $^{28}Si(\gamma,\alpha_0)$ cross section, obtained from the inverse reaction. The first is in good agreement with the latter. The integral E2, as E1 and E0 form factors are to be in fair agreement with predictions GT and Tassie models.

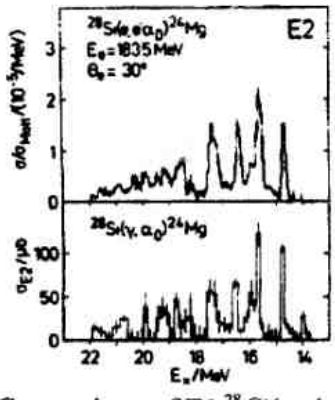

Fig.24. The E2 strength distribution in ^{28}Si, obtained from $^{28}Si(e,e'\alpha_0)$ angular correlations at the momentum transfer q=0.47 fm^{-1} (top), compared with $^{28}Si(\gamma,\alpha_0)$ cross section, deduced from $^{24}Mg(\alpha,\gamma_0)$ reaction[6].

Comparison of E1 $^{28}Si(e,e'\alpha_0)$ cross sections, extracted from ACF(a) and the multipole decomposition, described above[6,7], together with $^{28}Si(\gamma,\alpha_0)$ reaction[9](bottom) is presented

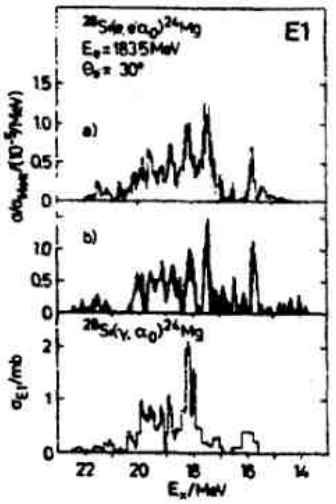

on Fig.25. There is the fair agreement between two methods in error limits. The agreement at 18-22 MeV energy region is also observed for the photoreaction, but its cross section is smaller at lower energies. A choice of one solution for E1 and E0 from two mathematically equivalent ones at an ACF equation decision has been made according to their form factor dependence from the momentum transfer. All multipole components $^{28}Si(e,e'\alpha_0)$ are strongly structured. Resonances are well reproduced at different momentum transfers.

Fig.25. The integrated E1-strength, obtained from the $^{28}Si(e,e'\alpha_0)$ angular correlations(a), the model-independent multipole decomposition(b), $^{28}Si(\gamma,\alpha_0)$ photoreaction (bottom).

The E2(E0) strength in $^{28}Si(e,e'\alpha_0)$ is 3.0% of the isoscalar EWSR. As for p-shell nuclei α_1-decay is more intensive, ~ 14% of EWSR. All α - channel is 20% EWSR comparatively with 16% in $(\alpha,\alpha'\alpha_0)$ reaction[6].

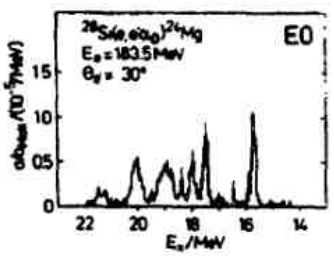

Fig.26. The E0 strength distribution, extracted from $^{28}Si(e,e'\alpha_0)$ reaction by the angular correlations(ACF).

The $^{40}Ca(e,e'\alpha_0)$ multipole decomposition of ACF has showed a small presence of the E1 fraction and the main contribution of E2 and E0 multipoles in the ^{40}Ca GR region. In the 10-17.4 MeV excitation energy region the E2 strength is ~8% and E0 -13% EWSR.

The substantial contribution of IsGQR direct decay in light nuclei with $A \leq 40$ has been shown in $(\alpha,\alpha'\alpha)$ reactions [1]. To the beginning of $(e,e'c)$ experiments the data have indicated, that a statistical decay was dominated at medium nuclei. This problem besides others was investigated for $^{58,60}Ni,^{64}Zn$ nuclei.

4.3 Medium nuclei: $^{58,60}Ni,^{64}Zn$

The model-independent multipole decomposition of E1 and E2(E0) GR in $^{58}Ni(e,e'\alpha)$ and $^{58}Ni(e,e'\alpha_0)$ reactions is presented on Fig.27. The E1 GR has an asymmetric complicated shape, which can be interpreted as an isospin splitting into $T_<$ with the maximum at ~17 MeV and $T_>$ at~ 21.5 MeV. It is seen, the E2 $^{58}Ni(e,e'\alpha)$ reaction cross section rises as E1 one, has a symmetric shape, but its maximum is at energy of ~16 MeV, lower than E1. The $^{58}Ni(e,e'\alpha_0)$ cross sections in both cases rise together with all α - reaction with an (22 ± 4)% intensity, have symmetric form and peaks ~16.5 and 14.5 MeV for E1 and E2 GR.

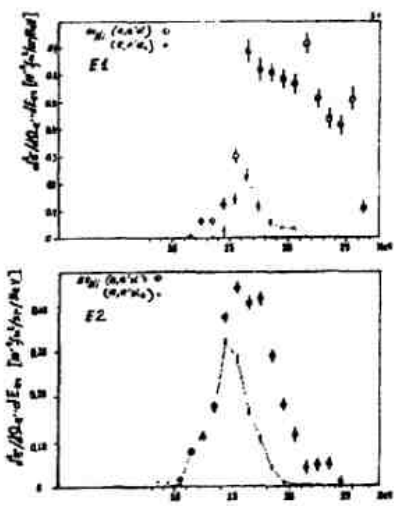

Fig.27. The E1(top) and E2(E0)(bottom) GR in $^{58}Ni(e,e'\alpha)$ and $^{58}Ni(e,e'\alpha_0)$-(dotted curves), reactions.

The $^{58}Ni(e,e'\alpha_1)$ multipole decomposition to E1 and E2(E0) components is shown on Fig.28. As in the α_0-decay case an α_1 - channels as for E1 and E2(E0) GR have a resonance shape(ratio 2:1).

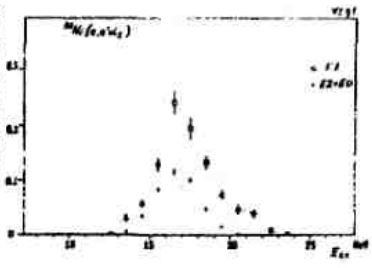

Fig.28. The multipole decomposition of $^{58}Ni(e,e'\alpha_1)$ reaction into E1(open circles) and E2(E0) (dots) GR at the momentum transfer q=0.27 fm^{-1}

The $^{58}Ni(e,e'\alpha_0)$ multipole decomposition from angular correlations for E1,E2,E0 multipoles is shown on Fig.29. The E0 fraction is small, ~5% of total strength. Its cross section is raised a little at the region of ~ 17 MeV. The E2 -channel up to energy of E2 maximum at14.5 MeV is expired the all α -cross section.

Fig.29. The multipole decomposition of $^{58}Ni(e,e'\alpha_0)$ cross section at the momentum transfer q=0.27 fm^{-1} for E1, E2, E0 components. E1 – dots, E2 – open circles, E0 – black triangles.

Parameters of α,α_0,α_1-decay channels at q=0.27 fm^{-1} are presented in Table 4.

Table 4. MGR parameters of $^{58}Ni(e,e'\alpha_i)$, $\alpha_i=\alpha,\alpha_0,\alpha_1$-cross sections at q=0.27 fm^{-1}.

	MGR parameters			
α_i	$E\lambda$	E_{max},MeV	Γ,MeV	$\%(\sigma_i/\sigma_t)$
α_0	1	16,0 ± 0,2	3,5 ± ,3	66,0 ± 4,0
	2	14,8 ± 0,3	3,0 ± 0,3	29,5 ± 2,0
	0	17,0 ± 0,5	2,0 ± 1,0	4,5 ± 1,0
α_1	1	16,5 ± 0,4	3,0 ± 0,3	68,0 ± 7,0
	2+0	16,5 ± 0,4	3,3 ± 0,4	32,0 ± 4,0
α	1	19,0 ± 0,5	10,0 ± 0,5	65,0 ± 6,0
	2+0	16,0 ± 0,5	5,5 ± 0,5	35,0 ± 5,0

The ratio of E1/E2(E0) multipoles is similar in error limits for every channel and equals ~ 2:1.
The energy maximum for E1 is shifted in α_0,α_1-channels at~ 3 MeV, although actually the E1 has a rather flat maximum starting from ~ 17 MeV. This fact reflects also its large width. Other widths are compatible.

The ratio was found ~0.5 in inclusive experiments, what is possible connected with errors because of small α -cross sections and uncertainties in a multipole decomposition.
.The big difference is observed also in exclusive ones in the interval 0.11-0.4. This ratio for ^{16}O was extracted to be~5, for ^{28}Si ~1, ^{40}Ca ~0.3[21].

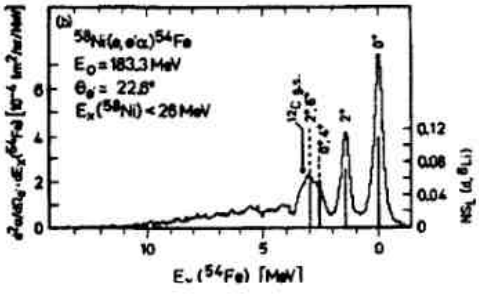

The $^{58}Ni(e,e'\alpha)$ reaction vs the ^{54}Fe excitation energy is presented on Fig.31. The main fraction of α -decay is α_0,α_1 and a group of $0^+,2^+,4^+,6^+$ states up to~ 4 MeV.

Fig.30. The $^{58}Ni(e,e'\alpha)$ cross section at the momentum transfer q= 036 fm^{-1} vs the ^{54}Fe excitation energy.

The $^{58}Ni(e,e'\alpha)$ cross section was compared with spectroscopic factors for ^{54}Fe resolved levels in the Fig. 30. From it the decay to the ground and first excited state of ^{54}Fe could presumably be direct one.
The α - direct decay at light nuclei was supposed to be comparable with the analogical proton one[1]. For medium nuclei it was checked at $(e,e'\alpha)$ experiment (see Fig.31, where are presented $^{64}Zn(e,e'p,\alpha)$ reactions at the momentum transfer q=0.36 fm^{-1}.

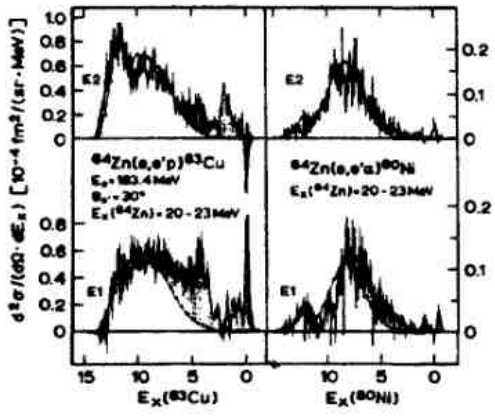

The comparison of the separated E1 and E2 GR in ^{64}Zn (Fig.31) with respective HF predictions shows, that for E1 the direct decay in α -channel at least two times (~15%) less than in p – one $(33 \pm 3)\%$. For p -reaction the E2(E0) GR direct decay probability is $(21 \pm 3)\%$, at α -channel the statistical decay dominates in some contradiction with ^{58}Ni (Fig.30).

Fig.31. The population ^{63}Cu and ^{60}Ni p – and α -channels from the ^{64}Zn E1 and E2(E0) GR between the 20-23 MeV excitation energy. The dotted curves are the statistical HF predictions [6].

In summary, the $(e,e'c), c = p,\alpha$ data for light and medium nuclei at low momentum transfers were compared with each other, photo-, hadron, inverse reactions and analyzed. The model-independent multipole decomposition is divided spectra into E1, E2(E0) GR or E2, E0 separately for α_0 -channel. The population of the ground and low-lying states of residual nuclei was considered. The substantial contribution of GR direct decay is observed for light nuclei. At medium nuclei the proton direct decay is 33% for E1 and 21% for E2. In α -channel the statistical decay for medium nuclei, as shown by comparison with HF predictions, is dominated. The RPA – calculations, including 2p-2h configurations and a continuum, are required.

References

1. H.Uberall, Electron scattering from complex nuclei, v.2, Academic Press, NY, 1979 K.T. Knoepfle and J. Wagner, Electric and Magnetic Giant Resonances in Nuclei, ed. by J.Speth, Int. Rev. Nucl. Phys.,7, 233, 1991
2. W.E. Kleppinger and J.D. Walecka, Ann. Phys.146, 349,1983
3. B.S. Ishkhanov, V.V. Varlamov, Phys. At. Nucl. 67,1664,2004. V.V. Varlamov et al, Photonuclear data 1976-1995, Moscow, MSU, 1983
4. V. Dmitriev et al, Nucl. Phys. A464, 237, 1987
5. L.S. Cardman, Nucl. Phys. A354, 173, 1981
6. S. Khan, K.T.Knopfle,..,B.Dolbilkin et al, Physics with MAMI A, ed. by D Drechsel and T. Walcher, Mainz, FRG, 187, 1988
7. B.S. Dolbilkin et al, Ukr.Fis.J, 37, 30, 1992
   B.S. Dolbilkin and V.P. Lisin, Vopr. atom. nauki and techn.,4, 147, 1990
8. J.R. Calarco, Nucl. Phys. A569, 363, 1994
9. R.L. Gulbranson et al, Phys. Rev.C27, 470, 1983
10. S. Oikawa and K. Shoda, Nucl. Phys., A277, 301, 1977
11. B.S. Dolbilkin et al, Z. Phys., A311,107, 1988
12. B.S. Dolbilkin, Proc. VI Int. School. IENP, World Scientific, 260, 1990
13. L. Meyer-Schutzmeister et al, Phys.Rev. C17, 56, 1978
14. O.A. Rumyantsev and M.G.Urin, Isv. AN RAS, ser. Phys., 55, 866, 1991
15. D.J.DeAngelis et al, Phys. Rev. C52, 61, 1995
16. J.P. Fritsch et al, Phys. Rev. Lett. 68, 1667, 1992
17. K.T. Knopfle et al, Phys. Lett. B74, 191, 1978
18. L.A.A. Terremoto et al, Phys. Rev. C56, 2597, 1997
19. S.C. Fultz et al, Phys. Rev. C4, 149, 1971
20. H. Diesener et al, Phys. Lett. B352,201, 1995
21. B.S. Dolbilkin et al, Izv. AN SSSR, ser.phys. 55, 967, 1991
22. P. Neumann-Cosel, Nucl. Phys. A687, 132c, 2001

Origins of the Fragmentation of Multipole Resonances Strengths in Light Open Shell Nuclei

N.G. Goncharova, N.D. Pronkina

Skobeltsyn Institute of Nuclear Physics, Moscow State University, 119992 Moscow, Russia

1. Particle-core coupling version of Shell Model.

Discovered in photoabsorption reactions, the giant resonances now are properly studied in electroexcitation of nuclei, where the multipolarity of excitation operators varied with growing momentum transfer and a large number of multipole resonances (MR) was revealed. The theoretical efforts in description of the magnitudes, energy distributions and partial characteristics of MR were only partly successful. Distribution and values of the multipole resonances (MR) strengths in open shell nuclei, especially in deformed ones, represent a challenge to the theory.

The main hindrance in theoretical investigation of MR in open shell nuclei is that the usual microscopical approach based on the conception of "particle-hole" doorway states is unfit for such nuclei.

One of the possible means to build a set of basic configurations which could be used as doorway states in the microscopic description of multipole resonances in open shell nuclei is to take into account the distribution of the "hole" among the states of residual (A-1) nuclei. The information on these distributions could be extracted from direct pick-up reaction spectroscopy.

In this paper would be shown some results of MR calculations based on the "particle-core coupling" version of shell model (PCC SM).

In PCC approach wave functions of excited nuclear states are expanded to a set of low-lying states of (A-1) nuclei coupled with a nucleon in a free orbit [1]:

$$\left|J_f,T_f\right\rangle = \sum_{(J'),j'} \alpha_f^{(J'),j'} \left|(J'E'T')_{A-1} \times (n'l'j'):J_f,T_f\right\rangle \qquad (1)$$

The basic configurations for MR in nuclei under investigation were built on those states of residual nuclei which have non vanishing spectroscopic factor $S=C^2N$ of pick-up reaction :

$$\left|J_i,T_i\right\rangle = \sum_{(J'),j} C_i^{(J'),j} \left|(J'E'T')_{A-1} \times (nlj):J_i,T_i\right\rangle \qquad (2)$$

Without violating the Pauli principle, PCC basis can be extended to include the configurations coupled to low-lying collective excitations of the target nucleus.

Matrix elements of operators in the space of (1,2) configurations could be represented as sums of m.e. one-particle transitions multiplied on spectroscopic amplitudes Z:

$$\left\langle J_f T_f M_T \left\| \hat{B}^J_{TM_T} \right\| J_i T_i M_T \right\rangle = \sum_{i,J_i,J_f} < j_f \left\| \hat{O}^J_{TM_T} \right\| j_i > \sqrt{2}\sqrt{2J_i+1} \cdot Z^J_{TM_T}(j_f j_i) \quad . \qquad (3)$$

The information on the structure of final and initial states of nucleus is embedded in spectroscopic amplitudes Z:

$$Z^{J}_{TM_T}(j_f j_i) = \sqrt{(2T+1)(2T_i+1)(2J_f+1)}\left\langle T_i M_T T0 \middle| T_f M_T \right\rangle \times$$
$$\sum_{J'T'} C_i^{JT,j_i} \alpha_f^{J'T',j_f} (-1)^{J'-J_i+j_f-J} W(J_i J_f j_i j_f; JJ')(-1)^{T'-T_i+1/2-T} W(T_i T_f \frac{1}{2}\frac{1}{2}; TT'). \quad (4)$$

The matrix elements of PCC Hamiltonian involve the excitation energies of final nuclei levels:

$$\hat{H}_{ij} = (E' + \varepsilon_j + E_c)\delta_{ij} + \hat{V}_{ij}, \quad (5)$$

The estimation of magnitudes of residual interaction matrix elements was based as well on probabilities of pick-up reactions and corresponds to following scheme:

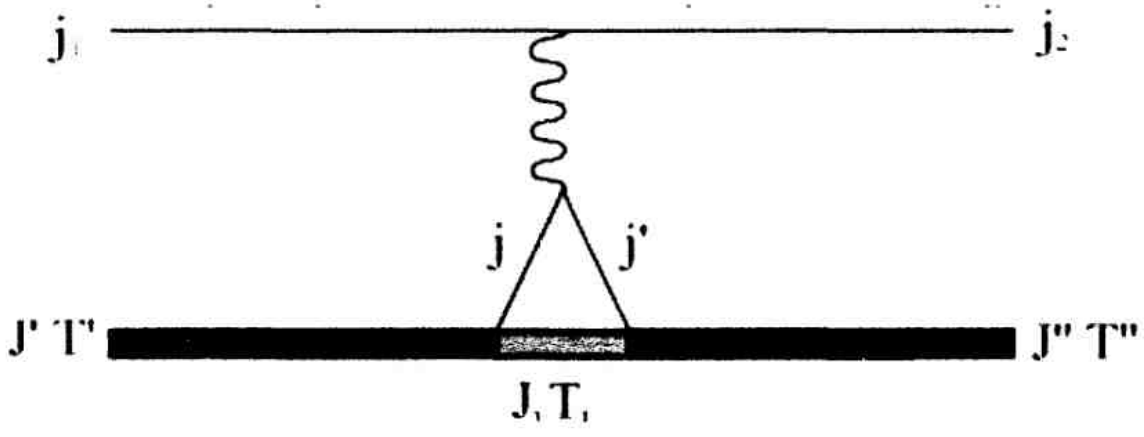

This paper represents PCC SM results for distributions of $1\hbar\omega$ isovector multipole resonance in photo- and electroexcitation cross section of sd-shell nuclei ^{22}Ne, ^{24}Mg ,^{26}Mg, ^{32}S, ^{34}S, ^{28}Si an ^{40}Ca. Some of these nuclei have considerable deformation in ground states. Their ground state deformations could not be measured directly. The parameters of deformation β for these even-eve nuclei, estimated in [2], vary from 0.25 (^{34}S) up to 0.6 (^{24}Mg). In this work were used spectroscopi factors for sd-shell nuclei presented in [3].

This paper endeavors to show that connection between direct and resonance reactions could be used to get rather realistic microscopic description of MR' strength fragmentation.

2. Form factors of multipole $1\hbar\omega$ resonances.

Cross sections of electroexcitation contain information on nucleus structure in the form factors:

$$\frac{d^2\sigma(e,e')}{d\Omega d\omega} = \frac{4\pi\sigma_M}{\eta_R}\left\{\left(\frac{q_\mu^4}{q^4}\right)F_L^2(q,\omega) + \left(\frac{q_\mu^2}{2q^2} + tg^2\frac{\theta}{2}\right)F_T^2(q,\omega)\right\} \quad (7)$$

Transverse form factor is a sum of multipole form factors

$$F_T^2(q,\omega) = \sum_{J=1}^{J_{max}}\left\{F_{EJ}^2(q,\omega) + F_{MJ}^2(q,\omega)\right\}$$

The form factors of multipole resonances (MR) in nuclear electroexcitation cross section are functions of momentum q transferred to nucleus and for the transverse part is determined by the interplay of orbital and spin components of nucleon current:

$$\hat{T}^{el}_{JM}(q)=\frac{q}{2M}\sum_{i=1}^{A}\{\hat{g}_i j_J(qr_j)\left[Y_J(\Omega_j)\times\hat{\sigma}_j\right]^{JM}+$$

$$+\frac{2\hat{e}_i}{q}(\sqrt{\frac{J+1}{2J+1}}j_{J-1}(qr_j)[Y_{J-1}(\Omega_j)\times\hat{\nabla}_j]^{JM}-$$

$$-\sqrt{\frac{J}{2J+1}}j_{J+1}(qr_j)\left[Y_{J+1}(\Omega_i)\times\hat{\nabla}_i\right]^{JM})\}$$

$$\hat{T}^{mag}_{JM}(q)=\frac{iq}{2M}\sum_{i=1}^{A}\{\hat{g}_j(\sqrt{\frac{J+1}{2J+1}}j_{J-1}(qr_i)\left[Y_{J-1}(\Omega_i)\times\hat{\sigma}_j\right]^{JM}-$$

$$-\sqrt{\frac{J}{2J+1}}j_{J+1}(qr_j)\left[Y_{J+1}(\Omega_i)\times\hat{\sigma}_j\right]^{JM})- \qquad ,(8)$$

$$-\frac{2\hat{e}_i}{q}\left(j_J(qr_j)\left[Y_J(\Omega_i)\times\hat{\nabla}_j\right]^{JM}\right)\}$$

where $\hat{e}=\frac{1}{2}+\frac{\hat{\tau}_3}{2}$; $\hat{g}=g_{Is}+g_{Iv}\hat{\tau}_3$.

The relative contribution of spin current component grows with momentum transfer and with multipolarity of MR. The higher miltipolarity dominate at higher transferred q. On the Fig. 1 are shown the q-dependence of summed transverse 1 ω EJ and MJ form factors calculated for ^{28}Si nucleus with HOWF. The positions of the maxima of summed form factors don't depend on nucleus.

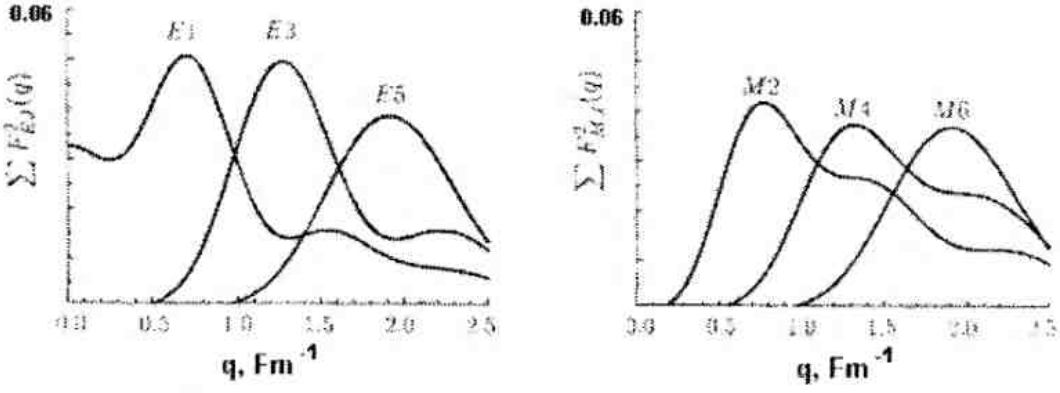

Fig 1

3. E1 resonances in photoexcitation

E1 resonances in photon absorption cross sections are determined by orbital nucleon current only. On the figures 2-7 are shown the results of PCC calculations for the form factors F^2 of dipole isovector resonances E1 at $q=E_\gamma$ together with experimental data for several sd-shell nuclei with non-filled shells. (F^2 of excited states with isospin $T=T_0$ - plain bars; $T=T_0+1$ – crossed bars).

The energy distribution of E1 form factors at photopoint in PCCSM reflects the peculiarities in spectroscopy of pick-up reaction [3] on target nucleus .

3.1. E1 in ^{22}Ne

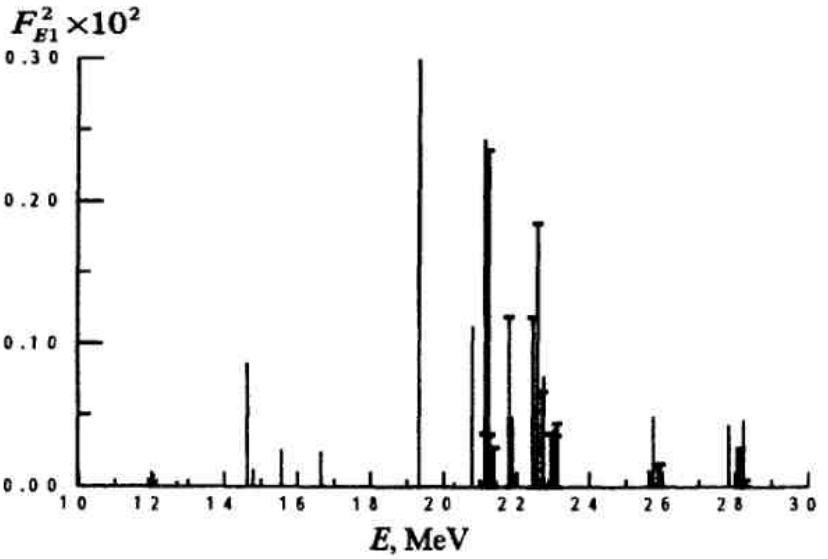

Fig. 2a

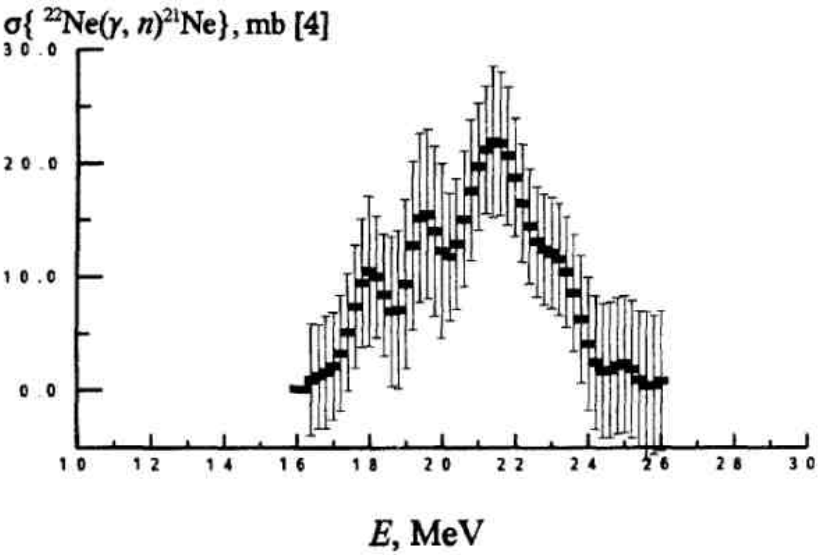

Fig. 2b

The PCC SM calculations for dipole resonance energy distribution in ^{22}Ne show that E1 strength is highly fragmented owing to isospin splitting and to wide spread of final nuclei states emerging in knockout reactions. The low energy part of Fig.2a (E< 17 MeV) is a result of transition from sd-shell.

3.2. E1 in ^{24}Mg

Among all even-even sd-shell nuclei ^{24}Mg has the largest deformation, displayed in low-lying states of rotational band. In collective description of dipole resonances in the deformed nuclei the peaks at about 20 and 25 MeV correspond to collective vibrations along and perpendicular to the axis of symmetry. PCCSM approach was based on spectroscopy factors of pick-up reactions [3]. The energy spread of states of residual nuclei with A-23, which were taken into account, is near 10 MeV.

$F_{E1}^2 \times 10^2$ $\sigma(\gamma, p)$, mb [5]

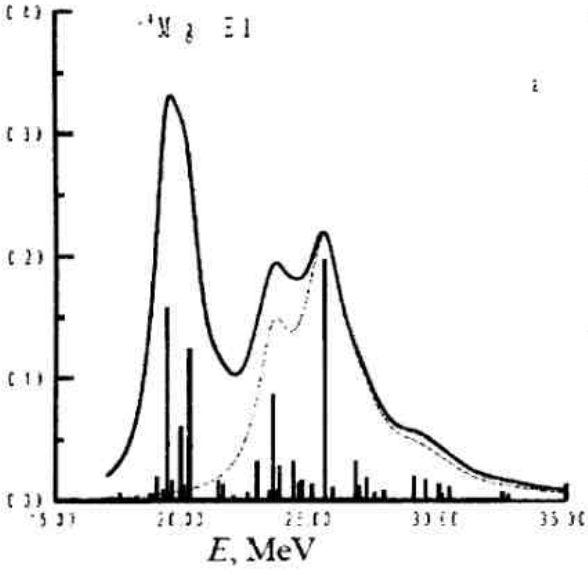

Fig. 3*a*

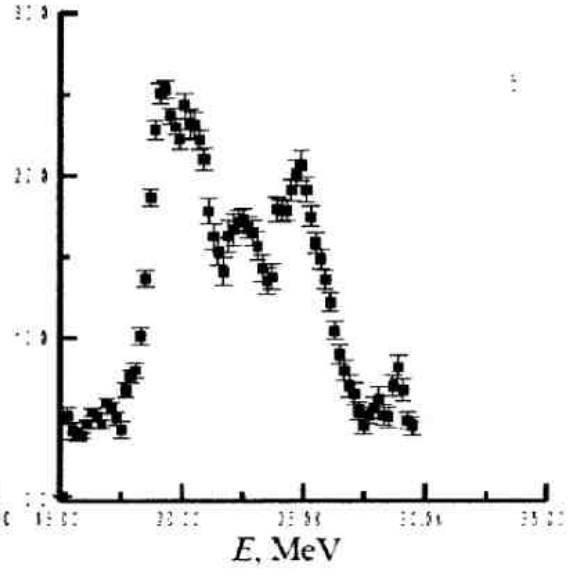

Fig.3*b*

The peak at 19-20 MeV is populated by transitions from $1d_{5/2}$ subshell, the 24 MeV peak is due to the transitions from 1p shell. The intermediate maximum constructed by transitions from both sd and 1p shells, with considerable contributions of configurations built on 2s and $1d_{3/2}$ hole states.

3.3. E1 in ^{26}Mg

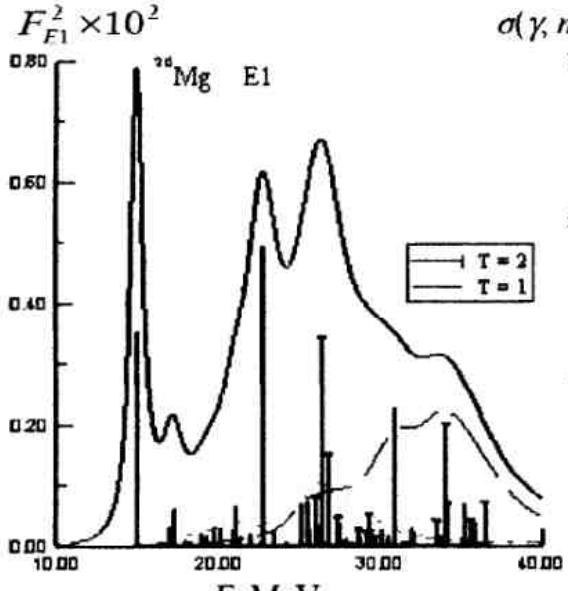

Fig.4*a*

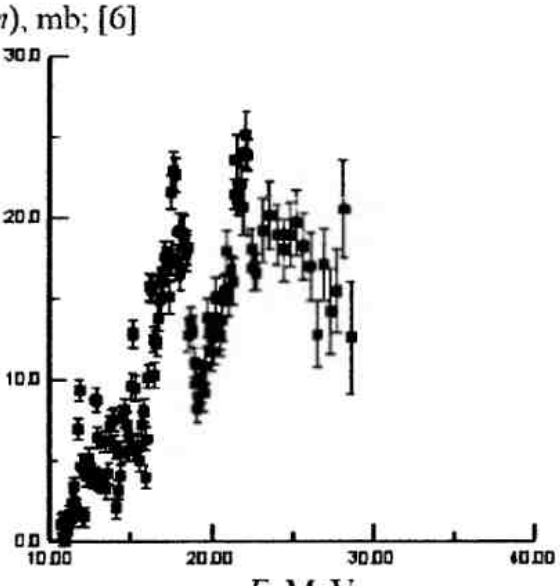

Fig.4*b*

The dipole resonance in ^{26}Mg nucleus has two isospin branches (T=1 – plain bars on the fig.4a and T=2 – crossed bars). The upper part of E1 energy distribution is enhanced by transitions from 1p shell with main peaks at ~31 and 35 MeV. The group of maxima at about 25 MeV contains configurations built on 2s and $1d_{3/2}$ subshells states; (γ, n) reactions in this region should populate not only $5/2^+$ but as well $1/2^+$ and $3/2^+$ states of ^{25}Mg.

3.6. E1 in S-32

$F_{E1}^2 \times 10^2$

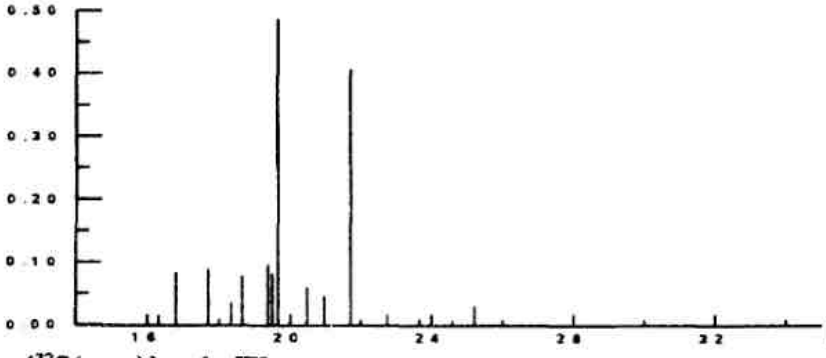

Fig.5a

$\sigma\{^{32}S(\gamma,n_{tot})\}$, mb [7]

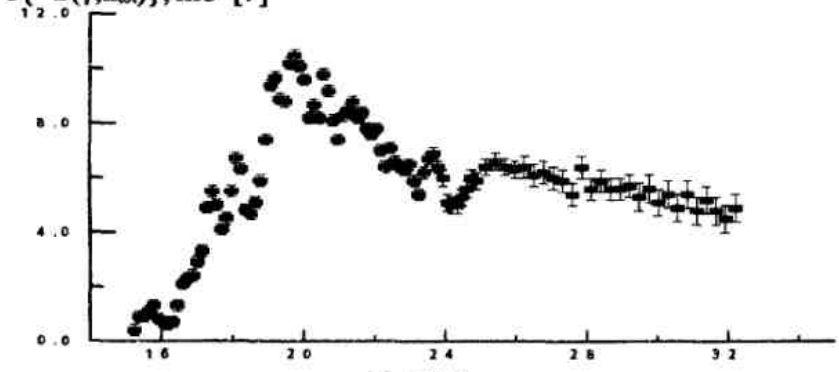

Fig.5b

E, MeV

3.6. E1 in S-34

$F_{E1}^2 \times 10^2$

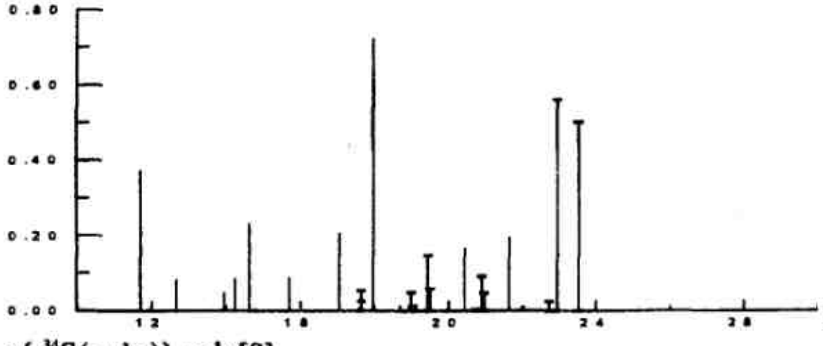

Fig.6a

$\sigma\{^{34}S(\gamma,abs)\}$, mb [8]

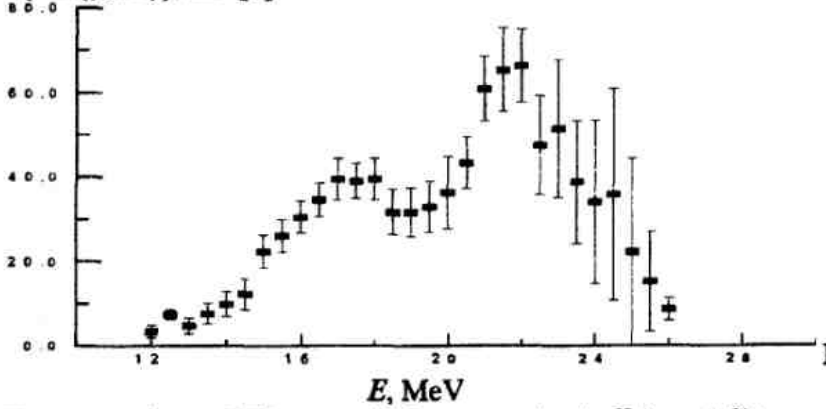

Fig.6b

E, MeV

The comparison of E1 strengths fragmentation in ^{32}S and ^{34}S reveals the influence of isospin splitting and the final nuclei energy spreading on the structure of dipole resonance.

4. M2 in sd-shell nuclei

On the Fig 7 are shown the results of PCC SM calculations for M2 form factors in ^{32}S at momentum transfer q=0.6 Fm^{-1} with comparison with the data of S-DALINAC experiment [10] performed up to energy excitation E=14 MeV. The renormalized value of g-factor was used. The spreading of the hole among 12 states of ^{31}S reveals in fragmentation of M2 strength.

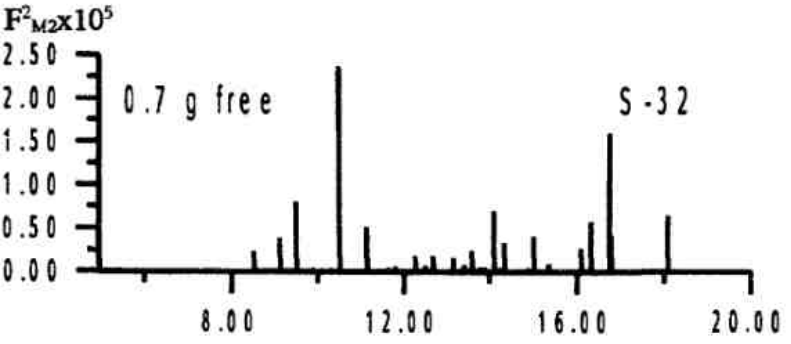

Fig.7a

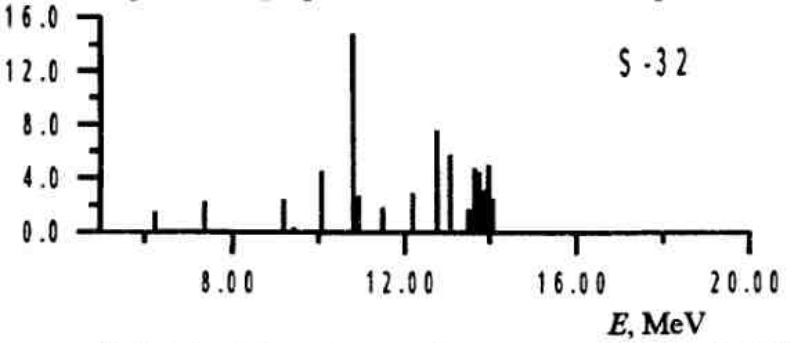

Fig.7b

In the excitation of magnetic resonances main role belongs to spin-multipole operators. For M2 resonances there are spin-dipole and spin-octupole operators in (8); the first one dominates at approximately $0<q<1Fm^{-1}$, the second one at $q>1Fm^{-1}$. The role of orbital current contribution into matrix elements of M2 transitions was estimated for M2 form factor $F_{M2}\times10^3$ (Fig.8) taking into account the effects of interference of spin and orbital parts of M2 operator ($g=0.7g_{free}$). It is clear that the orbital current plays a very significant role in M2 excitation (the similar results were obtained for orbital current contribution into M2 resonances in ^{28}Si and ^{24}Mg). This conclusion of shell model approach confirms the results of [11] where direct evidence for orbital magnetic quadrupole twist mode in nuclei was obtained.

Contributions of spin and orbital currents into matrix elements of M2.

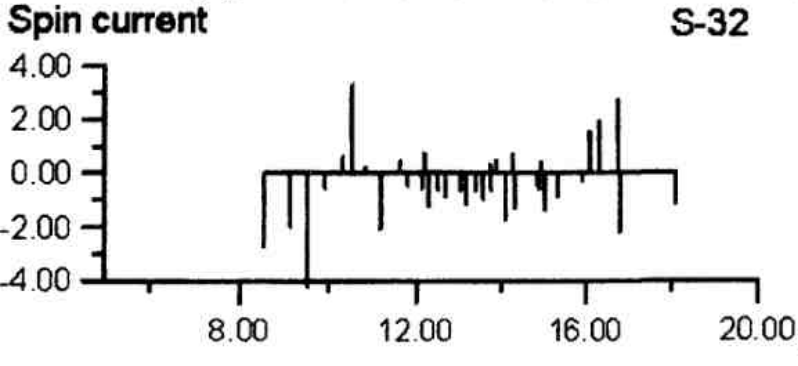

Fig 8a.

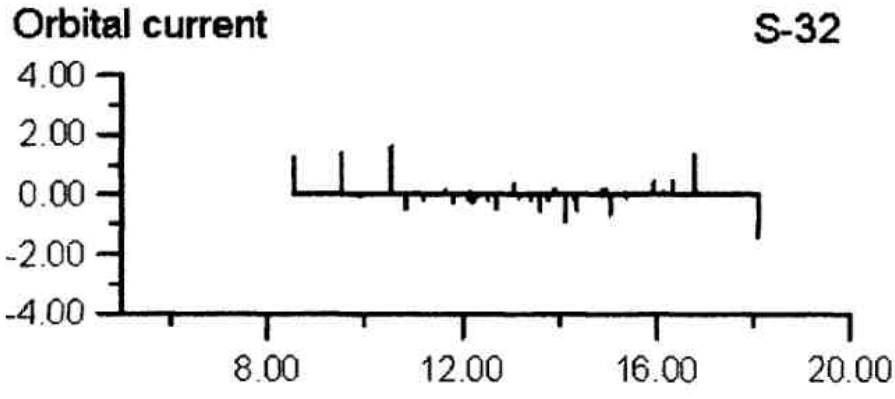

Fig 8b.

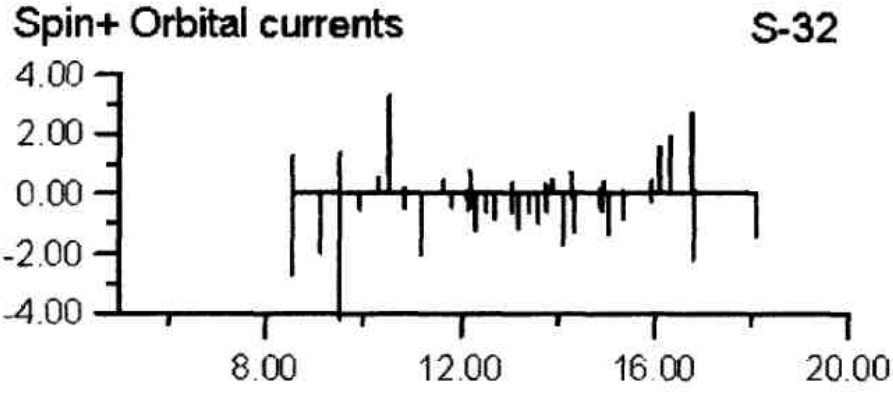

Fig 8c.

In the Fig.9 is shown the energy distribution for reduced probability B(M2) in ^{24}Mg. The fragmentation of M2 strength reflect the configurational splitting of resonance: the peaks in the 10 -16 MeV region of nuclear excitation correspond to transitions from sd-shell, the resonances at E>16 MeV are almost completely due to transitions from 1p shell. Unfortunately the S-DALINAC experiment for this nucleus was performed in the narrow range 11<E<13.4 MeV only.

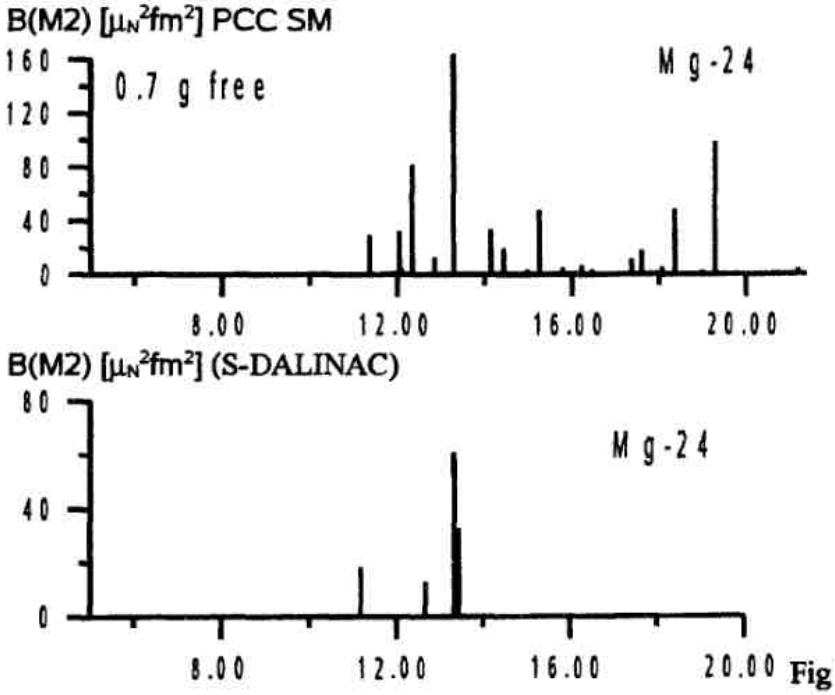

Fig 9.

4. M6 in sd-shell nuclei

The $1\hbar\omega$ resonances with maximal spin of magnetic electroexcitation reveal the influence of the hole distribution on MR fragmentation most obviously. The "doorway" states of M6 in sd-shell correspond to the transition $1d_{5/2} \rightarrow 1f_{7/2}$ only.

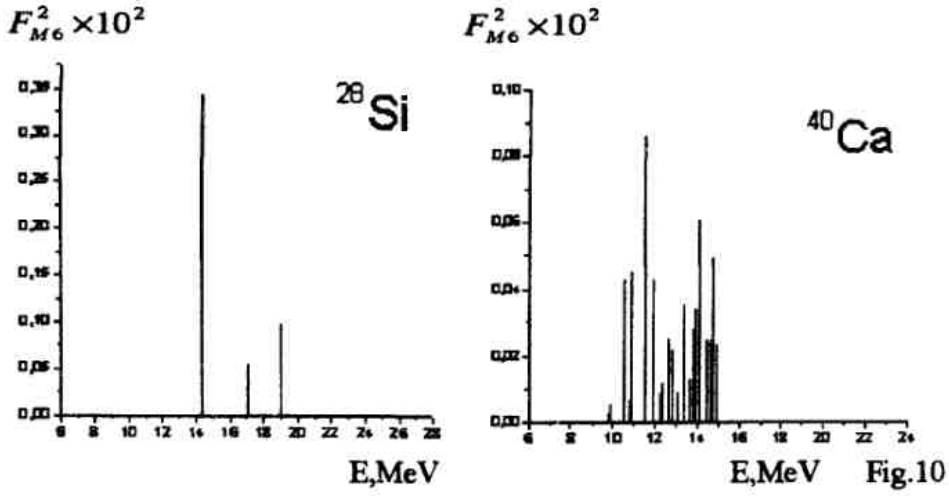

Fig.10

The role of hole spreading manifests in the fragmentation of 6^- T=1 states in ^{28}Si and ^{40}Ca (fig.10) according to PCCSM at q=1.8 Fm^{-1}. The M6 in ^{28}Si was the first of explored MR with maximal spin value. In (e,e') reaction on ^{40}Ca M6 was not detected. It is a result of very wide scattering of $5/2^+$ hole on 23 states in A=39 nuclei in a energy range from 2.8 up to 9.5 MeV and the following fragmentation of 6^- T=1 strength in ^{40}Ca nucleus.

The results of PCC calculations for M6 excited states in ^{26}Mg at momentum transfer q=1.8 Fm^{-1} are shown in the Fig.11 together with experimental data. (Plain bars represent T=1, crossed bars - T=2 states)

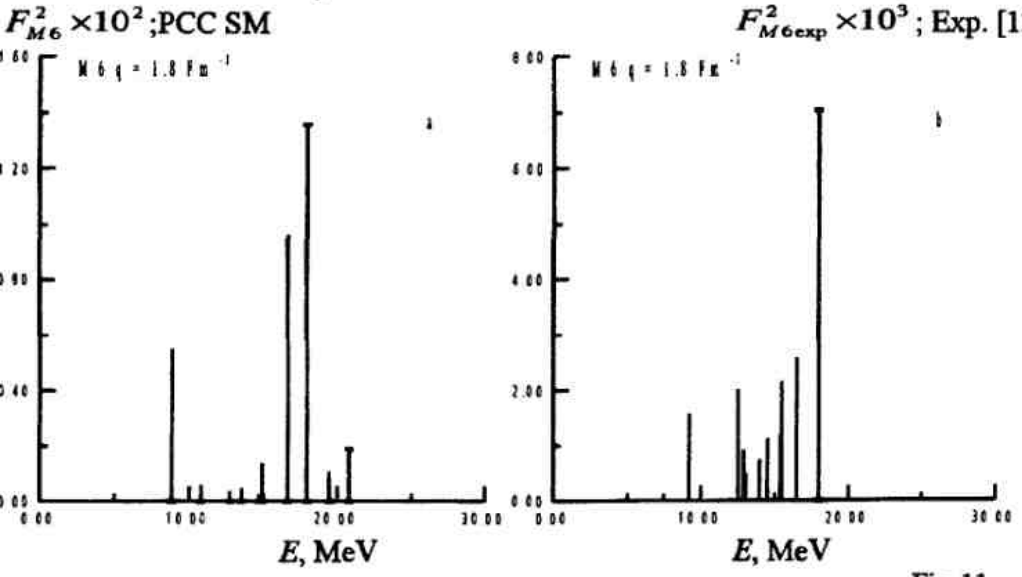

Fig.11

SUMMARY

- The deviation of (A) nucleus from closed shells or subshells reveals in a wide range of energy distribution for "hole" among the (A-1) nuclei states. In the PCC version of SM these distributions are taken into account in the microscopic description of multipole resonances.
- The energy spread of final nuclei states is the main origin of the multipole resonances fragmentation in open shell nuclei. Comparison of PCC SM results with experimental data on MR confirms the validity of this approach for a range of momentum transfer from "photopoint" up to $q \approx 2$ Fm^{-1}.
- The assumption that some very valuable information on MR in excited deformed nucleus is embedded in direct reactions data proved to be right.

REFERENCES

1. N.G.Goncharova, N.P.Yudin, Phys. Lett.**B29** (1969) 272.
2. S. Raman *et al*, Atomic Data & Nucl.Data Tables **78** (2001) 1.
3. P.M.Endt, Nucl. Phys. **A521** (1990) 1.
4. V.V.Varlamov, M.E.Stepanov, BRAS Physics **64** (2000) №3.
5. B.S. Ishkhanov *et al*, Nucl. Phys. **A186** (1972) 438.
6. S.C. Fultz, R.A. Alvarez, B.L. Berman *et al*, Phys.Rev. C **4** (1971) 149.
7. S.C. Fultz, J.T. Caldwell, B.L. Berman *et al*, Phys.Rev. **143** (1966) 790.
8. A.Veyssiere, H.Beil *et al*, Nucl. Phys. **A227** (1974) 513.
9. J. Vernotte *et al* , Nucl.Phys.**A655**(1999)415
10. F. Hoffmann, Diplomarbeit, IKP TUD (1997).
11. B. Reitz *et al,* Phys.Lett.B **532**(2002)179.
12. B.L. Clausen, R.J. Peterson, R.A. Lindgren, Phys. Rev. **C38** (1988) 589.

EXCITATION OF LOW-LYING STATE BY E3 TRANSITION REACTION WITH REAL PHOTONS

O.S. Shevchenko[1], Yu.M. Ranyuk[1], A.M. Dovbnya[1], V.I. Noga[1], E.L. Kuplennikov[1], A.A. Nemashkalo[1], I.G. Goncharov[1], V.N. Borisenko[1], V.Yu. Ponomarev[2]

[1]National Science Center "Kharkiv Institute of Physics and Technology", 61108, Kharkiv, Ukraine; [2]Institut für Kernphysik, Technische Universität Darmstadt, D-64289 Darmstadt, Germany

Abstract

The yield of the isomeric state ^{117m}Sn (E_{iso} = 314.58 keV) has been measured in (γ, γ') reaction by activation method with the bremsstrahlung end-point energy from 2.1 to 3.0 MeV. Only one intermediate state (IS) responsible for the isomer feeding has been found. The excitation energy of the IS (2.25 ± 0.05) MeV and photoproduction integral cross section (0.022 ±0.002) eVb have been deduced. Microscopic calculations within the Quasiparticle-phonon model have been performed to learn on the IS structure. We conclude that the IS is excited in the present experiment by the E3-transition.

Key words: ^{117}Sn(γ,γ')^{117m}Sn, E_0 = 2.1 - 3.0 MeV, deduced isomer integrated cross section, Quasiparticle-phonon model calculations.

PACS: 25.20.Lj, 27.60.+j

Isomers in atomic nuclei are the levels with the total angular momentum J_{iso} significantly different from the one of the ground state $J_{g.s.}$. They appear in the spectra due to the shell structure of a mean field and their excitation energy in odd-mass nuclei does not exceed a few hundred keV. For these reasons, decay
of isomers into the ground state is strongly hindered and their lifetime vary for milliseconds to days depending on the spin difference $\Delta J_{iso} = |J_{g.s.} - J_{iso}|$.

Isomers are populated after decay of intermediate state(s) (IS) with the energy of 2-4 MeV and finite branching to the isomeric level. These IS are excited, e.g., by bremsstrahlung radiation with the end-point energy of 2-5 MeV. The previous experiments [1,2,3,4] have already shown that the number of such IS which are linked to both the ground and isomeric states, is very small, i.e. one-two states per MeV in spherical nuclei. There was also a set of experiments in which the isomeric states were populated in the (γ,n) reaction via excitation and cascade decay of the giant dipole resonance [5,6].

Up to now, analysis of the IS excited in the bremsstrahlung technique has been performed only for nuclei with ΔJ_{iso} = 3, 4 involving *E1-E2* (or *E2-E1)* and *E2-E2* sequences for the isomer population [1,4,7]. The best studied example is ^{115}In [2,3,7,8,9] for which this type of experiments have been supplemented by nuclear resonance fluorescence (NRF) ^{115}In(γ,γ')^{115m}In studies [7].

In this letter we report our results on the isomer photoproduction in ^{117}Sn (the isotopic abundance is 7.68 %). It has the stable ground state with the spin and parity $J^{\pi}_{g.s.} = 1/2^{+}$. The isomeric state in this nucleus has the excitation energy E_{iso} = 314.58keV and $J^{\pi}_{iso} = 11/2^{-}$. Thus, the spin difference ΔJ_{iso} = 5 and at least the *E2 - E3* sequences is need to populate the isomer from the ground state. The $T_{1/2}$ value is very large for the isomeric state and equals to 13.60 days.

The decay scheme of the isomer in ^{117}Sn is presented in Fig. 1. Due to the presence of the J^{π} = 3/2+ level at E_x = 158.56 keV, the isomer decays predominately to this level by the M4 internal conversion process with the relative probability (γ-line

intensity) of I_γ = 2.113. For the direct decay to the ground state, I_γ = 0.000423. The 158.56 keV level decays into the ground state with I_γ = 86 by M1 + *E2* γ-transition.

The only work in which the ^{117m}Sn IS integrated cross sections have been determined is Ref. [3]. The experiments have been performed for the bremsstrahlung endpoint energies 4 and 6 MeV. The obtained integrated cross sections *(σI')* are (3.20 ±0.47) eVb and (8.80 ±0.26) eVb, respectively. Unfortunately, low experimental resolution did not allow the IS determination.

Our experiment have been carried out in the National Science Center "Kharkiv Institute of Physics and Technology" at the 3 MV electrostatic electron accelerator ELIAS having an energy resolution 50 kV and a beam intensity up to 500μ*A*. The investigation of the isomeric states population have been performed using activation technique.

Bremsstrahlung spectra have been generated by electrons irradiating of 0.5 mm

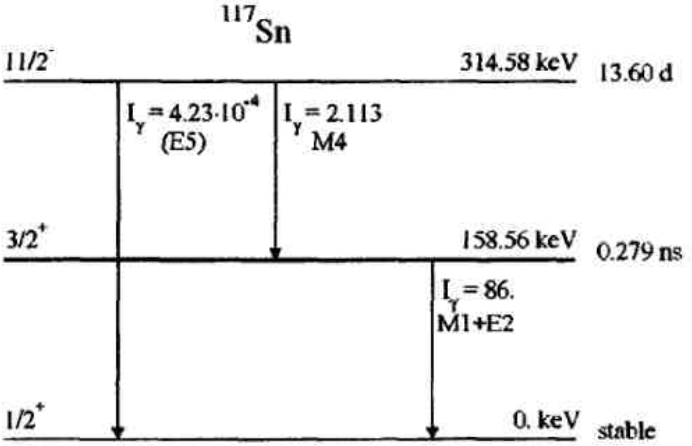

Fig. 1. Decay scheme of the isomeric $J^{\pi}_{iso} = 11/2^-$ state in ^{117m}Sn [10]. See text for details.

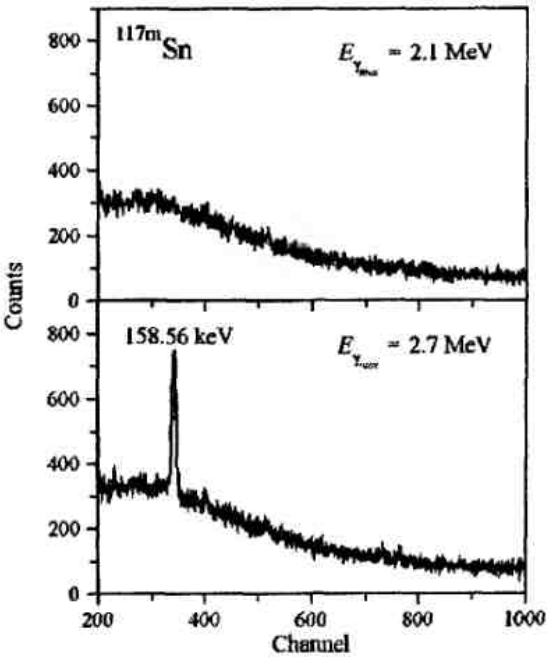

Fig. 2. γ-ray spectrum measured after bremsstrahlung irradiation of Sn target with the endpoint energy of 2.1 (top) and 2.7 MeV (bottom).

thickness Ta converter. Samples of natural Sn (0.2mm thick and 15mm in diameter) have been placed in the photon beam behind the converter. The photoactivities have been measured with Ge(Li) detector by observing the 158.56 keV γ-rays emitted in the cascade of the isomeric level decay. The detector sensitive volume is 50 cm^3 and the energy resolution is 2.5 keV for 1332 keV of ^{60}Co source. The schematic layout of photoactivation experiment and standard procedure for activation data development is described elsewhere [9].

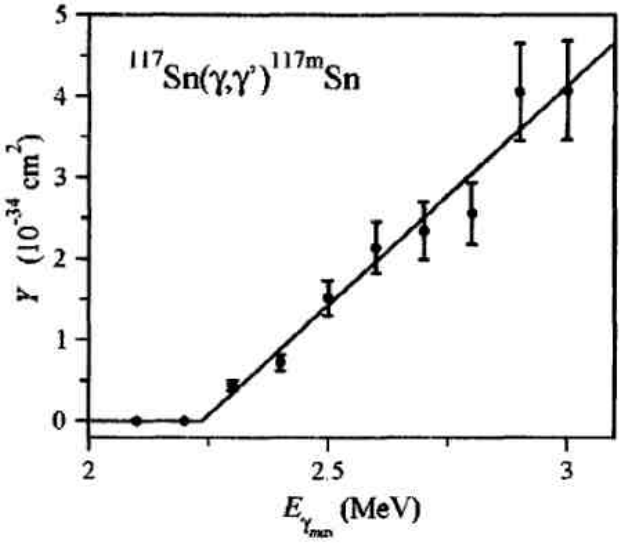

Fig. 3. The ^{117}Sn isomer yield as a function of the bremsstrahlung end-point energy. The

obtained spectra for two different values of the end-point energy $E_{\gamma_{max}}$ are shown in Fig. 2. The measurements have performed with the electron beam current I = 170 μA, irradiation time t_{irr} = 240 and 120 min, cooling time t_c = 28 and 31 min and spectra measurement time t_m = 60 min for $E_{\gamma_{max}}$ = 2.1 and 2.7 MeV, respectively.

The spectrum in the bottom part of Fig. 2 is typical for the end-point energy $E_{\gamma_{max}}$ > 2.25 MeV. The strong sharp line at 158.56 keV indicates that the $J^{\pi} = 3/2^+$ level at this energy is fed after cooling by decay of the isomeric state. The absence of such a line in the top part of Fig. 2 means that the isomer is not populated for $E_{\gamma_{max}}$ < 2.25 MeV.

The measured isomer yield $Y\left(E_{\gamma_{max}}\right)$ is presented in Fig. 3 as a function of the bremsstrahlung end-point energy. This quantity is defined as the number of activated nuclei N_{iso} normalized to the number of target nuclei N_T per cm^2 and the number of incident electrons N_e:

$$Y\left(E_{\gamma_{max}}\right) = \frac{N_{iso}\left(E_{\gamma_{max}}\right)}{N_t N_e} \qquad (1)$$

The error bars include systematic and statistical errors. Their average value is 10-15%. The solid line in Fig. 3 represents the χ^2 fit of the data points assuming the linear dependence of the isomer yield as a function of the end-point energy.
The linear dependence of the isomer yield breaks each time when the end-point energy of the bremsstrahlung radiation reaches the energy of an IS state feeding the

isomer. We conclude from the data in Fig. 3 that there is only one IS of this type in ^{117}Sn in the energy interval between 2 and 3 MeV. The excitation energy of this state is 2.25 ± 0.05 MeV.

The energy of the IS in ^{117}Sn obtained in the present experiment, is very close to the energy of the first 3^- state in the core ^{116}Sn nucleus which is 2.266 MeV. This allows us to suppose that the IS is excited from the ground state by the E3-transition.

The isomer yield can be also calculated as

$$Y\left(E_{\gamma_{max}}\right) = \int_{E_c}^{E_{\gamma_{max}}} \sigma_\gamma\left(E_\gamma\right) N\left(E_\gamma, E_{\gamma_{max}}\right) dE_\gamma \qquad (2)$$

where E_c is a cutoff energy, $\sigma_\gamma(E_\gamma)$ is the reaction cross section as a function of the photon energy E_γ and $N\left(E_\gamma, E_{\gamma_{max}}\right)$) represents the continuous bremsstrahlung spectral density with the end-point energy $E_{\gamma_{max}}$.

Accounting for the fact that only one IS has been found in the present experiment and assuming a small width of this level, reduces Eq. (2) to:

$$Y\left(E_{\gamma_{max}}\right) = \left(\sigma\Gamma\right)_{iso} N\left(E_{IS}, E_{\gamma_{max}}\right). \qquad (3)$$

The number of photons $N(E_{IS}, E_{\gamma max})$ with the IS energy E_{IS} for each bremsstrahlung end-point energy in Fig. 3 has been calculated by mathematical modeling of the bremsstrahlung spectra with GEANT 3.21 program [11]. The number of launches was 10^7 and we used E_c = 0.5 MeV and the interval of grouping of 0.01 MeV.

The integrated cross section for the isomer population in ^{117}Sn has been determined as (0.022 ± 0.002) eVb. This value is about two orders of magnitude lower than $(\sigma\Gamma)_{iso}$ for isomer population in nuclei with ΔJ_{iso} = 3 and 4 reported in Ref. [1] for ^{81}Br, Ref. [4] for ^{89}Y and Ref. [2] for ^{115}In. It has been concluded from theoretical analysis that the IS in these nuclei are excited from the ground state either by non-collective *E1*- transition in ^{81}Br [1] or by collective *E2*- transition in ^{89}Y [4] and ^{115}In [7]. Very small value of $(\sigma\Gamma)_{iso}$ in ^{117}Sn supports our guess that the IS is excited in this nucleus by the *E3*-transition and calls for theoretical analysis of low-lying states in ^{117}Sn.

Such an analysis has been performed within the Quasiparticle-phonon model (see for details Refs.[12,13,14]) which has been very successful in application to studies of the isomeric state population in nuclei with ΔJ_{iso} = 3 and 4 [1,4,7]. The ground and excited states of ^{117}Sn have been described by the wave function which includes quasiparticle-, [quasiparticle . 1 phonon]- and [quasiparticle . 2 phonons]-configurations. The model parameters have been adjusted to reproduce the experimental B(E2) and B(E3) values of the 2^+_1 and 3^-_1 states, respectively, in the neighboring even-even ^{116}Sn core nucleus.

Table 1
Properties of the IS in ^{117}Sn responsible for the isomer feeding.

	Energy (MeV)	$(\sigma\Gamma)_{iso}$ (eV b)
Experiment	2.25 ± 0.05	0.022 ± 0.002
Theory	2.44	0.026

The calculation reproduce very well the excitation energy of the $3/2^+_1$ state in ^{117}Sn (0.15 MeV) and slightly underestimate the energy of the isomeric $11/2^-_1$ state (0.17 MeV). Among many excited state in the energy interval between 1.5 and 3.5 MeV, we have found only one state which is linked to both, the ground and isomeric states. It is $7/2^-$ state at the excitation energy of 2.44 MeV with the wave function:

$$\left|7/2^-\right\rangle = 0.19\cdot 2f_{7/2} + 0.90\cdot\left[s_{1/2}\otimes 3^-_1\right]_{7/2} - 0.14\cdot\left[1h_{11/2}\otimes 2^+_1\right]_{7/2} + \ldots \qquad (4)$$

where 2^+_1 and 3^-_1 mean the lowest 2^+ and 3^- phonons of the core nucleus excitation.

This state is indeed excited from the ground state by the E3-transition to the second component of its wave function (4). Although this is the main component of the wave function, the state decays predominantly to the isomeric state from its third component by the E2-transition with the branching ratio $\Gamma_{iso}/\Gamma_{tot} = 0.97$. The calculated value of the cross section for the isomer population in ^{117}Sn(γ,γ') reaction via this state is 0.026 eVb and agrees very well with the experimental findings.

One finds in literature [10] two levels in ^{117}Sn at 2160 and 2280 keV, both of them have been assigned as $5/2^-$, $7/2^-$ from the $L = 3$ transfer in ^{117}Sn(p,p'). Apparently, the above discussed $7/2^-$ state in calculation corresponds to one of them. The calculation also yields $5/2^-$ state at 2.50 MeV with the $[3s_{1/2}\otimes 3^-_1]5/2^-$ configuration as the main component in its wave function. But this state has no branching to the isomeric state. Which of the levels at 2160 and 2280 keV is our IS can be distinguished in the NRF experiment from the energy of the line at $E_{IS} - E_{iso}$.

To conclude, the population of the isomer in ^{117}Sn has been studied in reaction with the bremsstrahlung radiation with the end-point energy from 2.1 to 3.0 MeV. Only one intermediate state responsible for the isomer feeding has been found in this energy interval. The properties of this state from the present experiment and theoretical analysis are summarized in Table 1. In our opinion, we have convincing evidence that this IS is excited in this extremely selective reaction by the E3-transition from the ground state.

[1]V.Yu. Ponomarev et al., Journ. of Phys. G: Nucl. Part. Phys. 16 (1990) 1727.
[2] P. von Neumann-Cosel et al., Phys. Lett. B 266 (1991) 9.[3] J.J. Carrol et al., Phys. Rev. C 43 (1991) 1238.
[4] M. Huber et al., Nucl. Phys. A 559 (1993) 253.
[5] Yu.P. Gangrskij, A.P. Tonchev, N.P. Balabanov, Phys. Part.& Nucl. 27 (1996) 426.
[6] N. Tsoneva et al., Phys. Rev. C 61 (2000) 044303.
[7] P. von Neumann-Cosel et al., Z. Phys. A 350 (1995) 303.
[8] D. Belic et al., Nucl. Instr. Meth. A 463 (2001) 26.
[9] O.S. Shevchenko et al., Problems of atomic science and technology. Series: Nuclear physics investigations 2005, N6, (45), p. 30-34.
[10] R.B. Firestone, Table of Isotopes, Eight edition: 1998.
[II] Application Software Group, GEANT – Detector description and simulation tool Version 3.21, CERN program library long writeup W5013, (CERN, Geneva, 1994).
[12] V.G. Soloviev, Theory of Atomic Nuclei : Quasiparticles and Phonons (Inst. of Phys. Publ., Bristol and Philadelphia, 1992).
[13] S. Gales, Ch. Stoyanov, A. I. Vdovin, Phys. Rep. 166 (1988) 125.
[14] J. Bryssinck et al., Phys. Rev. C 62 (2000) 014309.

MULTIPARTICLE PHOTONUCLEAR REACTIONS IN ^{203}Tl NUCLEUS

Zh.A. Asanov [1], A.N. Ermakov [2], B.S. Ishkhanov [2], I.M. Kapitonov [1], Kyaw Kyaw Htun [1], I.V. Makarenko [1], D.R. Salakhutdinov [1], V.A. Chetvertkova [1]

1. Lomonosov Moscow State University, the faculty of physics, Moscow, Russia

2. Skobeltsyn Institute of Nuclear Physics, Lomonosov Moscow State University, Moscow, Russia

The intensive maximum in photoabsorbtion cross sections – giant dipole resonance (GDR) – is a universal feature of atomic nuclei.

In the energy region of GDR maximum it decays as a rule by the emission of one neutron. Nowadays this field of cross sections is well known, there is a lot of experimental data.

At the γ-quanta energies more then 20-30 MeV photonuclear reactions with the emission of several nucleons are the most probable. The decay of excited nuclear states seems to occur primarily by the emition of neutrons in γ-quanta energy region of 30-70 MeV. Final nuclei produced are β+-radioactive. Such reactions are not well investigated, their mechanism is unknown. The subject of our research is to get experimental data about multiparticle photonuclear reactions. Nowadays multiparticle photonuclear reaction cross sections for the most nuclei are unknown [1]. The article deals with the experimental determination of yields of the following multiparticle photonuclear reactions: ^{203}Tl(γ, n)^{202}Tl, ^{203}Tl(γ, 2n)^{201}Tl, ^{203}Tl(γ, 3n)^{200}Tl, ^{203}Tl(γ, 4n)^{199}Tl.

The experiment was carried out using bremsstrahlung from the electron racetrack microtron RTM-70 in Skobeltsyn Institute of Nuclear Physics, Moscow State University [2]. RTM-70 microtron is a unique compact accelerator with maximum electron energy of 70 MeV, built with the use of permanent magnets based on rare-earth magnetic materials. It can be used as a source of bremsstrahlung with maximum γ-quanta energy of 70 MeV allowing to produce nuclei different from initial nuclei by up to 8 nucleons.

The experimental scheme is shown at fig. 1.

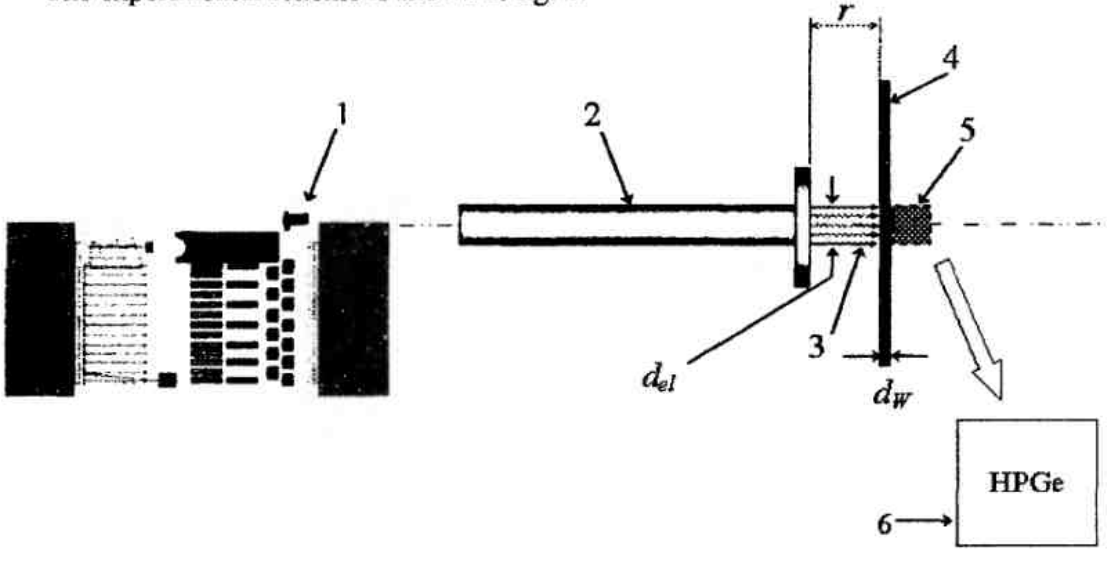

Fig. 1. Experiment scheme. 1 – microtron, 2 – external accelerator channel, 3 – electron beam, 4 – convertor, 5 – investigated Tl sample, 6 –HPGe detector.

Thallium (Tl) was the investigated sample. Stable Thallium isotopes have more then 200 nucleons, that's why photonuclear reaction yields are high and photonuclear reaction thresholds are low in Thallium isotopes.

The investigated sample with mass of 3.5 g was made of Tl NO_3. The sample consisted of the natural mixture of Thallium isotopes (^{203}Tl - 29.5 % , ^{205}Tl - 70.5 %). The Thallium target was irradiated with bremsstrahlung with maximum γ-quanta energy E_γ^m = 50 MeV during 1 h. The microtron electron beam current was 10 мА. The electron beam diameter (fig. 1) d_{el} = 10 mm, Tungsten converter thickness d_W = 2.5 mm. The spectra of residual activity of irradiated Tl sample were recorded by HPGe detector with the efficiency of 30 %. The detector energy resolution was 1.1 keV (for the 122 keV γ-ray), 2.0 keV (for the 1332 keV γ-ray). The spectra of residual activity of the sample were recorded during 5.5 h within 2 h after the activation. A series of 11 spectra measurements was made in order to measure half-lifes $T_{1/2}$ and to identify radioactive isotopes produced. Each spectrum measurement was made during 30 min. Half-lifes spanning the region from some hours to tens hours were measured. The summary spectrum measured during 5.5 h is shown in fig. 2.

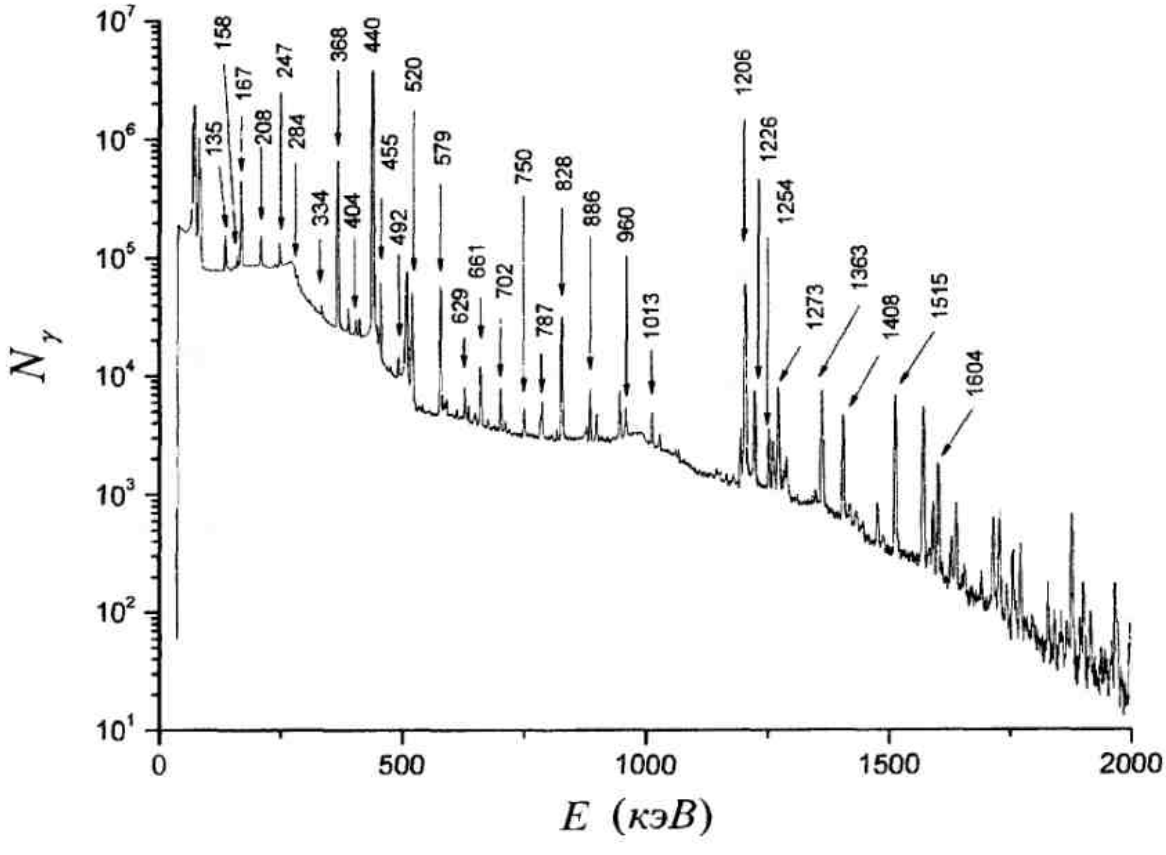

Fig. 2. Experimental γ-spectrum.

The natural mixture of Tl isotopes contains comparable values of ^{203,205}Tl isotopes. Photonuclear reactions in these isotops lead to producing the same isotopes. For example, ^{202}Tl nucleus can be produced both in ^{203}Tl(γ, n)^{202}Tl and ^{205}Tl(γ, 3n)^{202}Tl reactions. As the cross sections ratio σ(γ, n) / σ(γ, 3n) in this energy field is about ~ 50 ÷ 100, corresponding reactions in ^{205}Tl are suppressed in coparison with reactions in ^{203}Tl, because more nucleons are emitted. Therefore in the experimental data analysis the producing of the radioactive Tl isotopes was supposed to be caused only by reactions in ^{203}Tl nucleus.

In the experiment the maximum γ-quanta energy (E_γ^m = 50 MeV) exceeds thresholds of photonuclear reactions with the emission of up to 4 nucleons in the investigated ^{203}Tl nucleus.

γ-Peaks appropriate to ^{203}Tl(γ, n)^{202}Tl, ^{203}Tl(γ, 2n)^{201}Tl, ^{203}Tl(γ, 3n)^{200}Tl, ^{203}Tl(γ, 4n)^{199}Tl reactions are observed in the experiment (table 1). The table contains photonuclear reactions, their thresholds, half lifes of final β-radioactive nuclei. The energies and intensities of experimental γ-lines appropriate to these reactions and the nature of γ-transitions in $^{199\text{-}202}$Hg (energies (keV), spin-parity of initial and final states) are also shown. The accuracy of experimental values for intensities for the most γ-lines is about 1 % (for γ-line intensities ~ 10^4 – 10^5 counts). For γ-line intensities ~ 10^2 – 10^3 counts the accuracy increases to 10 %, for the most intensive γ-peaks the accuracy is no more then 0.1 %. Nuclear state and γ-transition energies are shown with the accuracy of ~ 1 keV.

The most intensive γ-transitions in ^{202}Hg, ^{201}Hg, ^{200}Hg, ^{199}Hg are observed in experimental spectra. The appropriate γ-transitions schemes for these nuclei are shown in fig. 3, 4. Experimental data allows to identify the decays of nuclei produced in multiparticle photonuclear reactions with great validity: there are 16 γ-lines corresponding to ^{203}Tl(γ, 3n)^{200}Tl and 10 γ-lines corresponding to ^{203}Tl(γ, 4n)^{199}Tl in the spectra.

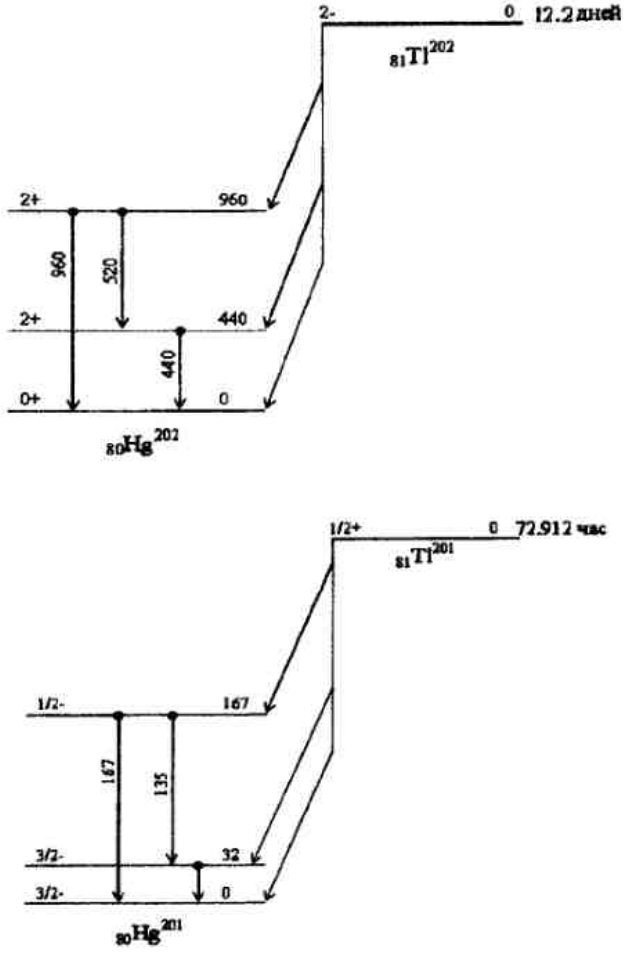

Fig. 3. Decay schemes of ^{202}Tl and ^{201}Tl nuclei ground states.

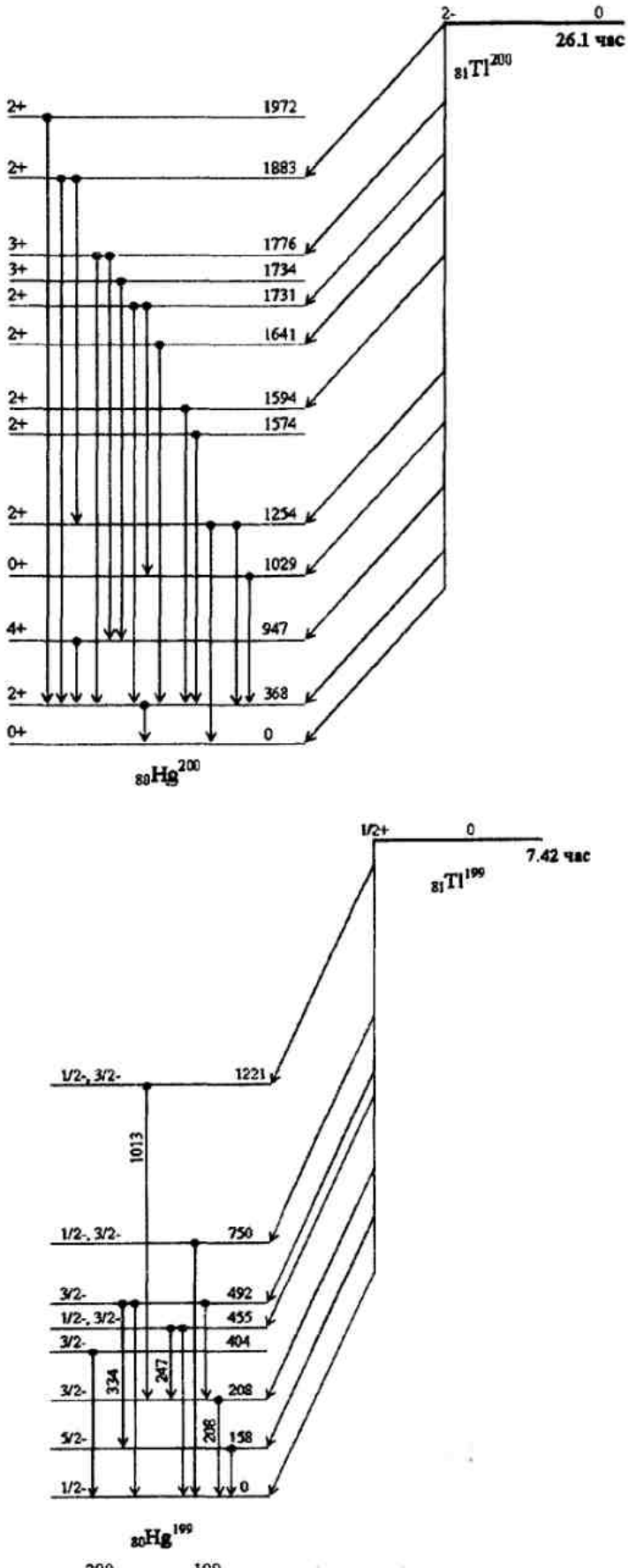

Fig. 4. Decay schemes of ^{200}Tl and ^{199}Tl nuclei ground states.

For photoproton reactions lead to production of stable final nuclei. Therefore photoproton reactions were not considered.

Photonuclear reactions with the emission of up to 4 nucleons in the investigated ^{203}Tl nucleus were observed in the experiment. According to experimental data the observed photonuclear reaction yields were calculated (table 2). The reaction yield values were normalized to ^{203}Tl(γ, n)^{202}Tl reaction yield. The following corrections were made: corrections for the detector efficiency, corrections for absorption in the investigated sample.

The reaction yield values decreases with the increase of neutrons number, we can observe photonuclear reactions which yield values are less then (γ, n) reaction yield value for 3 orders. It demonstrates the high sensitivity of photonuclear reaction method for the analysis of nuclei far from β-stablity strip.

The work is supported by President of Russia, grant RF NSh-5365.2006.2.

[1] The Centre for Photonuclear Experiments Data of the Moscow Lomonosov State University Skobeltsyn Institute of Nuclear Physics http://cdfe.sinp.msu.ru/services/ensdfr.html

[2] V.I. Shvedunov, A.N. Ermakov, I.V. Gribov, E.A. Knapp, G.A. Novikov, N.I. Pakhomov, I.V. Shvedunov, V.S. Skachkov, N.P. Sobenin, W.P. Trower and V.R. Yajlijan, A 70 Mev racetrack microtron, Nuclear Instruments and Methods in Physics Research Section A: Accelerators, Spectrometers, Detectors and Associated Equipment, Volume 550, Issues 1-2, 11 September 2005, Pages 39-53.

Table 1

Photonuclear reactions in ^{203}Tl nucleus and appropriate γ-lines of experimental spectrum

Reaction	Threshold (MeV)	Final nucleus, product and half-life $T_{1/2}$ of β-decay	E_γ (keV)	Int_γ (counts)	γ-Transition nature
(γ, n)	7.85	$^{202}Tl \rightarrow {}^{202}Hg$ 12.23 d	440	$1.49 \cdot 10^{07}$	440 (2^+) → 0 (0^+)
			520	$2.09 \cdot 10^{05}$	960 (2+) → 440 (2+)
			960	$1.15 \cdot 10^{04}$	960 (2+) → 0 (0^+)
(γ, 2n)	14.72	$^{201}Tl \rightarrow {}^{201}Hg$ 72.912 h	167	$1.30 \cdot 10^{06}$	167 (1/2-) → 0 (3/2-)
			135	$2.31 \cdot 10^{05}$	167 (1/2-) → 32 (3/2-)
(γ, 3n)	22.92	$^{200}Tl \rightarrow {}^{200}Hg$ 26.1 h	368	$2.40 \cdot 10^{06}$	368 (2+) → 0 (0+)
			1206	$5.02 \cdot 10^{05}$	1574 (2+) → 368 (2+)
			579	$2.10 \cdot 10^{05}$	947 (4+) → 368 (2+)
			828	$1.21 \cdot 10^{05}$	1776 (3+) → 947 (4+)
			1515	$3.29 \cdot 10^{04}$	1883 (2+) → 368(2+)
			1363	$3.95 \cdot 10^{04}$	1731 (2+) → 368 (2+)

Table 1 (continue)

			1226	$3.13 \cdot 10^{04}$	1594 (2+) → 368 (2+)
			1273	$3.40 \cdot 10^{04}$	1641 (2+) → 368 (2+)
			661	$3.37 \cdot 10^{04}$	1029 (0+) → 368 (2+)
			886	$1.79 \cdot 10^{04}$	1254 (2+) → 368 (2+)
			1408	$1.94 \cdot 10^{04}$	1776 (3+) → 368 (2+)
			702	$1.54 \cdot 10^{04}$	1731 (2+) → 1029 (0+)
			1604	$8.79 \cdot 10^{03}$	1972 (2+) → 368 (2+)
			787	$1.98 \cdot 10^{04}$	1734 (3+) → 947 (4+)
			629	$1.26 \cdot 10^{04}$	1883 (2+) → 1254 (2+)
			1254	$1.00 \cdot 10^{04}$	1254 (2+) → 0(0+)
(γ, 4n)	29.94	$^{199}Tl \rightarrow {}^{199}Hg$ 7.42 h	455	$1.67 \cdot 10^{05}$	455 (1/2-, 3/2-) → 0 (1/2-)
			208	$2.35 \cdot 10^{05}$	208 (3/2-) → 0 (1/2-)
			247	$1.66 \cdot 10^{05}$	455 (1/2-, 3/2-) → 208 (3/2-)
			158	$1.26 \cdot 10^{05}$	158(5/2-) → 0 (1/2-)
			284	$9.15 \cdot 10^{04}$	492 (3/2-) → 208 (3/2-)
			334	$5.14 \cdot 10^{04}$	492 (3/2-) → 158 (5/2-)
			1013	$1.01 \cdot 10^{04}$	1221 (1/2-, 3/2-) → 208 (3/2-)
			404	$4.68 \cdot 10^{04}$	404(3/2-) → 0 (1/2-)
			492	$1.87 \cdot 10^{04}$	492 (3/2-) → 0 (1/2-)
			750	$8.92 \cdot 10^{03}$	750 (1/2-, 3/2-) → 0 (1/2-)

Table 2

Experimental values for photonuclear reaction yields in ^{203}Tl nucleus

Reaction	Reaction yield, relative units
(γ, n)	1.000 ± 0.001
(γ, 2n)	$(4.33 \pm 0.02) \cdot 10^{-02}$
(γ, 3n)	$(9.07 \pm 0.09) \cdot 10^{-03}$
(γ, 4n)	$(2.1 \pm 0.1) \cdot 10^{-03}$

Photon Nuclear Science with backward Compton gamma rays

Mamoru Fujiwara

Research Center for Nuclear Physics, Osaka University, Mihogaoka 10-1 Ibaraki, Osaka 567-0047, Japan

Abstract

Recent developments of the synchrotron radiation facilities and intense lasers are now guiding us to a new research frontier with probes of a high energy GeV photon beam and an intense and short pulse MeV γ-ray beam. We discuss new directions of the science developments with photo-nuclear reactions with the inverse Compton γ-rays for studying hadron structure, nuclear structure, astrophysics, materials science, as well as for nuclear technologies.

1 Introduction

In the scientific field called "photon nuclear science", many applications from basic science research to the biotechnology are performed with photon beams. Nuclear excitation, synchrotron radiation, bremsstrahlung, and inverse Compton scattering are used to obtain these photon beams. Starting from the observation of X rays by Röntogen in 1985, the applications now reaches at the sophisticated technology developments with help of the fast computer such as PET (positron electron tomography) and the observation of chemical dynamics. These fields will be more widely extended for contributing to nuclear science and human life.

Historically, the scientific developments have mostly been made by observing the emitted-, reflected-, and absorbed-lights from the objects. Observations were made by naked eyes for a long time in human history. The novel invention of microscopes in 1590 and telescopes in 1608 with optical-lens combination changed the means of observation very much, and triggered to investigate the microscopic world as well as the macroscopic world, the universe. After 400 years later, we have acquired the deep knowledge both on the microscopic and macroscopic worlds: The basic elements of the microscopic world consist of quarks, leptons, and their mediators (photon, gluons, bosons). The universe starts from a big bang, and creates nuclear elements through various reaction processes in stars in the circular transmigration. Many of these observations have been made by using the probe "photon".

In case of the studies of the microscopic world, interesting developments are now going on. For example, hadron physics are studied with GeV photon beam obtained via the inverse Compton scattering of laser photons by 8 GeV electrons at SPring-8 [1, 2, 3]. Recent experiments report that a new hadron consisting of 5 quarks (two u-quarks, two d-quarks and one anti s-quarks (called Penta-quark particle) may exist at 1540 MeV [4]. This report has triggered world-wide enthusiasm of further experimental and theoretical researches since there is no explicit reason of quark theory to prohibit the existence of hadron particles with four, five, six quarks and so on. Although the existence of the penta-quark particle are now in controversial situation since the new high statistics experiments at the Jefferson laboratory presented the negative results on the penta-quark particle at 1540 MeV [5, 6], the hunting of "pentaquark particles" continues in future until we understand the basic reason to govern the quark world.

Apart from the hadron physics with GeV photons, our scientific development with photons seems to arrive at the birth of a new era. The laser beam is extraordinary intensified with the usage of new optical crystals [7], making the laser acceleration possible. The operation of a high intensity free-electron laser (FEL) becomes feasible [8, 9], and it is possible to use a high power infrared laser with a kW level for further applications in combination with electron beam. Surprising discovery has been achieved in obtaining electron beam with laser acceleration in 2004 [10, 11, 12, 13]. Considering these recent developments of laser technologies, a new feasibility is now extended for a unique feasibility that is to utilize the inverse Compton process for obtaining a high intensity photon beam in the MeV energy region. Since the inverse Compton photons are naturally polarized, we can employ MeV γ-rays for new experiments with polarization observables. These samples are follows:

1. High precision measurements of nuclear resonance fluorescence and Mössbauer effects are much feasible for studying the nuclear structure, the basic symmetries like the parity non-conservation, materials science, bioscience, and archeology.

2. Application of nuclear physics for astrophysics: Simulation experiments by producing high-flux g-rays are feasible. We can approach to answer the questions concerning the nuclear synthesis in supernova sites.

3. Application for nuclear engineering: A very small amounts of nuclear contaminant would be possible to be detected if a high resolution and intensive photon beam is available [14].

4. Observation of basic quantum effects would be realized by using a high-intensity polarized photon beam.

In the present report, We wish to review the history of photo nuclear science and to discuss new developments in physics with the inverse Compton γ-ray beams. In Japan, China, Taiwan and Korea, excellent synchrotron radiation facilities are in operation or under construction. It would be a nice timing to discuss the possibilities performed with inverse Compton photon beam.

2 What is the future of inverse Compton photon beam?

Recent technologies to deliver a high intensity photon beam are enormously enhanced with an appearance of the 3rd generation synchrotron radiation facilities. Intrinsic feature of photon is the fact that photon is boson, which can be coherently overlapped in space and in time. For this reason, photon energy density increases without limitation whenever the coherence condition is satisfied. A good sample is the laser acceleration of monochromatic electron beam at E_e= 20-200 MeV with a resolution of about 5% [10, 11, 12, 13]. One can say that the dream predicted by Tajima and Dawson [15] in 1979 really comes true. The important aspect here is the fact that we can really control a high intensity photon in space and time. This feature is also used for the inverse Compton scattering process. Figure 1 shows a schematic illustration of the inverse Compton scattering. When the laser light is backscattered to the electron beam direction, the maximum photon energy

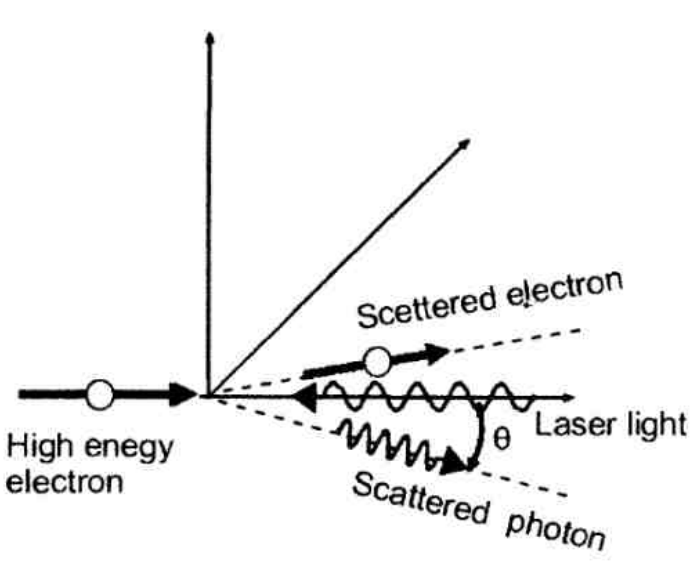

Figure 1: Scheme of inverse Compton process via the collision between high energy electron and laser light. When a laser light collides with a high energy electron, the photon is recoiled and is boosted up its energy by a factor of about $4\times\gamma^2$ thanks to the relativistic effect, where $\gamma=E_e/m_ec^2$ is the Lorentz-FitzGerald contraction factor.

becomes

$$E_\gamma^{max} = \frac{4\nu E_e^2}{(m_ec^2)^2 + 4\nu E_e}, \tag{1}$$

where ν is the energy of incidence laser, E_e is the energy of the electron beam, m_e is the electron mass. The features of the inverse Compton scattering are

1. high energies,
2. high linear and circular polarizations,
3. short pulse width, and
4. high emittance.

All these features stem from the properties of the electron beam. It is noted that when the energy of incidence laser photons is relatively high compared with the electron beam energy, almost mono-energy beam is available [16, 17, 18, 19, 20]. Thus, using this relativistic kinematic, it is possible for us to obtain the quasi-monochromatic photon beam at high energies.

An important question to be addressed is "how can we generate a high intensity photon beam?". In fact, the intensity of photon beam is weak in the past. This is a serious disadvantage in case of the nuclear physics experiment, which requires a high-intensity photon beam to deduce small nuclear cross-sections. The hadron beam intensity is now exceed to 10^{15} /second and widely used for the studies of nuclear science whereas the photon beam intensity in the MeV - GeV energy region remains at a level of 10^6 /second. This unfavorable situation for photon beams is now at the turning point thanks to the recent novel developments of

1. short-pulse and high-intensity electron gun,

2. acceleration of electron beam,

3. control system with high-speed personal computers, and

4. short-pulse and high-intensity laser.

At present, the modern storage ring can store the electron beam at the GeV energies with an intensity more than 100 mA (6×10^{17} electron/second). The laser intensity amounts to the 10 kW range. If this laser is a far-infrared laser with a wave length of 100 μm, the laser energy is about 0.01 eV. The photon intensity is 6×10^{20} /second. Assuming the laser and electron beams can be focused with the same size of the order 1 mm^2 and the inverse Compton process is used for obtaining a MeV photon, the intensity of such photons is estimated to amount to 10^{18} /second. This intensity is extremely higher than the present level of the photon intensity. Many scientists imagine a dream that the photon beam with an intensity of 5×10^{13} becomes feasible in the near future [21]. For example, Ruth et al., [22, 23] at the Stanford accelerator facility now test a new machine to obtain a photon beam in the X-ray energy region from the inverse Compton scattering. Ruth's statement is somewhat shocking. The essential point of his statement is the fact that big machines like a 3rd generation synchrotron radiation (SR) facility may not be necessary for developing the science with X-rays in future, and it would be possible to obtain a compact alternative machine delivering an intensive X-ray beam compatible with those from the expensive SR machine.

Remarkable developments of the free electron laser (FEL) are a remarkable mile stone in recent years. A high power FIR laser of 10 kW class is competitively developed [9, 24]. As an promising extension of this rapid scientific developments, the construction of the energy recovery linear-accelerator (ERL) facility is discussed [25]. If the dream comes true, the photon intensity from the inverse Compton scattering will reach at 10^{13} /second, and new kinds of nuclear photo-science will be promised. At TUNL (Triangle University Nuclear Laboratory), a high intensity photon beam has been achieved using the inverse Compton scattering process between the stored electron beam and the FEL light [26]. Some fruitful experiments aiming at the studies of nuclear physics and nuclear astrophysics are pursued with a photon intensity of 10^7 /second. If the photon intensity of the order 10^{13} /second will be realized, the world of these studies will be completely changed.

First, let's consider a different challenge of obtaining a high energy photon beam using the coherency in the collision process between electron and photon. Figure 2 illustrates what happens for the synchrotron radiation if the electrons move coherently in a dipole magnet. When a single electron is bent in the dipole magnet, the basic QED process is described in terms of the coupling constant with the bare electron charge e, resulting the radiation is proportional to $e\times e$. In this case, the intensity of synchrotron radiation is, of course, proportional to the number of electrons in the beam bunch passing through the dipole magnet. When the bunch of the electron beam is short enough to move together in the size of the wave length of radiated photons, a strong photon radiation is expected to be emitted thanks to the coherent effect. In fact, such enhanced radiations have been experimentally observed at the linear accelerator facility of Tohoku University [27].

Second, we consider the case of the inverse Compton scattering. Figure 3 shows three types of the Compton scattering processes. It is well known that the cross section of the Compton scattering process from the nucleus with an atomic number Z is proportional to Z^2. Since the individual protons in a nucleus are trapped in the nuclear potential governed by the strong force and the size of the nucleus is very small as the order of 10^{-13} cm, photon colliding with the nucleus interacts with protons coherently. The process with

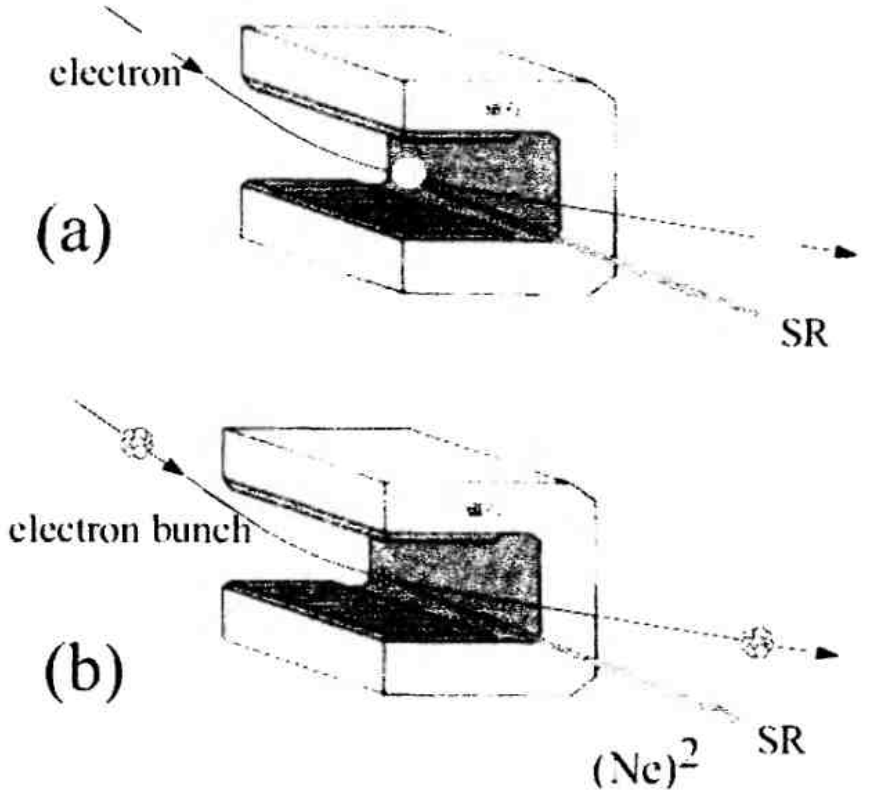

Figure 2: Synchrotron radiation with a single electron and an electron bunch with a number of N. If the N electrons in the bunch are bent in coherent in a dipole magnet, the synchrotron radiation from the electron bunch is enhanced by a factor of N^2 compared with that from a single electron.

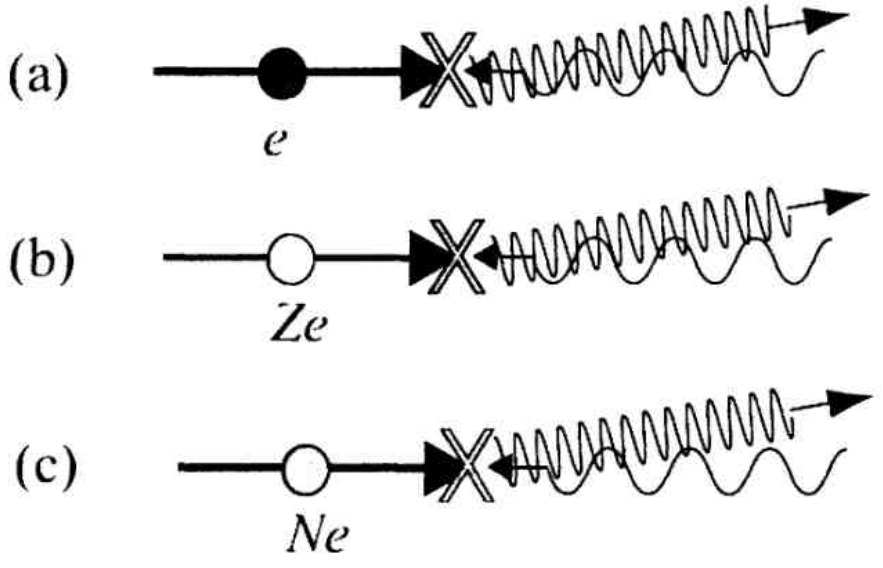

Figure 3: Compton scattering processes of photons from (a) single electron, (b) atomic nucleus with a charge Z, and (c) a beam bunch with N electrons. The scattering cross sections are given by $\sigma_T^e = \frac{8\pi}{3}(\frac{e\times e}{4\pi\epsilon mc^2})^2 = 6.7\times10^{25}$ cm^2, $\sigma_T^Z = Z^2\sigma_T^e$, and $\sigma_T^N = N^2\sigma_T^e$, respectively.

the electron bunch is more complex. Usually, the size of the electron beam bunch is not small, and the individual electrons in the beam bunch are not trapped in the potential, and moved randomly in the space of the beam size as a molecule of an ideal gas. If the electrons are trapped in the beam bunch and the size becomes small as the order of the wave length of incoming photons, the cross-section could be enhanced with the order proportional to $N^2 \times \sigma_T^e$, where σ_T^e, is the Thomson cross-section for the photon-electron scattering. This situation is illustrated in Fig. 3(b). In fact, the mirror or polished mirror-like metal surfaces used in our common life reflect light with a 100% reflectivity. This is due to that many electrons in metal move coherently against a photon, and as a result the photon is completely reflected.

Now let' consider the collision between photons and the shortly bunched electron-beam under the special condition illustrated in Fig. 4. What we wish is to trap the electrons in the beam bunch with a special potential. The key ingredient is the method for generating the electromagnetic field to confine electrons even for a short instance. On the basis of the idea given by Hartemann et al. [28], this trapping mechanism is given by irradiating the electron beam with a short-pulse and high-intensity laser along the same direction of the electron beam direction. Since the laser provides a very strong electromagnetic field, the electrons in the beam bunch is trapped for a short period. This kind of trapping mechanism of electrons is now a well known concept when we consider the FEL machine: the SASE (Self-Amplified Stimulated Emission) mechanism is the most important ingredient.

When the electron beam bunch is irradiated with a high intensity laser, some parts of the electron group in the beam would be confined in the laser potential for a short period. In the same instance, we shoot the electron beam from the forward direction with another laser light split from the same laser. For example, if 1000 electrons associate with the coherent scattering, the cross-section of the inverse Compton scattering is enlarged by a factor of 10^6. This means that the reflectivity of the laser becomes large, and the laser energy is boost up by a $4 \times \gamma^2$ factor as well. The possibility of obtaining the coherent scattering with many electrons is not small: The electron beam bunch with an intensity of μA with MHz repetition contains about 10^6 electrons. If 1000 among 10^6 electrons is confined in the laser potential in the short period of the laser irradiation, the coherent Compton scattering is expected to happen. Such trails with the N^2 effect in coherent inverse Compton scattering are made to generate a high flux X-rays and for the application of cancer therapy [17, 18, 19, 20].

At Kansai Photon Science Institute (KPSI), there is a betatron accelerator. The beam bunch from this betatron accelerator is rather short. A high intensity laser is also guided into the same experimental room. Thus, the KPSI is the best place to check the feasibility of the coherent inverse Compton scattering with the N2 effect. Another possibility of testing the N^2 effect is to use the electron beam from the laser acceleration. Recently, the laser acceleration of electron beam has been realized [7, 10, 11, 12, 13]. The beam bunch of this laser driven electron beam should be extremely small with a size much less than the laser wave length of about 0.1 μm. It is interesting to consider what happens when the laser collide with this electron beam from the laser driven acceleration (see Fig. 5). We can expect the same coherent inverse Compton scattering from the electron beam since the electron beam bunch is expected to be very short because of the laser acceleration mechanism.

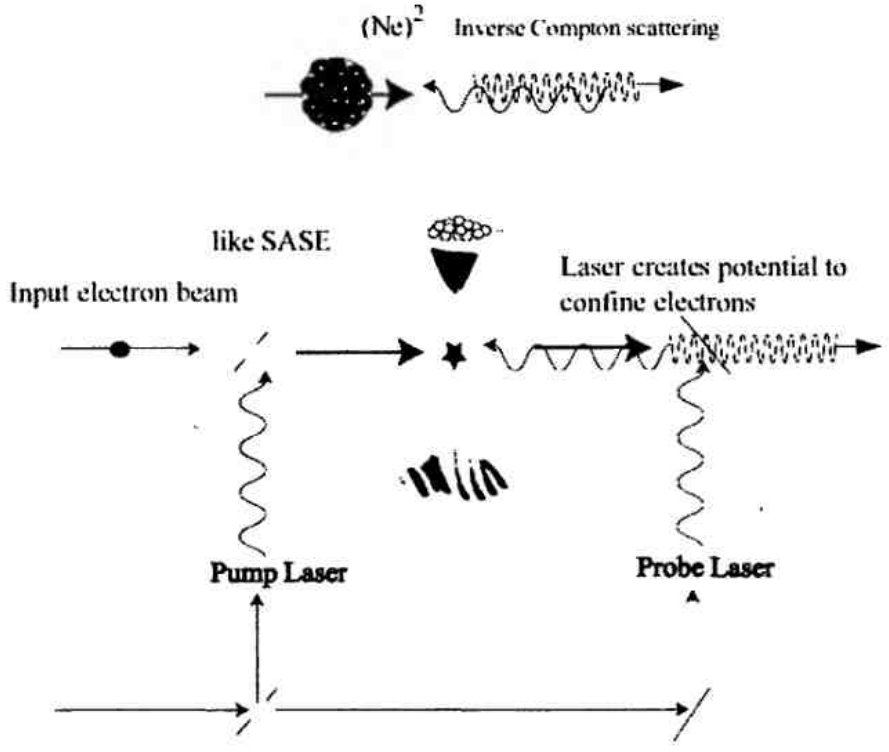

Figure 4: Scheme illustration of the coherent backscattered Compton process via the collision between high energy electron and laser light. When a laser light collides with a high energy electron, the photon is recoiled and is boosted up its energy by a factor of about $4\times\gamma^2$ thanks to the relativistic effect, where $\gamma = E_e/mc^2$ is the Lorentz-FitzGerald contraction factor. When a bunch of the electrons are trapped in a strong laser potential, the electrons in the potential move coherently, and scatter photon with a large cross-section. In such case, the reflection rate is enhanced by a factor of $(Ne)^2$, where N is the number of electrons associated with the collision process.

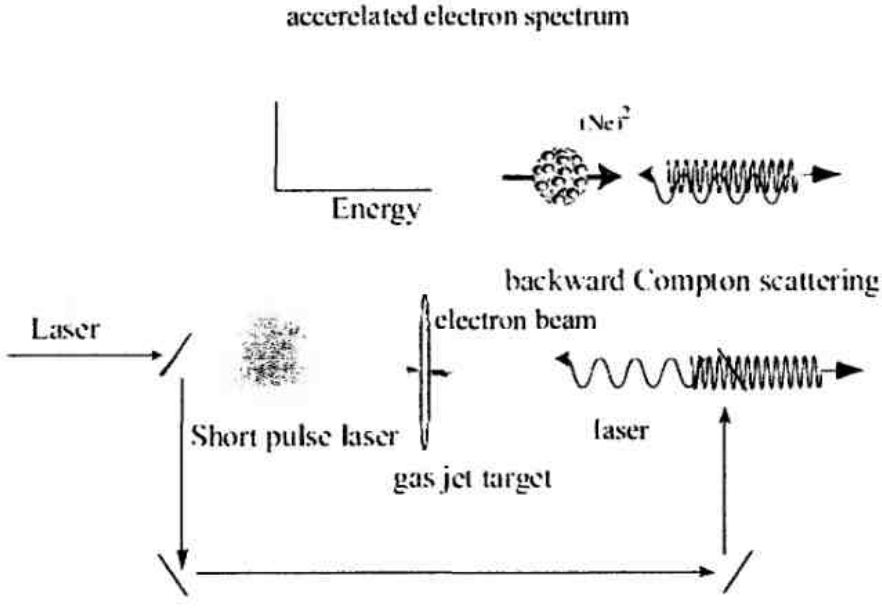

Figure 5: Scheme illustration of the coherent backscattered Compton process via the collision between high energy electrons from laser driven acceleration and laser light.

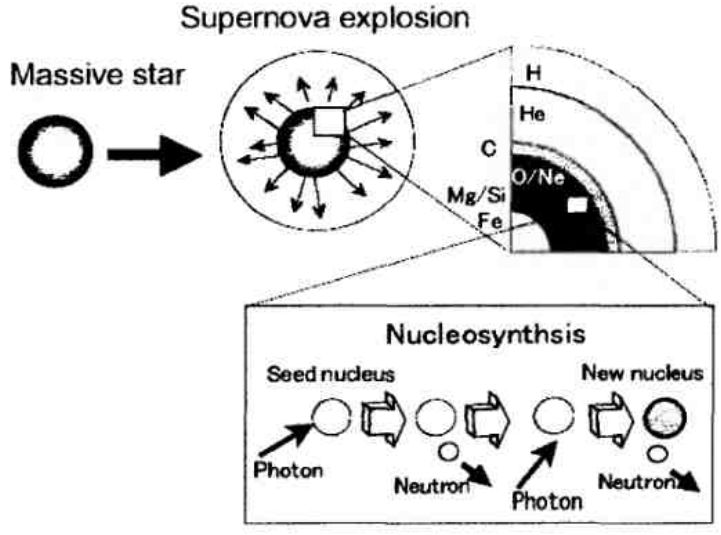

Figure 6: Schematic drawing to explain the production mechanism of p-nuclei in the strong photon field at supernova explosions. At the death of a star with a mass by about twenty times heavier than the mass of the sun dies, the core irons in the heavy star start to capture electrons and explode. As a result, nuclei at the core of star become neutron rich, leading to a neutron star. However, nuclei at the outside of the supernova star capture neutrons, and become heavier. This heavy nuclei are irradiated with extraordinary strong photons from the supernova explosion at the star center. There is a possibility to make neutron deficient nuclei after repeating two (γ,n) processes. This kind of nuclei is called "p-nuclei". (by courtesy of T. Hayakawa).

3 Nuclear Photon Science with high intensity γ-rays

A famous study of the nuclear structure using a photon beam has been made by Bothe and Gentner in 1937 [29]. They obtained the cross-section for the ^{63}Cu(γ,n) reaction from the radioactivity induced by γ-radiation from the Li(p,γ) reaction. The cross-section value is about 5×10^{-26} cm^2, which corresponds to those of exciting the giant dipole resonances (GDR) in nuclei. Actually, the existence of such GDR excitation mode has been commonly recognized from the work by Baldwin and Klaiber [30] in 1947. Since then, many discoveries were reported on the nuclear level excitations. The "nuclear giant resonances" have been one of the important subjects in nuclear physics for long time. "Photon" played an important role to probe the nuclear structure because the nature of photon is completely well understood in terms of QED. It should be noted that the observation of γ-ray de-excitation is also a powerful tool to study nuclear level structures.

Needless to say, the discovery of nuclear resonance fluorescence (NRF) is a benchmark event in the development of nuclear physics. Especially the finding of the recoil-less NRF by Mössbauer brought a great benefit for the materials science. Combining NRF methods with a high-resolution Ge detector, nuclear structure has been studied for many stable nuclei [31, 32, 33].

In recent years, demand to study the nuclear synthesis processes with photons increases since some new observations in cosmos are reported. Especially, the nuclear synthesis at the site of supernova explosion is considered to be of importance in understanding the story to create nuclear elements from light to heavy. In order to experimentally simulate the nuclear reaction processes in the photon fields at the supernova site, a extremely high-intensity photon-beam is required.

Figure 6 shows a scheme to illustrate the creation process of p-nuclei at the supernova site. The mechanism of the p-nucleus synthesis was one of the mysteries in astrophysics. Hayakawa et al., [34] conclude on the basis of the systematic nuclear-abundance ratio and of the theoretical network calculation that the p-nuclei are created by sequential two (γ,n) processes in ultra-high γ-ray fields at the supernova site. It becomes gradually clear that in our solar system, the elements up to heavy uranium are synthesized by repeating supernova explosions several times and the $s-$ and $r-$processes in stars of the Galaxy. Further detailed studies of the nuclear synthesis in cosmos are needed for understanding the birth history of the solar system, and the earth. Especially, the explosion mechanism of supernovae remains as an unsolved problem. Knowledge of detailed nuclear structures of the fp-shell nuclei is still required. The NRF experiments with high-intensity photon beams at E $\geq$ 5 MeV are useful to understand the level structures concerning the $E1$ and $M1$ excitations. The information on the $M1$ strengths in nuclei is especially important for the neutrino absorption calculations for construction of a large-scale detector to detect the supernova neutrinos, which are expected to appear within a few seconds when a supernova explosion happens. Thanks to the recent developments of nuclear theories, more sophisticated experiments are also required to refine the theoretical calculations. On basis of the new developments of shell-model and alpha-cluster calculations, new experiments for photo-absorption processes are urgent for further improvements of theories.

If a high-intensity photon beam via the inverse Compton scattering process, a great benefit in physics experiments is "linear and circular polarization". Circular polarized photon beam is useful for the parity non-conservation (PNC) experiment to study the weak-boson and nucleon coupling in nuclear medium. The origin of the mirror symmetery violation in β-decay is now well understood as a manifestation of the exchange process of charged weak bosons, W^+ and W^- after the PNC discovery by Wu [35], following the suggestion by Lee and Yang [36]. Observations of the PNC effect in nuclear excitation are not quite new. The trial to observe the PNC effect was first reported by Tanner in 1957 [37], followed by the famous work of Feynman and Gell-Mann [38] for the universal current-current theory of weak interaction. In the PNC effect in nuclear excitations, neutral weak boson Z^0 is responsible, and strongly coupled with the vertices of strong forces. The details of the PNC studies were reviewed, for example, in Refs. [39, 40, 41, 42]. The current problem is originated from the fact that weak meson-nucleon coupling constants deduced from various PNC experiments are not consistent. Haxton et al., [43] concluded that the experimental PNC results are still not satisfactory and more experimental as well as theoretical studies are needed.

Common methods of experimental PNC studies are to measure the parity mixing between the parity-doublet states. In the traditional experiment, one of the doublet levels is excited in the nuclear reaction. Then, the PNC effect is appeared as the asymmetry of emitted circularly polarized photons. Emitted circularly polarized photons are very difficult to be correctly measured.

Recently, we propose a new method for measuring the PNC effect in nuclei by measuring the excitation and de-excitation of the parity doublets using NRF [44, 45]. Let us consider electromagnetic excitation and decay of the lowest excited $1/2^-$ (E_x=109.9 keV) state in ^{19}F, for an example. It is assumed that the ground state with $J^\pi = 1/2^+$ and the first excited state with $1/2^-$ are the parity doublet. In this case, the first $1/2^-$ (E_x=109.9 keV) state in ^{19}F is excited by NRF. In the previous experiments for the circular polarization measurement of emitted γ-rays, one of the doublet levels was excited via a nuclear reaction, and the admixture of the configuration of the opposite parity was manifested as the asymmetry A_γ of γ-rays emitted from the excited states with a polarization, or

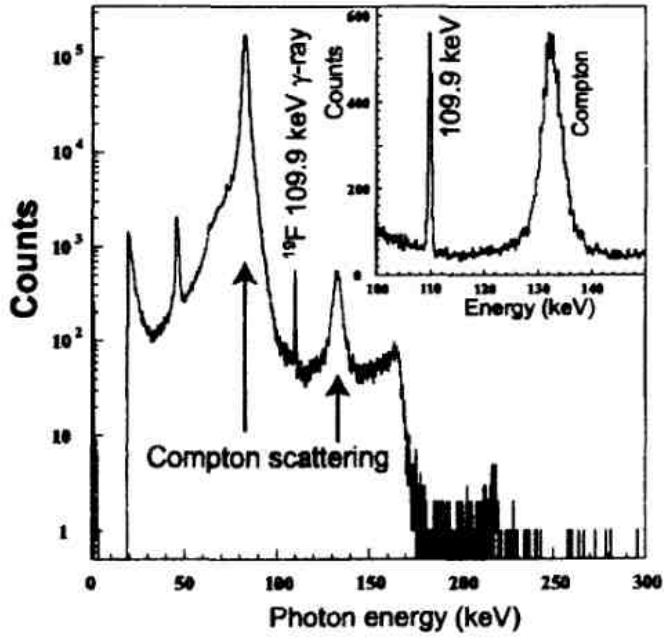

Figure 7: Photon spectrum to demonstrate the nuclear resonance fluorescence γ-rays from the 109.9 keV level in ^{19}F. A 110 keV Wigger photon beam with an energy resolution of about 100 eV has been used at SPring-8.

as the circular polarization P_γ of γ-rays emitted from unpolarized excited states. In the case of the $1/2^- \rightarrow 1/2^+$ transition in ^{19}F, the PNC value is reported as -8.5×10^{-5} [46] with 30% error bar. In case of ^{19}F, a high intensity photon source from the synchrotron radiation facilities at SPring-8, ESRF, and APS is available for the PNC measurement. At SPring-8, the intensity from a Wiggler system reaches at 10^{13} photons/second at $E =$ 109.9 keV with an energy width of about 0.1 keV. The NRF events for exciting the 109.9 keV $1/2^-$ state are expected to be around 10^8 /second for the LiF target with a thickness of 0.5 cm. This NRF event rate is high enough to examine the theoretical formula presented in the present work..

Figure 7 shows a sample NRF spectrum measured with a Ge detector at SPring-8 using a Wigller beam [47]. A strong excitation of the $1/2^-$ 109.9 keV level in ^{19}F is demonstrated. The accuracy of the measurement depends on the details of the experimental set-up (counting rates, detection solid angles etc.). According to our estimation we expect to achieve the accuracy better than 10-20% for one week measurement, which exceeds considerably the previous experiments in the traditional design. A serious difficulty stems from a high counting ratio of the Compton scattered γ-rays as backgrounds. One method to overcome this problem is to use a multi-segmented detector in order to greatly reduce the counting rate of each detector and obtain the necessary total counts of 10^{10} as the NRF events. The use of newly developed lutetium oxyorthosilicate (Lu_2SiO_5, LSO) and lutetium-yttrium oxyorthosilicate ($Lu_{2(1-x)}Y_{2x}SiO_5$, LYSO) crystals with a decay constant of about 40 ns and an energy resolution of 7-10% is also promising for the NRF measurement with a high-counting rate. Another way is to obtain a photon beam with an ultra high resolution of $\Delta E/E = 10^{-5}\sim10^{-6}$. In this case, the background photons due to Compton scattering are greatly reduced, and the γ-ray events due to the NRF process are relatively enhanced to get a high counting rate necessary for performing a high-statics PNC measurement.

If a high-energy photon beam with a high-intensity stronger than 10^8 /second will be

realized in near future, the following experiments with NRF, which have been difficult to be performed due to the lack of intensity, are feasible. The NRF process is only favorable to excite with the E1 and M1 modes. With linear polarized photons, E1 and M1 excitations are determined without any theoretical ambiguities. Samples of such experiments are relevant to

1. the transitions between the octupole-deformed states with the same spin and with different parities in the mass of about 180,
2. the collective excitations of scissor or troidal modes in medium-heavy nuclei,
3. photo-nuclear fission
4. $E1$ and $M1$ excitations near the particle emission thresholds for the network calculations in astrophysics.

For this purpose, we need to obtain the γ-ray beam with an energy higher than several MeV, which is only successful with the inverse Compton process. There are additional important studies that are relevant to the nuclear transmutation with (γ,n) reactions, the materials science with polarized positrons, the Mössbauer effect measurements with the NRF photons, and the medical application of the high-intensity photons.

4 Summary and final remarks

Thanks to the recent laser and accelerator technologies, it is turned out that photon beams in the energy range from sub-MeV to a few GeV become usable for various scientific developments. The subjects to be studied with such photon beams are

1. astrophysics applications of nuclear physics to draw the story of nuclear synthesis in the universe,
2. nuclear and hadron structures with high intensity and high polarization photon beams,
3. studies of basic symmetries in the nuclear and atomic processes,
4. feasibility studies of nuclear transmutation technologies with high-intensity photon beams in the energy range of 10-30 MeV,
5. application of polarized photon beams to generate polarized positrons, which are useful for materials science developments,
6. new technologies to generate the high intensity MeV photons with a full usage of the quantum effect of coherency.

Recently, in Japan, South-Korea, China, Taiwan, US, and EU countries, many scientists discuss to install the beam lines for inverse Compton scattering at the SR facilities. There are great possibilities of having a high-intensity photon beam due to the boson nature of light, which is not fully used in the past.

5 Acknowledgments

I thank T. Hayakawa, T. Kimura, T. Tajima, A.I. Titov, K. Kawase, H. Akimune, H. Ejiri, S. Dat'e, M. Itoh, Y. Ohashi, H. Ohkuma, Y. Sakurai, S. Suzuki, K. Tamura, H. Toki, and H. Toyokawa for fruitful discussions.

References

[1] M. Fujiwara, Nuclear Physics News **11** (2001) 28

[2] M. Fujiwara, Progress in Particle and Nuclear Physics **50** (2003) 461

[3] R.G.T. Zegers et al., Phys. Rev. Lett. **91** (2003) 092001, T. Ishikawa et al., Phys. Lett. B **608** (2005) 215, T. Mibe et al., Phys. Rev. Lett. **95** (2005) 182001, M. Sumihama et al., Phys. Rev C **73** (2006) 035214

[4] T. Nakano et al., Phys. Rev. Lett. **91** (2003) 012002

[5] B. McKinnon et al., Phys. Rev. Lett. **96** (2006) 212001

[6] S. Niccolai et al., Phys. Rev. Lett. **97** (2006) 032001

[7] G. Mourou, T. Tajima and S.V. Bulanov, Rev. Mod. Phys. **78** (2006) 309

[8] T. Brabec and F. Krausz, Rev. Mod. Phys. **72** (2000) 545

[9] R. Hajima and R. Nagai, Phys. Rev. Lett. **91** (2003) 024801, and references therein

[10] S.P.D.Mangeles et al., Nature **431** (2004) 535

[11] C.G. R. Geddes et al., Nature **431** (2004) 538

[12] J. Faure et al., Nature **431** (2004) 541

[13] E. Miura et al., Appl. Phys. Lett. **86** (2005) 251501

[14] J. Pruet, D.P. McNabb, C.A.Hagmann, F.V. Hartemann, and C.P.J. Barty, J. App. Phys. **99** (2006) 123102

[15] T. Tajima and S.M. Dawson, Phys. Rev. Lett. **43** (1979) 267

[16] V. Nelyubin, M. Fujiwara, T. Nakano, and B. Wojtsekhowski, Nucl. Instrum. Method Phys. Res., Sec A **425** (1999) 65

[17] S.G. Anderson et al., Appl. Phys. B **78** (2004) 891.

[18] W.J. Brown and F.V. Hartemann, PRST-AB **7** (2004) 060703

[19] D.J. Gibson et al., Phys. Plasmas. **11** (2004) 2857

[20] W. J. Brown et al., PRST-AB **7** (2004) 060702

[21] Y. Miyahara, Nucl. Instrum. Methods Phys. Res., Sect A **491** (2002) 366

[22] Z. Hung and R.D. Ruth, Phys. Rev. Lett. **80** (1998) 000976

[23] J. Arthur et al., Comceptual Design Report No. SLAC-R-593, Stanford Linear Accelerator Center, 2002.

[24] L. Merminga, D. R. Douglas, and G. A. Krafft, Ann. Rev. Nucl. Part. Sci., **53** (2003) 387

[25] JAEA proposal for ERL (2006)

[26] V. N. Litvinenko et al., Nucl. Instrum. Methods Phys. Res., Sect. A **407** (1998) 8

[27] T. Nakazato et al., Phys. Rev. Lett. 63 (1989) 1245.

[28] F.V. Hartemann, A.L. Troha, E.C. Landahl, J.R. van Meter, and T. Tajima, preprint.

[29] W. Bothe and W. Gentner, Z Physik **106** (1937) 236

[30] G.C. Baldwin and G.S. Klaiber, Phys. Rev. **71** (1947) 3

[31] For example, U.E.P. Berg and U. Kneissl, Rev. Nucl. Part. Sci. **37** (1987) 33

[32] P. Mohr et al., Phys. Rev. C **69** (2004) 032801.

[33] N. Pietralla et al., Phys. Rev. Lett. **88** (2002) 012502

[34] T. Hayakawa et al., Phys. Rev. Lett. **93** (2004) 161102

[35] C.S. Wu et al., Phys. Rev. **105** (1957) 1414

[36] T.D. Lee and C.N. Yang, Phys. Rev. **104** (1956) 254.

[37] N. Tanner, Phys. Rev. **107** (1957) 1203

[38] R.P. Feynman and M. Gell-Mann, Phys. Rev. **109** (1958) 193

[39] E.G. Adelberger and W.C. Haxton, Ann. Rev. Nucl. Sci. **35** (1985) 501

[40] B. Desplanques, Phys. Rep. **297** (1998) 1

[41] B.R. Holstein, "Weak Interaction in Nuclei", (Princeton University Press, 1989)

[42] Symmetries and Fundamental Interaction in Nuclei" ed. By W.C. Haxton and E.M. Henley, World Scientific Publishing Co. Pte. Ltd. 1995 p.17.

[43] W.C. Haxton, C.-P Liu and M.J.Ramsey-Musolf, Phys. Rev. C 65 (2002) 045502

[44] M. Fujiwara and A. I. Titov, Phys. Rev. C 69 (2004) 065503

[45] A.I. Titov, M. Fujiwara, and K. Kawase, J. Phys. G: Nucl. Part. Phys. 32 (2006) 1097

[46] E. G. Adelberger et al., Phys. Rev. Lett. 34 (1975) 402.

[47] K. Kawase et al., RCNP annual report (2004) pp. 27.

New opportunities in the physics of quasielastic knockout of mesons from nucleon by high-energy electrons

D.K. Fedorov[1], V.E. Lyubovitskij[2], V.G. Neudatchin[1], I.T. Obukhovsky[1]

[1] *Institute of Nuclear Physics, Moscow State University, Vorobievy Gory, Moscow 119899, Russia*
[2] *Institut für Theoretische Physik, Universität Tübingen, Auf der Morgenstelle 14, D-72076 Tübingen, Germany*

Abstract

The $p(e,e'\pi^+)n$ cross section is evaluated on the basis of the constituent quark model. It is shown that the contribution of baryon s- and u-poles can be modeled by a nonlocal extension of the Kroll-Rudermann contact term. This contribution is in an interference with the pion t-pole that is essential to improve the description of recent JLab data at the invariant mass $W \lesssim 2$ GeV and $Q^2 \lesssim 1.6$ GeV^2/c^2. The contribution of the ρ-meson t-pole to the σ_T is discussed on the basis of the tensor variant of ρ-meson field. Some predictions are made for σ_L and σ_T cross sections at higher W and Q^2.

1 Introduction

Recent JLab data on the forward pion electroproduction $p(e,e'\pi^+)n$ at intermediate energies, $Q^2 = 0.6$ - 1.6 GeV^2/c^2, $W \simeq 1.95$ GeV (Fpi1 Collaboration [1]), $Q^2 = 1.6$ - 2.45 GeV^2/c^2, $W \simeq 2.1$ - 2.3 GeV (Fpi2 Collaboration [2]), contain a wealth of information on the meson cloud of nucleon, which can be further used in many applications in the nuclear physics. The Rosenbluth separation of longitudinal and transverse cross sections in these experiments, $\sigma = \sigma_T + \varepsilon\sigma_L + \ldots$, allows investigations to be made separately for π- and ρ-meson clouds as the pion vertices $\pi\pi\gamma^*$ and $\pi NN(N^*)$ contribute generally to the σ_L, while $\rho\pi\gamma^*$ and ρNN contribute exclusively to the σ_T.

In Ref. [1] the JLab Fπ1 Collaboration extracted from the data the charged pion form factor $F_\pi(Q^2)$ using a Regge model for high energy meson electroproduction [3] (the VGL model). The new data on σ_L and σ_T can be also used for study of the strong nucleon form factors $F_{\pi NN}$ and $F_{\rho NN}$. Recall that nowadays there are only indirect data on the cut-off parameters $\Lambda_{\pi N}$, $\Lambda_{\rho N}$ in the form factors $F_{\pi NN}(t) = \frac{\Lambda^2_{\pi N} - M^2_\pi}{\Lambda^2_{\pi N} - t}$, $F_{\rho NN}(t) = \frac{\Lambda^2_{\rho N} - M^2_\rho}{\Lambda^2_{\rho N} - t}$. The "soft" values $\Lambda \approx 0.7$ - 0.8 Gev/c follows from the fit of meson exchange currents in nuclei, and the "hard" ones $\Lambda \approx 1.2$ - 1.7 Gev/c are usually used in meson-exchange models of NN interaction.

The process $p(e,e'\pi^+)n$ corresponds to the Feynman diagrams in Fig. 1, and the problem is how to extract from the cross section the data on the t-pole amplitude (Fig. 1a). It can be

made at quasielastic knockout kinematics which is characteristic of Fpi1 - Fpi2 experiments. In a broad sense, the term "quasielastic knockout" means that a high-energy projectile (electron, proton, etc.) instantaneously knocks out a constituent — an electron from an

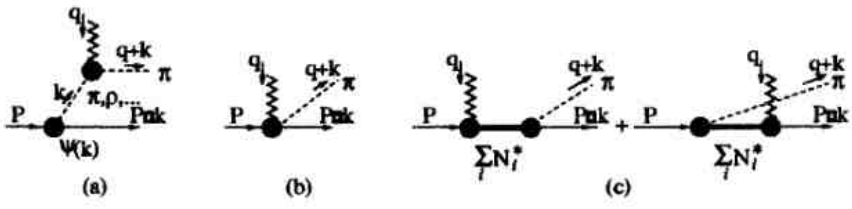

Figure 1: Hadron diagrams for $N(e,e'\pi)N'$ reaction. Fat points denote vertex form factors.

atom [4], a nucleon or claster from a nucleus [5], or a meson from nucleon [6] — transferring a high momentum in an "almost free" binary collision to the knockout particle and leading to controllable changes in the internal state of the target. It is a good tool for study of the constituent initial-state w.f. $\psi(\mathbf{k})$: at small momentum $t = k_0^2 - \mathbf{k}^2$ transfered to the target (and at large momentum Q^2 transfered to the constituent) the cross section $d\sigma/dt$ is proportional to the momentum distribution of the constituent in the target ($|\psi(\mathbf{k})|^2$).

The procedure for reggeization according to [3] (Fig. 2) is quite natural for the meson (π, ρ, b_1, ...) t-pole diagrams, however, the authors of Ref. [3] have been forced to add the nucleon s-pole term (in a "reggeized by hand" form and with a common Q^2-dependent form factor) to ensure gauge invariance. The combination of amplitude in Fig. 2 is very artificial

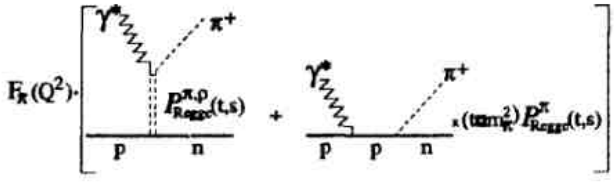

Figure 2: Diagram representation of the $p(e,e'\pi^+)n$ reaction in the VGL model.

and leads only to a reasonable description of the σ_L, while the σ_T does not obtain a realistic description. It is also inconvenient for extraction of the strong form factors.

Here we show that an alternative (microscopic) description of quasi-elastic pion knockout from the proton can be obtained on the basis of a constituent quark model (CQM). An important argument based on the quark consideration [7] is that the contribution of the s- and u- channel diagrams in Fig. 1c is suppressed by a factor $1/Q^4$ in comparison to the contribution of the t-channel diagrams in Fig. 1a. In Refs. [7, 8, 9], the π- and ρ -exchange diagrams were calculated using the light-front dynamics. In principle, this made it possible to extract the strong πNN form factor $F_{\pi NN}(t)$ from comparison of a calculated longitudinal cross section $d\sigma_L/dt$ with the data at high momentum transfer $Q^2 \gtrsim 2$ -3 GeV^2/c^2. But in practice, the accessible data on high-quality Rosenbluth separation are limited by too small Q^2 and W, where the $s(u)$-contributions (Figs. 1b,c) cannot be neglected.

In contrast to those studies, in Ref. [6] the process $p(e,e'\pi^+)n$ was considered in the laboratory frame. In this case one is able to single out, in a natural way, the kinematic region where the recoil momentum of the final nucleon $P'^{\mu} = \{P'_0, -\mathbf{k}\}$ with $P'_0 \simeq M_N + \mathbf{k}^2/(2M_N)$ is small and where only the momentum $\mathbf{k}' = \mathbf{q} + \mathbf{k}$ of the knocked out meson is large. In that (quasi-elastic) region at $|t| \lesssim 0.1 - 0.2$ GeV^2 the 4-momentum $k = P - P'$ transfered

to the nucleon can be related to the 3-momentum $\mathbf{k}$, $k^\mu \simeq \{-\mathbf{k}^2/(2M_N), \mathbf{k}\}$, and both the initial $|N(P)>$ and the final-state $|N(P')>$ nucleons are non-relativistic ones. In the CQM each of them can be described by a non-relativistic quark wave function $|N_{3q}(P)\rangle = \Phi_N(\boldsymbol{\rho}_1, \boldsymbol{\rho}_2)\,|[2^3]_C[3]_{SI}S_z, I_z\rangle$, where C, S and I are color, spin and isospin respectively; $\boldsymbol{\rho}_1$ and $\boldsymbol{\rho}_2$ are the Jacobi coordinates of quarks and $\Phi_N(\boldsymbol{\rho}_1, \boldsymbol{\rho}_2)) = \mathcal{N}_N^{-1} e^{-\boldsymbol{\rho}_1^2/4b^2 - \boldsymbol{\rho}_2^2/3b^2}$ is a quark wave function with the b as a "quark radius" of the nucleon.

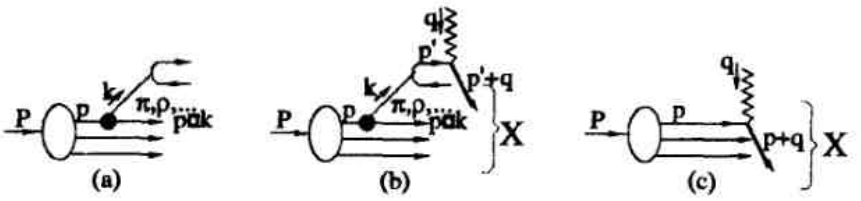

Figure 3: Nucleon structure (a) and the $p(e,e')X$ process (b+c) in the parton approach.

In description of the pion knockout process we start from a more general parton picture of the nucleon (Fig. 3a), which includes "nonperturbative" $\bar{q}q$ pairs (i.e. a meson cloud). In

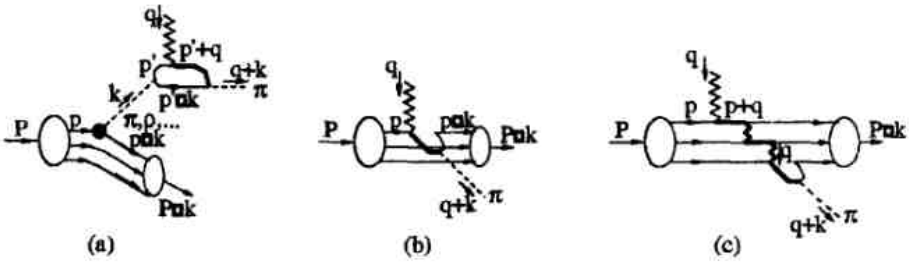

Figure 4: Quark hadronization into an exclusive channel (small W).

this picture the parton hadronization processes could be described by vacuum $\bar{q}q$ diagrams as it is shown in Fig. 4a,b,c (we use solid lines to distinguish the quarks which absorb a photon large momentum q).

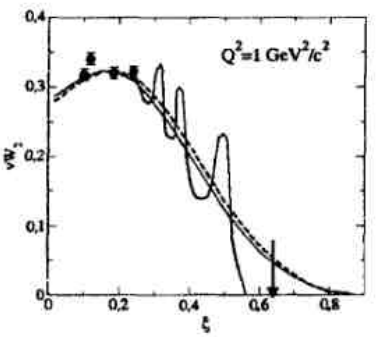

Figure 5: Bloom-Gilman duality, adapted from [10, 11].

A possibility of such description follows from quark-hadron duality (or exclusive-inclusive connection), observed in early 70s by Bloom and Gilman [10] (see a recent review in [11]). Namely, it was shown that, when averaged over some interval of the Nachtmann scaling

variable $\xi = 2x/(1+\sqrt{1+4M^2x^2/Q^2})$, the inclusive structure function νW_2 in the resonance region at low W, $Q \sim 1$ GeV, is approximately equal to the scaling structure function at much larger $Q^2 \gtrsim 5$ - 10 Gev^2/c^2 (Fig. 5)[1] It should be noted that at low W the exclusive resonance contributions dominate in the region of large $\xi \gtrsim 0.25$-0.3, while in the pion knockout region $\xi \approx 0.2 \pm 0.05$ the inclusive cross section is also close to the exclusive one. Thus, the exclusive cross section measured at low W, Q^2 is connected by Bloom-Gilman duality with the inclusive one determined in the scaling region at high W, Q^2.

It is not difficult to understand that the diagrams in Fig. 4a,b survive at large Q^2, while the quark diagram in Fig. 4c with virtual excitations of more than one quark is equivalent to the sum of hadron diagrams in Fig. 1c with virtual baryon excitations, but the latter ones are dying out with growing the Q^2 because of form factors in both vertices.

In the next section we shall evaluate the surviving amplitudes following the standard

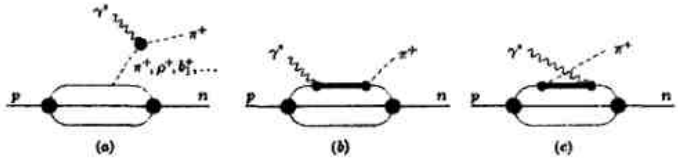

Figure 6: CQM diagrams for pion electroproduction.

diagrams of CQM depicted in Fig. 6.

2 Evaluation of σ_L and σ_T in terms of the CQM

The s- and u-pole quark diagrams in Figs. 6b,c at large momentum transfer Q^2 imply using the strong and e.-m. quark form factors. In the CQM one can take the Fourier transform of the pion wave function for the strong πqq vertex form factor (e.g. this can be shown [6] in terms of the $^3P_0$ model).

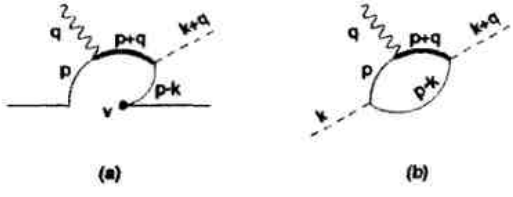

Figure 7: High momentum transfer diagrams for (a) pion electroproduction on a sole quark, (b) charge pion form factor.

Then, the quark amplitude for the s- or u-channel transition $\gamma^* + q \to q + \pi$ becomes proportional to the product of two form factors, the strong one $F_{\pi qq}$ and the electromagnetic form factor [2] of the constituent quark $F_q(Q^2)$. In the considered region of large Q^2 and W this product is equivalent to the pion electromagnetic form factor $F_\pi(Q^2) \simeq F_q(Q^2)F_{\pi qq}(Q^2)$ as it can be seen from Fig. 7.

[1] above $Q^2 \approx 5$ Gev^2/c^2 the duality prediction is similar numerically to the expectation from PQCD [12].

[2] It implies that the constituent quark is an extended object and has its own electromagnetic form factor, e.g. $F_q(Q^2) = 1/(1+Q^2/\Lambda_q^2)$ [13]. The parameter Λ_q is believed to be set by the chiral symmetry scale $\Lambda_q = \Lambda_\chi \simeq 4\pi f_\pi \sim 1$ GeV.

The quark diagram for pion form factor F_π is shown in Fig. 7b with the same notations of momentum variables as for the discussed s-pole diagram represented in Fig. 7a (with the scalar $\bar{q}q$ vertex v of the $^3P_0$ model). The solid line in both pictures shows the propagation of a large momentum $\mathbf{q} \gg \mathbf{k}$ transfered from the photon to the pion by a highly excited quark. It is intuitively clear that at fixed q^2 the contribution of this deeply off-shell quark into the both processes should be similar in value independently on details in diagrams in Fig. 7a and Fig. 7b. This assumption is formally confirmed by a simple calculation in terms of Gaussian wave functions [14]. As a result, in the considered kinematic region of quasi-elastic pion knockout both the t- and $s(u)$-contributions to the amplitude become proportional to a common form factor $F_\pi(Q^2)$ which can be factorized from the sum of t- and $s(u)$-pole diagram contributions. Recall that in a phenomenological approach [3] such common form factor was introduced *by hand* to preserve gauge invariance of the calculated amplitude.

The t-pole amplitude for the $\gamma^* q \to q'\pi^+$ process on the i-th quark (Fig. 6a) is

$$\mathcal{M}^{(i)\mu}_{q(t)} = ie\hat{G}^{(i)}_{\pi qq}\frac{F_\pi(Q^2)}{t-m_\pi^2}(k+k')^\mu, \quad \hat{G}^{(i)}_{\pi qq} = g_{\pi qq}\tau^{(i)}_-\sigma^{(i)}\cdot\mathbf{k}, \tag{1}$$

where $F_\pi(Q^2)$ is the pion electromagnetic form factor and $\hat{G}^{(i)}_{\pi qq}$ is the πqq vertex operator for the i-th quark.

The quark-level amplitude $\mathcal{M}^{\mu}_{q(t)}$ gives rise to the t-pole matrix element for π^+ electroproduction from the nucleon

$$\mathcal{M}^{\mu}_{N(t)} = \langle N_{3q}(P')|\sum_{i=1}^{3}\mathcal{M}^{(i)\mu}_{q(t)}|N_{3q}(P)\rangle, \tag{2}$$

which is proportional to the strong form factor $F_{\pi NN}(t) = \int d\boldsymbol{\rho}_1 d\boldsymbol{\rho}_2 e^{i\frac{2}{3}\mathbf{k}\cdot\boldsymbol{\rho}_2}|\Phi_N(\boldsymbol{\rho}_1,\boldsymbol{\rho}_2)|^2 = e^{-\mathbf{k}^2b^2/6}$, $t \simeq -\mathbf{k}^2$. At $b = 0.6$ fm, which is a typical scale in the CQM (at small $|t| \lesssim 0.2$ GeV^2 this Gaussian is very close to the monopole form factor with $\Lambda_{\pi NN} \simeq 0.7$ GeV), the matrix element (2) gives a reasonable description of the t-dependence of the differential cross sections in the JLab experiment (see, e.g., Ref. [6]). However, since the s- and u-channel quark contributions (Fig. 6b,c), which are required for gauge invariance, have not been taken into account, the results of such simple quark evaluation should be corrected by these contributions as it is shown in Fig. 8.

The matrix element for absorption of the longitudinal virtual photon ($\epsilon^{(0)\mu} = \frac{1}{Q}\{|\mathbf{q}|, q_0\hat{\mathbf{q}}\}$, $Q = \sqrt{-q^2}$) by a quark reads

$$\begin{aligned}\mathcal{M}^{(i)\mu}_{q(s+u)} &= -i\sqrt{2}\,g_{\pi qq}\,F_{\pi qq}(Q^2)\,F_q(Q^2)\\ &\times \left\{e_u\gamma^5\frac{1}{\not{p}_i'+\not{k}'-m_q}\gamma^\mu + e_d\gamma^\mu\frac{1}{\not{p}_i-\not{k}'-m_q}\gamma^5\right\}^{(i)},\end{aligned} \tag{3}$$

where $e_u(e_d)$ is the quark charge. In the lowest order of expansion in the small parameters M_N^2/W^2 and Q^2/W^2 the matrix element (3) reduces (see [14] for detail) to an effective $\gamma\pi qq$ interaction[3]

$$\mathcal{M}^{(i)\mu}_{q(s+u)}\epsilon^{(\lambda=0)}_\mu \simeq -i\frac{eg_{\pi qq}}{2m_q}\frac{M_NQ}{W^2}\frac{\tau^{(i)}_-(\boldsymbol{\sigma}^{(i)}\cdot\hat{\mathbf{q}})}{(1+\frac{|\boldsymbol{\varkappa}_2|}{m_q}cos\theta)}F_q(Q^2)F_{\pi qq}(Q^2), \tag{4}$$

[3]At the photon point $Q^2 = 0$, $\epsilon^{(\lambda)}_\mu = \{0, \hat{\mathbf{n}}_\perp\}$ and in the low-energy limit $k'_0 \to m_\pi$ the same quark calculation gives exactly rise to the Kroll-Ruderman term [15] for the threshold pion photoproduction.

where $F_q(Q^2)F_{\pi qq}(Q^2) \simeq F_\pi(Q^2)$.

We calculate the longitudinal part of differential cross section

$$\frac{d\sigma_L}{dt} = \frac{\mathcal{N}}{4\pi}\overline{|J^\mu_\pi \varepsilon^{(\lambda=0)}_\mu|^2}, \quad \mathcal{N} = m_N^2\left[(W^2 - M_N^2)\sqrt{(W^2 - Q^2 - M_N^2)^2 + 4W^2Q^2}\right]^{-1} \tag{5}$$

for quasi-elastic pion knockout taking into account both the t-pole contribution (1) and the s- and u-pole contribution (4),

$$\overline{|J^\mu_\pi \varepsilon^{(\lambda=0)}_\mu|^2} = \frac{1}{2}\sum_{spin}|\langle N_{3q}(P')|\sum_{j=1}^{3}\left[\mathcal{M}^{(j)\mu}_{q(t)} + \mathcal{M}^{(j)\mu}_{q(s+u)}\right]\varepsilon^{(\lambda=0)}_\mu |N_{3q}(P)\rangle|^2, \tag{6}$$

and compare the results with the JLab data [1] and to the Regge model [3] predictions (see Fig. 8 adapted from [14]). The CQM calculation of the right-hand side of Eq. (6) leads to a

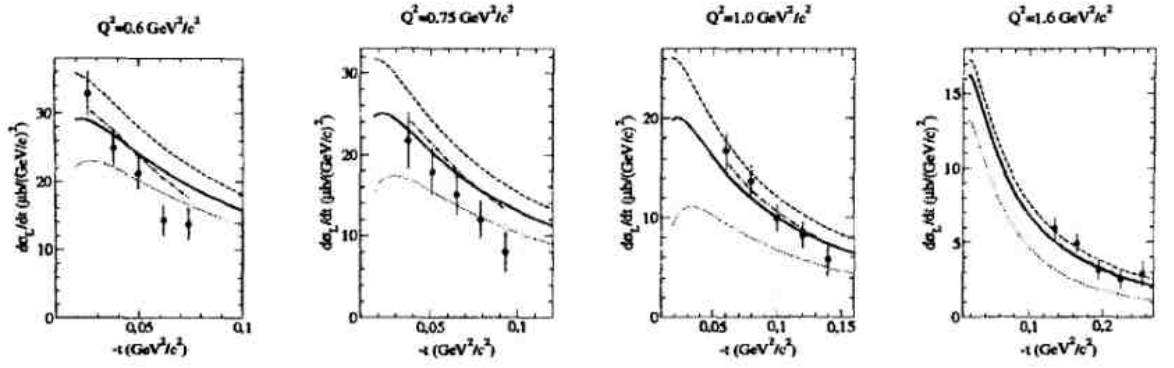

Figure 8: Longitudinal cross sections for the $p(e,e'\pi^+)n$ reaction calculated [14] with the amplitude (7) – solid lines; the contribution of the pion t-pole – dashed lines; the VGL model (adapted from [1]) – dash-dotted lines. The JLab $F\pi 1$ data [1].

simple matrix element for a non-relativistic nucleon wave function $\Phi_N(\boldsymbol{\rho}_1, \boldsymbol{\rho}_2)$. Using Eqs. (2) and (4) we obtain:

$$J^\mu_\pi \varepsilon^{(0)}_\mu \simeq i\tau_- \frac{e g_{\pi NN}}{2M_N} F_\pi(Q^2) F_{\pi NN}(t)\left[\frac{2\varepsilon^{(0)}\cdot k'\boldsymbol{\sigma}\cdot\mathbf{k}}{t - m_\pi^2} - \frac{M_N Q}{W^2}\boldsymbol{\sigma}\cdot\hat{\mathbf{q}}\right]. \tag{7}$$

The ρ-pole contribution to the transverse part of differential cross section $d\sigma_T/dt$ is proportional to the value $\overline{|J^\mu_\rho \varepsilon^{(\lambda=1)}_\mu|^2}$, where

$$J^\mu_\rho \varepsilon^{(\lambda)}_\mu = i\tau_- e g_{\rho\pi\gamma}\frac{M_\rho}{M_\pi} F_{\rho\pi\gamma}(Q^2)\frac{1+\varkappa_\rho}{2M_N} g_{\rho NN} F_{\rho NN}(t)|\mathbf{q}|\frac{i[\boldsymbol{\sigma}\times\mathbf{k}]\cdot\boldsymbol{\epsilon}^{(\lambda)}}{t - M_\rho^2} \tag{8}$$

and $\varepsilon^{(\lambda)\mu} = \{0, \boldsymbol{\epsilon}^{(\lambda)}\}$ for $\lambda = \pm 1$. .

However, for the ρ-meson t-pole amplitude which includes the $M1$ spin transition $\rho + \gamma^*_T \to \pi$ the relativistic correction are more important than for the pion t-pole amplitude. It can be seen, e.g., from a simple comparison of Eqs. (7) and (8). The t-pole amplitude in Eq. (7) is proportional the factor $\boldsymbol{\sigma}\cdot\mathbf{k}$ which is a non-relativistic one at $\mathbf{k}^2 \ll m_N^2$, while the amplitude (8) in parallel with a non-relativistic factor $\boldsymbol{\sigma}\times\mathbf{k}$ contains also a relativistic one $\sim |\mathbf{q}|$ with $\mathbf{q}^2 \gg Q^2$ ($\mathbf{q}^2/Q^2 \approx 7$ - 9 for the Fpi1 and Fpi2 kinematics). Note that in the full relativistic calculations presented in the next section the non-relativistic factor $\mathbf{q}^2$ is transformed into the Q^2.

3 Calculation of σ_T in terms of the tensor ρ-meson field

The pion t-pole contribution to the forward angle σ_T is too small

$$\frac{d\sigma_T^\pi}{dt} = \mathcal{N} 2\alpha\, F_\pi^2(Q^2)\, g_{\pi NN}^2 F_{\pi NN}^2(t) \frac{t^2}{(M_\pi^2 - t)^2} sin^2\theta_\pi \tag{9}$$

to reproduce the experimental cross section as the t-pole denominator $(M_\pi^2 - t)$ in (9) is compensated by a very small nominator -t, $-t/(M_\pi^2 - t) \approx 1$. Thus, the ρ-pole dominates in the $d\sigma_T/dt$, but the traditional approach to the ρ-exchange in terms of the vector ρ-meson field V_μ leads to a very small contribution to the cross section

$$\frac{d\sigma_T^\rho}{dt} = \mathcal{N}\alpha\, g_{\rho\pi\gamma}^2 \frac{m_N^2}{M_\pi^2} F_{\rho\pi\gamma}^2(Q^2) F_{\rho NN}^2(t) \frac{-tQ^2}{(M_\rho^2 - t)^2} sin^2\theta_\pi, \tag{10}$$

as the deeply off-shell ρ-meson denominator $(M_\rho^2 - t)$ dampens the cross section because of the factor $-t/(M_\rho^2 - t) \ll 1$.

Fortunately, there is an alternative description of the ρ-meson in terms of a tensor field $W_{\mu\nu}$ proposed in 80th on the basis of non-linear realization of chiral symmetry (see, e.g., one of the recent works [16]). The ρ-meson matrix elements calculated in terms of V_μ and $W_{\mu\nu}$ fields are equal on mass shell $t \to M_\rho^2$, but they differ considerably in the off-mass shell region $M_\rho^2 - t \approx m_N^2$.

The tensor variant of ρNN interaction

$$\begin{aligned} \mathcal{L}_{\rho BB}^W &= R_{D/F}\langle \bar{B}\sigma^{\mu\nu}(W_{\mu\nu}, B)_\pm\rangle + S_{D/F}\langle \bar{B}\gamma^\mu([D^\nu, W_{\mu\nu}], B_\pm)\rangle \\ &+ U_{D/F}\langle \bar{B}\sigma^{\lambda\nu}(W_{\mu\nu}, [D_\lambda, [D^\mu, B]])_\pm\rangle, \quad W_{\mu\nu} = \frac{1}{2}\sum_{a=1}^{8} \lambda_a W_{\mu\nu}^a, \end{aligned} \tag{11}$$

where $R_{D/F}$, $S_{D/F}$ and $U_{D/F}$ are D- and F-coupling constants for the baryon octet B, is more complicated than the traditional vector variant

$$\mathcal{L}_{\rho NN}^V = \frac{1}{2}\bar{N}\left(G_{\rho NN}\vec{V}_\mu\gamma^\mu - \frac{F_{\rho NN}}{2M_N}\sigma^{\mu\nu}\partial_\nu\vec{V}_\mu\right)\cdot\vec{\tau}N \tag{12}$$

The $\rho\pi\gamma$ vertex and the ρ-meson propagator in the tensor variant does not also coincide with those in the vector one. However, in both variants the final result for the pion knockout amplitude is the same

$$\begin{aligned} T_{\gamma p\to n\pi^+}^{(V)} = -\frac{e}{2\sqrt{2}}\frac{g_{\rho\pi\gamma}}{M_\pi}\epsilon^{\rho\sigma}(q)\bar{u}_n(p')\left\{\left(G_{\rho NN} + \frac{\left(\frac{k^2}{M_\rho^2}\right)}{4m_N^2}F_{\rho NN}\right)\frac{2m_N}{M_\rho^2 - k^2}\sigma_{\rho\sigma}\gamma_5\right. \\ \left. -\frac{2m_N}{M_\rho^2 - k^2}\left[G_{\rho NN}\frac{P_\rho\gamma_\sigma - P_\sigma\gamma_\rho}{2m_N} - F_{\rho NN}\frac{P_\rho\, k_\sigma - P_\sigma k_\rho}{4m_N^2}\right] i\gamma_5\right\} u_p(p), \end{aligned} \tag{13}$$

except the factor $\left(\frac{k^2}{M_\rho^2}\right)$ which is equal to k^2 for the variant V_μ and M_ρ^2 — for the $W_{\mu\nu}$. (In Eq. (13) the connections between tensor and vector coupling constants for $B = N$, $G_{\rho NN} = [m_N(U_F + U_D) - 2(S_F + S_D)]M_\rho/\sqrt{2}$, $F_{\rho NN} = -4\sqrt{2}m_N(R_F + R_D)/M_\rho$, are taken into account). Both results are equal each other on the mass shell $k^2 \to M_\rho^2$, but in the region $(k^2 - M_\rho^2) \approx m_N^2$ the cross section $d\sigma_T^{\rho(W)}/dt$ is greater than the $d\sigma_T^{\rho(V)}/dt$ in an order of magnitude.

4 Results and discussion

In our calculation we use a standard (monopole-like) representation for the pion charge form factor $F_\pi(Q^2) = \Lambda_\pi^2/(\Lambda_\pi^2 + Q^2)$ with Λ_π^2 =0.54 GeV^2/c^2, which is close to the recent theoretical evaluation [17] and correlates well with the recent JLab data [1]. For the $\rho\pi\gamma$ magnetic spin-flip form factor we use the same formula, but with a free cut-off parameter $\Lambda_{\rho\pi}$ and fit the σ_T data at $\Lambda_{\rho\pi}^2$ =0.8 GeV^2/c^2. We think that a future more accurate analysis of the σ_T data can shed light on the proper value of $\Lambda_{\rho\pi}$. For the $\rho\pi\gamma$ coupling constant we take the value $g_{\rho\pi\gamma} = 0.103$, which is fixed by the partial decay width $\Gamma_{\rho\to\pi\gamma} = 67$ KeV, and use the conventional values $G_{\rho NN}(0) = 6.2$ and $F_{\rho NN}(0) = 33.79$ for the ρNN coupling constants.

Apart from the above values we vary only one free parameter, Λ_{str}, in the monopole representation of the strong πNN and ρNN form factors, $F_{\pi NN}(t) = F_{\rho NN}(t)/F_{\rho NN}(0) = \Lambda_{str}^2/(\Lambda_{str}^2 - t^2)$. The range 0.6 - 0.8 GeV/c for the Λ_{str} corresponds to a reasonable value $b \simeq$ 0.5 - 0.6 fm for the radius of the "quark core" of nucleon in the CQM. At a realistic values $\Lambda_{str} = 0.7$ GeV/c and $g_{\pi NN} = 13.5$ our results (the solid lines in Fig. 9) are in a reasonable agreement with the Fpi1 data on σ_L and σ_T. Recall that our previous results [14] with a good description of the σ_L (Fig. 8) fail to describe the σ_T on the basis of the relativistic amplitude (10) for the vector variant V_μ. Now, with a more appropriate tensor variant $W_{\mu\nu}$ we can predict the σ_L and σ_T cross sections for the future Fpi2 data (Fig. 9) at higher Q^2, W.

In our calculation we model the s- and u-channel non-resonance contributions to the σ_L by a nonlocal extension of the Kroll-Ruderman contact term obtained in the CQM. The corresponding amplitude behaves as $\sim \frac{m_N Q}{W^2} F_\pi(Q^2)$ at large Q^2 and leads to an essential improvement of the description of σ_L at low $Q^2 \lesssim 1$ GeV^2/c^2 (Fig. 8, solid and dashed curves). At intermediate values $Q^2 \gtrsim 1$ GeV^2/c^2, which correspond to a quasielastic mechanism of pion knockout, the calculated σ_L is close to the experimental data, but at lower Q^2 the agreement with the Fpi1 data becomes worse. Nevertheless our results are close to the σ_L calculated with the Reggeon-pole exchange in the VGL model (dash-dotted lines in Fig. 8 and 8).

Our calculation shows that the transverse cross section should be critically dependent on the ρ-meson t-pole contribution (this was first shown in Ref. [7] and then supported in Ref. [18]). Thus, at high Q^2 and W the experimental data on σ_T can be used for the direct measurement of the strong ρNN form factor. By our results the Fpi1 data on σ_L and σ_T are compatible with the soft cut-off parameter $\Lambda_{str} = 0.7$ GeV/c common for the $F_{\pi NN}$ and $F_{\rho NN}$ form factors.

More accurate data on σ_L and σ_T at higher $Q^2 \gtrsim 2$ - 3 GeV^2/c^2 would be very useful to obtain further information on the above discussed strong and electromagnetic vertices.

References

[1] J. Volmer *et al.* Phys. Rev. Lett. **86** (2001) 1713; J. Volmer, Ph.D. thesis, Vrije Univ., Amsterdam, 2000 (unpublished).

[2] G. Huber, D. Mack and H. Block, JLab experiment E01-004(2003); E. J. Beise, AIP Conf. Proc. **698** (2004) 23 [Nucl. Phys. A **751** (2005) 167].

[3] M. Vanderhaeghen, M. Guidal, and J.-M. Laget, Phys. Rev. C **57** (1998) 1454; Nucl. Phys. A **627** (1997) 645.

[4] V.G. Neudatchin, YU.V. Popov, and Yu.F. Smirnov, Uspekhi Fiz. Nauk **69**, 1111 (1999).

[5] V.G. Neudatchin, A.A. Sakharuk, V.V. Kurovsky, and Yu.M. Tchuvil'sky, Phys. Rev. C **51**, 784 (1995).

[6] V.G. Neudatchin, I.T. Obukhovsky, L.L. Sviridova, and N.P. Yudin, Nucl. Phys A **729**, 124 (2004).

[7] J. Speth and V. R. Zoller, Phys. Lett. B **351** (1995) 533.

[8] J. Speth and A. W. Thomas, Adv. Nucl. Phys. **24** (1997) 83.

[9] N. N. Nikolaev, A. Szczurek and V. R. Zoller, Z. Phys. A **349** (1994) 59.

[10] E.D. Bloom and F.J. Gilman, Phys. Rev. Lett. **25**, 1140 (1970).

[11] W. Melnitchouk, R. Ent and C. Keppel, Phys. Rept. **406** (2005) 127.

[12] A. De Rújula, H. Georgi, and H.D. Politzer, Ann. Phys. (N.Y.)**103**, 315 (1975).

[13] F. Cardarelli, I. L. Grach, I. M. Narodetsky, E. Pace, G. Salme and S. Simula, Phys. Rev. D **53** (1996) 6682.

[14] I.T. Obukhovsky, D. Fedorov, A. Faessler, Th. Gutsche, and V.E. Lyubovitskij, Phys. Lett. B **634**, 220 (2006).

[15] N. M. Kroll, M. A. Ruderman, Phys. Rev. **93** (1954) 233.

[16] B. Kubis and Ulf-G. Meissner, Nucl. Phys. A **679**, 698 (2001).

[17] P. Maris and P. C. Tandy, Phys. Rev. C **62** (2000) 055204; A. Faessler, T. Gutsche, M. A. Ivanov, V. E. Lyubovitskij and P. Wang, Phys. Rev. D **68** (2003) 014011.

[18] N.P. Yudin, L.L. Sviridova, and V.G. Neudatchin, Phys. At. Nucl. **61** (1998) 1577.

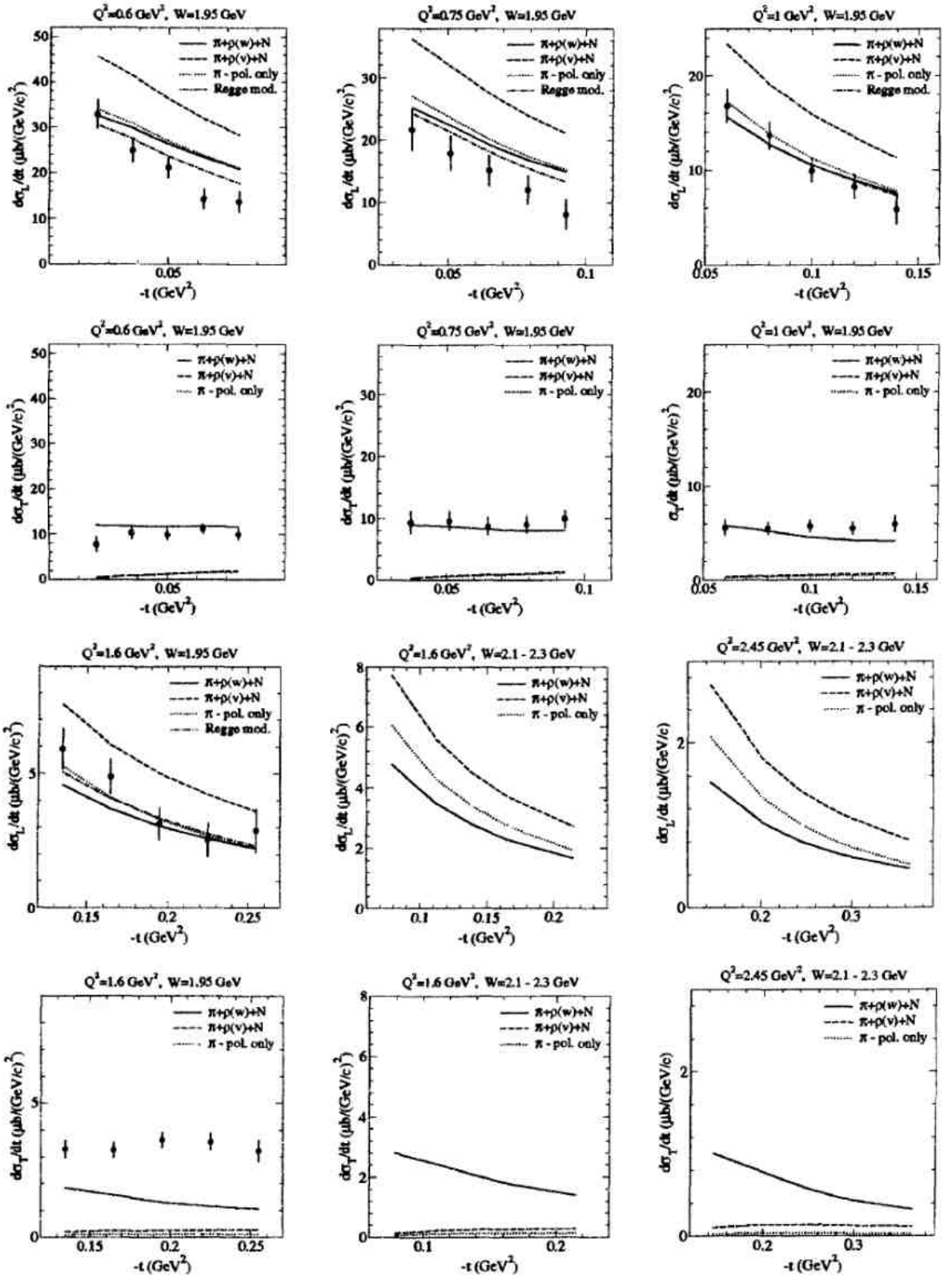

Figure 9: Longitudinal and transverse cross sections for the $p(e, e'\pi^+)n$ reaction calculated in the full model with tensor (solid) and vector (dashed) variants of the ρ-meson fields. The pion t-pole contribution (dotted) and the VGL model results (dash-dotted) adapted from [14] and [1] respectively.. Comparison with the JLab $F\pi 1$ data [1] and predictions for Fpi2.

NEW RELATIONAL DATABASE FOR EXPIREMENTAL AND MODEL MESON PHOTOPRODUCTION DATA IN INTERNET

A.D.Belyaev[2], V.V.Chesnokov[3], A.S.Ignatov[1], V.G.Nedorezov[1], N.N.Peskov[3], M.E.Stepanov[4], A.A.Turinge[2], V.V.Varlamov[3]

[1]Institute for Nuclear Research, Russian Academy of Sciences, Moscow, Russia; [2]Russian scientific center "Kurchatovski Institute", Moscow, Russia;[3]Skobeltsyn Institute of Nuclear Physics, Lomonosov Moscow State University, Moscow, Russia; [4]Faculty of Physics, Lomonosov Moscow State University, Moscow, Russia

1. Introduction

Recently we began development of new relational database for experimental and model meson photoproduction data in internet [1]. It's aim is to investigate the processes of photoproduction of pi-mesons, K-mesons and heavier mesons on free and bound nucleon in the nucleon resonance energy region (150 – 1500 MeV). Data on meson photoproduction is of great interest for solving several fundamental problems, including the investigation of static, dynamic and spin structure of nucleon, research for influence of nuclear matter on the nucleon structure, measurement of the fundamental sum rules, multipole analyses of electromagnetic interactions between nucleons and other. Work is based on data retrieved earlier and being retrieved nowadays from results of the experiment carried out by international collaboration GRAAL and also results from SP-ring-8 (Japan), Sibir2 (Russia), TJNAF (USA), MAMI-B (Germany) and others. The new database will include data on both static and dynamic features of nucleons obtained using data on cross sections of photoproduction of heavy mesons, mass, resonance magnitudes and widths, sum rules, anomalous magnetic moments of nucleon and other would be carried out. Those will be added by the data of simulation of photoproduction processes using GEANT and INC software. As a result we will have new fundamental information, which is necessary to develop hadron, quark and phenomenological models.

2. Data sources

In fact, data, gathered in this new database, will be a compilation of experimental results extracted from other databases and from publications directly, as the aim is to create a system, which will cover as many experiments as possible. As an example of source database we can outline HEPDATA REACTION DATABASE which was compiled by the Durham Database Group (UK) with help from the COMPAS group (Russia) [2]. Experiments, from which some data was taken, were mentioned above. But we can outline experimental results of international collaboration GRAAL [3]. Its work in recent years gave a lot of significant results in research of photoproduction of mesons on proton and neutron. That is why we intend to include its results fully.

Separately stays data retrieved from simulation using GEANT software. It will also be added including photoproduction on light and heavy nuclei.

→

Fig.1 Search interface of new relational database for experimental and model photoproduction of mesons in internet.

3. Principle of data presentation

The data files consist of twenty positions. They include such information as authors, year and reference of publication. Then it is the beam and target particles, products of reaction in any combination. Speaking about physical parameters they are observable, which is needed. Depending on it, the next positions are energies and angles in laboratory or c.m. reference frame. The search can be performed by any of parameter listed above. As the result one gets all other information including table with cross-section data.

On Fig.1 the search interface of photoproduction database is presented. It consists of two parts: reaction and bibliography. The interface is easy to understand and enough functional. As an example the results of search when we need information on full cross-section of reaction where outgoing particle is eta-meson published in European Physical Journal in 2002 year are given on Fig.2. We can see full reference, first author, target and outgoing particles and quantity, in which we are interested. On the left side of each result we can push "Level plot" button to see full table of cross-section data. It is presented on Fig.3. We can see full information on cross-section and also some extended information, such as all the authors, reaction, energy interval and comment on table of data.

LOMONOSOV MOSCOW STATE UNIVERSITY, SKOBELTSYN INSTITUTE OF NUCLEAR PHYSICS

CENTRE FOR PHOTONUCLEAR EXPERIMENTS DATA

Online Services | Partners | Links | About | Team | Publications | Contacts

CDFE => Online Services => Meson

Meson

Construct your query and output by sequental openings of needed fields.
One output field must be selected (not be blank) at least.

Reaction

Target	Z:	A:		
Incident	all	Z:	A:	
Outgoing	eta			
Quantity	sig			
Energy / Angle	Energy		MEV	Laboratory system
	Angle		ADEG	Center of mass system

Bibliography

Journal	European Physical Journal
Author	
Article title	
Year	2002
Volume	
Page	

Submit query | Clear all

[Online Services | Partners | About | Team | Publications | Contacts | Links | Russian]

If you have any questions, comments, and/or suggestions, please, contact
CDFE Head Vladimir V. Varlamov

© Programming by Vitaly V. Chesnokov

	Reference	Author	Target	Incident particle	Outgoing particle	Quantity
	European Physical Journal a15, 493, 2002	Hejny	deut	gamma	eta	sig
	European Physical Journal a15, 493, 2002	Hejny	he	gamma	eta++	sig

Fig.2 Results of search by parameters shown on Fig.1

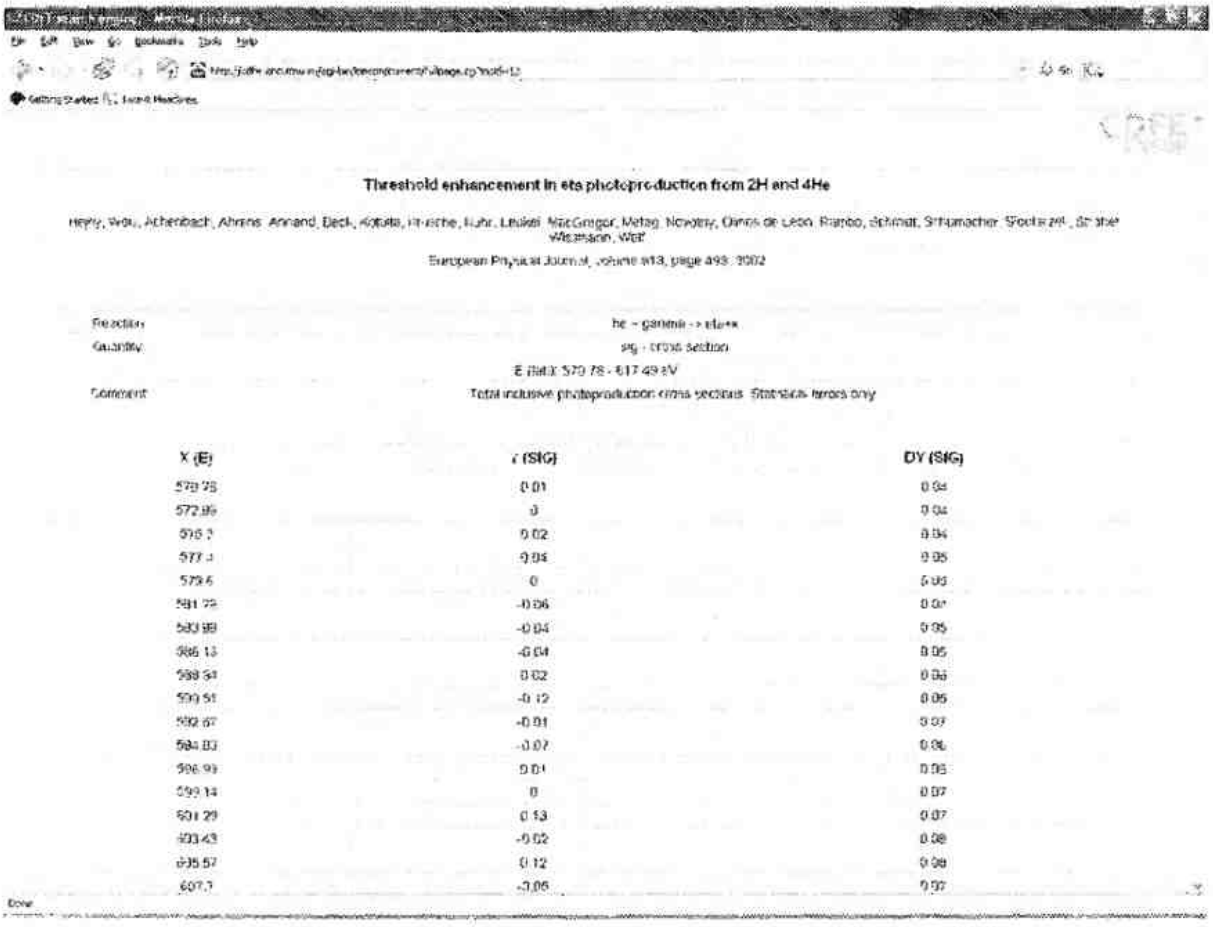

Threshold enhancement in eta photoproduction from 2H and 4He

Hejny, Metz, Achenbach, Ahrens, Annand, Beck, Kotulla, Hirsche, Kuhr, Leukel, MacGregor, Metag, Nowotny, Olmos de Leon, Rambo, Schmidt, Schumacher, Stoltenberg, Strate, Weissmann, Wolf

European Physical Journal, volume a13, page 493, 2002

Reaction	he - gamma - > eta++
Quantity	sig - cross section
	E (MeV): 570.78 - 617.49 eV
Comment	Total inclusive photoproduction cross sections. Statistical errors only

X (E)	Y (SIG)	DY (SIG)
570.78	0.01	0.04
572.89	0	0.04
575.0	0.02	0.04
577.1	0.04	0.05
579.6	0	0.05
581.72	-0.06	0.0
583.88	-0.04	0.05
586.13	-0.04	0.05
588.54	0.02	0.06
590.51	-0.12	0.06
592.67	-0.01	0.07
594.83	-0.07	0.06
596.99	0.01	0.05
599.14	0	0.07
601.29	0.13	0.07
603.43	-0.02	0.08
605.57	0.12	0.09
607.7	-0.05	0.07

Done

Fig.3 Full table of cross-section data of the selected publication. All authors and full information on reaction parameters and particle energies is also given.

The work is supported by RFBR grant № 05-07-90329-в.

References:

1. http://cdfe.sinp.msu.ru/services/meson/meson.en.html
2. http://durpdg.dur.ac.uk/HEPDATA/REAC
3 http://www.lnf.infn.it/~levisand/graal/graal.html

LOW ENERGY BRANCH OF THE GIANT DIPOLE RESONANCE IN PHOTO- AND ELECTRO-NUCLEAR REACTIONS

B.S. Dolbilkin
Institute for Nuclear Research RAS, Moscow, Russia

Abstract

An experimental information about a small resonance on the low energy side of the Electric Isovector Giant Dipole Resonance, observed in photo- and electro- nuclear reactions at the excitation energy $E_x \cong 52 \cdot A^{-1/3}$ MeV along the Periodic Table, near nucleon escape thresholds, is presented and discussed. Nuclei with the mass number A=58-208 and neutron excess are considered. A comparison of results with different probes is made. The Low Energy Dipole Resonance parameters:(1.5-3.0) % of photonuclear Sum Rules, width~ 1.5 MeV.

Giant Resonance excitations in nuclei, has been shown to be an universal nuclear phenomenon, upon which much interest has been focused, especially after the discovery of the Multipole Giant Resonances [1]. Experiments with a higher accuracy, especially made on the new generation of accelerators with continuous beams, have been investigated open problems of GR. In between, an interest has been initiated to other types of nuclear structure, as a Low Energy Dipole Resonance (LEDR) [2].

Measurements of the $^{58}Ni(e,e'c), c = p,\alpha$ reaction cross sections in the GR energy region 9-26 MeV at the momentum transfer interval q = 0.27-0.61 fm^{-1} and its subsequent multipole decomposition have been made in the coincidence experiment on continuous electron beam of the microtron MAMI A at Mainz, FRG. The primary electron beam on the target has been the energies 137 and 183 MeV, the electron scattering angle was 23-40^0. Kinematics of measurements is shown on Fig.1. Details of it were described elsewhere [3].

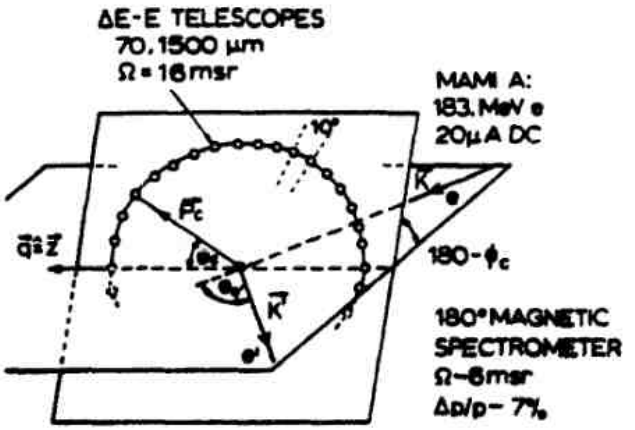

Fig.1. The kinematics of the $(e,e'c)$ experiment. The momentum transfer is directed along z-axis. Coincidences are between electrons in the magnetic spectrometer and $(\Delta E - E)$ telescopes, registrated the $(e,e'c)$ reaction products $c = p,\alpha$, protons and α -particles.

The obtained cross sections are shown on Fig.2 [3]. In addition, the (γ, p) [4] {together with $(e,e'p)$} and (γ,n) [5] reaction cross sections are also shown. More distinctly the small resonance at the energy excitation $E_x \sim 13$ MeV is seen in the $^{58}Ni(e,e'\alpha)$ reaction cross section (bottom). The cross section of the (γ,n) reaction has a resonance-like structure at the same energy, ~ 0.5 MeV above the reaction threshold. There are also irregularities about this energy (~ 13.5 MeV) in $^{58}Ni(e,e'p)$ and (γ,p) reaction cross sections.

Firstly at many experiments with electrons and hadrons a problem of the multipole decomposition has not been solved. From other side this problem does not exist in the photonuclear reactions, since its strong selectivity to E1 excitations.

The qualitative parameters of the resonance-like structures in the (γ,n) reaction cross sections,

measured with quasi-monochromatic photons, at energies 0.7-1.5 MeV higher reaction thresholds, are given at Table1[2,6].

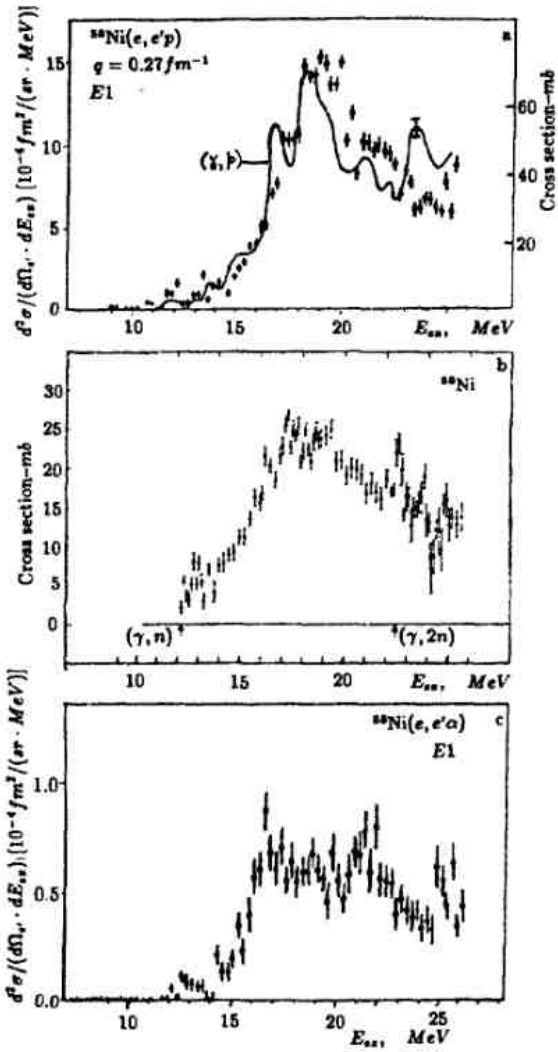

The energy of this dipole resonance is decreased from 13 MeV in ^{58}Ni to ~ 9 MeV in ^{208}Pb, showing the usual dependence for GR E_{max} ~ (50-53) $A^{-1/3}$ MeV at GT model.
The width is changed between 1.2 and 1.8 MeV. The maximum cross section is increased to heavy nuclei according Sum Rules. i.e. ~ proportional mass number A.
Ratio of integral cross sections to classic photonuclear Sum Rules is equal (1.5-3.0)%. The 2 times straggling probably depends from a low data accuracy in this energy excitation region.

Fig.2. The coincidence $^{58}Ni(e,e'p,\alpha)$ reaction cross sections together with $^{58}Ni(\gamma,p)$ (top) and (γ,n) (middle) ones

Parameters of resonance-like structures, observed in (γ,n) reaction cross sections for some nuclei in the A-range of 58-208 are shown in Table1.

Table 1. Resonance-like structure parameters of the near threshold resonance at (γ,n) reaction cross sections for nuclei mass numbers A=58 – 208 [2,6].

Nucleus	Threshold	E_x (MeV)	σ_{max} (mb)	Γ (MeV)	$\int\sigma dE$ (MeV×mb)	$\frac{\int\sigma dE}{\Gamma_{exp}}$	$E_x A^{-1/3}$ (γ,n)
^{58}Ni	12.2	13.0	4.0	1.5	10	3.0	52
^{60}Ni	11.4	12.7	7.0	1.2	13	2.0	50
^{64}Zn	11.9	12.9	6.5	1.5	15	2.0	52
^{74}Ge	10.2	12.2	8.0	1.5	20	2.0	51
^{76}Se	11.1	12.6	8.0	1.5	20	2.0	53
^{82}Se	9.2	12.2	10.0	1.5	24	2.5	53
^{96}Mo	9.2	11.5	13.0	1.5	31	2.0	53
^{108}Ag	9.2	10.5	15.0	1.5	35	2.0	50
^{121}Sb	9.2	10.8	20.0	1.2	39	2.0	53
^{140}Ce	9.2	10.0	20.0	1.8	56	2.3	52
^{144}Nd	7.8	9.5	16.0	1.5	50	2.0	50
^{150}Sm	8.0	9.5	20.0	1.5	55	2.5	51
^{153}Eu	8.6	9.5	15.0	1.5	35	1.5	51
^{165}Ho	8.0	9.3	15.0	1.5	35	1.5	51
^{153}Er	8.5	9.3	20.0	1.5	47	2.0	51
^{182}W	8.1	8.8	25.0	1.2	47	1.5	50
^{192}Os	7.56	8.5	20.0	1.5	47	1.5	50
^{208}Pb		9.0	25.0	1.5	59	2.0	53

The resonance- like structures with analogical properties are also observed in the total absorption cross sections (Table 2).

Table 2. Parameters of the near threshold resonance-like structure at photon total absorption cross sections [2,7,8]

Nucleus	E_x' (MeV)	σ_{max}	Γ (MeV)	$\int\sigma dE$	$\frac{\int\sigma dE}{\Gamma_{exp}}$	$E_x A^{-1/3}$ (MeV)
^{55}Mn	13.0	8.0	1.5	20.0	2.5	50
^{76}Se	12.5	12.0	1.5	28.0	2.0	53
^{82}Se	12.0	16.0	1.5	34.7	2.0	53

As it is seen from Table 2 the parameters of this resonance structure are analoqous ones of the (γ,n) reaction cross sections (Table 1).

Photon scattering spectra of ^{140}Ce and ^{144}Sm nuclei were measured at an endpoint energy E_γ = 9.9 MeV and angle 90^0 [9]. The E1 strength was found at the excitation energies near 6 MeV. In ^{140}Ce the resonance-like structure is seen at the 6.2 MeV energy with the width of an order 0.2 MeV and E1 strength ~ 1% of the EWSR. The threshold of neutron separation is 9.2 MeV. The authors suppose, that E1 strength registrated at the experiment can be explained as collective oscillations of excess neutrons against a $N \approx Z$ core [10]. Since the similarity of this excitation mechanism to that of the well known GDR, such kind of oscillations are often called " Pigmy Dipole Resonance"(PDR). But the essential difference their data from the parameters of Table 1 and 2 is supposed to assume different resonance nature.

Resonances has been also found at ^{nat}Ce in the elastic photon scattering experiment with tagged photons [11] at energies 6.5, 6.9, 7.9 and 8.3 MeV (Fig.3). Natural Ce was used with an abundance 88.5% of ^{140}Ce and 11.1% of ^{142}Ce with the (γ,n) threshold 7.2 MeV. Resonances at these energies, including most prominent ones, have not been observed at [9]. So the existence of PDR, at least in Ce needs future investigations.

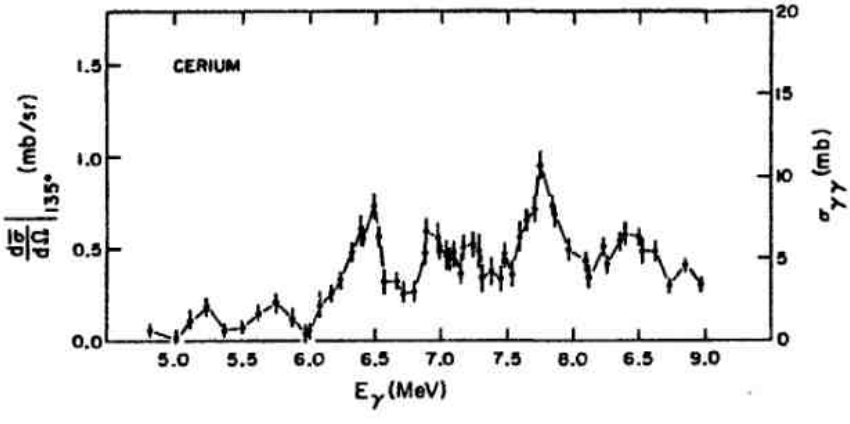

Fig.3. Elastic tagged photon scattering cross section for the natural ^{140}Ce

For mass numbers more $A > 50$ the most of (e,e') cross sections, measured at low momentum transfer, display resonance-like structures at the same excitation energies $E_x \approx 52 \cdot A^{-1/3}$ MeV, i.e. as well known GDR according G-T model. Similar irregularities at the same energy has been noticed in hadron experiments with deuterons, α -particles and other probes [2,3 and ref. therein].

However, since a multipole decomposition is a rather uncertain procedure in this type experiments, results of it were often ambiquous and would be interpreted differently. On this reason resonance-like structures were assigned mainly E2, sometimes E0 or E3 multipolarities.

An example for ^{58}Ni and ^{60}Ni nuclei is presented on Fig.4, where are shown total GDR cross sections on $^{58,60}Ni$ isotopes.

The each cross section is fitted by 4 Lorentz curves. The main GDR components are in a general accordance with theoretical predictions of the its isospin splitting. For comparison total (γ,n) cross sections are done for both nuclei. In the insets on the Fig.4 are shown form factors for the 13 MeV resonances. In difference from the classic GDR a mixture of E1 and E3 form factors is seen here.

A possible explanation was done in frames of hydrodynamic model with shearing vibrations [13] and later at the solution of the kinetic equation [14].

Energies and other parameters of torsional and toroidal vibrations have been estimated using an nuclear local velocity field and Sum Rules of RPA in frames of Fermi-gas model. As a result an dipole state of the isovector and isoscalar nature, connected with shearing vibrations, was predicted at the energy~$55A^{-1/3}$ MeV.E1 shearing vibrations are mixed with the usual Coulomb GDR. Their strength is a few % of the last one.

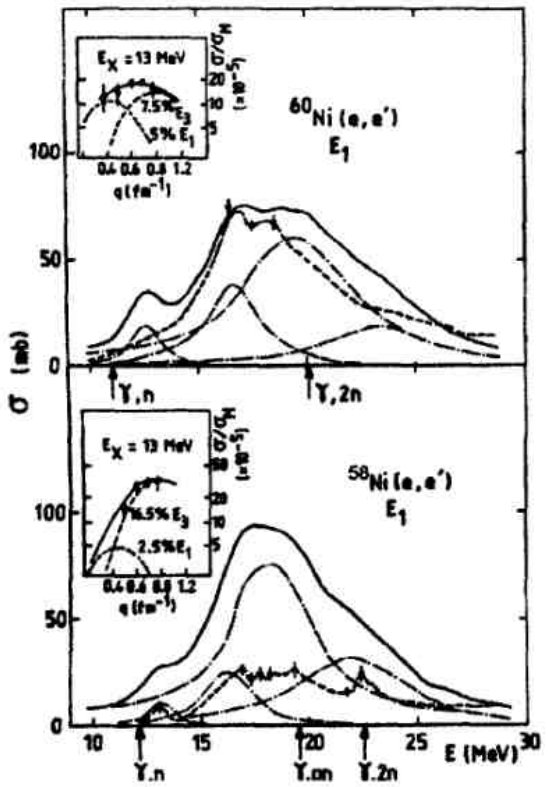

Fig.4. The E1 cross sections in the reactions $^{58}Ni(e,e')$ (below) and $^{60}Ni(e,e')$, calculated from B-values for dipole excitations [2,12]. In the insets form factors are for 13 MeV- resonances at each isotope. Curves with experimental points- total (γ,n) reaction cross sections [6].

The isovector E1 resonance has the same form factor q - dependence as classic GDR, as the isoscalar one – E3 form factor. Their sum results (Fig5) to conclusion about the resonance multipolarity as E2 transition.

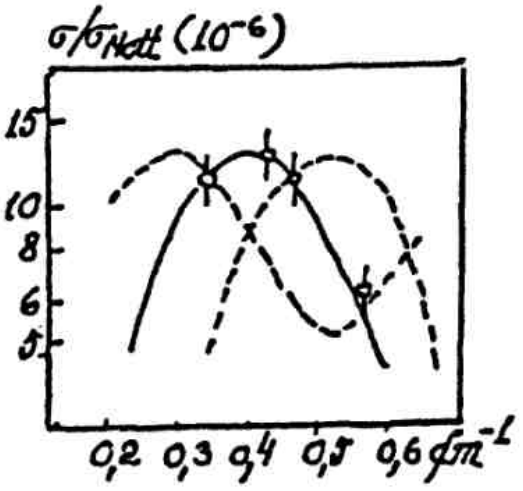

Fig.5. The E1,T=1 and E3, T=0 form factors. The E1,T=1 and E3, T=0 shearing vibration form factor mixture gives the usual E2,T=1 form factor. Experimental points would be followed the normal E2 form factor.

The energy dependence of the resonance at $E_x \approx 52 \cdot A^{-1/3}$ from different reactions and probes for the mass number A> 50 along the Periodic Table is presented on Fig.6. Results from the total photon absorption, (γ,n) and (e,e'), $(e,e'c)$ reactions are shown[2]. The dependence from $A^{-1/3}$ analogical to the usual GDR according to GT model.

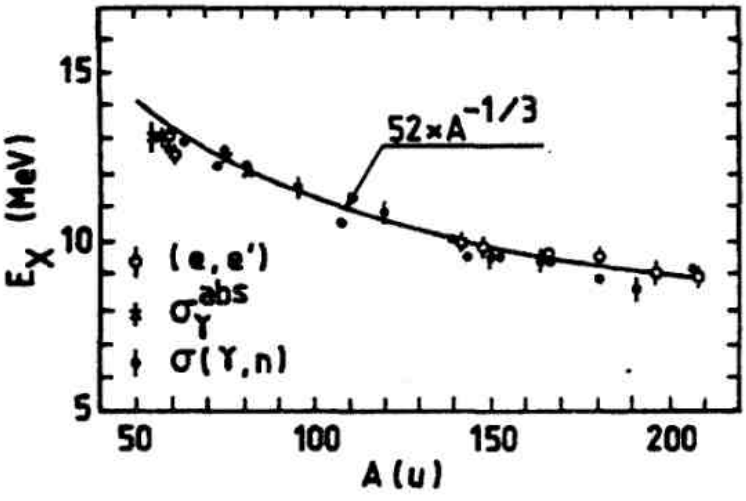

Fig.6. The excitation energy $E_x = 52 \cdot A^{-1/3}$ MeV in dependence from mass number A. Experimental (e,e') points include (e,e'p) results at A = 58,60[3].

In conclusion, the existence of resonance structure for nuclei with the mass number A>50 with the neutron excess is shown at photo- and electro- nuclear reactions with parameters: the excitation energy $E_x \approx (52 \pm 2) \cdot A^{-1/3}$ MeV, the width (1.2 ± 0.5) MeV and the integral cross section (2.0 ± 1.0)% part of the classic photonuclear Sum Rules. It would be useful to make experiments with different probes and better accuracy in the region of the mass number A>100 and continue microscopic theoretical calculations [15].

References:

1 H. Uberall, Electron scattering from complex nuclei, Academic, N.Y., 1971
F. Bertrand, Nucl. Phys. A354, 129,1981
2. B.S. Dolbilkin, Proc. 5th Course Int. School of IENP, Italy, 208,1985
3. B.S. Dolbilkin, et al, Z.Phys. A311,107, 1988
B.S. Dolbilkin, Proc. 8th Sem. EMIN, Moscow, 261, 1992.
4. B.S.Iskhanov et al, Sov. J. Nucl. Phys. 11, 272, 1970
5. S.C. Fultz et al, Phys. Rev. C10, 608, 1974
6. B. Berman and S.C. Fultz, Rev. Mod. Phys. 47, 713, 1975
7. B.S. Dolbilkin at al, Preprint FIAN-114, Moscow, 1969
8. G.M. Gurevich et al, Proc. 3rd Sem. EMIN, Nauka, Moscow, 60, 1976
9. P. Mohr et al, INPC2001,USA, AIP Conf. Proc.,610, 870, 2002
10. R Mohan et al, Phys. Rev. C3, 1740, 1971
11. R.M. Laszevsky, preprint Illinois Univ., USA,122, 1986
12. R.Pitthan et al, Phys.Rev.C21, 147, 1980
13. S. Semenco, JSNP, 34, 639, 1981
14. E.B. Balbutsev et al, J. Phys. G, Nucl. Phys. 12, 185, 1986
15. С.П. Камерджиев, Изв. РАН, сер. Физ., 61, 152, 1997

INCLUSIVE η-PHOTOPRODUCTION ON THE DEUTERON IN THE THRESHOLD REGION

A.I. Fix[1], M.I. Levchuk[2]

[1] *Tomsk Polytechnic University, Tomsk, Russia;*

[2] *B.I. Stepanov Institute of Physics, Belarussian Academy of Sciences, Minsk, Belarus*

About a decade ago, first experimental results for the total cross section of inclusive η-photoproduction on the deuteron in the near threshold region were reported by the Mainz group [1]. Later on, the TAPS Collaboration presented their data not only for the total cross section but also for the angular and momentum spectra of the emitted η-mesons [2].

A series of papers [3, 4, 5, 6, 7] was devoted to the theoretical study of the reaction $d(\gamma,\eta)np$, where contributions from the impulse approximation (IA) and the final state interactions (FSI) in the np- and ηN-subsystems were taken into account. It was claimed in Refs. [5, 6, 7] that such a model provides reasonable description of the data. On the contrary, the results of Refs. [3, 4] visibly underestimate the experimental cross sections. As is shown by the same authors in Ref. [4], very close to the threshold higher order terms in the multiple scattering series for the final ηNN interaction become very important, so that one has to use a rigorous three-body model. Indeed, according to the results of Ref. [4], inclusion of the 'three-body' effects leads to visible improvement of the theory. However, even in this case the theoretical total cross section is still too low in comparison to the data [1, 2].

Thus, there exists a principal disagreement between the predictions of Refs. [3, 4] and Refs. [5, 6, 7]. It seems especially surprising because it appears already within the IA, where the results, as direct calculations show, are quite insensitive to the model ingredients.

This unsatisfactory situation has motivated new calculations which we would like to present in this contribution. Our second goal is to consider a two-step mechanism which includes intermediate π-photoproduction with a subsequent $\pi N \to \eta N$ transition. Although this mechanism was already mentioned in Refs. [3, 4, 7], its contribution was not taken into account in those papers.

Below we give a brief overview of our model. All calculations refer to the c.m. frame. Let us denote by $k = (\omega, \vec{k})$, $p_d = (\varepsilon_d, -\vec{k})$, $q = (\varepsilon_\eta, \vec{q})$, $p_p = (\varepsilon_p, \vec{p}_p)$ and $p_n = (\varepsilon_n, \vec{p}_n)$ the 4-momenta of the initial photon and deuteron, the final η-meson, proton and neutron, respectively. A symbol E_γ is reserved for the lab photon energy. As independent kinematical variables we take the photon energy and the meson momentum $\vec{q}$, as well as the angles $\Theta_{\vec{p}}$ and $\phi_{\vec{p}}$ of one of the nucleons in the c.m. frame of the final np-pair. Using the equality

$$\sqrt{\vec{P}^2 + M_p^2} + \sqrt{\vec{P}^2 + M_n^2} = W_{pn} = \sqrt{(k + p_d - q)^2}, \tag{1}$$

where M_p and M_n are the proton and neutron masses, respectively, one can find the value $|\vec{P}|$. After boosting the momenta $\vec{P}$ and $-\vec{P}$ with the velocity $\vec{v} = -\vec{q}/(\omega + \varepsilon_d - \varepsilon_\eta)$, the momenta of the outgoing nucleons are obtained and, therefore, the kinematics is totally determined.

The differential cross section is given by

$$\frac{d\sigma}{d\vec{q}\,d\Omega_{\vec{p}}} = \frac{1}{(2\pi)^5} \frac{M_p M_n \varepsilon_d |\mathbf{P}|}{4k \cdot p_d \; \varepsilon_\eta W_{pn}} \; \frac{1}{6} \sum_{m_p m_n \lambda m_d} |\langle m_p m_n | T | \lambda m_d \rangle|^2, \tag{2}$$

where m_p, m_n, λ, and m_d are spin states of the proton, neutron, photon, and deuteron, respectively. To obtain the inclusive differential cross section $d\sigma/d\Omega_\eta$, the right hand side of Eq. (2) has to be integrated over the value of the η momentum $q = |\vec{q}|$ and the solid angle $\Omega_{\vec{p}}$:

$$\frac{d\sigma}{d\Omega_\eta} = \int_0^{q^{max}} q^2 dq \int d\Omega_{\vec{p}} \frac{d\sigma}{d\vec{q}\,d\Omega_{\vec{p}}}. \tag{3}$$

The maximum value q^{max} can be found from Eq. (1) at $W_{pn} = M_p + M_n$.

We take into account contributions to the reaction amplitude from the diagrams displayed in Fig. 1. First three diagrams are those considered in Refs. [3, 4, 5, 6, 7]. The new mechanism is shown in Fig. 1*d*. In our calculations we use the Bonn CD potential [8] in order to generate the deuteron wave function and the half-off shell NN-scattering amplitude. We have checked that the results obtained with different NN-potentials are very close to each other, i.e. the calculation is practically insensitive to the model used for NN-interaction. An elementary $\gamma N \to \eta N$ operator is taken from the MAID01 isobar model [9]. Note, however, that similar results are obtained with a simpler model used in Refs. [3, 4, 5, 6, 7] where η-photoproduction proceeds exclusively through excitation of the $S_{11}(1535)$ resonance, $\gamma N \to S_{11}(1535) \to \eta N$. The ηN-interaction and $\pi N \to \eta N$ reaction are treated in the same manner via the $S_{11}(1535)$-excitation, i.e. as $\eta N \to S_{11}(1535) \to \eta N$ and $\pi N \to S_{11}(1535) \to \eta N$ transitions, respectively. Finally, an elementary operator for π-photoproduction on the nucleon, needed for evaluation of the diagram 1*d*, is taken from the MAID03 model [10].

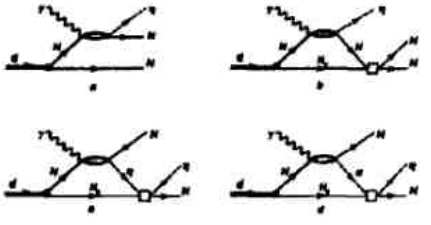

Figure 1: Diagrams considered in the present paper.

We begin the discussion with comparison of our angular and momentum spectra of η-mesons with the corresponding results presented in Ref. [7]. Both calculations are performed in the IA (diagram 1*a*). The dashed lines in Fig. 2 show our predictions using exactly the same model ingredients as in Ref. [7]. One can see drastic disagreement between two calculations especially very close to the threshold. It is difficult to find any reasonable explanation of this situation. At the same time, we have found very good agreement with the IA calculations from Refs. [3, 4]. As is seen in Fig. 2, slight sensitivity to the elementary η-photoproduction operator appears only above 650 MeV.

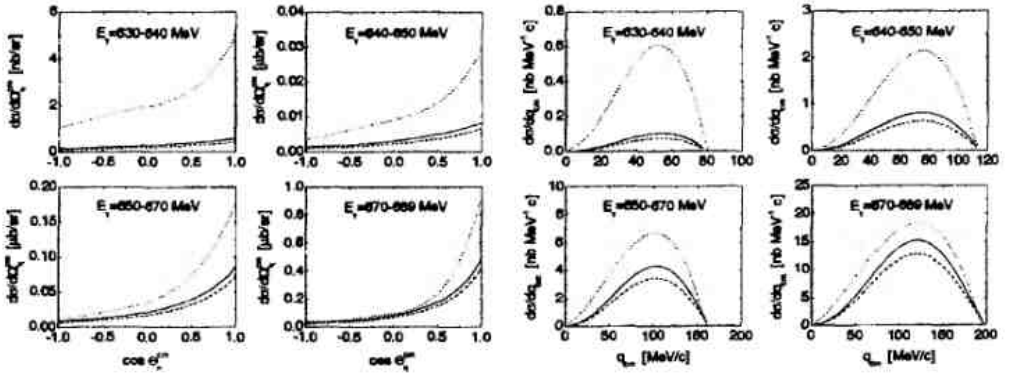

Figure 2: Two left panels: the angular distribution of the c.m. differential cross section in the IA averaged on the corresponding energy intervals. Dashed and solid lines are our results with an elementary η-production operator from Ref. [5] and MAID01 model [9], respectively. The doted lines are the predictions of Ref. [7]. Next two panels: the same for the momentum distribution.

In Fig. 3 we present our results for the total cross section from threshold to 700 MeV. The notable effect of the diagram Fig. 3*d* at $E_\gamma \geq 635$ MeV is readily seen. Adding the

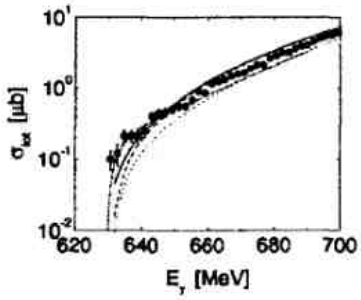

Figure 3: Total cross section for the reaction $d(\gamma,\eta)np$. Dotted and dashed lines correspond to contributions from diagrams in Fig. 1*a-c* and 1*a-d*, respectively. Solid line includes the coherent cross section from Ref. [4]. Dash-dotted line is the prediction of Ref. [7] for the reaction $d(\gamma,\eta)np$. The $\gamma d \to \eta X$ data are from Ref. [2].

contribution from the coherent channel $\gamma d \to \eta d$ calculated in Ref. [4] we obtain the $\gamma d \to \eta X$ cross section. One can see the reasonable description of the data above 640 MeV if the diagram 1*d* is included. But four data points just above breakup threshold clearly overestimate the predictions. Reasons for the disagreement remain to be elucidated. As is seen in Fig. 3, our predictions for the total cross section do not agree with those from Ref. [7]. In particular, if diagram 1*d* is disregarded our total cross section at $E_\gamma = 640$ MeV is by about a factor of 2.5 lower. Of course, this disagreement is expected in view of the substantial discrepancies of two calculations in IA. We think that even though the authors of Ref. [7] presented very good description of the data [1, 2] in the near-threshold region, the discrepancy discussed above, makes the situation much less clear. Further investigations are needed before we can make firm conclusions about our understanding of the low-energy η-photoproduction on the deuteron.

This work was supported by the Deutsche Forschungsgemeinschaft (SFB 443) and by Belarus RFFR (grants F05-168 and F05-303).

References

[1] B. Krusche *et al.*, Phys. Lett. B **358**, 40 (1995).

[2] V. Hejny *et al.*, Eur. Phys. J. A **13**, 493 (2002).

[3] A. Fix and H. Arenhövel, Z. Phys. A **359**, 427 (1997).

[4] A. Fix and H. Arenhövel, Eur. Phys. J. A **19**, 275 (2004).

[5] A. Sibirtsev, Ch. Elster, J. Haidenbauer, and J. Speth, Phys.Rev. C **64**, 024006 (2001).

[6] A. Sibirtsev, S. Schneider, Ch. Elster, J. Haidenbauer, S. Krewald, and J. Speth, Phys. Rev. C **65**, 044007 (2002).

[7] A. Sibirtsev, S. Schneider, Ch. Elster, J. Haidenbauer, S. Krewald, and J. Speth, Phys. Rev. C **65**, 067002 (2002).

[8] R. Machleidt, Phys. Rev. C **63**, 024001 (2001).

[9] W.-T. Chiang, S.-N. Yang, L. Tiator, and D. Drechsel, Nucl. Phys. **A700**, 429 (2002).

[10] D. Drechsel, O. Hanstein, S. S. Kamalov, and L. Tiator, Nucl. Phys. **A645**, 145 (1999).

ROLE OF SPIN EFFECTS IN THE NUCLEON CHARGE-EXCHANGE PROCESS $n + p \to p + n$ AT ZERO ANGLE

V.L.Lyuboshitz and V.V.Lyuboshitz†

Joint Institute for Nuclear Research,
141980 Dubna, Moscow region, Russia
† *E-mail: Valery.Lyuboshitz@jinr.ru*

1. Isotopic structure of NN-scattering

Taking into account the isotopic invariance, the nucleon-nucleon scattering is described by the following operator:

$$\hat{f}(\mathbf{p},\mathbf{p}') = \hat{a}(\mathbf{p},\mathbf{p}') + \hat{b}(\mathbf{p},\mathbf{p}')\hat{\boldsymbol{\tau}}^{(1)}\hat{\boldsymbol{\tau}}^{(2)}\,. \tag{1}$$

Here $\hat{\boldsymbol{\tau}}^{(1)}$ and $\hat{\boldsymbol{\tau}}^{(2)}$ are vector Pauli operators in the isotopic space, $\hat{a}(\mathbf{p},\mathbf{p}')$ and $\hat{b}(\mathbf{p},\mathbf{p}')$ are 4-row matrices in the spin space of two nucleons; $\mathbf{p}$ and $\mathbf{p}'$ are the initial and final momenta in the c.m. frame, the directions of $\mathbf{p}'$ are defined within the solid angle in the c.m. frame, corresponding to the front hemisphere.

One should note that the process of elastic neutron-proton scattering into the back hemisphere is interpreted as the charge-exchange process $n + p \to p + n$.

According to (1), the matrices of amplitudes of proton-proton, neutron-neutron and neutron-proton scattering take the form:

$$\hat{f}_{pp\to pp}(\mathbf{p},\mathbf{p}') = \hat{f}_{nn\to nn}(\mathbf{p},\mathbf{p}') = \hat{a}(\mathbf{p},\mathbf{p}') + \hat{b}(\mathbf{p},\mathbf{p}')\,;$$

$$\hat{f}_{np\to np}(\mathbf{p},\mathbf{p}') = \hat{a}(\mathbf{p},\mathbf{p}') - \hat{b}(\mathbf{p},\mathbf{p}')\,; \tag{2}$$

meantime, the matrix of amplitudes of the charge transfer process is as follows:

$$\hat{f}_{np\to pn}(\mathbf{p},\mathbf{p}') = 2\hat{b}(\mathbf{p},\mathbf{p}') = \hat{f}_{pp\to pp}(\mathbf{p},\mathbf{p}') - \hat{f}_{np\to np}(\mathbf{p},\mathbf{p}')\,. \tag{3}$$

It should be stressed that the differential cross-section of the charge-exchange reaction $\hat{f}_{np\to pn}(\mathbf{p},\mathbf{p}')$, defined in the front hemisphere $0 \le \theta \le \frac{\pi}{2}$, $0 \le \phi \le 2\pi$ (here θ is the angle between the momenta of initial neutron and final proton, ϕ is the azimuthal angle), should coincide with the differential cross-section of the elastic neutron-proton scattering $\hat{f}_{np\to np}(\mathbf{p},-\mathbf{p}')$ into the back hemisphere by the angle $\widetilde{\theta} = \pi - \theta$ at the azimuthal angle $\widetilde{\phi} = \pi + \phi$ in the c.m. frame. Due to the antisymmetry of the state of two fermions with respect to the total permutation, including the permutation of momenta ($\mathbf{p}' \to -\mathbf{p}'$), permutation of spin projections and permutation of isotopic projections ($p \leftrightarrows n$), the following relation between the amplitudes $\hat{f}_{np\to pn}(\mathbf{p},\mathbf{p}')$ and $\hat{f}_{np\to np}(\mathbf{p},-\mathbf{p}')$ holds [1] :

$$\hat{f}_{np\to pn}(\mathbf{p},\mathbf{p}') = -\hat{P}^{(1,2)}\hat{f}_{np\to np}(\mathbf{p},-\mathbf{p}')\,, \tag{4}$$

where $\hat{P}^{(1,2)}$ is the operator of permutation of spin projections of two particles with equal spins; the matrix elements of this operator are [2]: $\langle m_1' m_2' \mid \hat{P}^{(1,2)} \mid m_1 m_2\rangle = \delta_{m_1' m_2}\delta_{m_2' m_1}$. For particles with spin 1/2 [1,2]

$$\hat{P}^{(1,2)} = \frac{1}{2}(\hat{I}^{(1,2)} + \hat{\boldsymbol{\sigma}}^{(1)}\hat{\boldsymbol{\sigma}}^{(2)}), \tag{5}$$

where $\hat{I}^{(1,2)}$ is the four-row unit matrix, $\hat{\boldsymbol{\sigma}}^{(1)}$, $\hat{\boldsymbol{\sigma}}^{(2)}$ – vector Pauli operators. It is evident that $\hat{P}^{(1,2)}$ is the unitary and Hermitian operator:

$$\hat{P}^{(1,2)} = \hat{P}^{(1,2)+}, \quad \hat{P}^{(1,2)}\hat{P}^{(1,2)+} = \hat{I}^{(1,2)}. \tag{6}$$

Taking into account the relations (5) and (6), the following matrix equality holds:

$$\hat{f}^{+}_{np\to pn}(\mathbf{p},\mathbf{p}')\hat{f}_{np\to pn}(\mathbf{p},\mathbf{p}') = \hat{f}^{+}_{np\to np}(\mathbf{p},-\mathbf{p}')\hat{f}_{np\to np}(\mathbf{p},-\mathbf{p}'). \tag{7}$$

As a result, the differential cross-sections of the charge-exchange process $n+p\to p+n$ and the elastic np-scattering in the corresponding back hemisphere coincide at any polarizations of initial nucleons:

$$\frac{d\sigma_{np\to pn}}{d\Omega}(\mathbf{p},\mathbf{p}') = \frac{d\sigma_{np\to np}}{d\Omega}(\mathbf{p},-\mathbf{p}'). \tag{8}$$

However, the separation into the spin-dependent and spin-independent parts is different for the amplitudes $\hat{f}_{np\to pn}(\mathbf{p},\mathbf{p}')$ and $\hat{f}_{np\to np}(\mathbf{p},-\mathbf{p}')$!

2. Nucleon charge-exchange process at zero angle

Now let us investigate in detail the nucleon charge transfer reaction $n+p\to p+n$ at zero angle. In the c.m. frame of the (np)-system, the amplitude of the nucleon charge transfer in the "forward" direction $\hat{f}_{np\to pn}(0)$ has the following spin structure:

$$\hat{f}_{np\to pn}(0) = c_1\hat{I}^{(1,2)} + c_2\left[\hat{\boldsymbol{\sigma}}^{(1)}\hat{\boldsymbol{\sigma}}^{(2)} - (\hat{\boldsymbol{\sigma}}^{(1)}\mathbf{l})(\hat{\boldsymbol{\sigma}}^{(2)}\mathbf{l})\right] + c_3\,(\hat{\boldsymbol{\sigma}}^{(1)}\mathbf{l})(\hat{\boldsymbol{\sigma}}^{(2)}\mathbf{l})\,, \tag{9}$$

where $\mathbf{l}$ is the unit vector directed along the incident neutron momentum. In so doing, the second term in Eq. (9) describes the spin-flip effect, and the third term characterizes the difference between the amplitudes with the parallel and antiparallel orientations of the neutron and proton spins.

The spin structure of the amplitude of the elastic neutron-proton scattering in the "backward" direction $\hat{f}_{np\to np}(\pi)$ is analogous:

$$\hat{f}_{np\to np}(\pi) = \widetilde{c}_1\hat{I}^{(1,2)} + \widetilde{c}_2[\hat{\boldsymbol{\sigma}}^{(1)}\hat{\boldsymbol{\sigma}}^{(2)} - (\hat{\boldsymbol{\sigma}}^{(1)}\mathbf{l})(\hat{\boldsymbol{\sigma}}^{(2)}\mathbf{l})] + \widetilde{c}_3(\hat{\boldsymbol{\sigma}}^{(1)}\mathbf{l})(\hat{\boldsymbol{\sigma}}^{(2)}\mathbf{l}). \tag{10}$$

However, the coefficients $\widetilde{c}$ in Eq.(10) do not coincide with the coefficients c in Eq.(9). According to Eq.(4), the connection between the amplitudes $\hat{f}_{np\to pn}(0)$ and $\hat{f}_{np\to np}(\pi)$ is the following:

$$\hat{f}_{np\to pn}(0) = -\hat{P}^{(1,2)}\hat{f}_{np\to np}(\pi)\,, \tag{11}$$

where the unitary operator $\hat{P}^{(1,2)}$ is determined by Eq.(5).

As a result of calculations with Pauli matrices, we obtain:

$$c_1 = -\frac{1}{2}(\widetilde{c}_1 + 2\widetilde{c}_2 + \widetilde{c}_3); \quad c_2 = -\frac{1}{2}(\widetilde{c}_1 - \widetilde{c}_3); \quad c_3 = -\frac{1}{2}(\widetilde{c}_1 - 2\widetilde{c}_2 + \widetilde{c}_3). \tag{12}$$

Hence, it follows from here that the "forward" differential cross-section of the nucleon charge-exchange reaction $n+p\to p+n$ for unpolarized initial nucleons is described by the expression:

$$\frac{d\sigma_{np\to pn}}{d\Omega}(0) = |c_1|^2 + 2|c_2|^2 + |c_3|^2 =$$

$$= \frac{1}{4}|\widetilde{c}_1 + 2\widetilde{c}_2 + \widetilde{c}_3|^2 + \frac{1}{2}|\widetilde{c}_1 - \widetilde{c}_3|^2 + \frac{1}{4}|\widetilde{c}_1 - 2\widetilde{c}_2 + \widetilde{c}_3|^2 = |\widetilde{c}_1|^2 + 2|\widetilde{c}_2|^2 + |\widetilde{c}_3|^2. \qquad (13)$$

Thus,

$$\frac{d\sigma_{np\to pn}}{d\Omega}(0) = \frac{d\sigma_{np\to np}}{d\Omega}(\pi),$$

just as it must be in accordance with the relation (8).

3. Spin-independent and spin-dependent parts of the cross-section of the reaction $n + p \to p + n$ at zero angle

It is clear that the amplitudes of the proton-proton and neutron-proton elastic scattering at zero angle have the structure (9) with the replacements $c_1, c_2, c_3 \to c_1^{(pp)}, c_2^{(pp)}, c_3^{(pp)}$, $c_1, c_2, c_3 \to c_1^{(np)}, c_2^{(np)}, c_3^{(np)}$, respectively. It follows from the isotopic invariance (see Eq. (3)) that

$$c_1 = c_1^{(pp)} - c_1^{(np)}, \quad c_2 = c_2^{(pp)} - c_2^{(np)}, \quad c_3 = c_3^{(pp)} - c_3^{(np)}. \qquad (14)$$

In accordance with the optical theorem, the following relation holds, taking into account Eq.(14):

$$\frac{4\pi}{k}\mathrm{Im}\, c_1 = \frac{4\pi}{k}(\mathrm{Im}\, c_1^{(pp)} - \mathrm{Im}\, c_1^{(np)}) = \sigma_{pp} - \sigma_{np}, \qquad (15)$$

where σ_{pp} and σ_{np} are the total cross-sections of interaction of two unpolarized protons and of an unpolarized neutron with unpolarized proton, respectively (due to the isotopic invariance, $\sigma_{pp} = \sigma_{nn}$); $k = |\mathbf{p}| = |\mathbf{p}'|$ is the modulus of neutron momentum in the c.m. frame of the colliding nucleons [1].

Taking into account Eqs. (9), (13) and (15), the differential cross-section of the process $n + p \to p + n$ in the "forward" direction for unpolarized nucleons can be presented in the following form, distinguishing the spin-independent and spin-dependent parts:

$$\frac{d\sigma_{np\to pn}}{d\Omega}(0) = |c_1|^2 + 2|c_2|^2 + |c_3|^2 = \frac{d\sigma^{(si)}_{np\to pn}}{d\Omega}(0) + \frac{d\sigma^{(sd)}_{np\to pn}}{d\Omega}(0). \qquad (16)$$

In doing so, the spin-independent part $\frac{d\sigma^{(si)}_{np\to pn}}{d\Omega}(0)$ in Eq.(16) is determined by the difference of total cross-sections of the unpolarized proton-proton and neutron-proton interaction:

$$\frac{d\sigma^{(si)}_{np\to pn}}{d\Omega}(0) = |c_1|^2 = \frac{k^2}{16\pi^2}(\sigma_{pp} - \sigma_{np})^2(1 + \alpha^2), \qquad (17)$$

where $\alpha = \mathrm{Re}\, c_1/\mathrm{Im}\, c_1$. The spin-dependent part of the cross-section of the "forward" charge-exchange process is

$$\frac{d\sigma^{(sd)}_{np\to pn}}{d\Omega}(0) = 2|c_2|^2 + |c_3|^2. \qquad (18)$$

Meantime, according to Eqs. (10), (12) and (13), the spin-dependent part of the cross-section of the "backward" elastic np-scattering is

$$\frac{d\sigma^{(sd)}_{np\to np}}{d\Omega}(\pi) = 2|\widetilde{c}_2|^2 + |\widetilde{c}_3|^2. \qquad (19)$$

[1] We use the unit system with $\hbar = c = 1$.

We see that $\frac{d\sigma^{(sd)}_{np\to pn}}{d\Omega}(0) \neq \frac{d\sigma^{(sd)}_{np\to np}}{d\Omega}(\pi)$.

Further it is advisable to deal with the differential cross-section $\left.\frac{d\sigma}{dt}\right|_{t=0}$, being a relativistic invariant ($t = -(p_1-p_2)^2 = (\mathbf{p}-\mathbf{p}')^2-(E-E')^2$ is the square of the 4-dimensional transferred momentum). In the c.m. frame we have: $t = 2k^2(1-\cos\theta)$ and $\frac{d\sigma}{dt} = (\pi/k^2)\frac{d\sigma}{d\Omega}$. So, in this representation, the spin-independent and spin-dependent parts of the differential cross-section of the "forward" charge transfer process $\left.\frac{d\sigma_{np\to pn}}{dt}\right|_{t=0}$ are as follows: $\left.\frac{d\sigma^{(si)}_{np\to pn}}{dt}\right|_{t=0} = (\pi/k^2)\,|c_1|^2$, $\left.\frac{d\sigma^{(sd)}_{np\to pn}}{dt}\right|_{t=0} = (\pi/k^2)\,(2|c_2|^2+|c_3|^2)$, and we may write, instead of Eq.(16):

$$\left.\frac{d\sigma_{np\to pn}}{dt}\right|_{t=0} = \left.\frac{d\sigma^{(sd)}_{np\to pn}}{dt}\right|_{t=0} + \frac{1}{16\pi}(\sigma_{pp}-\sigma_{np})^2(1+\alpha^2)\,. \qquad (20)$$

Now it should be noted that, in the framework of the impulse approach, there exists a simple connection between the spin-dependent part of the differential cross-section of the charge-exchange reaction $n+p\to p+n$ at zero angle $\left.\frac{d\sigma^{(sd)}_{np\to pn}}{dt}\right|_{t=0}$ (not the "backward" elastic neutron-proton scattering, see Section 2) and the differential cross-section of the deuteron charge-exchange breakup $d+p\to(pp)+n$ in the "forward" direction $\left.\frac{d\sigma_{dp\to(pp)n}}{dt}\right|_{t=0}$ at the deuteron momentum $\mathbf{k}_d = 2\mathbf{k}_n$ ($\mathbf{k}_n$ is the the initial neutron momentum). In the case of unpolarized particles we have [3,4,5]:

$$\left.\frac{d\sigma_{dp\to(pp)n}}{dt}\right|_{t=0} = \frac{2}{3}\left.\frac{d\sigma^{(sd)}_{np\to pn}}{dt}\right|_{t=0}. \qquad (21)$$

In doing so, this formula remains still valid if one takes into account the deuteron D-wave state [5].

It is easy to understand also that, due to the isotopic invariance, the same relation (like Eq. (21)) takes place for the process $p+d\to n+(pp)$ at the proton laboratory momentum $\mathbf{k}_p = \mathbf{k}_n$ and for the process $n+d\to p+(nn)$ at the neutron laboratory momentum $\mathbf{k}_n$.

Thus, in principle, taking into account Eqs. (20) and (21),the modulus of the ratio of the real and imaginary parts of the spin-independent charge transfer amplitude at zero angle ($|\,\alpha\,|$) may be determined using the experimental data on the total cross-sections of interaction of unpolarized nucleons and on the differential cross-sections of the "forward" nucleon charge transfer process and the charge-exchange breakup of an unpolarized deuteron $d+p\to(pp)+n$ in the "forward" direction.

At present there are few *reliable* experimental data on the differential cross-section of the deuteron charge-exchange breakup on a proton. However, the analysis shows: if we suppose that the real part of the spin-independent amplitude of charge transfer $n+p\to p+n$ at zero angle is smaller or of the same order as compared with the imaginary part ($\alpha^2 \leq 1$), then it follows from the available experimental data on the differential cross-section of charge transfer $\left.\frac{d\sigma_{np\to pn}}{dt}\right|_{t=0}$ and the data on the total cross-sections σ_{pp} and σ_{np} that the main contribution into $\left.\frac{d\sigma_{np\to pn}}{dt}\right|_{t=0}$ is provided namely by the spin-dependent part $\left.\frac{d\sigma^{(sd)}_{np\to pn}}{dt}\right|_{t=0}$.

If the differential cross-section $\frac{d\sigma}{dt}$ is given in the units of $mbn/(\frac{GeV}{c})^2$ and the total cross-sections are given in mbn, then the spin-independent part of the "forward" charge transfer cross-section may be expressed in the form :

$$\left.\frac{d\sigma^{(si)}_{np\to pn}}{dt}\right|_{t=0} \approx 0.0512\,(\sigma_{pp}-\sigma_{np})^2(1+\alpha^2). \qquad (22)$$

Using (22) and the data from the works [6,7,8], we obtain the estimates of the ratio $\left.\frac{d\sigma^{(si)}_{np\to pn}}{dt}\right|_{t=0} / \left.\frac{d\sigma_{np\to pn}}{dt}\right|_{t=0}$ at different values of the neutron laboratory momentum k_n:

1) $k_n = 0.7\ \frac{GeV}{c}$; $\left.\frac{d\sigma_{np\to pn}}{dt}\right|_{t=0} = 268\ mbn/(\frac{GeV}{c})^2$; $\sigma_{pp} - \sigma_{np} = -22.6\ mbn$;

$$\left.\frac{d\sigma^{(si)}_{np\to pn}}{dt}\right|_{t=0} / \left.\frac{d\sigma_{np\to pn}}{dt}\right|_{t=0} \approx 0.1\,(1+\alpha^2).$$

2) $k_n = 1.7\ \frac{GeV}{c}$; $\left.\frac{d\sigma_{np\to pn}}{dt}\right|_{t=0} = 37.6\ mbn/(\frac{GeV}{c})^2$; $\sigma_{pp} - \sigma_{np} = 10\ mbn$;

$$\left.\frac{d\sigma^{(si)}_{np\to pn}}{dt}\right|_{t=0} / \left.\frac{d\sigma_{np\to pn}}{dt}\right|_{t=0} \approx 0.136\,(1+\alpha^2).$$

3) $k_n = 2.5\ \frac{GeV}{c}$; $\left.\frac{d\sigma_{np\to pn}}{dt}\right|_{t=0} = 17.85\ mbn/(\frac{GeV}{c})^2$; $\sigma_{pp} - \sigma_{np} = 5.5\ mbn$;

$$\left.\frac{d\sigma^{(si)}_{np\to pn}}{dt}\right|_{t=0} / \left.\frac{d\sigma_{np\to pn}}{dt}\right|_{t=0} \approx 0.085\,(1+\alpha^2).$$

So, it is well seen that, assuming $\alpha^2 \lesssim 1$, the spin-dependent part $\left.\frac{d\sigma^{(sd)}_{np\to pn}}{dt}\right|_{t=0}$ provides at least $(70 \div 90)\%$ of the total magnitude of the "forward" charge transfer cross-section.

The preliminary experimental data on the differential cross-section of "forward" deuteron charge-exchange breakup $d+p \to (pp)+n$, obtained recently in Dubna (JINR, Laboratory of High Energies), also confirm the conclusion about the predominant role of the spin-dependent part of the differential cross-section of the nucleon charge-exchange reaction $n + p \to p + n$ in the "forward" direction.

This work is supported by Russian Foundation of Basic Research
(Grant No. 05-02-16674)

REFERENCES

1. V.L.Lyuboshitz, V.V.Lyuboshitz. Proceedings of the XI International Conference on Elastic and Diffractive Scattering (Blois, France, May 15 - 20, 2005), Gioi Publishers (Vietnam), 2006, p.223

2. V.L. Lyuboshitz and M.I. Podgoretsky. Phys.At.Nucl. **59 (3)**, 449 (1996).

3. N.W. Dean. Phys.Rev. D **5**, 1661 (1972); Phys.Rev. D **5**, 2832 (1972).

4. V.V. Glagolev, V.L. Lyuboshitz, V.V. Lyuboshitz, N.M. Piskunov. JINR Communication **E1-99-280**, Dubna, 1999 .

5. R. Lednicky, V.L. Lyuboshitz, V.V. Lyuboshitz. Proceedings of XVI International Baldin Seminar on High Energy Physics Problems, vol.I, JINR **E1,2-2004-76**, Dubna, 2004, p.199 .

6. P.F. Shepard *et al*, Phys. Rev. D **10**, 2735 (1974).

7. T.J. Delvin *et al*, Phys. Rev. D **8**, 136 (1973).

8. J.L. Friedes *et al*, Phys. Rev. Lett. **15**, 38 (1965).

Dipole resonance in ^{18}O nucleus

N.G. Goncharova, M.N.Machekhina, N.D. Pronkina
Skobeltsyn Institute of Nuclear Physics, Moscow State University, 119992 Moscow, Russia

The main problem in theoretical investigation of multipole resonances (MR) in open shell nuclei is that the usual microscopical approach based on the conception of "particle-hole" doorway states is unfit for such nuclei. Description of E1 resonance in open shell nucleus ^{18}O was performed in the "Particle-Core Coupling" version of Shell Model (PCCSM) [1]. In this method the distribution of "hole" states among the states of residual nucleus with A=17 was taken into account using spectroscopy factors S of direct pick-up $^{18}O(d,t)^{17}O$ [2] reaction :

Energy, MeV	**J^P**	**S**	**Isospin**
0.0	$5/2^+$	1.53	T=1/2
0.87	$1/2^+$	0.21	T=1/2
3.06	$1/2^-$	1.08	T=1/2
4.55	$3/2^-$	0.12	T=1/2
5.09	$3/2^+$	0.10	T=1/2
5.38	$3/2^-$	0.53	T=1/2
5.94	$1/2^-$	0.06	T=1/2
8.20	$3/2^-$	0.15	T=1/2
8.69	$3/2^-$	0.10	T=1/2
9.15	$1/2^-$	0.10	T=1/2
11.08	$1/2^-$	0.96	T=3/2
12.47	$3/2^-$	0.24	T=3/2
13.64	$5/2^+$	0.29	T=3/2
16.58	$3/2^-$	0.93	T=3/2
18.14	$3/2^-$	0.17	T=3/2

The basic configurations in PCCSM calculations of 1^- states with isospin 1 and 2 were built as

$$\left|1^-,T_i\right\rangle=\sum_{(J'),j} C_i^{(J'),j}\left|(J'E'T')_{A-1}\times(nlj):1^-,T_i\right\rangle,\ \text{where}\ C_i=\sqrt{S_i\Big/\sum_j S_j}.$$

The basis founded on spectroscopy factors of $^{18}O(d,t)^{17}O$ reaction contains 32 configurations with isospin T=1 and 16 with T=2. Diagonal matrix elements of Hamiltonian include the energies of residual nucleus states:

$$\hat{H}_{ij}=(E'+\varepsilon_j+E_c)\delta_{ij}+\hat{V}_{\text{int},ij}.$$

The calculations of residual interaction matrix elements between basic configurations were performed as:

$$\left\langle(J''T''E''),j_2:J_fT_f\left|\hat{V}_{\text{int}}\right|(J'T'E'),j_1:J_fT_f\right\rangle=\sum_{J,T}\times\sum_{j,j'}\left\langle J'T'E'\left|J_iT_i,j^{-1}\right\rangle\right\langle J_iT_i,j'^{-1}\left|J''T''E''\right\rangle$$

$$\times(2J+1)(2T+1)\sqrt{(2J'+1)(2T'+1)(2J''+1)}\sqrt{(2T''+1)}\cdot W(J_ijJ_fj_1;J'J)W(J_ij'J_fj_2;J''J)\times$$

$$W(T_i\frac{1}{2}T_f\frac{1}{2};T'T)W(T_i\frac{1}{2}T_f\frac{1}{2};T''T)\left\langle j^{-1}j_1:JT\left|V_{\text{int}}\right|j'^{-1}j_2:JT\right\rangle.$$

This scheme corresponds the following diagram:

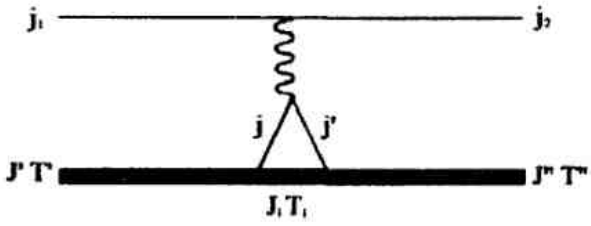

The results of PCCSM calculations for E1 transverse form factor at photopoint are shown in the Fig.1a together with experimental results for the cross section of $^{18}O(\gamma,n)\,^{17}O$ reaction [3]. The widths of 1^- excited states in ^{18}O were estimated approximately as $\Gamma(E) = 0.05MeV + 0.1(E - E_{thr})$; $E_{thr} = 8.044MeV$.

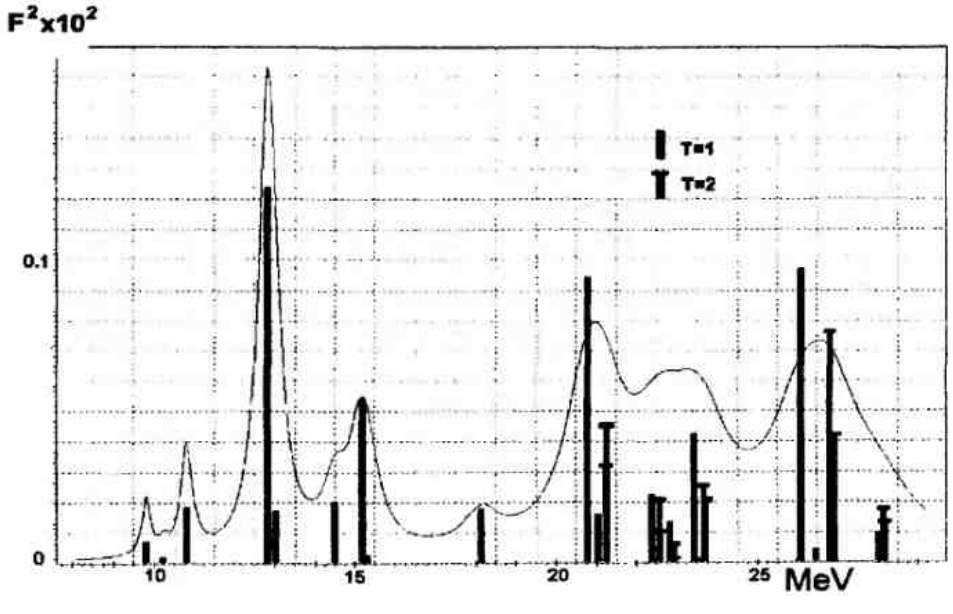

Fig1a

$^{18}O(\gamma,n)^{17}O$ [3]

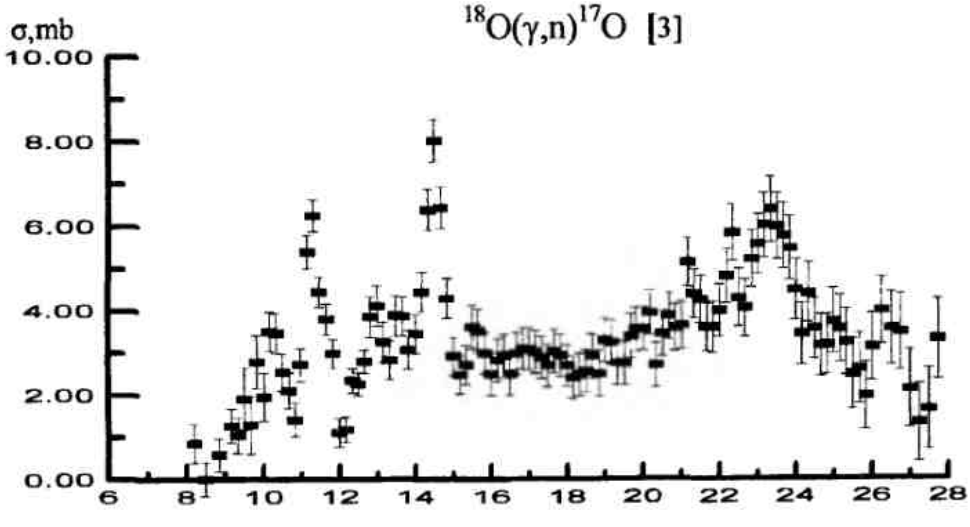

Fig 1b

The comparison of the figures shows that PCC SM approach reproduces the main characteristics of experimental E1 fragmentation. The energy distribution of E1 form factors at photopoint in PCCSM reflects the peculiarities in spectroscopy of pick-up reaction on target

nucleus (Table 1). According to [2] the knock-out of a neutron from ^{18}O with almost equal probabilities leads to states in ^{17}O with positive and negative parities. The last ones correspond to excitation of ^{16}O.

At the energies 16-27 MeV govern the transitions from 1p-shell of target nucleus. In this area of excitation energies the negative parity states of residual nuclei are populated. In this energy region the residual ^{17}O nucleus appears mostly in excited states above neutron separation energy and E1 excitation contributes to $^{18}O(\gamma,2n)^{16}O$ channel.

The lowest two peaks at ~9 MeV and ~10.5 MeV (pigmy resonance) correspond to neutron transitions from sd-shell. The maximum at ~12.5 MeV contains configurations connected with transitions from both sd-shell and 1p-shell: the dominating configuration $\left|(1/2^-, 3.09MeV)\times(nlj):1^-, T=1\right\rangle$ is built on the ^{17}O excited state.

1. N.G.Goncharova, N.P.Yudin, Phys. Lett.**B29**, 272 (1969).
2. J.H. Kelley et al , Nucl. Phys.A**564**,1 (1993).
3. U.Kneissl,K.H.Leister et al, Nucl.Phys.A**272**,125 (1976)

INTERMEDIAYE STATES UNDER PHOTOEXCITATION OF ^{115m}In, ^{113m}In, ^{111m}Cd AND ^{87m}Sr AT AN ENERGY TO 3.0 MeV

O.S. Shevchenko, A.N. Dovbnya, Y.N. Ranyuk, E.L. Kuplennikov, A.A. Nemashkalo, V.I. Noga

National Science Center "Kharkov Institute of Physics and Technology" 1, Akademichna St., 61108 Kharkov, UKRAINE

At the National Science Center "Kharkov Institute of Physics and Technology" the 3 MeV electrostatic electron accelerator ELIAS with an electron beam intensity to 500 μA was employed to investigate the photoproduction of isomers ^{115m}In [1], ^{113m}In [1], ^{111m}Cd [2] ^{87m}Sr produced in the (γ,γ') reactions under effect of bremsstrahlung beam at low energies.

As is known the natural indium is a mixture of two isotopes: ^{113}In (4.3%), ^{115}In (95.7%) therefore it possible to irradiate both isotopes simultaneously and to reduce, to the minimum, the relative error of measurements. The ^{113}In and ^{115}In nuclei have similar structures. Their first levels, being isomeric states with an energy E_{iso}= 392 and 336 keV, respectively, have the spin and parity $J^{\pi} = 1/2^-$ and half periods $T_{1/2}$ = 1.66 and 4.49 hours. Their ground state is characterized by $J^{\pi} = 9/2^+$. The isomer ^{115m}In decays into the ground state with a relative probability I_γ = 45.8%, the isomer ^{113m}In – with I_γ = 64.2%, and both via the M4 γ-transition

At present time the ^{115}In(γ,γ')^{115m}In reaction is well-studied and we have studied it mainly to check the reliability of the used experimental technique and the correctness of the methods of experimental data processing. As for the ^{113}In(γ,γ')^{113m}In reaction, practically, it is not studied despite the fact that the isotope ^{113}In is always present in studying the ^{115}In(γ,γ')^{115m}In reaction and using the target of a natural isotope composition. Somehow, it can be explained by the fact that the abundance of the isotope ^{113}In is less by a factor of 22 than that of the isotope ^{115}In.

The experimental facility and procedure are described in detail in [1]. The experiments were carried out using the activation methods. The measurements are conducted in the range of electron beam energies from 1.0 to 3.0 MeV with a step of 0.2 MeV. The electron beam having the 2 mm diameter and current of 200 μA was decelerated in the running water-cooled tantalum radiator of a 0.5 mm thickness. The total electron flux arriving onto the radiator was determined by means of the device of a Faraday cup type. The induced activity in the target was determined with the help of a Ge(Li) γ-spectrometer, with an effective volume of about 40 cm^3, which was connected with a 4096 channel pulse analyzer. The obtained γ-spectra were processed with the personal computer aid. Figure 1 presents the yield of ^{113}In(γ,γ')^{113m}In and ^{115}In(γ,γ')^{115m}In reactions as a function of the limiting energy of photon bremsstrahlung spectrum $E_{\gamma max}$. The error in the yield definition is the sum of the systematic and statistic errors. The systematic error is the sum of the error in the definition of the detector photon efficiency, electron flux measurement and target thickness. The isomer yield $Y(E_{\gamma max})$ is determined as:

$$Y(E_{\gamma max}) = \frac{N_{iso}(E_{\gamma max})}{N_e N_T}$$

where N_{iso} is the number of isomer nuclei produced in the target, N_e is the number of electrons arrived onto the radiator, N_T is the number of nuclei per cm^2 of the target.

As is seen from Fig.1a and 1b, the reaction yield of both isotopes behaves similarly and sharply increases in the range of limiting energy from 1.6 to 3.0 MeV that, evidently, is conditioned by the presence of high-intensity activation levels of 1999, 2420 keV for the isotope ^{115}In and 1802, 2378 keV for the isotope ^{113}In.

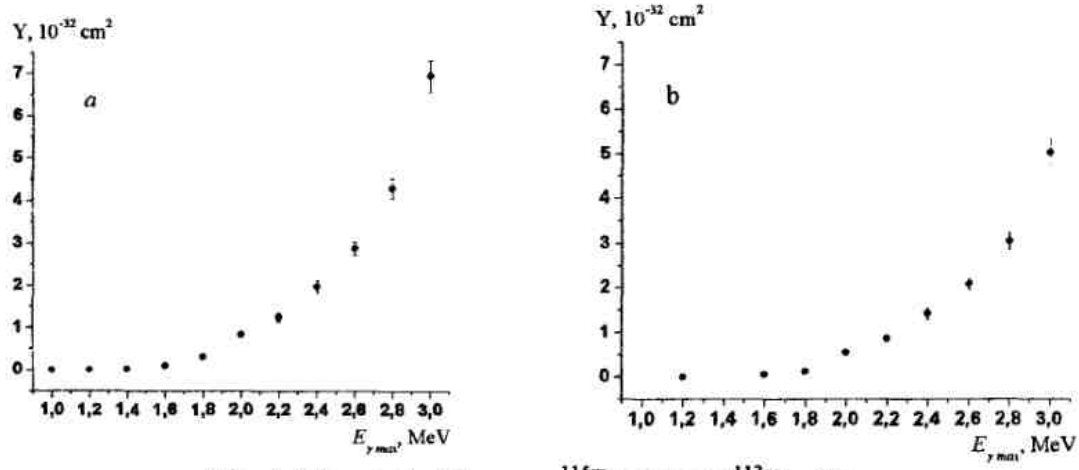

Fig. 1. The yield of isomers ^{115m}In (*a*) and ^{113m}In (*b*)

The obtained dependences of the isomeric state yields $Y(E_{\gamma max})$ for all the nuclei under study were used to separate the photoactivation integrated cross-sections $(\sigma\Gamma)^j_{exp}$ for the intermediate levels j. The photon spectrum of bremsstrahlung electrons in the Ta radiator was calculated by the program GEANT3.21. The statistics consisted of 10^7 starts, the class interval was 1 keV, the cascade cutoff energy by photons and electrons was 0.5 MeV. The errors in the definition of integrated cross-sections are the sum of statistic and systematic errors. The additional calculations of corresponding $(\sigma\Gamma)^j_{theor}$ were carried out on the base of characteristics for the levels ^{113}In and ^{115}In given in the literature [3], where the life times of intermediate levels and probabilities of transition into the ground and isomeric states were known. Our values of $(\sigma\Gamma)^j_{exp}$ are in accord with the theoretical results and similar data of other scientific centers (see [1,2]), which used different experimental geometry and photon sources.

The even-odd ^{111}Cd nucleus consists of 48 protons and 69 neutrons. The ground state $J^\pi = 1/2^+$ is stable. The energy $E_{iso} = 396.214$ keV, $T_{1/2} = 48.54$ min, $J^\pi = 11/2^-$. The decay into the ground state occurs via the E2 γ- transition with $I_\gamma = 94\%$, as well as, via the cascade through the level with 245.390 keV energy due to the emission of the E3 photon with 150.824 keV energy and $I_\gamma = 28.1\%$. The first quantum takes off the spin 3 and the second – spin 2. Fig. 2 presents one of the radiation spectra of the activated ^{111}Cd target. This spectrum was obtained after irradiation by photons with $E_{\gamma max} = 3.0$ MeV during 1 hour. Experimental points of the ^{111}Cd(γ,γ')^{111m}Cd reaction yield are shown in Fig. 3. The direct lines in Fig. 3 are the results of linear fitting to the corresponding points.

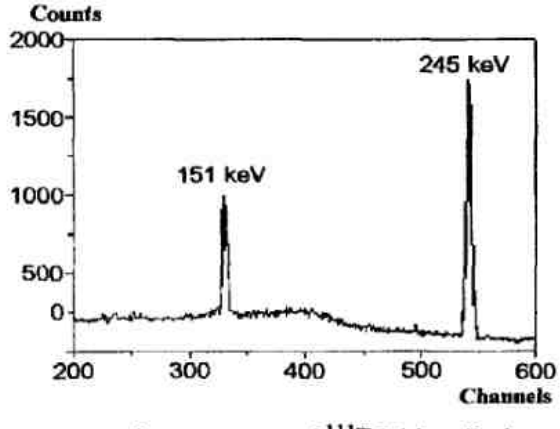

Fig. 2. The spectrum of ^{111m}Cd irradiation

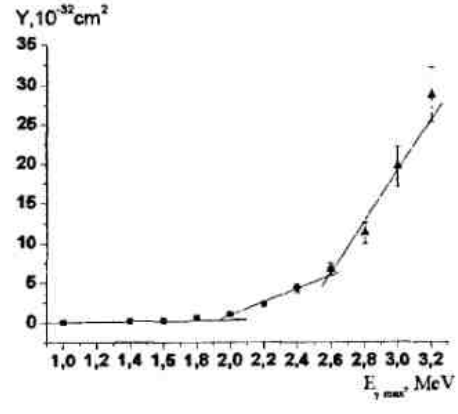

Fig. 3. ^{111}Cd(γ,γ')^{111m}Cd reaction yield

As is seen from Fig. 3, the yield function presents a broken line increasing with the energy, which has breaks at energies corresponding to the excitation energies of the next activation levels. In the spaces between the activation levels the energy dependence Y is close to the linear segments. The activation experiment does not allow one to determine reliably the points of breaks in the energy dependence of the yield, in other words, the position of activation levels. They can be determined from the spectroscopic data. According to [3], for 100 levels in the range of the excitation energy from 417 to 2978 keV, the ^{111}Cd nuclei has only three states of 1151, 2006 and 2495 keV, which suit, by the rule of selection, to the activation states. These levels are in good agreement with our experimental data and their integral cross-sections were equal to (0.06±0.02), (0.35±0.06) and (1.2±0.4) eV·b [2].

^{87}Sr is the even-odd nucleus. It is composed of 38 protons and 48 neutrons. The ground (isomeric) state is characterized by the parameters $J^{\pi}=9/2^{+}$ ($E_{iso}=388.532$ keV, $T_{1/2}=2.803$ hours, $J^{\pi}=1/2^{-}$). The decay into the ground state is realized via the M4 γ-transition and $I_{\gamma}=81.9\%$. The activation experiment with ^{87}Sr has been carried out on the target of 0.2mm and 15 mm thick, which were irradiated by γ-quanta in the energy range $1.4 \le E_{\gamma\,max} \le 3.1$ MeV. There the electron beam current was varying within 200-50 μA. The experimental results are presented in Figs. 4 and 5 where shown is one of the activated target radiation spectra obtained for the 2.7 MeV electron beam and the yield of isomer $Y(E_{\gamma\,max})$ ^{87m}Sr. The spacing of experimental points looks as a typical broken line. The breaks indicate, on the energy scale, the positions of activation levels, i.e. the levels partly decaying via the isomeric state. The right lines in the figure are the result of linear fitting to the corresponding points. Analysis of the reaction yield current showed that the intermediate states ^{87m}Sr take place at energies of ~1228, ~1770, ~1920 and ~2656 keV. The integrated cross-sections $(\sigma\Gamma)^{j}_{exp}$, determined for these states were equal to (0.090±0.013); (0.009±0.001); (0.07±0.01) and (3.8±0.4) eV·b.

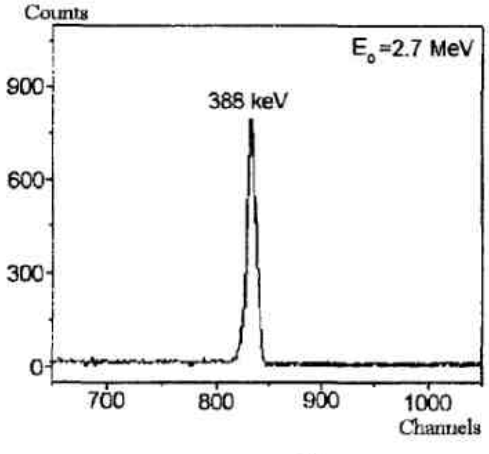

Fig. 4. The spectrum of ^{87m}Sr irradiation

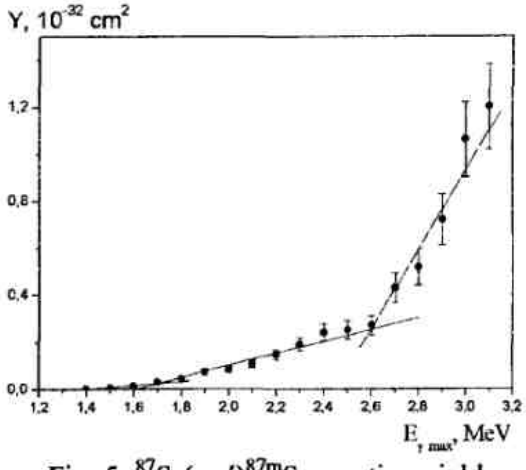

Fig. 5. ^{87}Sr(γ,γ')^{87m}Sr reaction yield

[1] O.S. Shevchenko, A.N. Dovbnya, Yu.N. Ranyuk, A.A. Nemashkalo, I.G. Goncharov, V.N. Borisenko, V.I. Noga, I.I. Shapoval, E.L. Kuplennikov. Photoexcitation of isomers ^{115m}In and ^{113m}In at energy to 3 MeV. Vestnik Khar'kovskogo Universiteta. Seriya: Fizika. 2005. No. 3/28/. P. 81-86 (in Russian).

[2] O.S. Shevchenko, A.N. Dovbnya, Yu.N. Ranyuk, A.A. Nemashkalo, I.G. Goncharov, V.N. Borisenko, V.I. Noga, I.I. Shapoval, E.L. Kuplennikov. Photoexcitation of isotope ^{111m}Cd at E_{γ} < 3 MeV. Ukrains'kij Fisycnij Zhournal. 2006. V. 51. P.115-119 (in Ukrainian).

[3] Firestone R.B. Table of Isotopes. Wiley. New York. 1996.

SHADOWING EFFECT OF PHOTOABSORPTION AT INTERMEDIATE ENERGIES AND NUCLEON-NUCLEON CORRELATION FUNCTION IN NUCLEAR MATTER

A.V. Stepanov, V. P. Zavarzina
Institute for Nuclear Research, Russian Academy of Sciences
60-th October Anniversary Prospect 7a, 117312 Moscow, Russia

The nature of the high-energy photon interaction with complex nuclei was actively studies over a period of a few last decades. A dramatic feature of this interaction in the shadowing effect observed in the dependence of the photoabsorption cross section on the nuclear-target mass number, with is similar to the effect previously observed in the hadron-nucleus scattering. A theoretical analysis of this experimental result, which is based on the Vector Dominance Model (VDM), has revealed a possibility to gain information on hadronic components of the photon distribution function from experimental data. From VDM vector mesons are of crucial importance among these components, primarily ρ- meson (for details see [1] and the references therein).

The expression for the total cross section of γ-ray quantum interaction with a target nucleus of mass number A_T can be written using the optical theorem:

$$\sigma_{\gamma A_T}(E_\gamma) = A_T \sigma_{\gamma N}(E_\gamma) - \Delta\sigma, \qquad (1)$$

Here $\sigma_{\gamma N}(E_\gamma)$ is the total interaction cross section for a γ-ray quantum of energy E_γ, with a nucleon and $(-\Delta\sigma)$ is the contribution of the shadowing effect.

Excluding the channels with vector mesons from consideration, we arrive at an equation describing the propagation of γ-ray quantum in nuclear matter and including the photon polarization operator (the "effective optical potential"):

$$V = P\hat{H}Q\ \frac{1}{E - Q\hat{H}Q + i\varepsilon}\ Q\hat{H}P \qquad (2)$$

Here $\hat{H}$ is the Hamiltonian of a photon + target nucleus + vector meson compound system. The projection operators have conventional values (see, for example, [2,4]). P selects the subspace of the photon target nucleus system states and Q selects the subspace of the vector meson + target nucleus system states.

For the term which takes into account the shadowing effect in (1) the following expression is obtained [2]:

$$\Delta\sigma = -2\frac{\Omega}{v_0}\,\mathrm{Im}\left\langle \Psi_i^{(+)} \middle| V \middle| \Psi_i^{(+)} \right\rangle \qquad (3)$$

Here $\Psi_i^{(+)}$ is the exact wave function of the photon + nucleus system in the initial state, Ω is the normalization volume, and v_0 is the relative velocity of the incident photon and the target nucleus.

Hereafter, the following expression for the wave function $\Psi_i^{(+)}$ is used in calculation of the cross section:

$$\Psi_i^{(+)} = \left|0_T\right\rangle \left|\vec{k}_\gamma\right\rangle .$$

Here $|0_T\rangle$ is the ground-state wave function of the target nucleus and $|\vec{k}_\gamma\rangle$ is a plane wave which describes the propagation of a photon with momentum $\vec{k}_\gamma$. In what follows $\hbar = c = 1$ is assumed.

In the expression for the Green function of the intermediate state in (2)

$$G = \frac{1}{E - Q\hat{H}Q + i\varepsilon} \qquad (4)$$

intranuclear motion of nucleons is usually ignored. This permits summation over a complete system of wave functions of a target nucleus in the intermediate state (the convolution

approximation), the eikonal approximation being used for the vector meson propagator in the field $g^{(v)}(\vec{r}_1,\vec{r}_2)$ of static nuclear matter [5],[6]. The studies of the shadowing effect were carried out not only for high photon energies but also for intermediate ones (1-3 GeV) [7].

As a result, it became possible to express the summand $\Delta\sigma$ in (1) in terms of a four-fold integral over space coordinates ($\vec{r}_1 = (\vec{b}, z_1)$, $\vec{r}_2 = (\vec{b}, z_2)$) ($\vec{b}$ is the impact parameter) of the product

$$g^{(v)}(\vec{r}_1,\vec{r}_2)\, K(\vec{r}_1,\vec{r}_2;0),$$

where

$$K(\vec{r}_1,\vec{r}_2;0) = \langle 0_T | \hat{\rho}(\vec{r}_1,0)\hat{\rho}(\vec{r}_2,0) | 0_T \rangle \qquad (5)$$

is the static pair correlation function of the nuclear density $\hat{\rho}(\vec{r},0)$ in the ground state,

$$\hat{\rho}(\vec{r},t) = e^{-iH_T t}\left|\sum_{l=1}^{A_T}\delta(\vec{r}-\vec{r}_l)\right| e^{-iH_T t}$$

is the nuclear density operator in the Heisenberg representation, t is time, $\vec{r}_l$ is the radius vector of the l-th nucleon, and $\hat{H}_T$ is the target-nucleus Hamiltonian. We obtain an estimate of the effect of the intranuclear motion of nucleons on the shadowing effect in the interaction of intermediate-energy photons with complex nuclei. To do this, we invoke the temporal-correlation-function (TCF) method. This method was previously used by the authors to calculate the total interaction cross section of incident particles with nuclei and the first-order optical potential when the interaction of a projectile particle with individual nucleon of the target nucleus resulted in the resonance excitation in the intermediate state [8-10]. In the case of complex nuclear target the excitation of such a resonance is followed by a change of the state of motion relative to the internal degrees of freedom. To allow for the effect of this motion, one should go beyond the convolution approximation. The TCF method offers such an opportunity.

In the problem under consideration, the vector meson, which moves in nonstatic nuclear matter, is the intermediate-state resonance. Using as before ([8-10]) both the short-time t and factorization approximations [11], we obtain for the central region of intermediate and heavy nuclei, where inhomogeneity of nuclear medium can be neglected, the standard expression for $\Delta\sigma$ [5,7], in which the static correlation function $K(\vec{r}_1,\vec{r}_2;0)$ (5) is replaced by TCF

$$K(\vec{r}_1,\vec{r}_2;t) = \langle 0_T | \hat{\rho}(\vec{r}_1,t)\hat{\rho}(\vec{r}_2,0) | 0_T \rangle \approx \qquad (6)$$

$$\approx \frac{1}{\Omega}\int \frac{d\vec{q}}{(2\pi)^3} e^{-i\vec{q}(\vec{r}_1-\vec{r}_2)} e^{itq^2/2M_N} \langle 0_T | e^{i\vec{q}\hat{\vec{p}}t/M_N} | 0_T \rangle F_T(\vec{q}), \qquad (7)$$

where M_N is the nucleon mass, $\hat{\vec{p}} = -i\nabla$ is the nucleon momentum operator in the target nucleus, and

$$F_T(\vec{q}) = \langle 0_T | \sum_{l,l'=1}^{A_T} e^{i\vec{q}\vec{r}_l} e^{-i\vec{q}\vec{r}_{l'}} | 0_T \rangle =$$

$$= \langle 0_T | \hat{\tilde{\rho}}(\vec{q})\hat{\tilde{\rho}}(-\vec{q}) | 0_T \rangle \approx | \langle 0_T | \hat{\tilde{\rho}}(\vec{q}) | 0_T \rangle |^2 .$$

Here $\langle 0_T | \hat{\tilde{\rho}} | 0_T \rangle$ is the static form factor of the target nucleus in the ground state and $\hat{\tilde{\rho}}(\vec{q})$ is the Fourier transform of the density operator $\hat{\rho}(\vec{r})$.

We shall assume the nucleon-nucleon correlations with a characteristic scale $\sim 1/q_F$ to be the most significant for the intermediate γ-quantum (and vector meson) energies; here q_F is the

Fermi momentum. Then the magnitude of the integral in (7) is determined by the region of characteristic momentum values $q \sim q_F$. Assuming $q \sim q_F$ in $\exp(iq^2t/2M_N)$ and $\exp(i\vec{q}\hat{\vec{p}}t/M_N)$, we come to

$$K(\vec{r}_1,\vec{r}_2;t) \approx \langle 0_T | \exp(i\vec{q}_F\hat{\vec{p}}t/M_N) | 0_T \rangle \exp(iq_F^2 t/(2M_N)) K(\vec{r}_1,\vec{r}_2;0). \qquad (8)$$

Thus we obtained two additional factors in comparison with the standard result. The first correction factor $\langle 0_T | \exp(i\vec{q}_F\hat{\vec{p}}t/M_N | 0_T \rangle$ takes into account the effect of the Fermi motion (the "Doppler broadening") [8]-[10]. The second factor, which includes the nucleon "recoil", can be involved in the expression for the vector meson propagation function $q^{(v)}(\vec{r}_1,\vec{r}_2)$. Correspondingly, this leads to a displacement of the pole position in the propagator $q^{(v)}$ owing to an effective increase of the ρ-meson mass.

We assume for estimations that $t \sim 1/\Gamma_V \sim (0{,}15\ \text{GeV})^{-1}$ and the Fermi energy $E_F = q_F^2/2M_N$ is 30 MeV, so that $q_F^2/(2M_N)\frac{1}{\Gamma} \approx 0{,}2$. Then it is easy to see that the "Doppler broadening" effect may be neglected, and the ρ-meson mass shift owing to the "recoil" of nuclear nucleons in the intermediate state is of the order of E_F. It is known [12] that the shift Δm_v of the ρ-meson mass in a nuclear medium due to the meson interaction with nuclear nucleons is of the order of or even less than 50 MeV. However, even such a low value of Δm_v has a pronounced effect on the magnitude of the shadowing effect [13].

Therefore, in accurate calculations of the shadowing effect with allowance for the modification of the vector-meson mass owing to its interaction with a nuclear medium (the dynamic effect), the intermediate-state excitation of the degrees of freedom of the nucleon intranuclear motion (kinematic effect) should also be taken into consideration.

Another source of improvement of the standard result of calculation of the shadowing effect in nuclear photoabsorption is noteworthy. This is the inclusion of noneiconal corrections to the vector meson propagator in nuclear matter. Unfortunately, the expression for this Green function in the first approximation of the noneikonal expansion [14] obtained by the authors in [15] is rather cumbersome. One can hardly rely with confidence on the results obtained from an analysis of the corresponding expressions for the total interaction cross section, reaction cross sections, etc., because the magnitudes of noneikonal corrections may differ essentially for different parameters, for example, for real and imaginary parts of zero-angle scattering amplitude [16]. The employment of the small perameter [13] 1/kR (k and R are the nucleus momentum and radius, respectively) which does not include the ratio of the potential characteristic value to the kinetic energy of the particle moving in this potential, can be justified under conditions of strong absorption of a projectile particle incident on the nucleus with a sharp boundary. However, it is completely unjustified in the conditions of the problem under consideration. In the case of the propagation of a ρ-meson produced in the interaction of an intermediate-energy γ-quantum with a nucleus, the ratio U/T_ρ of the characteristic value of the potential U to the ρ-meson kinetic energy is small compared to unity. This is favorable for the fulfillment of the applicability condition of the eikonal approximation, $k_\rho RU/T_\rho \leq 1$ for $k_\rho R \gg 1$. Here k_ρ is the ρ-meson momentum.

In conclusion we note that the result of the eikonal approximation can be refined in the context of approaches other than the noneikonal expansion method [14]. The analysis of compact expressions for the Green function of ρ-meson in nuclear matter which can be obtained using these methods [17] confirm the above conclusions on small corrections to the results of the eikonal approximation for the description of the intermediate-energy ρ-meson motion in nuclear matter.

REFERENCES

1. W. Weise. Phys. Rep. 13 (1974) 53; G. Piller, W. Weise. Phys. Rep. 330 (2000) 1.
2. M.L. Coldberger and K.M. Watson. Collision Theory, John Wiley& Sons, inc., New York – London – Sudney. 1964. (Moscow, Mir, 1967).
3. V.V. Balashov. Kvantovaya Teoriya Stolknovenii (Quantum Collision Theory). Moscow. MGU (Moscow State University). 1985.
4. J. Taylor. Scattering Theory: Theory of Nonrelativistic Collisions. Wiley, New York. 1972; (Moscow, Mir. 1975).
5. T.H. Bauer et al. Rev. of Mod. Phys. 50 (1978) 261; S. Boffi et al. Nucl.Phys.A 606 (1996) 421.
6. L.B. Bezrukov, E.V. Bugaev. Yadernaya fizika. V.33 (1981) 1195.
7. F. Falter et al. Phys. Rev.C 62 (2000) 031602; F. Falter et al. Phys. Rev.C 64 (2001) 024608.
8. V.P. Zavarzina, A.V. Stepanov. Bulletin of the Lebedev Physics Institute № 10 (1995) 4; Izv. RAS, seriya fizich. 61 (1997) 2170.
9. V.P. Zavarzina, A.V. Stepanov. Bulletin of the Lebedev Physics Institute. № 6 (1997) 39; ibid. №7 (1997) 20; Izv. RAS, seriya fizich. 62 (1998) 2195.
10. V.P. Zavarzina, A.V. Stepanov. Bulletin of the Lebedev Physics Institute. № 9 (1998) 36; Izv. RAS, seriya fizich. 64 (2000) 113.
11. V. Vineyard. Phys. Rev. 110 (1958) 999; A.V. Stepanov. Preprint INR. 1976. П-0046; A.A. Chumbalov et al. Z. Phys. A 328 (1987) 195; C. Bennhold, H.Tanabe. Nucl. Phys.A530. (1999) 625.
12. V.L. Eletsky, B.L. Ioffe. Phys. Rev. Lett.78 (1997) 1010; L.A. Kondratyk et al. Phys. Rev. C58 (1998) 1078.
13. Jan-C Alam et al. Phys. Rev. C66 (2002) 042202.
14. S.J. Wallace. Ann. of Phys. 78 (1973) 190.
15. V.P. Zavarzina, A.V. Stepanov. Soviet Physics Lebedev Institute Reports № 3 (1988) 14.
16. V.P. Zavarzina, A.V. Stepanov. Yadernaya Fizika. 43 (1988) 858; ibid. 54 (1991) 44; Izv. RAS, seriya fizich. 55 (1991) 960.
17. A. Baker. Phys. Rev.D 6 (1972) 3462; V.P. Zavarzina et al. Izv. AN SSSR, seriya fizich. 43 (1979) 2441.

STUDY OF THE REACTIONS BETWEEN LIGHT NUCLEI IN THE ASTROPHYSICAL ENERGY REGION USING THE PLASMA HALL ACCELERATOR

Vyach.M.Bystritsky[1], Vit.M.Bystritskii[2], L.D.Butakov[3], V.V.Gerasimov[1], G.N.Dudkin[3], A.R. Krylov[1], B.A.Nechaev[3], V.M.Padalko[3], S.S.Parzhitskii[1], A.V.Petrov[3], N.M.Polkovnikova[3], J.Wozniak[4]

[1]Joint Institute for Nuclear Research, Dubna, Russia; [2] Department of Physics and Astronomy, University of California, Irvine, USA; [3]Federal State Scientific Institution "Scientific Research Institute of Nuclear Physics ",Tomsk, Russia; [4] Faculty of Physics and Applied Computer Science, AGH, University of Science and Technology, Cracow, Poland

Abstract. Using the plasma accelerator based on the pulse Hall ion source, the first measurements of the astrophysical S-factor of the d+d→^{3}He + n reaction were performed for deuteron energies 9.1 and 9.9 keV. The observed values of the S-factor and effective cross sections $\tilde{\sigma}_{dd}$ for dd reaction are in agreement with the results obtained by us earlier in the experiments at liner plasma accelerators (in a configuration of both direct and inverse Z-pinch). The preliminary results have confirmed the fact that the proposed technique can be effective to study nuclear reactions between light nuclei in the astrophysical energy region.

I. Introduction

Interest in studying reactions between light nuclei (pd , dd, d^{3}He and d^{6}Li reactions) in the region of astrophysical energies 2-12 keV is caused by a possibility of verifying symmetries in strong interactions, determining the contribution to interaction from exchange currents, checking the standard Solar model [1]. Research of the given processes in the indicated energy region is rather problematic since intensity of the beams of the accelerated particles produced by classical accelerators are extremely low ($I \approx 10^{12} - 10^{13}$ 1/s), and cross sections of nuclear reactions in the astrophysical energy region are extremely small (10^{-39} - 10^{-33} cm^2). An impetus to the current intensive study of reactions between light nuclei has become the possibility of using for these purposes pulsed high-current plasma accelerators and energy-precise linear ion accelerators of energy 4-100 keV [2-4]. Plasma accelerators with the liner plasma formation in the direct and inverse Z-pinch configuration allowed quantitative information on the astrophysical S-factors and effective cross sections of the pd and dd reactions (pd→^{3}He + γ; dd→^{3}He + n) in the ultralow energy region to be obtained for the first time [2,4]. The results obtained for the first time have confirmed the fact that the proposed technique can be effectively used to study nuclear reactions in the astrophysical energy region. It is necessary to note that highly accurate measurement of cross sections of the pd, dd and d^{3}He reactions with the use of the plasma in the Z-pinch configuration is rather problematic. The absence of reproducibility of the experimental conditions from "shot" (the act of the accelerator operation) to "shot" caused by the specificity of the work of accelerators of this class imposes certain restrictions on accuracy of measurement of parameters of the investigated processes.

This stimulated development of alternative methods for formation of intense charged-particles beams in the ultralow energy region. For further research of reactions with light nuclei we developed and built a pulsed ion source with the closed Hall current allowing acceleration of plasma ions H^+, D^+ and $^3He^+$ in the energy range 2-12 keV. In this work the preliminary results of measuring the astrophysical S-factor and effective cross sections for the dd reaction in the experiment at the created accelerator.

2. Measurement method

Experimental determination of the astrophysical S-factor and effective cross section of the dd reactions is based on measurement of the neutron output and parameterization of the dependence of the cross section reaction $\tilde{\sigma}_{dd}$ on the deuteron collision energy:

$$S(\bar{E}) = \frac{N_n^{exp}}{N_d n_t \varepsilon_n \int_0^{\infty} f(E)dE \int_0^{\infty} \frac{e^{-2\pi\eta}}{E'(E,x')} dx'}, \quad (1) \qquad \tilde{\sigma}_{dd} = N_n^{exp} / N_d n_t \varepsilon_n \tilde{l}, \quad (2)$$

where N_n^{exp} is the yield of the detected neutrons, N_d is the number of deuterons hit in the target, $Z_1 = Z_2 = 1$ is the deuteron charge, $\mu = m_d$ is the reduced mass of the colliding particles, n_t is the deuteron density of the target, $\eta'(E) = Z_1 Z_2 e^2 (\mu/E')^{1/2}$, ε_n is the efficiency of the neutron registration, E' are the collision energies of deuterons with the target nuclei after passage of a target layer of thickness x ', $\bar{E}$ is the average energy of the deuteron collision, f (E) is the energy distribution of the deuterons hitting the target, $\tilde{l}$ is the effective target thickness defined from the expression $N_n(\tilde{l}) = 0.9 N_n^{tot}$ (N_n^{tot} is the yield of neutrons from the dd reaction in the case of an the infinitely thick target).

3. Experimental procedure

The experimental setup (Fig.1) includes the plasma accelerator on the basis of the Hall ion source, a solid-state CD_2 target from installed in the accelerator chamber, two detectors for detection of 2.5 MeV neutrons, diagnostic equipment for collecting information on parameters of the accelerated-ion flow generation process, an electrostatic multigrid mass-spectrometer of charged particles for measurement of the deuteron energy distribution .

The CD_2 solid-state target was of the 25 cm^2 area. Neutrons were detected by two detectors of thermal neutrons, each being an assembly of 10 proportional ^3He counters [5]. Current of accelerated ions at the output of the Hall source was measured by means of the Rogovsky belt, and the current density in various sections of the beam hitting the target surface was determined with the collimated Faraday cylinders. The energy distribution of ions was measured by our electrostatic multigrid mass-spectrometer of the charged particles whose operation was based on the braking potential method.

4. Analysis of the results

Figure 2 shows the energy distribution of deuterons measured by the mass-spectrometer during data taking in the experiment on the study of the dd reaction. Using the function describing the given energy distributions, the values describing the experimental conditions (E_d =9.1±0.3 keV, E_d =9.9±0.3 keV, FWHM =1.3 keV, N_d (9.1) = (4.1±0.5)·10^{14}, N_d (9.9) = (7.95±0.3)·10^{14}, n_t =(8.00±0.08)·10^{22}, ε_n =(1.27±0.11)·10^{-2}, N_n^{exp} (9.1)=4 and N_n^{exp} (9.9) = 12), and formulas (1) and (2) we determined the values of the astrophysical S-factor and the effective dd-reaction cross:

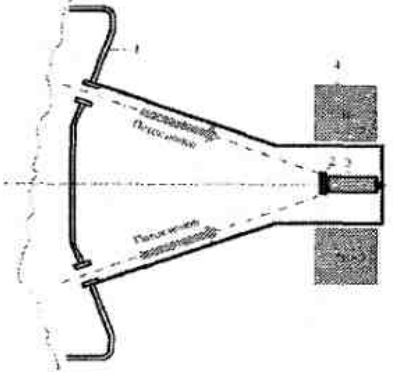

Fig. 1. Experimental setup: (1) Hall ion source plasma accelerator, (2) CD_2 deuterium target, (3) electrostatic mass spectrometer, (4) ^3He detector of thermal neutrons

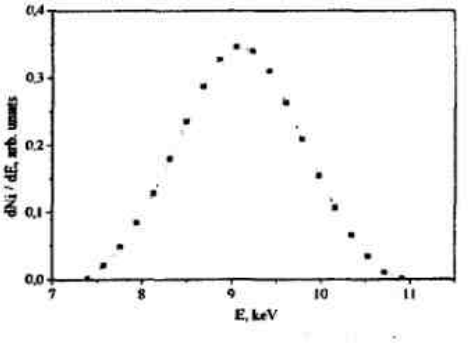

Fig. 2. Deuteron energy distribution

$\widetilde{S}$ (4.7) = (31.9±16.9 ±3.2) keV b, $\widetilde{\sigma}_{dd}$ (4.3 < E_{coll} <5.1) = (3.2 ± 1.7 ± 0.3) 10^{-31} cm^2 ;

$\widetilde{S}$ (5.1) = (38.9±11.7 ±3.1) keV b, $\widetilde{\sigma}_{dd}$ (4.7 < E_{coll} <5.5) = (6.6 ± 2.0 ± 0.5) 10^{-31} cm^2 .

The first errors here are the statistical errors and the second are the systematical ones.

These values of the S($\bar{E}$) and $\widetilde{\sigma}_{dd}$ agree within measurement errors with the results of the direct and inverse Z-pinch experiments and with the calculations by the model of the interaction of a low-energy deuteron beam with the deuterium-containing solid-state target (see fig. 3).

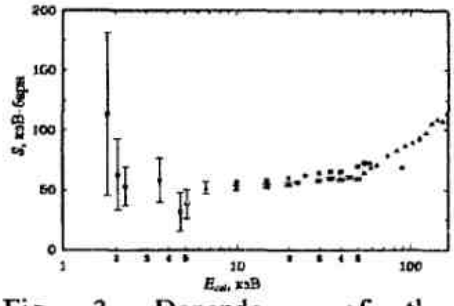

Fig. 3. Dependence of the reaction astrophysical S-factor on the deuteron collision energy: •, ○ are the results of the experiments with the inverse Z-pinch [2]; ■, ▲ are the results of [7] and [6] respectively; □ is the present work

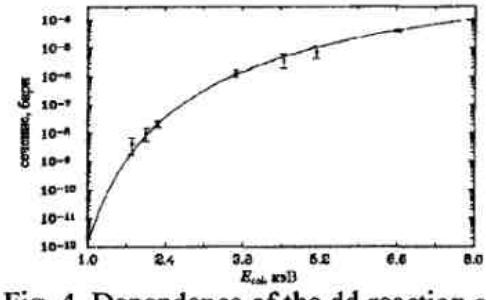

Fig. 4. Dependence of the dd reaction cross section on the deuteron collision energy. The curve – calculated dependence obtaining with S = 53.8 keV·b: ■ – [6]; •, ○ – are the results of the experiments with the inverse Z-pinch [2]; □ – is the present work

The experimental results obtained with the plasma Hall accelerator indicate that, the developed technique holds promise for detailed study of reaction mechanisms between light nuclei in the region of ultralow energies.

This work was supported by the Russian Foundation for Basic Research, Grant No 06-02-17182 and the grant of Plenipotentiary of Poland in JINR.

References

1. A new approach in the experimental studies of nuclear reactions at ultralow energies, V.M.Bystritsky et al., Nucleonika 42 (1997) 775 - 793.
2. Measurement of the astrophysical S-factor for dd interaction at ultralow deuteron – collision energies using the inverse Z pinch, V.M. Bystritsky , V.V. Gerasimov, A.R. Krylov et al., Physics of Atomic Nuclei 66 (2003) 1731- 1738.
3. First measurement of the d(p,γ)^{3}He cross section down to the soar Gamow peak, C. Casella, H. Costantini, A. Lemut et al., Nucl. Phys. A706 (2002) 203 - 216 and references there in.
4. Study of the pd reaction at ultralow energies using hydrogen liner plasma V.M. Bystritsky , Vit.M. Bystritskii, G.N. Dudkin, V.V. Gerasimov, A.R. Krylov, G.A. Mesyats, B.A. Nechaev, V.M. Padalko, S.S. Parzhitskii, F.M. Pen'kov, N.A. Ratakhin, J.Wozniak, Physics of Atomic Nuclei 68 (2005) 1777- 1786.
5. ^{3}He detectors in experiments at the powerful pulsed accelerators, V.F.Boreiko, V.M.Bystritsky, V.M. Grebenyuk et. al., NIM A 490 (2002) 344- 355.
6. Low-energy fusion cross sections of D + D and D + ^{3}He reactions, A. Krauss, H.W. Becker, H.P. Trautvetter et al., *Nucl. Phys. A* 465 (1987) 150 - 172.
7. Differential cross sections at low energies for ^{2}H(d,p)^{3}H and ^{2}H(d,n)^{3}He, R.E. Brown and N. Jarmie, *Phys. Rev. C* 41 (1990) 1391-1400.

Experimental methods for calibration of coordinate detectors for high energy gammas and electrons

A.D.Belyaev[1], V.M.Ionov[2], V.G.Nedorezov[2], N.V.Rudnev[2], A.A.Turinge[1]

RRC "Kurchatov Institute", Moscow, Russia; [2]Institute for Nuclear Research RAS, Moscow, Russia.

Methods of calibration of coordinate detectors for high energy gammas and electrons are leveloped. The calibration system consists of 2 thin scintillators, 4 photomultipliers, electronic nodules, PC and software. Results obtained with a source of beta-particles (^{90}Sr) are presented. The following experiment is proposed for calibrations of drift chambers in frame of the scientific program "ELISe" [1] (Electron – Ion Storage ring) using the GAMMA station at the Kurchatov ynchrotron "Siberia-2" [2], which gives a possibility to study photonuclear reactions with the nergies up to 2.5 GeV and realize applied physics tasks.

Each drift chamber straw tube has a thickness of 126 microns including base polyamide KAPTON on Al (0.2 μm) cowered by "C"-layer (5 μm). Straw length = 60 cm; Inner diameter = 7.5 ± 0.003 mm. Gas mixture is Ar/CO2 (80/20), HV = 1850 V.

Experimental set-up is shown in fig.1,2.

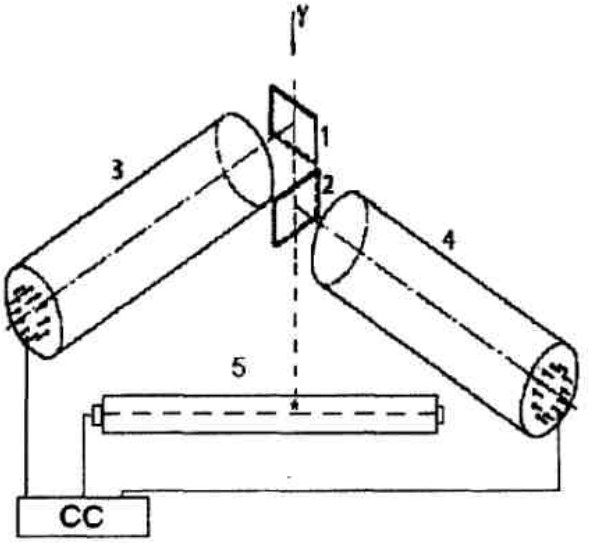

Fig.1

Experimental set-up.
1, 2 – scintillators (polystyrene), dimensions : 17 x 14 x 0.3(1.5)mm;
3,4 – photomultipliers (PMT-85);
5– drift chamber;
CC – coincidence circuit.

Fig.2

Source – (^{90}Sr); pmt – photomultiplier; sci – scintillator; ampl – amplifier; discr – discriminator; d.l.- delay line; c.c. – coincidence circuit; l.t. – level translator; QDC – charge-digital converter; crate. – CAMAC crate; Ccpc5 – controller.

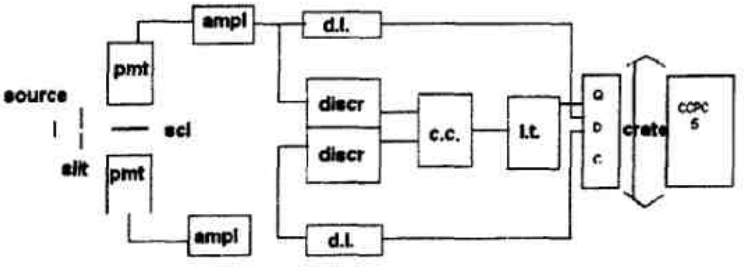

To process information coming from the QDC unit two programs were developed which use the resources of program packages MathCad and Excel:

- ImportCCPC
- InputVariablesCCPC.

The first program shows the beta spectrum of electrons which passed the scintillator. The second one is used to comment experimental conditions.

User interface of the ImportCCPC and InputVariablesCCPC programs is shown in fig.3.

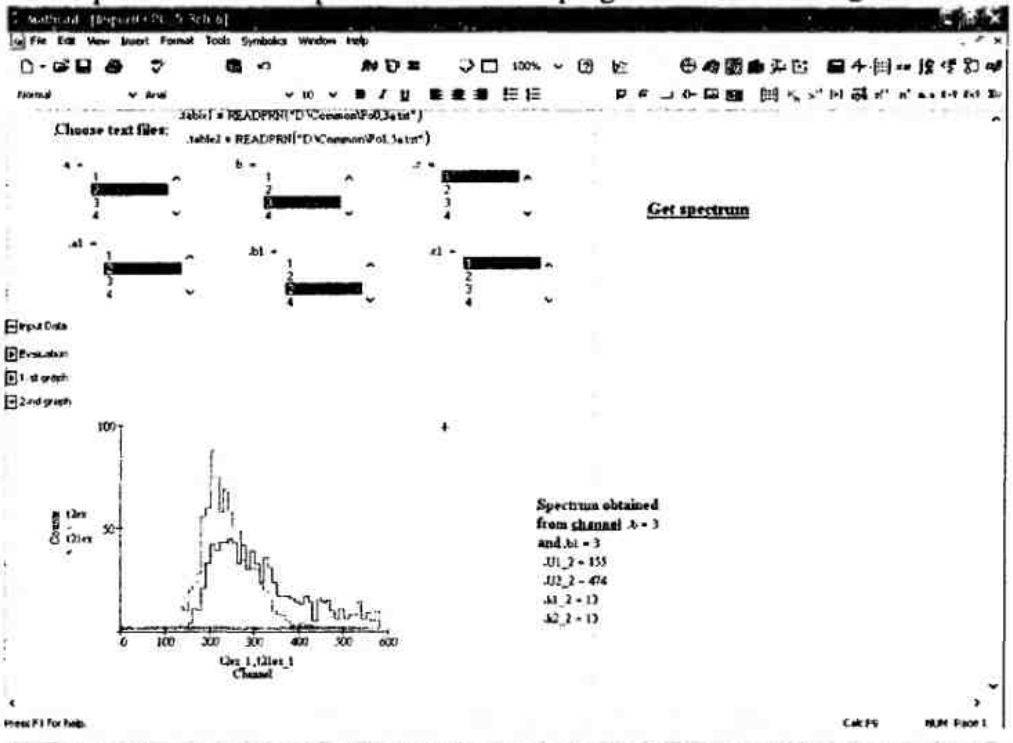

Fig. 3 Selection of the channel and presentation of the results.

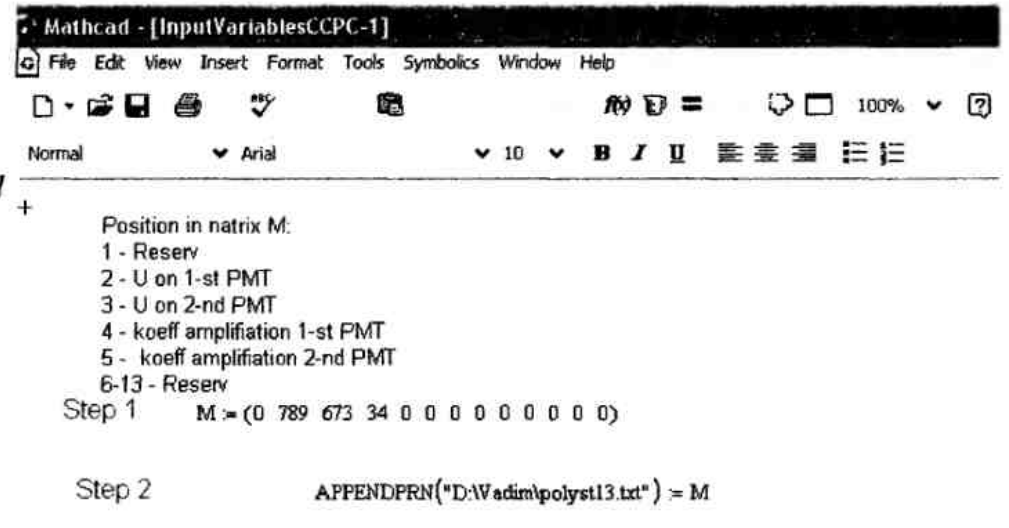

Fig.4. Protocol of the experimental conditions.

Experimental spectrum of beta-particles of ^{90}Sr for 0.3mm and 1.5mm scintillator thicknesses is shown in fig.5.

Fig.5.

Energy loss spectrum of electrons in scintillators of 17 mm length (0.3 and 1.5 mm thickness).

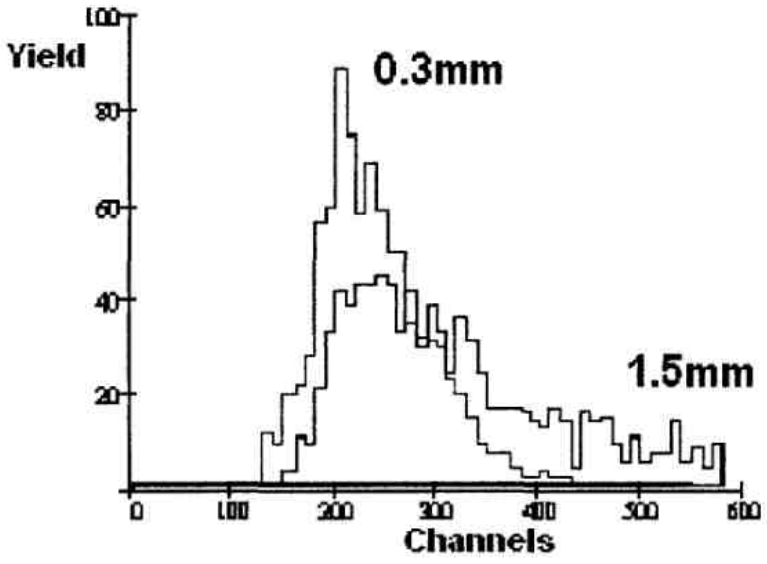

As shown in fig.1, scintillator plates were situated in parallel to the beam axis. Therefore, the energy loss distributions are similar for both thickness (0.3 and 1.5 mm) of the plates. The slight difference is seen, nevertheless, which is caused by the electron scattering (escape) from the scintillators. The distributions presented in fig.5 were normalized on the total number of events.

The result of measurements shows that the coordinate calibration of the drift chambers will be possible with accuracy of 0.3mm, at least, using the gamma beam of the storage ring "Siberia-2" at RRC "Kurchatov Institute".

This work is supported by RFBR, grant 04-02-16996

1. H.Simon, e.a. ,V.Lisin, A.Mushkarenkov, V.Nedorezov, A.Polonski, N.Rudnev, A.Turinge e.a. (ELISe collaboration). Technical Proposal for ELISe Experiment , GSI (2005).

2. А.Д.Беляев, Н.В.Руднев, В.Г.Недорезов, А.А.Туринге. Фотоделение ядер-актинидов в области нуклонных резонансов: первый фотоядерный эксперимент на накопителе электронов «Сибирь-2». Ядерная физика, 67, 8 (2004) 1-5.

ЭМИН-2006
Труды XI Международного семинара по электромагнитным взаимодействиям ядер
Москва, 21-24 сентября 2006 года
(на английском языке)
Ответственный за выпуск *А. Д. Полонский*
Электронная версия отредактирована и предоставлена авторами
Дизайнер обложки *Н.Л. Нольде*, фотограф *Е. Ю. Еремин*
Подписано в печать 12.03.2007
Ф-т 60x84/8. Уч.-изд.л. 10,8 Печ.л. 13,5 Зак. № 21756 Тираж 110 экз.

Бесплатно
Отпечатано на компьютерной издательской системе с
Издательский отдел Института ядерных исследований
Российской академии наук
117312, Москва, проспект 60-летия Октября, 7а